Université de Montréal

Détection et caractérisation de naines brunes et exoplanètes avec un filtre accordable pour applications dans l'espace

par
Patrick Jon Ingraham

Département de physique
Faculté des arts et des sciences

Thèse présentée à la Faculté des études supérieures
en vue de l'obtention du grade de Philosophiæ Doctor (Ph.D.)
en Faculté des arts et des sciences

le 28 janvier, 2013

Université de Montréal
Faculté des études supérieures

Cette thèse intitulée:

Détection et caractérisation de naines brunes et exoplanètes avec un filtre accordable pour applications dans l'espace

présentée par:

Patrick Jon Ingraham

a été évaluée par un jury composé des personnes suivantes:

Pierre Bastien,	président-rapporteur
René Doyon,	directeur de recherche
Pierre Bergeron,	membre du jury
Jean-Luc Beuzit,	examinateur externe
Karen Waldron,	représentant du doyen de la FES

Thèse acceptée le: 28 janvier, 2013

RÉSUMÉ

Cette thèse porte sur la capacité à détecter des compagnons de faible intensité en présence de bruit de tavelures dans le contexte de l'imagerie à haute gamme dynamique pour l'astronomie spatiale. On s'intéressera plus particulièrement à l'imagerie spectrale différentielle (ISD) obtenue en utilisant un étalon Fabry-Pérot comme filtre accordable. Les performances d'un tel filtre accordable sont présentées dans le cadre du Tunable Filter Imager (TFI), instrument conçu pour le télescope spatial James Webb (*JWST*).

La capacité de l'étalon à supprimer les tavelures avec ISD est démontrée expérimentalement grâce à un prototype de l'étalon installé sur un banc de laboratoire. Les améliorations de contraste varient en fonction de la séparation, s'étendant d'un facteur $\sim$10 pour les séparations supérieures à 11 λ/D jusqu'à un facteur $\sim$60 à 5 λ/D. Ces résultats sont cohérents avec une étude théorique qui utilise un modèle basé sur la propagation de Fresnel pour montrer que les performances de suppression de tavelures sont limitées par le banc optique et non pas par l'étalon. De plus, il est démontré qu'un filtre accordable est une option séduisante pour l'imagerie à haute gamme dynamique combinée à la technique ISD. Une seconde étude basée sur la propagation de Fresnel de l'instrument TFI et du télescope, a permis de définir les performances de la technique ISD combinée avec un étalon pour l'astronomie spatiale. Les résultats prévoient une amélioration de contraste de l'ordre de $\sim$7 jusqu'à $\sim$100, selon la configuration de l'instrument. Une comparaison entre ISD et la soustraction par rotation a également été simulée. Enfin, la dernière partie de ce chapitre porte sur les performances de la technique ISD dans le cadre de l'instrument Near-Infrared Imager and Slitless Spectrograph (NIRISS), conçu pour remplacer TFI comme module scientifique à bord du Fine Guidance Sensor du *JWST*.

Cent quatre objets localisés vers la région centrale de la nébuleuse d'Orion ont été caractérisés grâce à un spectrographe multi-objet, de basse résolution et multi-bande (0.85-2.4 μm). Cette étude a relevé 7 nouvelles naines brunes et 4 nouveaux candidats de masse planétaire. Ces objets sont utiles pour déterminer la fonction de masse initiale sous-stellaire et pour évaluer les modèles atmosphériques et évolutifs futurs des jeunes objets stellaires et sous-stellaires. Combinant les magnitudes en bande H mesurées et

les valeurs d'extinction, les objets classifiés sont utilisés pour créer un diagramme de Hertzsprung-Russell de cet amas stellaire. En accord avec des études antérieures, nos résultats montrent qu'il existe une seule époque de formation d'étoiles qui a débuté il y a environ 1 million d'années. La fonction de masse initiale qui en dérive est en accord avec des études antérieures portant sur d'autres amas jeunes et sur le disque galactique.

Keywords : Instrumentation astronomique, planètes extrasolaires, techniques d'analyse de données, naines brunes, objet de masse planétaire, Orion, étalon Fabry-Pérot, JWST, imagerie spectrale différentielle.

ABSTRACT

This thesis determines the capability of detecting faint companions in the presence of speckle noise when performing space-based high-contrast imaging through spectral differential imagery (SDI) using a low-order Fabry-Perot etalon as a tunable filter. The performance of such a tunable filter is illustrated through the Tunable Filter Imager (TFI), an instrument designed for the James Webb Space Telescope (*JWST*).

Using a TFI prototype etalon and a custom designed test bed, the etalon's ability to perform speckle-suppression through SDI is demonstrated experimentally. Improvements in contrast vary with separation, ranging from a factor of $\sim$10 at working angles greater than 11 λ/D and increasing up to a factor of $\sim$60 at 5 λ/D. These measurements are consistent with a Fresnel optical propagation model which shows the speckle suppression capability is limited by the test bed and not the etalon. This result demonstrates that a tunable filter is an attractive option to perform high-contrast imaging through SDI. To explore the capability of space-based SDI using an etalon, we perform an end-to-end Fresnel propagation of *JWST* and TFI. Using this simulation, a contrast improvement ranging from a factor of $\sim$7 to $\sim$100 is predicted, depending on the instrument's configuration. The performance of roll-subtraction is simulated and compared to that of SDI. The SDI capability of the Near-Infrared Imager and Slitless Spectrograph (NIRISS), the science instrument module to replace TFI in the *JWST* Fine Guidance Sensor is also determined.

Using low resolution, multi-band (0.85-2.4 μm) multi-object spectroscopy, 104 objects towards the central region of the Orion Nebular Cluster have been assigned spectral types including 7 new brown dwarfs, and 4 new planetary mass candidates. These objects are useful for determining the substellar initial mass function and for testing evolutionary and atmospheric models of young stellar and substellar objects. Using the measured H band magnitudes, combined with our determined extinction values, the classified objects are used to create an Hertzsprung-Russell diagram for the cluster. Our results indicate a single epoch of star formation beginning $\sim$1 Myr ago. The initial mass function of the cluster is derived and found to be consistent with the values determined

for other young clusters and the galactic disk.

Keywords: Astronomical Instrumentation, Extrasolar Planets, Data Analysis and Techniques, Brown Dwarfs, Planetary Mass Objects, Orion, Fabry-Perot etalon, JWST, Spectral Differential Imaging

CONTENTS

RÉSUMÉ . . . . . **iii**

ABSTRACT . . . . . **v**

CONTENTS . . . . . **vii**

LIST OF TABLES . . . . . **x**

LIST OF FIGURES . . . . . **xi**

LIST OF ABBREVIATIONS . . . . . **xxiv**

DEDICATION . . . . . **xxvi**

ACKNOWLEDGMENTS . . . . . **xxvii**

CHAPTER 1: INTRODUCTION **1**

1.0.1 Planetary Atmospheres 3

1.0.2 Planet Detection Techniques 6

1.1 The Challenges of Direct Imaging 17

1.1.1 Diffraction 18

1.1.2 Aberrations 20

1.2 Direct Imaging Techniques 24

1.2.1 Adaptive Optics 24

1.2.2 Coronagraphy 26

1.2.3 Speckle Suppression Techniques 29

1.3 Recent Successes and the Future of High-Contrast Imaging Instrumentation 33

1.4 This Thesis 36

1.5 Student Declaration 38

Bibliography 40

CHAPTER 2: HIGH-CONTRAST IMAGING PERFORMANCE OF A TUNABLE FILTER FOR SPACE-BASED APPLICATIONS I: LABORATORY PERFORMANCE 48

2.1 Introduction 49
2.2 Test Bed Description 52
2.3 Etalon Prototype 55
2.4 Etalon Calibration 57
2.4.1 Calibration of Gap Size Versus Capacitance 58
2.4.2 Etalon Plate Parallelization 60
2.4.3 Verification of the On Orbit Calibration Procedure 60
2.5 Speckle-Suppression Performance 64
2.5.1 Simulated Performance 66
2.6 Discussion 68
2.7 Conclusion 72
Bibliography 72

CHAPTER 3: HIGH-CONTRAST IMAGING PERFORMANCE OF A TUNABLE FILTER FOR SPACE-BASED APPLICATIONS II: DETECTION AND CHARACTERIZATION CAPABILITIES 77

3.1 Introduction 78
3.2 The TFI Instrument 82
3.3 Optical Model 85
3.4 Planet-Detection with SDI 91
3.4.1 SDI Without a Coronagraph 96
3.5 Simulated SDI Observations of Known Systems 97
3.5.1 HR 8799 97
3.5.2 Fomalhaut b 99
3.6 Roll Subtraction 101
3.7 SDI with NIRISS 103

3.7.1 Atmosphere Characterization with NIRISS 105
3.8 Conclusion 106
Bibliography 109

CHAPTER 4: NEAR-INFRARED (*JHK*) SPECTROSCOPY OF YOUNG STELLAR AND SUBSTELLAR OBJECTS IN ORION . . 116
4.1 Introduction 117
4.2 Observations 119
4.2.1 Spectroscopic Observations 121
4.3 Spectroscopic Data Reduction 122
4.4 Spectral Classification 125
4.4.1 Spectral Fitting Procedure 128
4.4.2 Comparison to Previous Observations 138
4.5 Results 143
4.5.1 Early M Dwarfs 143
4.5.2 Brown Dwarf Candidates 145
4.5.3 PMO Candidates 146
4.5.4 Objects Exhibiting *J* Band Emission Features 148
4.6 Discussion 149
4.6.1 HR Diagram 150
4.6.2 Cluster Membership 153
4.7 Determination of the IMF 157
4.8 Conclusion 162
4.9 Acknowledgements 164
Bibliography 164
4.A Comparison to Previous Observations 167

CHAPTER 5: CONCLUSION 175

LIST OF TABLES

2.I The wavefront error budget of the test bed. 67

3.I TFI optimal coronagraphic configurations for a given separation. The number in the Lyot stop name is the throughput percentage. Each stop was designed to be used at specific separations and to be robust against pupil shear. 84

3.II The on-axis prescription of *JWST* and the TFI instrument. 88

4.I Summary of Spectroscopic Observations 122

4.II Properties of Observed Sources 130

4.III Adopted Temperature Scale 150

4.IV Previously Classified Objects 169

LIST OF FIGURES

1.1 Exoplanet candidates and their associated detection method. The 998 data points are from the Interactive Extra-solar Planets Catalog (Schneider 2010) as of May 23, 2012. Each detection method is subject to observational biases which limit the types of planets it can detect. 2

1.2 Luminosity vs time relationship for solar metallicity red dwarf stars (blue), brown dwarfs (green), and EGPs (red). The gold and magenta dots indicate when 50% of the deuterium and 50% of the lithium has burned, respectively. Due to the increased luminosity, younger EGP's are easier to image directly than their older counterparts. From Burrows et al. (2001). 4

1.3 Planet-to-star flux ratio for a 1 M_{Jup} EGP orbiting a G2V star at 4 AU as a function of age from 0.5 to 6.0 μm. The peak emission is observed at 4 μm which is only observable from space, however, the sharp peaks at shorter wavelengths can be utilized when performing direct imaging. From Burrows et al. (2004). 5

1.4 *Left:* Original light curve of HD209458, obtained using a 10 cm aperture ground-based telescope allowed the measurement of the planet radius to be 1.27 ± 0.02 $R_{\rm Jup}$ with a corresponding inclination angle of $87.1^\circ \pm 0.2^\circ$. The dotted lines show a light curve when the planets radius is 10% different from the determined value. From Charbonneau et al. (2000). *Right:* Follow-up observations using the Hubble Space Telescope yields a radius of 1.347 ± 0.060 $R_{\rm Jup}$, with an inclination angle of $86.68^\circ \pm 0.14^\circ$. Despite the increase in precision of the data from the Hubble Space Telescope, the radius and orbital inclination uncertainties remain relatively unchanged. This is because uncertainties in the mass and radius of the host star are the dominant source of error. From Brown et al. (2001). 9

1.5 Effects on the light curve of the lensing star possessing a planet. The properties of the light curve provide information on the planet to star mass ratio. Follow-up observations of the lens star are required to obtain its mass, which is then used to determine the mass of the planet. From Queloz (2006). 12

1.6 The observed light curve of the OGLE-2005-BLG-390. The black line shows the best-fitting model to the data, whereas the orange dashed line indicates the single lens model, where a planet is not present. The long-dashed grey curve indicates the best binary source model, the only other candidate for explaining the light curve. However, this model is rejected by the data. From Beaulieu et al. (2006). 13

1.7 The period variations of PSR1257+12. The solid line indicates the period changes predicted by the two planet system. From Wolszczan & Frail (1992). 16

1.8 Quantity of light scattered into the outer regions of the PSF is a function of the pupil shape. Each upper box, containing the pupil shape, has a side of 7 meters whereas each lower box, containing the focal plane, has a side of 1 mm. The pupils shown from left to right are: a 2.4 meter diameter aperture, a 6.4 meter diameter aperture, the same 6.4 meter diameter aperture with a 1m secondary mirror obstruction with supports, a 6.4 meter diameter segmented mirror with a secondary obstruction. All PSF's are computed using an effective focal length of 134 metres, and a wavelength of 2 μm and assume no intensity nor phase errors. All PSF's are displayed in a log scale. 19

1.9 Effects of atmospheric turbulence on the diffraction limited PSF of a telescope. The leftmost image shows a diffraction limited PSF. The centre image shows the effect of a long exposure, where the PSF is seeing limited. The rightmost image is a short exposure, where the atmosphere is frozen in time, and the atmospheric speckles are observed. Adapted from Hardy (1998). 21

1.10 Typical closed-loop adaptive optics imager. The wavefront sensor measures the instantaneous phase error which is used to calculate the required optical path difference in order to flatten the wavefront. This optical path difference is applied using a deformable mirror before the wavefront sensor allowing improvement on the original correction. From McLean (2008). 25

1.11 A Lyot coronagraph is used to reduce the light of the primary star's PSF. The core of the PSF is removed using an occulter at a focal plane, whereas the rings of the PSF are masked at a re-imaged pupil plane. Because coronagraphs require very high Strehl ratios to be efficient, they must be used in conjunction with adaptive optics, or in space. From Murakawa et al. (2004). 27

1.12 An dual imaging SSDI instrument splits the beam to create two images of adjacent wavelengths. Each channel is assigned a corresponding filter. Subtracting the resulting images removes the atmospheric speckles and exposes the difference in flux between the two wavelengths of the planet. An artificial companion which is 5 magnitudes fainter than its primary with a separation of 0.5″ has been inserted into image A. Although invisible in the original image, it is clearly visible in the difference image. From Racine et al. (1999). 30

1.13 When observing with a altitude-azimuth telescope mount, the telescope pupil orientation remains constant, however the field rotates throughout the observation. This is normally counteracted by the rotation of the instrument. In the case of ADI, this rotator is turned off to maintain the PSF stability. Image by Chris Thalmann. . . . 32

1.14 To date, only four exoplanetary systems orbiting main sequence stars have been directly imaged. *Top Left:* 1RXS J160929.1-210524 in Upper Scorpius (Lafrenière et al. 2008). *Top right:* Two epochs of Beta Pictoris b (Lagrange et al. 2010). *Lower right:* Formalhaut b (Kalas et al. 2008). *Lower left:* The three exoplanets surrounding HR 8799 (Marois et al. 2008). 34

2.1 Two system setups of the test bed. The three collimated beams of the calibration setup, shown in red, are passed through the etalon with the insertion of a pickoff mirror. Upon removal of the mirror, the f/28 science beam is passed through the etalon (shown in green). 53

2.2 Lyot mask used as the system stop in the test bed. The dark regions correspond to the transmissive regions of the mask. 54

2.3 The short-wave etalon prototype, conceptually identical to the TFI etalon but built to work at ambient temperatures with a bandpass of 0.9-2.0 μm. The three capacitive displacement sensors are shown with the threaded rod and springs holding the plates against their associated PZTs. 56

2.4 Measured spectrum (solid line) obtained at the largest possible operating gap. Overplotting a theoretical spectrum (dashed line) reveals a gap size of 7.88 μm. The theoretical spectrum includes an 8% loss due to Fresnel reflection. The difference in line width and intensity is expected of a poorly parallelized etalon. 59

2.5 **Left:** A basic schematic of the calibration components. Three pencil beams, each positioned near a capacitive displacement sensor, are propagated though the etalon and are focused onto a detector using an f/28 lens. **Right:** The three spots on the detector. The difference in intensity between the spot indicates the gap size is different at each pencil beam position on the etalon. 62

2.6 Stepping over order 5 of the 1.550 μm laser which corresponds to a gap of 3.889 μm. Channels 0, 1 and 2 are shown as black triangles, red diamonds, and blue squares respectively. Each channel's profile is fit using a Gaussian. **Left:** The original gap vs wavelength relationship containing a 480 nm wedge across the 40mm clear aperture. **Right:** The 12th iteration of the parallelization process yielding an mean offset of -2 nm from the desired gap with a 8 nm wedge across the aperture. The vertical line indicates the target peak for each channel. 63

2.7 **Left:** The 1.647 μm PSF obtained using the test bed. The upper right-hand corner shows a ghost. **Right:** The corresponding theoretical PSF obtained from the Fresnel propagation of the test bed. Each image has a field of view of 29' by 29'. 65

2.8 **Left:** The observed difference image between the 1.647 and 1.660 μm PSFs. **Right:** The corresponding theoretical difference image obtained using the Fresnel propagation of the test bed. Each image has a field of view of 29' by 29'. 66

2.9 Speckle-suppression performance of the etalon is determined by comparing the measured 1.647 μm PSF 5σ contrast curve (solid line) with the 5σ contrast curve of the difference image (dash-dotted line). Comparing the theoretical 5σ contrast curve for the 1.647 μm PSF (red long-dashed line) with that of the theoretical difference image (triple-dot-dashed line) shows the maximum achievable contrast assuming no etalon is present. The combined photon and readout noise limit is shown as the brown short-dashed line. The contrast curve is truncated at 22 λ/D (13.4') to avoid any contamination from the ghost. 69

2.10 The speckle-suppression performance limits based on different noise contributions. The form of the modeled 1.647 μm PSF 5σ contrast curve (solid black line) is dominated by the diffraction from the highly structured Lyot stop used in the test bed. The fundamental limit where no noise, no WFE, and no image manipulation error are present is shown as a dotted red line. The WFE of the optical components (orange dash-dotted line, virtually superimposed on the dotted red line) does not contribute an appreciable amount of error. The dominant effect on the measured contrast is the chromatic aberration induced by the lenses (blue dashed line). At large separations, the photon and readout noise become the limiting error source. 70

3.1 The optical design of the TFI instrument. The light from the telescope is directed into the instrument using the Pick-Off mirror that houses four occulters. The beam is then collimated and the filter and Lyot wheel reside at a conjugate pupil with the etalon located just afterwards. The three-mirror camera then focuses the beam onto the HAWAII 2-RG detector. 83

3.2 The simulated TFI coronagraphic PSFs at 4.220 μm (left) and 4.700 μm (center) shown in log scale. Their resulting difference image (right), shown in a linear scale, is created by radially scaling the 4.700 μm PSF inwards by the ratio of the wavelengths then subtracting the two images. The remaining speckle pattern is a result of the chromaticity of the Talbot effect. The positive-negative signature of a companion is seen towards the upper right. The field-of-view of each image is $8.9\times8.9''$ 87

3.3 Speckle-suppression achieved using a simple difference as a function of wavelength separation. The plotted portions of each coronagraphic setup show the regions of highest achievable contrast assuming a 2% pupil shear. The $0.75''$ occulter is not shown for clarity as it produces similar results to the $0.58''$ occulter and only exceeds its performance in the case of a larger pupil shear. The reduction in contrast with increasing wavelength separation is a result of the PSF speckle pattern decorrelating due to the Talbot effect. 92

3.4 The planet-to-star contrast corresponding to a 10σ detection of a companion for the $0.58''$ and $0.75''$ occulters and C71N Lyot stop. The solid curve shows the contrast achieved when no coronagraph is used. The dashed red curves indicate the coronagraphic performance for the given setup. The SDI contrast performance is dependent upon the companion's atmosphere. Two limiting cases are shown: a flat spectrum (blue dot-dashed line) and where the companion exhibits an extremely sharp spectral feature (purple dotted line). The optical wavelengths used for performing SDI with a given occulter is shown in each legend and justified in the text. . . 94

3.5 The planet-to-star contrast corresponding to a 10σ detection of a companion for the $1.50''$ and $2.00''$ occulters and C66N and C21N Lyot stops. The curves are identical to those described in Figure 3.4. 94

3.6 The planet-to-star contrast corresponding to a 10σ detection of a companion without using a coronagraph. The solid curve shows the contrast of the non-coronagraphic PSF. The case of a flat spectrum is shown as the blue dot-dashed line, where the case of the companion exhibiting an extremely sharp spectral feature is shown as the purple dotted line. The curves are identical to those described in Figure 3.4. The rightmost plot is a zoomed in section of the left plot to show the innermost working angles. 96

3.7 The difference image of the simulated HR 8799 system created from subtracting the 3.90 and 4.41 μm coronagraphic images using the $0.58''$ occulter with the C71N Lyot stop. Planets b, c and d are easily detected but planet e falls too close to the occulter to be accurately modeled. The difference image shown has a $3.9''$ by $3.9''$ field-of-view where each image corresponds to 10 minutes of exposure time. 98

3.8 The extracted fluxes of HR 8799 c (left) and d (right). Each wavelength corresponds to 10 minutes of exposure time. In both cases, TFI will be able to differentiate between the different cloud models. 99

3.9 The extracted spectro-photometry of Fomalhaut b after being observed for three hours at each wavelength. TFI will be able to detect and characterize Fomalhaut b if it is a self-luminous object on the order of 0.5 M_J. 100

3.10 Roll subtraction is an alternative method to SDI to attenuate speckles and is limited by pointing error. This plot shows the achieved contrast of a difference image obtained at 4.0 μm using roll subtraction with a roll angle of $\pm 5^{\circ}$, for two different pointing offsets. This figure illustrates that roll subtraction performs as well as SDI at small separations and surpasses the SDI performance at large separations. 102

3.11 The SDI performance using the NIRISS 3.8 and 4.3 μm filters (left) as well as the 3.8 and 4.3 μm filters (right). SDI offers a factor of $\sim$10-15 improvement in contrast depending on the separation. Contrary to non-coronagraphic measurements with TFI, there is no overwhelming advantage between detecting planets of varying spectral scenarios. 105

3.12 The SDI performance using the NIRISS 3.8 and 4.8 μm filters. SDI offers a factor of $\sim$5-10 improvement in contrast depending on the separation. No advantage is measured between the two companion spectral type scenarios. 106

3.13 The flux ratios of various Ames-Cond model atmospheres using three NIRISS filters. Each solid-colored line represents a different temperature and the dotted lines represent different surface gravities. The ovals indicate a 2.5% uncertainty. 107

3.14 The flux ratios of various Ames-Dusty model atmospheres using three NIRISS filters. Each solid-colored line represents a different temperature and the dotted lines represent different surface gravities. The ovals indicate a 2.5% uncertainty. 108

4.1 A mosaic of the north-west (right) and south-west (left) Orion *H* band pre-imaging observations. The blue arrows indicate the location of the objects where an accurate spectral type was determined. The red arrows indicate objects whose spectra indicated either a highly absorbed object (A_V>8) or an object showing only emission lines. 120

4.2 A range of fits are possible for object 038-112 whose spectrum has a relatively low S/N. The most-common fit is the M8.50 template, shown as the blue dashed line. The earliest and latest fits are shown as the red dash-dot and green dash-triple-dot lines. 135

4.3 Two fits to the same object (108-556) where the uncertainty in the wavelength solution dominates the spectral typing uncertainty. . . 136

4.4 Objects 080-117 (upper plot) and 095-059 (lower plot) are examples of objects flagged as having a "Mediocre fit" in Table 4.II. These objects spectra exhibit variations from the spectra in our spectral library resulting in an uncertainty in the spectral type. Their assigned spectral type and uncertainty should be regarded as subject to unaccounted uncertainty. 137

4.5 Comparison of our extracted spectra to the previously observed objects of Lucas et al. (2001) demonstrates the accuracy of our spectral reduction. In all cases, the reddening and reddening-law used by Lucas et al. (2001) was adopted for comparison. 139

4.6 Comparison of the spectral classification of object 055-230 as performed by Weights et al. (2009) (M9.5, red dash-dot line) and this work (M6.0, blue dashed line). The observed spectrum of this object was also the subject of Figure 4.5 and shown to exhibit the same spectral shape in H and K bands as previous observations. This demonstrates the usefulness of SED fitting over large bandpasses. 140

4.7 Comparison of the inconsistent spectral type classifications between our work and Weights et al. (2009). In both cases, the blue dashed line indicates the spectral template for our classification, whereas the red dash-dot-dash line indicates the spectral template associated with the previous classification. 142

4.8 This shows a subset of the objects having spectral types between M1 and M5.75. This spectral range corresponds to the temperature range of M stars having a mass greater than the hydrogen burning limit assuming a cluster age of 1 Myr. 144

4.9 This is a subsample of the objects having a spectral classification between M6 and M8.5. This corresponds to the temperature range for brown dwarfs when an age of 1 Myr is assumed. The red line indicates the best fitting spectral template (shown in the label) to the observed spectra. 146

4.10 Spectra of all objects with spectral classifications greater than M8.75. This corresponds to the temperature range for objects in the planetary mass regime (M<13M_J) assuming an age of 1 Myr. The red solid line indicates the best fitting spectral template (shown in the label) to the observed spectra. 147

4.11 Objects showing *J* band emission features that influence the spectral classification. In all cases, the emission appears to originate from the actual object and not from adjacent nebular contamination. The red line indicates the best fitting spectral template (shown in the label) to the observed spectra. 149

4.12 HR diagram of all of classified objects. Objects exhibiting *J* band emission features (that potentially jeopardize the spectral characterization) are indicated by a black '×'. The solid, triple-dot-dash, dashed, and long-short-dashed lines represent evolutionary models for cluster ages of 1, 5, 10 and 50 Myr respectively. 152

4.13 Comparison of objects 077-127 and 064-315 to the best fitting low gravity spectral template (dashed blue line) and a high gravity synthetic spectrum (red dash-dot line) indicative of a foreground field dwarf. 154

4.14 Comparison of object 077-452 and 016-534 to the best fitting low gravity spectral template (dashed blue line) and a high gravity synthetic spectrum (red dash-dot line) indicative of a foreground field dwarf. Because both objects are generally well fitted by both low-gravity objects and field dwarfs, their membership to the cluster is uncertain. 156

4.15 The *H*-band luminosity function of our survey. The solid black line indicates all point sources in the field. The blue dot-dashed line indicates all objects for which we have assigned a spectral type. The red dashed line indicates all objects for which we have a spectral type or have been spectroscopically determined to either have high extinction (A_V>8) or to be non-stellar. 158

4.16 The IMF derived from our survey. The red solid line indicates our best fit of a log-normal distribution to the corrected data. The dashed and dot-dashed orange lines represent the Chabrier (2003) IMF and system IMF respectively. The dashed blue line represents the IMF fit derived by Rio et al. (2012). 161

4.17 Comparison of the spectral classification of object 023-123 as performed by Weights et al. (2009) (>M9.5, represented as L0, red dash-dot line) and this work (M6.25, blue dashed line). 172

LIST OF ABBREVIATIONS

ADI	Angular Differential Imagery
ALTAIR	ALTtitude conjugate Adaptive optics for the InfraRed
AO	Adaptive Optics
AU	Astronomical Unit
BD	Brown Dwarf
CoRoT	COnvection ROtation and planetary Transits
DM	Deformable Mirror
EGP	Extrasolar Giant Planet
E-ELT	European Extremely Large Telescope
ELT	Extremely Large Telescope
EPICS	Exo-Planet Imaging Camera and Spectrograph
ExAO	Extreme Adapative Optics
FGS	Fine Guidance Sensor
FOV	Field of View
FSM	Fine Steering Mirror
FWHM	Full Width at Half Maximum
GPI	Gemini Planet Imager
HiCIAO	High-Contrast Coronagraphic Imager for Adaptive Optics
HARPS	High Accuracy Radial velocity Planet Searcher
HST	Hubble Space Telescope
IFS	Integral Field Spectrometer
JWST	James Webb Space Telescope

MIRI	Mid-Infrared Imager
NASA	National Aeronautics and Space Administration
NIRCam	Near Infrared Camera
NIRSpec	Near Infrared Spectrograph
NIRISS	Near Infrared Imager and Slitless Spectrograph
NRM	Non-Redundant Mask
OPD	Optical Path Difference
OTE	Optical Telescope Element
PECO	Pupil-Mapping Exoplanet Coronagraphic Observer
PIAA	Phase Induced Amplitude Apodization
PMO	Planetary Mass Object
PSF	Point Spread Function
PTV	Peak-to-Valley
PZT	Piezoelectric Transducers
RV	Radial Velocity
SCExAO	Subaru Coronagraphic Extreme Adaptive Optics
SED	Spectral Energy Distribution
SPHERE	Spectro-Polarimetric High-Contrast Exoplanet Research
S/N	Signal-to-noise ratio
SDI	Spectral Differential Imagery
SSDI	Simultaneous Spectral Differential Imagery
TFI	Tunable Filter Imager
TRIDENT	TRiple-Imageur DÉcouvreur de Naine T
VLT	Very Large Telescope
WFE	Wavefront Error
WFS	Wavefront Sensor

Pour ma femme,

Sandrine Jacqueline Claudine Ingraham

ACKNOWLEDGMENTS

Numerous people have provided support throughout the course of my thesis to which I wish to express my gratitude. First and foremost is my advisor, René Doyon, whose patience, knowledge, perseverance and experience has been invaluable. Furthermore, his attention to detail, work ethic, and desire to push technology to further scientific research, is nothing short of inspirational. I also wish to thank Roberto Abraham, Neil Rowlands and Alan Scott who have all greatly contributed to my understanding and experience in the fields of astronomical science and instrumentation. Working with with David Lafrenière, Etienne Artigau and Loic Albert has also been a great pleasure. I also want to acknowledge my officemates Lison Malo, Denise Laflamme, and Mathilde Beaulieu who have patiently listened to me stumble over my words and have helped me navigate the french language for several years. Finally, I wish to acknowledge my family. They have been a constant source of support throughout my entire education. For their patience and understanding I am deeply indebted.

CHAPTER 1

INTRODUCTION

Less than two decades ago, the only known planets in the Universe were those in our solar system. However, the last twenty years have been revolutionary for the field of planetary science leading to the construction of future ground and space-based missions specifically designed for exoplanet detection. The first confirmed planetary mass objects orbiting an extrasolar object were found around the pulsar PSR 1257+12 using radio telescopes (Wolszczan & Frail 1992). Although this system is not a typical star/planet system, the discovery fuelled the possibility of detecting exoplanetary systems analogous to our solar system. With the discovery by Mayor & Queloz (1995) of a Jupiter-mass companion to 51 Pegasi, a solar like star, the age of extrasolar planet detection and characterization had begun.

The detection of exoplanets is challenging due to the dominance of the host star, to both the fractional contribution to the centre of mass and the system's total luminosity therefore detection of an orbiting planet requires measurements of extreme precision. Depending on the system's properties, some detection strategies are better suited than others. Therefore, in order to gain a complete and thorough understanding of the exoplanet population, several approaches must be considered. No single detection method can extract all the necessary information to explain the formation and frequency of exoplanets.

With the development of new technologies, new observing techniques, and a more detailed understanding of both stellar and planetary atmospheres, the frequency of discoveries has increased significantly. Figure 1.1 shows the 998 candidate planets as of May 23, 2012, which have been detected using a variety of methods. Currently, there are no known planets orbiting a sun-like star with a mass equal to or less than that of Earth (Schneider 2010), however, this statistic is most likely the representation of a selection effect which occurs because more massive objects are easier to detect. Understanding the observational biases is a critical aspect of comprehending exoplanets frequency and

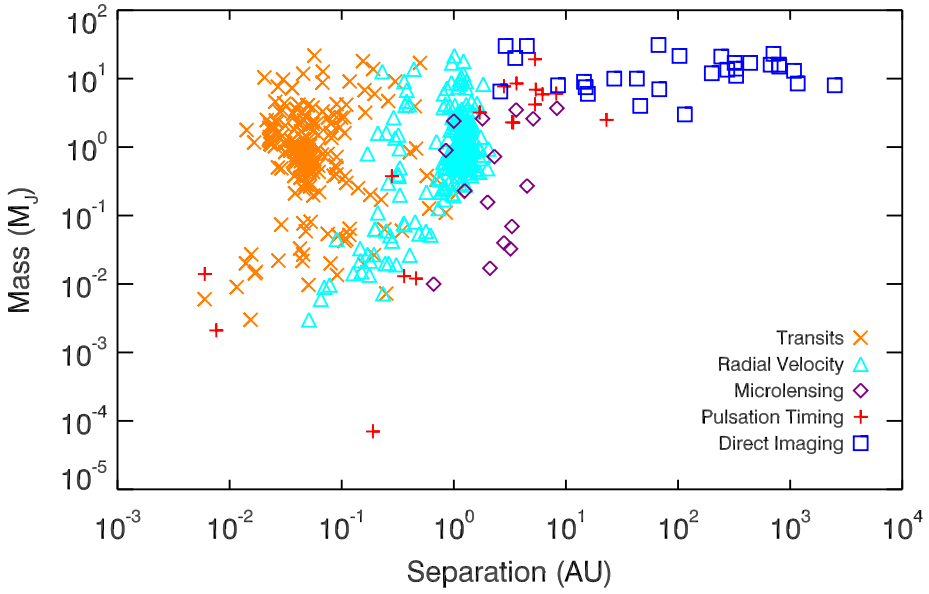

Figure 1.1: Exoplanet candidates and their associated detection method. The 998 data points are from the Interactive Extra-solar Planets Catalog (Schneider 2010) as of May 23, 2012. Each detection method is subject to observational biases which limit the types of planets it can detect.

formation mechanisms. The ability to detect a planet is not only affected by its mass, size, and separation but also its atmospheric properties. The atmospheric component is especially important when considering the direct imaging of a companion. Utilizing the atmospheric features permits increased detection probability by exploiting its properties which differ greatly from the host star.

In this chapter, I summarize the different techniques of exoplanet detection and how they overcome the difficulties imposed by the large luminosity and mass differences between the planet and star. The introduction discusses the different types of exoplanets and their atmospheres with emphasis on the spectral features that facilitate their characterization and detection. The main exoplanet detection methods with their observational limits and biases are then discussed. The direct imaging method and its specific challenges are discussed in depth in section 1.1. Several partial solutions and their limitations are explained in section 1.2, as well as the ability to combine their information to obtain a more complete physical understanding of the star and exoplanet system. The past

achievements and future of direct imaging are discussed in section 1.3. This thesis, outlined in section 1.4, characterizes the performance of a new technique used to directly image exoplanets using a space-based telescope.

1.0.1 Planetary Atmospheres

Prior to the discovery of exoplanets, the field of planetary science was limited to studying only the planets in our own solar system. Due to the obvious differences in composition and orbital separation, the field was generally divided into two categories: terrestrial planets and gas giants. Many of the same difficulties are encountered when searching for both Earth-like planets and gas giants. However, the difficulty is a function of the planet's mass, luminosity, and orbital separation, therefore extrasolar giant planets (EGPs) are more easily detected than Earth-like planets. For this reason, this paper places less emphasis on detecting Earth-like planets and focuses on EGPs and the atmospheric properties which affect their detectability and characterization.

1.0.1.1 Extrasolar Giant Planets

In many respects, EGPs share many similarities with brown dwarfs (BD). A BD is defined as a sub-stellar object with an insufficient mass to sustain hydrogen burning. Although the mass at which hydrogen is able to fuse is dependent upon the metallicity, these bodies generally have masses ranging from 75 $M_{\rm Jup}$ to 13 $M_{\rm Jup}$ (Spiegel et al. 2011). The evolution of a BD is relatively simple, burning deuterium and lithium very early in their evolution then cooling and compressing over time. For objects with a mass below 13 $M_{\rm Jup}$, there is insufficient mass to maintain the burning of deuterium. These objects are known as sub-brown dwarfs, rogue planets, or free-floating planets, should they not be orbiting a star. These objects never have an internal heat source, therefore they only cool and compress over time.

EGP's exhibit many of same traits as BDs. Both types of objects experience fully convective cores, spectra dominated by molecular bands, an evolution that is not driven by an internal heat source, and their emissions are primarily in the infrared. Depending

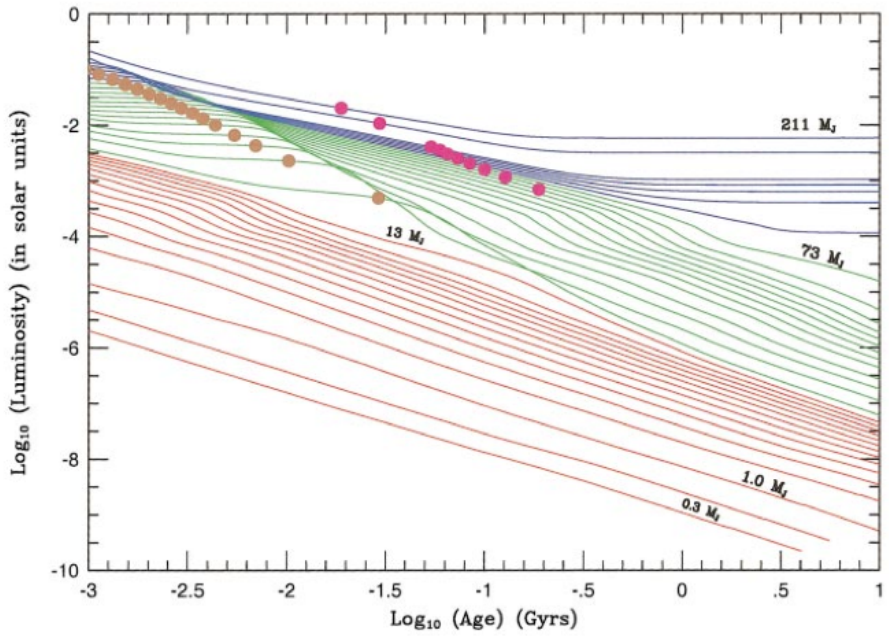

Figure 1.2: Luminosity vs time relationship for solar metallicity red dwarf stars (blue), brown dwarfs (green), and EGPs (red). The gold and magenta dots indicate when 50% of the deuterium and 50% of the lithium has burned, respectively. Due to the increased luminosity, younger EGP's are easier to image directly than their older counterparts. From Burrows et al. (2001).

on the orbital separation, mass, age and composition, the temperatures of EGP's may range from ∼100K to ∼2000K (Sudarsky et al. 2003). The luminosity versus time relationship for solar metallicity red dwarf stars, brown dwarfs, and EGP's are shown in Figure 1.2 (Burrows et al. 2001).

The luminosity for a main sequence star becomes relatively constant with time after the start of hydrogen burning which is shown by the blue lines in Figure 1.2. For both brown dwarfs and exoplanets, the luminosity is seen to steadily decrease with age. This infers that if an observer aims to detect the photons emitted from the planet, it will be easier if the planet is younger. For example, if one considers a Sun-Jupiter system analogue, a young Jupiter is 1000x brighter than an old Jupiter (like ours). Naturally, the spectrum of a sub-stellar object is a function of mass, radius, age, and composition. This makes identification more difficult due to the large parameter space. However, for an

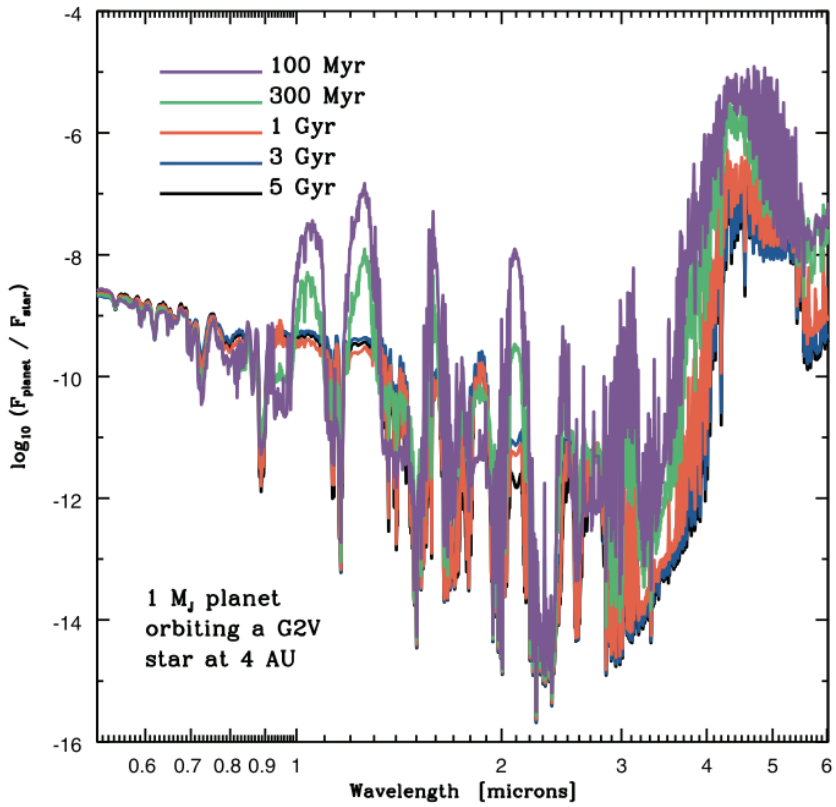

Figure 1.3: Planet-to-star flux ratio for a 1 M_{Jup} EGP orbiting a G2V star at 4 AU as a function of age from 0.5 to 6.0 μm. The peak emission is observed at 4 μm which is only observable from space, however, the sharp peaks at shorter wavelengths can be utilized when performing direct imaging. From Burrows et al. (2004).

exoplanet, the metallicity can be inferred from the parent star, since they form from the same cloud or conglomeration of material. This parameter is of particular importance due to the dominance of molecular features in its spectrum. The spectra of EGP's are dominated by CO_2, CH_4, H_20, and NH_3 absorption features, whose depths are primarily dependant upon temperature, which is a function of age. These differences are shown in Figure 1.3, where a 1 $M_{\rm Jup}$ planet is shown as a function of age (Burrows et al. 2004). The spectrum of an exoplanet varies significantly with orbital radius (Fortney et al. 2007). This is due to the irradiation of the planet from the light of the host star which adds significant energy to the upper atmosphere (Baraffe et al. 2003; Barman et al. 2005; Sudarsky et al. 2003). Having knowledge of a suspected exoplanet's spectrum prior to

observation can be advantageous when attempting to image a planet directly. This is discussed in greater detail in section 1.2.3.1.

1.0.1.2 Terrestrial Planets

The discovery of a habitable planet is often considered the primary scientific objective of planet finding. Naturally, not every terrestrial planet is habitable (e.g. Mercury), therefore a study of their atmosphere is necessary. The *Habitable Zone* is considered to be the orbital radius at which liquid water can exist (Kasting & Catling 2003, and references therein). This distance is dependent upon the luminosity of the host star, with the cooler stars having habitable zones closer in (Joshi et al. 1997). The distance from the host star is important because the orbital periods of these planets are smaller. Both the distance and period have implications on their detectability. This is discussed in more detail in the following sections.

The presence of liquid water can be detected using the absorption bands in the atmosphere's spectra. Other molecular bands are of interest as well, such as CO_2 because of its relative ease of detectability, and also CH_4 and O_3. These molecules are referred to as *biomarkers* because they are formed from biological processes and indicate the presence of life. Unfortunately, detecting these compounds is difficult because the light coming from a terrestrial planet is dominated by reflected light, and not light which is emitted from the planet itself. However, the wavelength dependence of the planet's reflected light, or *albedo*, offers insight into its composition. The reflected light is expected to be detected prior to the planets actual photons (Cahoy et al. 2010). Terrestrial planet spectroscopy is currently beyond the capabilities of all existing instruments, however, such information is vital to keep in mind when designing future planet finding missions.

1.0.2 Planet Detection Techniques

The large contrast difference between the host star and exoplanet makes the traditional astronomer's *point and shoot* imaging and spectroscopy methods impossible with standard instruments. For this reason, several indirect methods are used to sample the

many different types of planets of varying mass and semi-major axis. Each type of observation possesses different strengths and weaknesses which are discussed in the following subsections. A combination of methods is often used to confirm a detection and to extract more physical information about the planet's characteristics.

1.0.2.1 Radial Velocity

The radial velocity (RV) method senses the presence of planets by measuring the central star's motion with respect to the centre of mass, or barycentre, via its Doppler shift. The difference in wavelength between a spectral line from an observed source and a calibrated source (e.g. a hydrogen lamp) allows the determination of the velocity along the line of sight of the host star. The radial velocity (V_{R}) and orbital velocity are related by the sine of the inclination angle i. Using the equations for the centre of mass and Kepler's third law, the radial velocity can be related to the planets mass (M_{pl}), the stellar mass (M_*), the semi-major axis a, and the gravitational constant G, as shown in equation 1.1.

$$V_{\mathrm{R}} = M_{\mathrm{pl}} \sin(i) \left(\frac{G}{a M_*} \right)^{1/2} \tag{1.1}$$

Assuming the stellar mass is known, observing the radial velocity over the full cycle of a planet's orbit provides information on the semi-major axis, eccentricity, period, and planet's mass. Moreover, these measurements are all independent of the distance to the system. The large disadvantage is that the masses are always a function of the inclination angle, which cannot be measured using the RV technique. Therefore, the derived masses of the planets are only lower limits. If the companion also transits in front of the star, this ambiguity can be resolved, and the mass of the planet can be determined. The transit method is discussed in the next section.

Current instrumentation to detect exoplanets, like the High Accuracy Radial velocity Planet Searcher (HARPS, Mayor et al. 2003), uses highly stabilized spectrographs with a simultaneous wavelength calibration system. Observations are focused around stable stars, normally of spectral types F,G and K. The age of the star is also an important fac-

tor, young stars have too few spectral lines whereas late type stars are too faint. Another promising endeavour is the search of planets in the habitable zone around M-stars. Because the habitable zone is at smaller orbital separation ($\sim$0.1 AU), the orbital periods are shorter and therefore more easily detectable. However, the active nature of M-stars increases the difficultly of performing the measurement. A recently proposed instrument aims to overcome this difficultly by performing spectropolarimetry in the infrared (Donati 2010). Any stellar oscillations (eg. star spots) modify the magnetic field resulting in the polarization of light. Therefore observing in a polarimetric mode allows the separation of the signal induced by the star vs the signal induced by the planet. Future extremely large telescopes (ELTs) will also have high resolution spectrographs, such as CODEX, for the European Extremely Large Telescope (E-ELT) (Pasquini et al. 2010).

The measurement uncertainty of radial velocities has four contributing effects: instrumental noise, stellar oscillations, photon noise and signals from unseen planets. The latter two are resolved by simply increasing observation time, whereas the effects of stellar oscillations can be reduced by proper target selection and stellar modelling, or observing in a polarimetric mode. Current instrumentation has already allowed the detection of 705 planets via radial velocity. The star HD 40307 (K0V) is known to have 3 super-earths in orbit, with masses of 4.2, 6.9 and 9.2 Earth masses and periods of 4.3, 9.6 and 20.5 days (Mayor et al. 2009). These observations had an average uncertainty of 32 cm/s, whereas detecting an Earth-mass planet requires approximately 5–10 cm/s accuracy (Vogt 2009).

1.0.2.2 Transits

When an exoplanet passes in front of its host star, the measured flux of the star is reduced. Once the planet no longer intercepts the line of sight between the observer and star, the luminosity returns to its normal level. This photometric measurement, referred to as a *light curve*, contains within its shape a wealth of information about both the star and planet.

If the mass of the host star is known, which is often derived from stellar evolution models, the characteristics of the light curve can be used to obtain several properties of

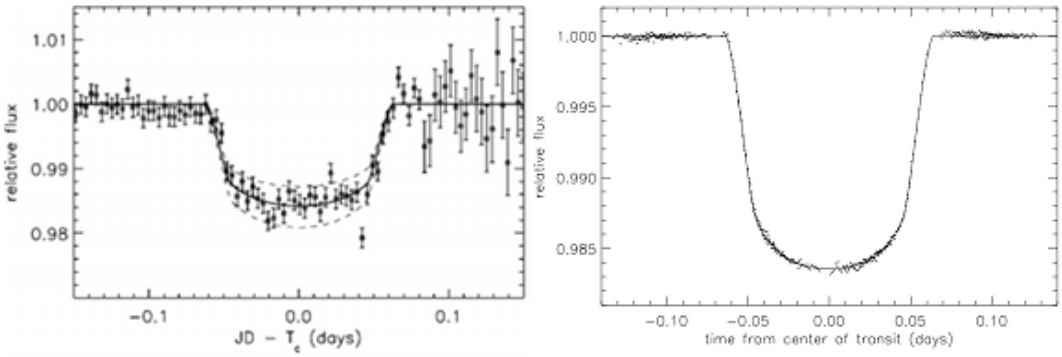

Figure 1.4: *Left:* Original light curve of HD209458, obtained using a 10 cm aperture ground-based telescope allowed the measurement of the planet radius to be 1.27 ± 0.02 $R_{\rm Jup}$ with a corresponding inclination angle of $87.1^\circ \pm 0.2^\circ$. The dotted lines show a light curve when the planets radius is 10% different from the determined value. From Charbonneau et al. (2000). *Right:* Follow-up observations using the Hubble Space Telescope yields a radius of 1.347 ± 0.060 $R_{\rm Jup}$, with an inclination angle of $86.68^\circ \pm 0.14^\circ$. Despite the increase in precision of the data from the Hubble Space Telescope, the radius and orbital inclination uncertainties remain relatively unchanged. This is because uncertainties in the mass and radius of the host star are the dominant source of error. From Brown et al. (2001).

the system. Observing successive transits of an extrasolar planet passing in front the host star is a direct calculation of the orbital period. This alone allows the calculation of the orbit's semi-major axis and orbital speed using Kepler's Laws (and assuming a circular orbit). The length of the transit gives information about the inclination angle and the curvature of the light curve gives information about the stellar limb darkening. The depth of the light curve is a function of the square of the ratio between the radius of planet and the stellar radius. Therefore, if the light curve is sufficiently well sampled, one may obtain the star and planet radii, the angle of inclination, and information about the stellar limb darkening. When this information is combined with the mass derived using the RV method, a measurement of the average density is obtained. This critical parameter provides insight on whether the planet is terrestrial or gaseous.

The probability of observing a transit is proportional to the stellar radius divided by the semi-major axis of the orbit. Therefore, planets with smaller semi-major axes are observed more frequently. Moreover, planets with large orbital inclinations will not

transit, making detection impossible via a simple light curve. The light curve alone does not provide any information about the planet's atmosphere or mass. However, due to the on-off nature of the eclipse, it is possible to obtain information about the optically thin edges of the atmosphere via spectroscopy during the transit, as was performed on HD209458 by Charbonneau et al. (2002). This type of observation is advantageous because unlike direct imaging, it is not necessary to isolate the light from the planet from the light from the star. If we assume the planet emits like a blackbody, the effective temperature of the planet (T_{eff}) can be approximated using equation 1.2, where σ is the Stephan-Boltzmann constant and R_p is planetary radius determined from the depth of the light curve. The planet's flux (F_p) is determined by measuring the difference in flux between when the planet is beside the star, and during the second eclipse, where it is behind the star and no light from the planet reaches the observer.

$$F_p = 4\pi R_p^2 \sigma T_{eff}^4 \tag{1.2}$$

The major shortcomings of the transit technique is the large number of false detections, primarily due to stellar variability, and the inability to measure the planet's mass. These issues can be largely resolved when combining the measured orbital information via the transit method, with the information obtained using the radial velocity method.

To date, 231 planets have been discovered using the transit method and confirmed using RV measurements. Nearly all of these objects lie outside the habitable zone. One exception is Kepler-22b, a super-earth orbiting a solar-type star that has been confirmed as residing inside the habitable zone (Borucki et al. 2012). More planet discoveries such as this one are expected from both the CoRoT (Barge et al. 2008) and Kepler (Basri et al. 2005) space missions over their lifetimes. Characterizing the atmosphere of an exo-earth using the method described in the paragraph above is not possible using any current telescopes. However, with the James Webb Space Telescope, to be launched in 2018, a very basic detection of an atmosphere may be possible for super-earths orbiting M-type stars. A great concern of the habitability of a planet orbiting an M-star is the large temperature difference caused by the tidal locking of their rotation periods. This temperature

difference would be partially smoothed out if an atmosphere is present due to its circulation. Using *JWST* mid-infrared photometry, if a day-to-night temperature difference is measured, it is a strong indication an atmosphere is present, even without spectroscopy (Deming et al. 2009). Such an observation would make the object an excellent candidate for spectroscopic follow-up with future missions.

1.0.2.3 Microlensing

A consequence of general relativity, the most direct path of a photon (a geodesic) is modified when in the presence of a gravitational potential. Therefore, if a lensing object of mass M_L, creating a gravitational potential at a distance d_L, passes directly between the observer and a distant source at a distance d_S, the image of the distant source is modified. In the case of a strong lens, where the gravitational field is very large (ie. a galaxy cluster), a perfect ring will be formed of radius θ_E, the Einstein radius, which is given by equation 1.3, where G is the gravitational constant and c is the speed of light.

$$\theta_E = \left(\frac{4GM_L}{c^2} \, \frac{(d_S - d_L)}{d_L d_S} \right)^{1/2} \tag{1.3}$$

In the case of weak lensing, the path is only slightly deviated, and the ring cannot be resolved. Therefore, the observed effect is a smooth brightening and dimming of the distant object as the lensing object passes through the line of sight. This effect generally occurs over the period of several weeks. If the lensing object has a planet, the light curve is of a particular nature, as shown in Figure 1.5. The change in magnification with time is a non-linear function dependent upon the the projected distance in units of the Einstein radius between the observer and the lens. Although more massive objects do create a larger magnification, if the alignment of the lensing star and planet is good, very low mass sources are detectable.

If the lensing star possesses a planet, the planet's orientation with respect to the star will cause a secondary effect on the magnification. If the planet is directly along the line of sight between the observer and the background source, the magnification will appear as a uniform curve. However, should the planet be adjacent to the lensing star, the planet

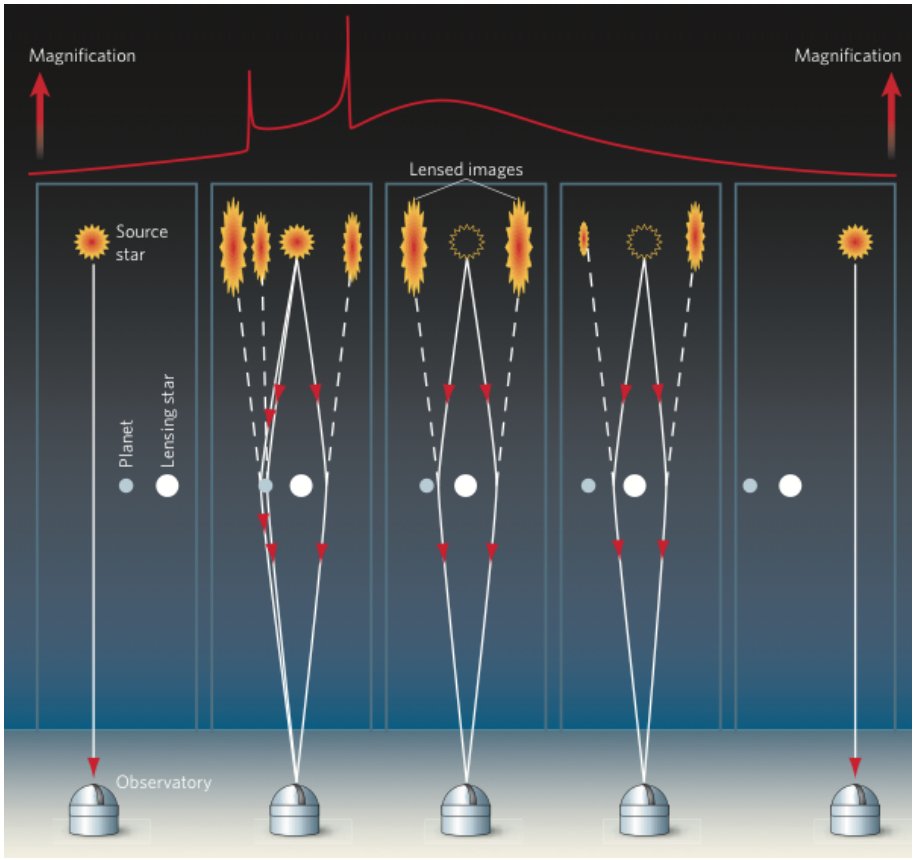

Figure 1.5: Effects on the light curve of the lensing star possessing a planet. The properties of the light curve provide information on the planet to star mass ratio. Follow-up observations of the lens star are required to obtain its mass, which is then used to determine the mass of the planet. From Queloz (2006).

will cause a lens as well, providing further magnification and a sharp intensity peak. As the planet passes the point of strongest magnification, the primary star becomes the dominant lensing source, and the magnification becomes dominated by the lens star, as shown on the right side in Figure 1.5. Using the light curve, the planet to star mass ratio, and the orbital separation can be directly determined. Follow up observations of the lens star determines its distance and spectral type, which allows the determination of the stellar and planet masses. The variation on the light curve is also sensitive to multiple planets (Wambsganss 1997).

Because there is no control over the lensing source, there is very little observational

bias towards certain types of host stars. Moreover, microlensing is most sensitive to planets whose orbital radii are on the order of 1 θ_E, but if the alignment is good, very small masses can be detected. Figure 1.6 shows the light curve of OGLE-2005-BLG-390Lb, a 5.5 Earth mass planet at a separation of 2.6 AU from an M-dwarf star. However, even if the alignment is poor, very large masses can still be detected. This allows a large coverage of parameter space for a wide range of stellar types, which provides a unbiased sample to test the planet formation theories. Moreover, microlensing is able to detect planets around stars which lie at large distances (several kpc) therefore allowing a measurement of planet frequency vs galactic radius. No other method allows such a calculation.

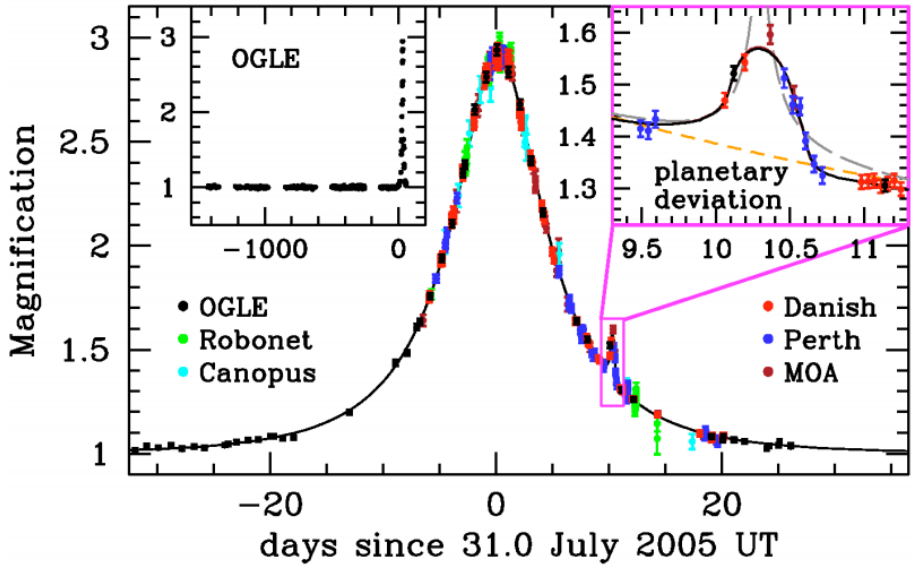

Figure 1.6: The observed light curve of the OGLE-2005-BLG-390. The black line shows the best-fitting model to the data, whereas the orange dashed line indicates the single lens model, where a planet is not present. The long-dashed grey curve indicates the best binary source model, the only other candidate for explaining the light curve. However, this model is rejected by the data. From Beaulieu et al. (2006).

The probability of a disc star lensing a bulge star is $\lesssim 10^{-6}$, therefore large numbers of bulge stars must be simultaneously monitored in order to observe a significant amount of lenses (Gould & Loeb 1992). This high stellar density requirement makes observing

from space the ideal environment, where the telescopes resolution limit is not defined by the atmosphere (Bennett et al. 2004). To date, 15 planets have been discovered via microlensing (Schneider 2010).

1.0.2.4 Astrometry

Similar to the RV method, an astrometric measurement is performed by measuring the gravitational effect of a planet on the host star via the angular shift in position of the star with time. Given a sufficient number of data points, fitting an ellipse yields all of the orbital parameters of the star about the system's centre of mass, including the orbital inclination. For the simplified case of a non-inclined circular orbit, the angular displacement (α) about the centre of mass over one period (T) is given by equation 1.4. Therefore, if the host star's mass (M_*) and distance (d_*) is known, the measurement of α and T can be used to determine the mass of the planet.

$$\alpha[radians] = \frac{m_p}{d_*}\left(\frac{G}{4\pi^2}\right)^{1/3}\left(\frac{T}{M_*}\right)^{2/3} \tag{1.4}$$

Contrary to the RV and transit methods, and similarly to direct imaging, astrometry is more sensitive to detecting planets with large separations. Another advantage is that astrometric detections can be performed on several different stellar types, which provides an unbiased sample of environments when doing statistical analyses. The disadvantages of the astrometric measurement technique is that in order to determine the orbit, several epochs must be observed. In the case of large separations, this could be on the order of a decade. Performing high precision astrometric measurements from the ground is limited due to the incoherent blurring of the atmosphere. Detecting a Jupiter around the Sun at a distance of 10 pc requires a precision of 0.49 milliarcseconds, therefore any astrometric detection of planets must be done from space.

To date, no exoplanets have been discovered using this technique. However, the presence of already discovered exoplanets has been confirmed, the first of which was Gliese 876 by Benedict et al. (2002), using the Hubble Space Telescope (*HST*). The astrometric sensitivity of *HST* is on the order of a few milliarcseconds. The future space

mission Gaia will have an astrometric precision on the order of 10 microarcseconds and is expected to detect and measure the orbits and masses of 700 EGPs with masses greater than 2-3 M_{Jup} within 50 pc (Casertano et al. 2008). These objects will also be very good candidates for direct imaging. Finding Earth-like planets requires sensitivities far beyond that of Gaia. For an Earth-mass planet orbiting a solar mass star at 1 AU at a distance of 10 pc, the astrometric amplitude is 0.6 microarcseconds. Such precision requires a space-based interferometer such as the proposed space observatory SIM Lite (Unwin et al. 2008).

1.0.2.5 Pulsation Timing

Analogous to transit observations, it is possible to detect orbiting bodies by examining the variation in flux originating from the system even if the companions are not transiting the object. The first confirmed planetary mass objects were detected by examining the constant pulsations originating from their host, pulsar PSR 1257+12, at radio wavelengths. A pulsar is an extremely dense, fast rotating neutron star whose rotation and magnetic field axes are mis-aligned. This results in a pulse of flux occurring whenever the neutron star rotates such that a magnetic pole is directed towards the observer. When the pulsar is part of a multiple bodied system, the objects orbit a common centre of mass. The periodic variation in the physical position of the pulsar results in the time interval between the pulses, or the frequency of the pulses, to arrive early or late relative to its mean value, as shown in Figure 1.7. By measuring the oscillations about the mean as a function of time, the masses and separations for the companions can be deduced.

Although the precision of the pulsar's timing permits an unparalleled mass determination, the fundamental problem behind studying planets around pulsars is that there is no information regarding planets' sizes, compositions, nor atmospheres. Furthermore, planets orbiting pulsars do not appear to be very abundant. To date, only 16 planets orbiting pulsars have been found. However, planetary mass objects orbiting pulsating stars have also been discovered.

Certain phases in stellar evolution promote pulsations inside stars that can be determined from variations in their intensity. The field of astroseismology exploits the

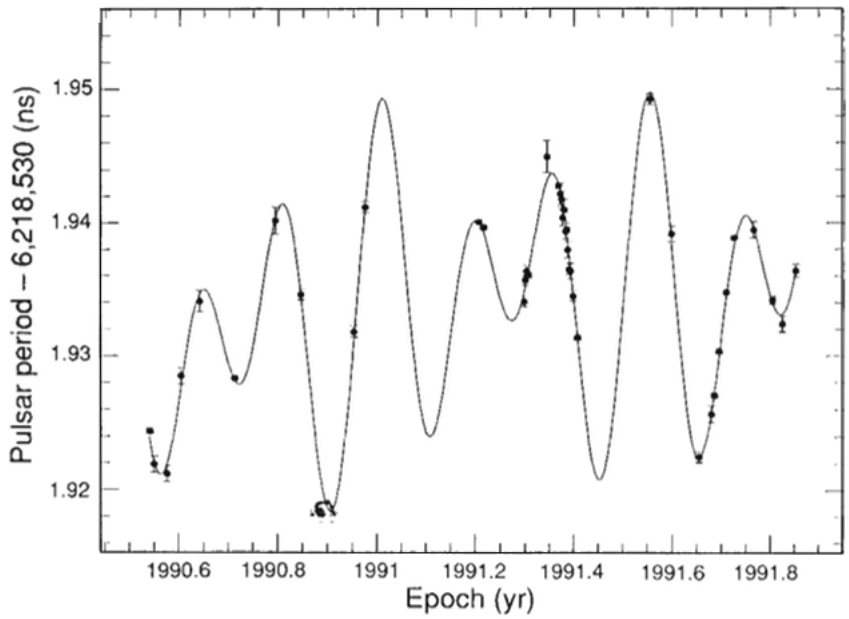

Figure 1.7: The period variations of PSR1257+12. The solid line indicates the period changes predicted by the two planet system. From Wolszczan & Frail (1992).

intensity variations to measure stellar pulsation which in turn can be used to constrain the internal structure of stars. In studying the pulsations of subdwarf star KIC05807616 with the Kepler space telescope (Basri et al. 2005), small intensity variations, at frequencies too low to be a result of stellar pulsation, were discovered (Charpinet et al. 2011). This signal is attributed to reflected light off the surface of two planets orbiting the star at 0.0060 and 0.0076 AU. Studies using this method are in their infancy and hence only the two planets mentioned previously have been discovered using this technique. Findings such as these are made possible by the continuous long-term, high-cadence, high signal-to-noise observations of the Kepler space telescope. Having such stringent observing requirements is a large disadvantage for this technique. Furthermore, as this technique measures reflected light, systems exhibiting high orbital inclinations are not detectable.

1.0.2.6 Direct Imaging

The most conceptually basic exoplanet detection technique is direct imaging. This is performed by pointing the telescope at the target and exposing for a sufficient time to detect the planet. With a sufficient number of observations at different epochs, and the mass of the central star, the orbital parameters may be determined. Moreover, it is possible to obtain planetary spectra to directly measure its atmospheric composition. Similar to astrometry, direct imaging is more adept to imaging objects with large separations.

The planet's luminosity determines the necessary exposure time to detect the object. Due to the cold temperature of Jovian objects ($\sim$150K), their thermal signature is extremely weak at visible wavelengths. The light observable at these wavelengths is heavily dominated by the reflected light of the host star. Observing in the infrared offers a greater opportunity to detect the planets photons since the peak of the blackbody is in this region. However, even in the infrared, imaging a planet is a nontrivial task. If one considers the most nearby star, Proxima Centauri, which lies at a distance of 1.3 pc, the angular separation of a planet at the orbital radius of Jupiter is a $4''$. Detecting a planet at 1 AU requires an angular separation of $0.76''$. However, to attempt to understand planet formation, several thousand stars must be observed which requires observing at far greater distances and therefore much smaller separations. This becomes a very challenging task.

1.1 The Challenges of Direct Imaging

Direct imaging has several associated challenges for which no solution exists. In the case of a perfect telescope, the physical effects of diffraction set fundamental limits on the achievable contrast measurements. This limit is further degraded by imperfections of the telescope's optical surfaces, plus the effects of observing in a non-steady state environment. With the help of new technologies, instrument designs, observation and data reduction techniques, the detection limits are being constantly improved. This section outlines the most fundamental aspects which limit the ability to perform high-contrast imaging.

1.1.1 Diffraction

A plane wave of wavelength λ, or wavefront ($W(x,y)$), propagating in free space is described by its associated electric field which is represented by equation 1.5. The term $A(x,y)$ represents the variation in amplitude and ϕ represents the variation in phase.

$$W(x,y) = A(x,y)e^{i\phi(x,y)} \tag{1.5}$$

As the light propagates through an aperture of finite size described by the pupil function $P(x,y)$, it diffracts and creates an intensity pattern which can be represented by equation 1.6, where $\mathscr{F}\mathscr{T}$ indicates the Fourier Transform [1].

$$\text{PSF}(x',y') = |\mathscr{F}\mathscr{T}[W(x,y)P(x,y)]|^2 \tag{1.6}$$

For a telescope with a circular aperture of diameter D, the PSF is an Airy disc, whose size is dependent upon the wavelength and diameter, as shown in Figure 1.8. The angular size of the Airy disc determines the resolving power of the optical system, which is defined as the diffraction limit.

The diffraction limit is the measure of an optical system's resolving power and is a measure of the full width at half the maximum (FWHM) of the central peak, whose angular width is described by equation 1.7.

$$\alpha[''] = 206265 * \frac{\lambda}{D} \tag{1.7}$$

The spatial FWHM of the Airy disc is obtained by multiplying the right side of equation 1.7 by the effective focal length of the associated imaging system. Any object or planetary system whose separation is smaller than the diffraction limit, cannot be resolved. In order for an object to be resolved via the Rayleigh Criterion, where the position of the central maximum of one Airy disc coincides of first dark ring of another, the peaks must be separated by an angle of at least $0.61\lambda/D$. The Rayleigh criterion

1. This equation is only valid when the interference pattern is observed sufficiently far away from the aperture.

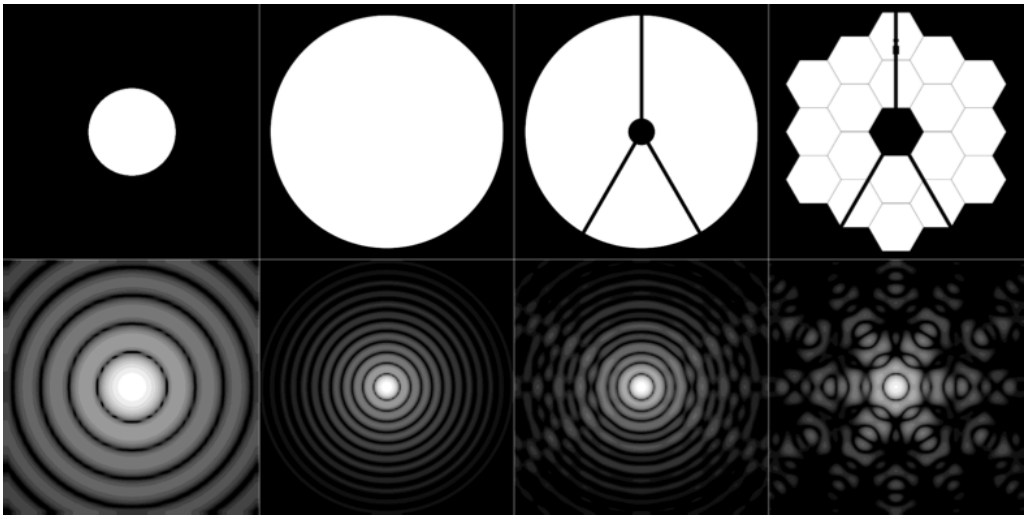

Figure 1.8: Quantity of light scattered into the outer regions of the PSF is a function of the pupil shape. Each upper box, containing the pupil shape, has a side of 7 meters whereas each lower box, containing the focal plane, has a side of 1 mm. The pupils shown from left to right are: a 2.4 meter diameter aperture, a 6.4 meter diameter aperture, the same 6.4 meter diameter aperture with a 1m secondary mirror obstruction with supports, a 6.4 meter diameter segmented mirror with a secondary obstruction. All PSF's are computed using an effective focal length of 134 metres, and a wavelength of 2 μm and assume no intensity nor phase errors. All PSF's are displayed in a log scale.

implies that the larger the telescope and the shorter the wavelength, the easier it is to detect planets. However, planet detection is limited more from the light scattered outside the primary peak, than the diffraction limit itself.

If we consider a perfectly flat and uniform wavefront[2], the central peak contains 83.9% of the total energy and the remaining energy is scattered outside the core into the surrounding rings. As the aperture changes form, due to a secondary mirror or spider, the amount of light scattered outside of the core increases. Segmented mirrors, like the one shown in Figure 1.8 amplify the problem further. The scattered light is problematic due to the large difference in luminosity between the planet and star. For example, the brightness ratio, or *contrast*, between third ring of the Airy disk and the central peak is 10^{-3}. However, as shown in Figure 1.3, detecting a Jupiter-like planet requires a contrast

2. A plane of constant phase

of 10^{-9}. Therefore, at this separation, the scattered light of the PSF dominates the signal of the planet by a factor of 10^6, rendering it undetectable. The first step in building a telescope optimized for high-contrast imaging is to use a design with an unobstructed primary mirror, such as an off-axis Gregorian telescope. This reduces the amount of scattered light, however the standard Airy pattern still remains. Managing this scattered light is accomplished using a coronagraph which is described in section 1.2.2.

1.1.2 Aberrations

Although the physical resolution limit is described by the diffraction limit, obtaining this limit for a real imaging system is extremely difficult. In the previous section, a perfectly flat and uniform wavefront was assumed. However, all optical systems aberrate the flat wavefront of the object [3], which causes a deformation of the PSF.

The aberrations induced by the system are a result of a variety of causes. Certain aberrations are a natural consequence of the telescopes design, such as spherical aberration. Other aberrations arise from polishing and figuring errors of the optical components themselves. All aberrations cause undesired phase errors, and therefore scatter light from the central core of the PSF to the outer regions. Low frequency aberrations result in the light being scattered to the inner sections of the PSF which causes a deformation of the core whereas higher order aberrations affect the outer regions (rings) of the PSF.

The amount of PSF degradation due to aberrations is characterized by the Strehl Ratio, which is a measure of the peak intensity of the PSF for an aberrated system, expressed as a fraction of the peak intensity of a non-aberrated system. The Strehl ratio can be approximated using equation 1.8, where σ_ϕ is the optical path difference (OPD) in waves. When observing from the ground, the largest source of aberrations comes from the atmosphere.

$$S = e^{-(2\pi\sigma_\phi)^2} \tag{1.8}$$

3. The wavefront emitted from an object is actually spherical, but when observing a piece of the wavefront at large distances (e.g. a star), the wavefront can be approximated to be flat.

1.1.2.1 The Atmosphere

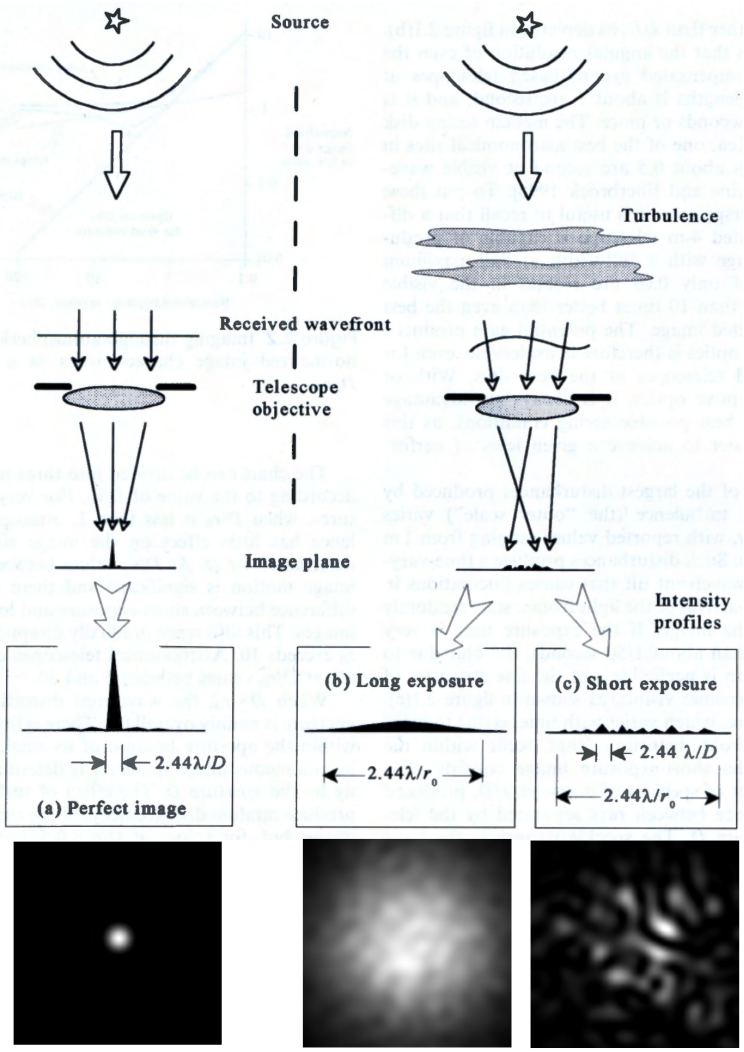

Figure 1.9: Effects of atmospheric turbulence on the diffraction limited PSF of a telescope. The leftmost image shows a diffraction limited PSF. The centre image shows the effect of a long exposure, where the PSF is seeing limited. The rightmost image is a short exposure, where the atmosphere is frozen in time, and the atmospheric speckles are observed. Adapted from Hardy (1998).

Aberrations induced by the atmosphere are a result of the index of refraction of air varying with pressure, temperature and wavelength. Assuming a static atmosphere, this results in a bending and slight dispersion of the incoming light. However, the atmo-

sphere's turbulent nature results in the creation of eddies on several different length scales. The turbulent cells each have unique pressures and temperatures resulting in a varying index of refraction. This causes the atmosphere to act like a series of weak lenses. Therefore, as the wavefront passes through the turbulent atmosphere, different sections propagate through different cells and undergo different optical path lengths. This causes phase errors, as shown in Figure 1.9. The spatial correlation, or structure function, of the atmospheric turbulence is characterized by the model of Kolmogorov (1941). The power spectrum of the atmospheric phase error is proportional to the spatial frequency raised to the power of -11/3. This shows that the majority of phase aberrations are contained in low frequency modes.

Because the wavefront is affected by the turbulence, the PSF is also affected, as shown in equation 1.6. Over a long exposure ($\sim$1s), the atmosphere causes a blurring of the PSF. The narrow central peak is smeared out, and the surrounding rings are no longer resolvable. This new form of PSF is called the *seeing disk*, which is shown in the middle image in Figure 1.9. The size of this disk is related to the correlation length of the atmosphere, or the size of a turbulent cell. The correlation length is expressed using the Fried Parameter r_0, shown in equation 1.9 (Fried 1965), and is a function of wavelength (λ), zenith angle (z), and the structure for the refractive index variations $C_n(h)$ integrated through each layer of the atmosphere (dh). In a qualitative sense, the Fried parameter represents the maximum aperture size that is diffraction limited while in the presence of the turbulence. Therefore, if a telescope aperture is smaller than r_0, the telescope's resolution is diffraction limited at λ/D. If the aperture is larger than r_0, the resolution is *seeing limited* defined by λ/r_0 for a long exposure. Typically, for $\lambda = 0.5$ μm, r_0 ranges between 10 to 20 cm for observing good observing sites. This means that having a telescope larger than r_0 only increases the amount of light collected, and does not increase the resolution beyond the size of a $\sim$20 cm telescope.

$$r_0(\lambda, z) = 0.185\lambda^{6/5}\cos^{3/5}(z)\left(\int C_n^2(h)dh\right)^{-3/5} \tag{1.9}$$

The PSF of a very short exposure, shown in the right image of Figure 1.9, shows a

pattern of speckles each of size λ/D. The number of speckles in a very short exposure is approximately $(D/r_0)^2$. A subsequent exposure will show a different pattern of speckles, caused by the OPD's induced by the changing atmosphere. The coherence time τ_0 of the atmosphere, which is defined as the amount of time in which change in phase error induced by the atmosphere is less than one radian, is shown in equation 1.10. The coherence time is a function of the windspeed v and Fried Parameter r_0,

$$\tau_0 = 0.314\frac{r_0}{v} \tag{1.10}$$

In order to obtain diffraction limited resolutions in the presence of the atmosphere, one must correct for phase variations caused by the OPD's at the rate at which the atmosphere evolves. Another option is to perform the observations from space.

1.1.2.2 Quasi-static Aberrations

Even when observing from space where there is no atmospheric aberrations, telescopes cannot achieve a perfect Strehl ratio. Aberrations in the optical elements result in the scattering of light similar to that of atmospheric speckles. The aberrations are caused by surface errors of the individual optics, as well as deformation of surfaces due to thermal expansion and/or compression. The induced phase aberrations are directly related to the surface smoothness and are therefore wavelength dependent. Using the root mean squared (RMS) surface error δ (in metres), and the wavelength λ (in metres), the RMS phase aberration (in waves) is calculated using equation 1.11. Note that this can be used to approximate the Strehl ratio using equation 1.8.

$$\sigma_\phi = \frac{\delta}{\lambda} \tag{1.11}$$

Analogous to the atmosphere, these aberrations cause light to scatter outside the core of the PSF causing speckles throughout. However, contrary to atmospheric speckles, these speckles do not average out over time to create a smooth halo profile. The speckles are *quasi-static* and change form only when the physical surface is altered. This alteration generally occurs over a period of hours and is often caused by telescope flexure,

thermal deformation, or a change of filter. The unique quasi-static nature of the speckles allows possible removal via data reduction techniques.

1.2 Direct Imaging Techniques

The natural form of a telescopes PSF is not akin to planet detection due to the large amount of light scattered outside the core. This effect is amplified when wavefront errors are introduced via optical components and the atmosphere. Due to the large contrast between the planet and star, the scattered light from the star dominates any photons being emitted or reflected by the planet. Due to the different nature of the wavefront aberrations, each introduction of wavefront error requires different correction and/or compensation.

1.2.1 Adaptive Optics

An adaptive optics system is designed to measure the wavefront aberrations induced by the atmosphere then calculate a correction and execute it in real time. Figure 1.10 shows a basic optical design of an adaptive optics (AO) system. The incoming light from the object is a flat wavefront which becomes aberrated due to the atmosphere. The wavefront then passes through the telescope and is focused to a focal plane. The light continues through this focal plane to a lens which both collimates the incoming beam, and images the telescope pupil onto a deformable mirror (DM). Having the telescope pupil imaged onto the DM is critical as it allows the shape of the deformable mirror to be directly related to the phase difference at the telescope pupil. The light is reflected off the DM to a converging lens, whose light is subsequently split using a dichroic. The dichroic transmits light in the infrared (IR) which focuses on to a science detector, while the visible light is reflected into a separate channel. The visible light is fed into a wavefront sensor (WFS) which measures the aberrations of the wavefront at the deformable mirror. Using the measured wavefront, a computer is used to calculate the OPD's which need to be induced at the DM in order to re-create a flat wavefront.

In this AO system, the WFS measures the wavefront after it has been corrected allow-

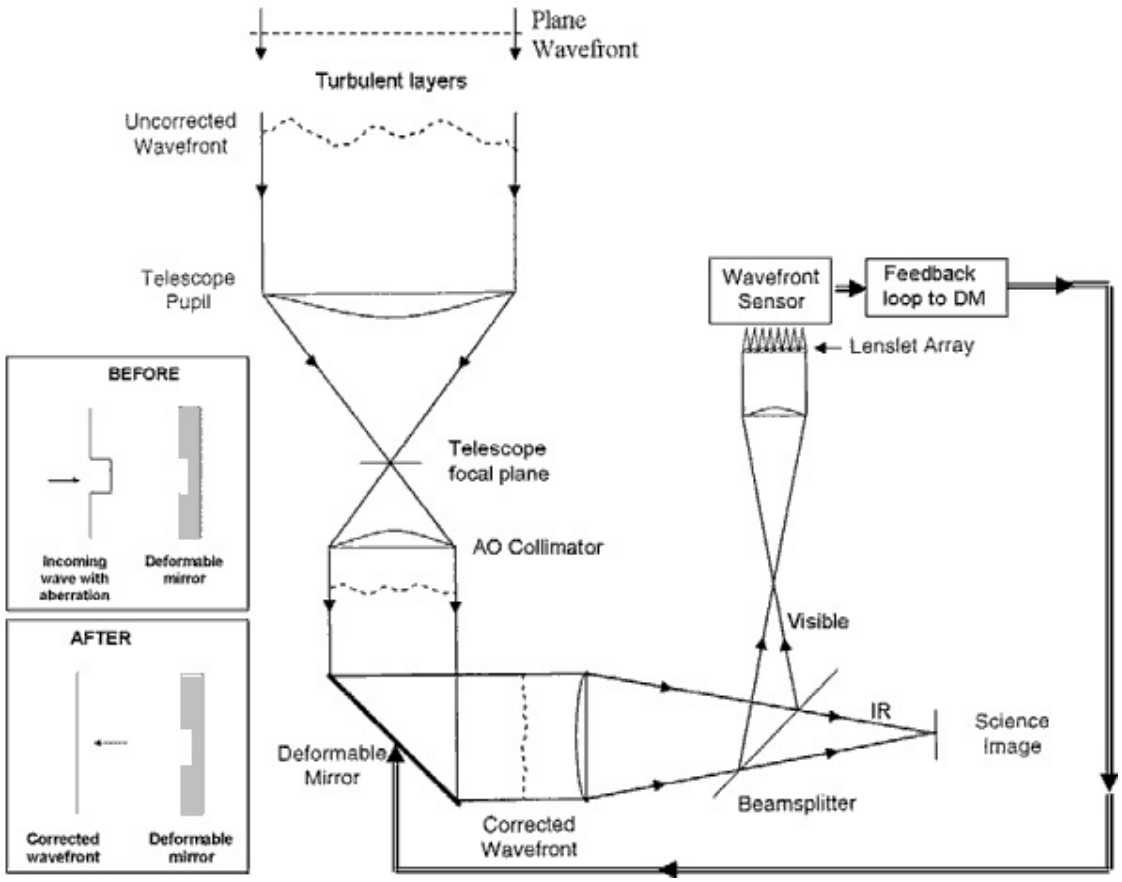

Figure 1.10: Typical closed-loop adaptive optics imager. The wavefront sensor measures the instantaneous phase error which is used to calculate the required optical path difference in order to flatten the wavefront. This optical path difference is applied using a deformable mirror before the wavefront sensor allowing improvement on the original correction. From McLean (2008).

ing a further enhancement of the original correction. This is referred to as a closed-loop AO system. The frequency of correction is dependent upon the atmospheric coherence time and Fried parameter, which is wavelength dependent. Current AO systems, such as ALTAIR on the Gemini telescope operate at $\sim$ 1kHz and obtain Strehl ratios of $\sim$0.18 in H-band, and $\sim$0.35 in K-band, depending upon atmospheric conditions (Christou et al. 2010).

The performance of an AO system is limited by two factors, the ability to measure the wavefront, and the ability to correct it. To sample the wavefront, the WFS divides

the pupil up into sections, or subapertures. The number of subapertures across the pupil determines the maximum measurable spatial frequency aberration. The number of actuators on the DM should roughly correspond to the number of subapertures on the WFS in order to be able to correct the frequencies which are being measured. In an ideal situation, the wavefront should be sampled in sizes of r_0, however, this is rarely feasible due to the number of photons required per subaperture at the required frequency of correction. Because AO systems measure and correct only low order aberrations, the resultant PSF is a diffraction limited core, with seeing limited halo. The size of the diffraction limited core is proportional to the number of corrected frequencies. Quasi-static speckles are present in the PSF because the WFS only detects aberrations occurring before the dichroic, therefore any surface errors occurring after the WFS are uncorrected. Moreover, any high spatial frequency aberrations not sensed by the WFS are also uncorrected. The high frequency atmospheric speckles form a smooth halo, however the high spatial frequency surface aberrations result in the PSF having several superimposed quasi-static speckles. Although AO is able to compensate for atmospheric turbulence, quasi-static speckles are still present and the original problem of the telescopes PSF scattering light outside the core remains.

1.2.2 Coronagraphy

Invented by Bernard Lyot in 1939, the coronagraph was first used to view the solar corona whose form was invisible due to the scattered light in the wings of the PSF (Lyot 1939). Now adapted to be used with stars other than our sun, the Lyot coronagraph is arguably the most popular form of coronagraph. This is primarily attributed to its ease of fabrication.

Following Figure 1.11, in entering the telescope, the primary star is observed to be on the optical axis, whereas the companion is slightly off axis. When the light encounters the first focal plane, the rings of the primary star's PSF make the companion invisible. To block the central peak of the primary star, a occulting mask is placed at the focal plane whose width is typically a few λ/D. Note that the wings of the PSF and the light from the companion are unobstructed. The beam then passes through a lens, which collimates

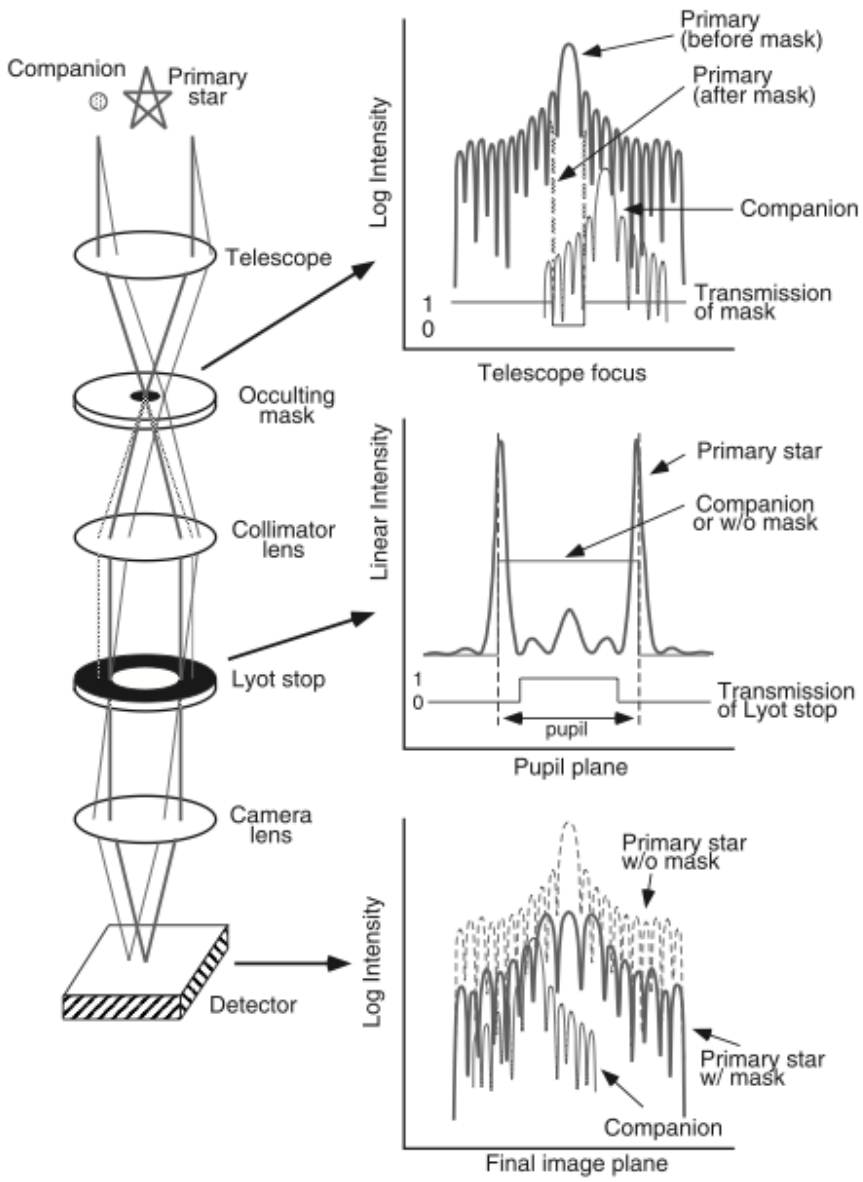

Figure 1.11: A Lyot coronagraph is used to reduce the light of the primary star's PSF. The core of the PSF is removed using an occulter at a focal plane, whereas the rings of the PSF are masked at a re-imaged pupil plane. Because coronagraphs require very high Strehl ratios to be efficient, they must be used in conjunction with adaptive optics, or in space. From Murakawa et al. (2004).

the beam and forms an image of the telescope pupil. However, the intensity of the re-imaged pupil is significantly different due to the presence of the occulter at the first focal plane. The image on the focal plane is the Fourier transform of the aperture, therefore the low frequency information towards the core of the PSF, and the higher frequency information is in the wings. The re-imaged pupil plane is the Fourier transform of the focal plane, however, applying an occulting mask removes the power in the low frequencies, therefore acting as a high-pass filter. The remaining light from the primary star is found at the edge of the pupil, and light diffracting off the occulter scatters outside the pupil, therefore a mask, called a Lyot mask, is applied to block out this remaining light. Consequently, this mask also blocks out some of the light of the companion. Therefore, there exists a balance between size of the occulter and Lyot mask in order to obtain the most efficient coronagraph. The design and functionality of a coronagraph are directly related to the Strehl ratio. When the wavefront is not well corrected, the amount of light in the wings increases, which in turn requires a smaller Lyot mask, and thus decreases the throughput. A significant gain in contrast is not obtained until Strehl ratios of 90% or more are acheived (Sivaramakrishnan et al. 2001).

Other types of coronagraphs exist which mimic the Lyot design, such as the Apodized Lyot coronagraph (Soummer et al. 2003). This employs masking the pupil so that its intensity profile is a prolate. This form is invariant to the finite Fourier transform and therefore does not scatter light into the outer regions. A different approach is to remap the pupil using secondary optics as is done using the Phase Induced Amplitude Apodization (PIAA) coronagraph (Guyon et al. 2005). This system provides excellent contrasts and small separations but has yet to be tested outside of a laboratory (Guyon et al. 2010b). Rather than changing the pupil, it is also possible to modify the occulter which is done for the Four Quadrant Phase Mask Coronagraph (Rouan et al. 2000). In place of the occulting mask, a four-quadrant binary phase mask (0, π) covering the full field of view is inserted at the focal plane. This nulls the signal from the primary star rather than masking it and the light of the companion is unobstructed. All types of coronagraphs are able to greatly suppress the wings of the PSF but offer no solution to the problem of quasi-static speckles.

1.2.3 Speckle Suppression Techniques

Both adaptive optics and coronagraphs are used to increase the contrast of an observation prior to the photons reaching the detector. When aiming to remove the noise caused by uncorrected atmospheric turbulence or quasi-static speckles, novel observing techniques and post-observation image processing are involved. This section outlines methods of removing and/or reducing the impact of speckle noise.

1.2.3.1 Simultaneous Speckle Differential Imaging

Conceived by Racine et al. (1999), Simultaneous Speckle Differential Imaging (SSDI) aims to reduce the impact of speckle noise which is not corrected by adaptive optics. The goal is to reduce speckle noise by exploiting a sharp spectral feature, such as the 1.6 μm methane feature which is present in a cool companion, but not in the warm host star. By acquiring simultaneous images of the system on and off the feature, both images exhibit the same atmospheric perturbations and therefore the same residual atmospheric speckles. Because the speckle pattern and PSF is chromatic, one image must be re-scaled prior to any image manipulation. After rescaling, subtracting the images allows the removal of the speckle pattern and the detection of the atmospheric feature. An example of this process is shown in Figure 1.12. This method was first tested on-sky using CO (2.30/0.03 μm) and K-continuum (2.26/0.05 μm) filters and obtained a speckle attenuation of 3 magnitudes, or a factor of $\sim$16. This showed that SSDI is effective at removing speckles and upon further development, may yield better results.

The effectiveness of SSDI, as performed by Racine et al. (1999), is limited by the evolution of the PSF profile with wavelength. In the case of an optical system free of aberrations (Strehl ratio equals 1), the PSF undergoes a scaling and intensity variation which is correctable via image processing. However, when the wavefront is aberrated and undergoes an optical path difference δ, the wavefront error being a function of wavelength (from equation 1.11), means that each image possesses a different Strehl (from equation 1.8). This leads to a variation in intensity of the speckle pattern that causes residuals upon subtraction. These residuals limit the effectiveness of SSDI when only

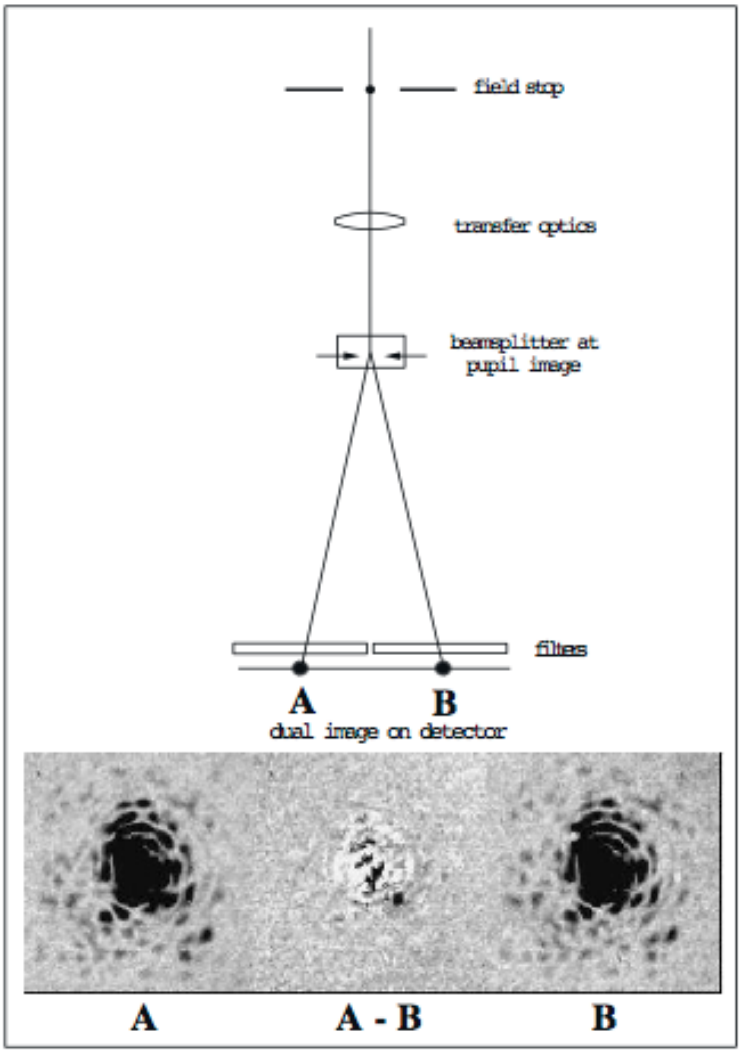

Figure 1.12: An dual imaging SSDI instrument splits the beam to create two images of adjacent wavelengths. Each channel is assigned a corresponding filter. Subtracting the resulting images removes the atmospheric speckles and exposes the difference in flux between the two wavelengths of the planet. An artificial companion which is 5 magnitudes fainter than its primary with a separation of $0.5''$ has been inserted into image A. Although invisible in the original image, it is clearly visible in the difference image. From Racine et al. (1999).

two wavelengths are observed.

Using images obtained at three wavelengths, Marois et al. (2000) shows that this variation in PSF evolution can be largely overcome using a unique subtraction method

entitled the *double difference*. Their simulations showed that imaging the methane feature through three different wavelengths can attenuate the speckle noise to the level of the photon noise (a factor of $\sim 10^4$). This technique led to the development of several instruments designed to perform SSDI using multiple wavelength channels.

The construction of TRIDENT, an SSDI imager used on the Canada-France-Hawaii telescope, was built to simultaneously image a star at three different wavelengths sampling the 1.6 μm methane feature found in cold companions (Marois et al. 2005). TRIDENT was able to obtain a speckle suppression factor of ~ 2, due to non-common path aberrations introduced by the several optical surfaces after the beam splitters. Similar results were obtained by a similar SSDI instrument built for the Very Large Telescope (VLT) and the MMT (Biller et al. 2004; Close et al. 2005). Such results showed that the instrument design and elements must keep the optical path differences to a few nanometers in order to allow significant reduction of the speckle noise. This result was later confirmed experimentally by introducing a holographic diffuser at the focal plane to destroy the coherence of the light prior to passing through the optics specific to each channel (Lafrenière et al. 2007a). Later SSDI instruments, such as the Near Infrared Coronagraphic Imager (NICI) (Chun et al. 2008) and the HiClAO instruments (Hodapp et al. 2008), are built to minimize the effects of non-common path aberrations however it is not clear that their performance will surpass TRIDENT or the VLT-SDI instrument.

Another method to reduce the effects of non-common path aberrations is to divide the focal plane using a lenslet array. The beam can then be collimated and passed through a disperser to create an integral field spectrograph. This method destroys the coherence of the beam at the focal plane, which eliminates the effects of non-common path aberrations. Moreover, it allows simultaneous imaging spectroscopy which can utilize the SSDI technique to reduce atmospheric speckle noise (Sparks & Ford 2002). This setup may also utilize another speckle suppression technique, Angular Differential Imaging (ADI).

1.2.3.2 Angular Differential Imaging

Due to the mis-alignment between the axis of the Earth's rotation and the axis of the celestial sphere, objects move in arcs across the sky. As one tracks a star throughout the night, following its arc, they will observe the surrounding stars in the field rotate about the star relative to the horizon, as shown in Figure 1.13. One of the consequences of observing with an altitude-azimuth telescope mount is the requirement to compensate for the field rotation. This is normally accomplished by de-rotating the instrument at the same rate as the field. During the tracking of the object, the orientation of the telescopes pupil remains in the same position with respect to the zenith angle, however the rotation of the instrument causes PSF instabilities due to instrument flexure. The flexure causes the speckle pattern to change over time resulting in very poor PSF subtraction, and as a result, very poor contrasts.

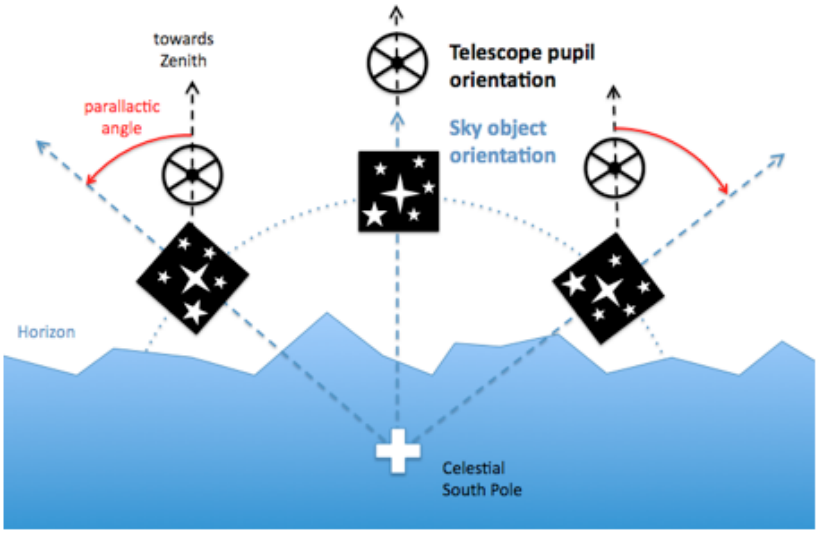

Figure 1.13: When observing with a altitude-azimuth telescope mount, the telescope pupil orientation remains constant, however the field rotates throughout the observation. This is normally counteracted by the rotation of the instrument. In the case of ADI, this rotator is turned off to maintain the PSF stability. Image by Chris Thalmann.

If the field rotator (often referred to as a Cassegrain rotator) is turned off, the PSF stabilizes significantly. However, in the case of a star/planet system, the field rotation

causes the planet to appear to orbit star. Although generally an undesired effect, this rotation can be used to reduce the speckle noise. By taking several short images throughout the field's rotation, the images can be de-rotated using post-processing techniques, then combined to increase the signal of the companion. Taking a median of the non-rotated images results in increasing the signal to noise ratio of the speckles, while eliminating the signal of the planet. Subtracting one frame from the other results in the removal of the speckles, while conserving the flux from the planet. This technique is called Angular Differential Imaging, and has obtained speckle noise attenuation of $\sim 10^2$ (Marois et al. 2006). Rather than using a simple median, more robust speckle subtraction can be performed using a Locally Optimized Combination of Images (LOCI, Lafrenière et al. 2007b). This increases the performance by a factor of ~ 3 in the inner regions of the image.

One of the primary advantages of ADI is its synergy with SSDI. As discussed in the previous section, SSDI instruments perform well in subtracting the residual atmospheric speckles but are limited by the non-common path aberrations of each wavelength channel. ADI is limited in its ability to remove atmospheric residuals, but is very powerful in removing the quasi-static speckles caused by the non-common path errors. The disadvantage of ADI is its time efficiency, since one must wait for the field to rotate. The rotation time is proportional to the radial separation from the host star, therefore detecting planets at small separations with ADI is not feasible. In the case of space telescopes, the ADI method is more efficient since the field rotation is controlled by the telescope roll, and not the Earth's rotation. Moreover, there is no atmospheric speckles, and the PSF stability is greater which further enhances the performance of ADI.

1.3 Recent Successes and the Future of High-Contrast Imaging Instrumentation

To date, only three exoplanetary systems around main sequence stars have been detected and confirmed using direct imaging. For the planet orbiting 1RXS J160929.1-210524 in Upper Scorpius, shown in the upper left of Figure 1.14, AO imaging alone allowed sufficient contrast to resolve the planet (Lafrenière et al. 2008). In the case of

HR 8799 (Marois et al. 2008) and Beta Pictoris b (Lagrange et al. 2010), shown in the lower left and upper right of Figure 1.14 respectively, ADI was performed to reduce the speckle noise and resolve the planets. To date, the only system discovered using a coronagraph is Formalhaut b, using the Hubble Space telescope (Kalas et al. 2008). However, its original classification as a planet has been called into question (Janson et al. 2012; Marengo et al. 2009). The lack of coronagraphic discoveries is most likely due to the current limits of AO systems, which are presently unable to provide adequate Strehl ratios to make coronagraphs efficient for ground-based observations.

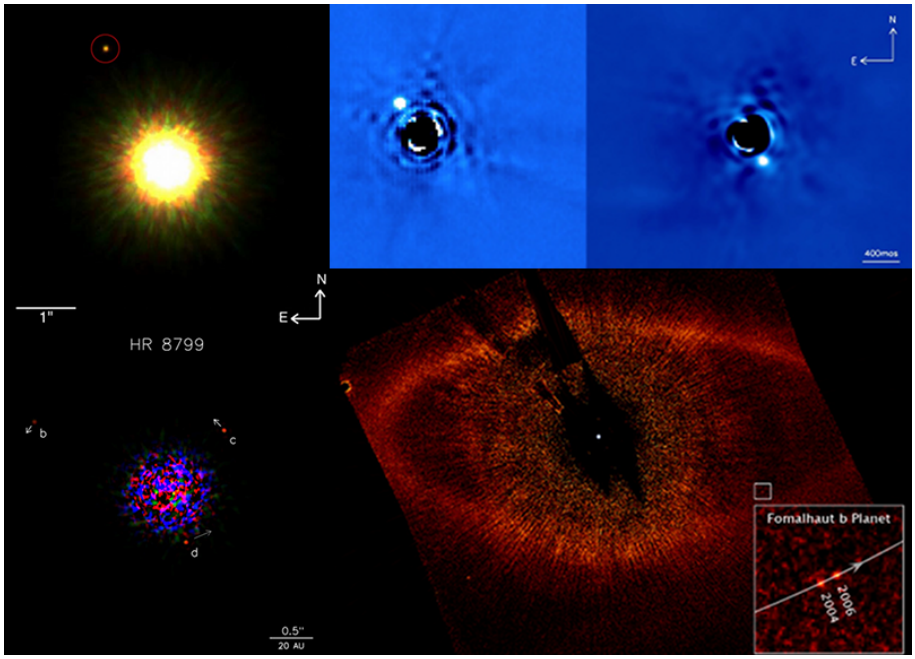

Figure 1.14: To date, only four exoplanetary systems orbiting main sequence stars have been directly imaged. *Top Left:* 1RXS J160929.1-210524 in Upper Scorpius (Lafrenière et al. 2008). *Top right:* Two epochs of Beta Pictoris b (Lagrange et al. 2010). *Lower right:* Formalhaut b (Kalas et al. 2008). *Lower left:* The three exoplanets surrounding HR 8799 (Marois et al. 2008).

Currently entering their integration and testing stage, three different extreme adaptive optics (ExAO) imagers are scheduled for first light in late 2012 and/or early 2013. These systems all include coronagraphs to suppress the light scattered into the outer regions of the PSF. The Gemini Planet Imager (GPI, Macintosh et al. 2008) uses an internal cal-

ibration system built to reduce and remove quasi-static speckles formed all the way to the occulter. The science instrument is a lenslet based integral field spectrometer (IFS) which destroys the coherence of the light prior to passing through the filters, disperser, and camera lenses. This is done to reduce the effects of non-common path aberrations discussed in section 1.2.3.1. A similar system, SPHERE (Spectro-Polarimetric High-contrast Exoplanet Research), is being built for the Very Large Telescope (Beuzit et al. 2008). Both systems expect to obtain contrasts better than 10^{-7} at $0.5''$ and are predecessors of the proposed planet finders for the extremely large telescopes. The Thirty Meter Telescope (TMT) will host the Planet Formation Imager (PFI, Macintosh et al. 2006) and the European Extremely Large Telescope will host the Exo-Planet Imaging Camera and Spectrograph (EPICS, Kasper et al. 2008). The Subaru Coronagraphic Extreme AO (SCExAO, Martinache & Guyon 2009) project is designed to image the innermost regions of stars ($<0.2''$) using a PIAA coronagraph and will also host an IFS.

The future of space-based exoplanet imaging is more uncertain. The only planned space telescope with high-contrast imaging capabilities is the James Webb Space Telescope (*JWST*). It is scheduled for launch at the end of this decade and will have imaging capabilities between 1–28.5 μm. Due to the segmented nature primary mirror, shown on the right most image of Figure 1.8, the telescope is not ideal for exoplanet detection. However, the high Strehl ratios and the superb PSF stability drove three instruments, the Near-Infrared Camera (NIRCam), the Mid-Infrared Instrument (MIRI) and the Tunable Filter Imager (TFI) to house coronagraphs. Due to cryogenic operational issues that could not be resolved prior to the instruments scheduled delivery, TFI has been reconfigured to the Near Infrared Imager and Slitless Spectrograph (NIRISS), however this too features an mode for high-contrast observations. The large advantage of *JWST* will be its unique access to wavelengths which are unobservable from the ground. The 4–5 μm region is the peak of the spectral energy distribution of EGP's allowing the greatest chance to detect its emitted photons.

The next space mission has yet to be decided. One of the possibilities includes a star shade for *JWST* which would fly 67 000 km in front of *JWST* blocking the light of the primary star before it enters the telescope (Soummer et al. 2010). Other possibilities

include the Terrestrial Planet Finder Coronagraph, or the Terrestrial Planet Finder Interferometer (Beichman et al. 1999). However, both concepts are expected to be extremely expensive due to the large amount of technology needed to be developed for these missions. Smaller space missions have also been proposed, such as the Pupil-mapping Exoplanet Coronagraphic Observer (PECO) satellite (Guyon et al. 2010a), which is a 1.4 meter telescope optimized specifically for exoplanet detection. Until more information is learned using the currently planned instruments, any large investment on a multi-billion dollar space mission appears unlikely (Committee for a Decadal Survey of Astronomy and Astrophysics and National Research Council 2010).

1.4 This Thesis

Detecting and characterizing exoplanets using direct imagery offers the ability to explore a parameter space complementary to what is being studied using RV and transit observations. Currently, direct imaging observations are limited by stray light from the primary star that manifests itself as quasi-static speckles in the image plane and masks the signal originating from the planet. The primary goal of this thesis is to explore the ability of an etalon to attenuate these speckles using SDI and determine the capability to detect and characterize the light originating from any faint companion. Originally, the TFI was be constructed on the reverse side of the Fine Guidance Sensor, operating with a spectral resolution of $\sim$100 between 1.5–5 μm with a 2.2'$\times$2.2' field of view (Doyon et al. 2010). The coronagraphic mode offered four different occulting spots with four Lyot masks, including a non-redundant mask. TFI would have been the first instrument to perform SDI in space, however, unlike TRIDENT and the other SSDI imagers, TFI was not designed to observe multiple wavelengths simultaneously, therefore the speckles suppression performance is highly dependent upon the telescope and instrument stability. The capabilities also rely upon the use of a Fabry-Perot etalon acting as a tunable narrowband filter, which has never been used to perform SDI. Although TFI has been reconfigured and the etalon and coronagraph has been removed. The already built hardware and instrument design are an ideal test scenario to determine the space-based

high-contrast imaging capabilities of tunable filters.

The second chapter of this thesis demonstrates the speckle suppression abilities of an etalon. To change central wavelengths of the filter, the size of the etalon gap must be adjusted. Because the filtering of a Fabry-Perot involves multiple reflections inside the etalon, any non-common path aberrations as a result of the change in gap are amplified. This in turn, affects the PSF stability and hence the SDI performance. In order to determine the SDI capabilities of the TFI etalon, a prototype etalon was constructed and tested using a custom test-bed at the Université de Montréal. The results of these tests as well as simulations of their expected performance is presented.

Unlike ground-based AO instruments, *JWST* has no deformable optics to correct for phase aberrations induced by the optical components, therefore all quasi-static speckles must be removed via differential imaging techniques. The performance modelling of the instrument has previously been done by assuming a total wavefront error from the telescope and instrument, and then using the Fraunhofer approximation (equation 1.6) to obtain PSFs for varying wavelengths. Such a characterization often over-estimates the performance of both the coronagraph and SDI capabilities. The third chapter of this thesis is dedicated to a thorough and accurate characterization the performance of *JWST*+TFI by performing an end-to-end polychromatic Fresnel propagation. This is performed by propagating a plane wave through the entire telescope and instrument. The analysis accounts for non-common path errors introduced at each component along the optical path, both in and out of the pupil planes. This model is used to determine the optimal observational configuration and to develop planet detection techniques optimized to an SDI observation. Having an accurate SDI performance characterization permits the determination the detection limits of such an instrument. Moreover, because the detection efficiency of SDI is dependent upon atmosphere of the companion, an accurate characterization of the SDI capabilities will help determine which atmospheric properties should be exploited when aiming to detect exoplanets. Lastly, the SDI performance of NIRISS, using its medium-band interference filters is determined. The results indicate that an SDI observing mode should be implemented and that SDI can still provide a significant contrast improvement.

In line with the general theme of this thesis, the detection and characterization of exoplanets, the last chapter is devoted to study the young stellar and substellar population of the Orion Trapezium Cluster. More specifically, we present the results from new infrared spectroscopic observations aiming to detect and characterize young low-mass stars, brown dwarfs and planetary mass objects (PMO) or free-floating planets in the cluster. The data from our survey is used to derive a measurement of the substellar initial mass function for the cluster which is compared to the galactic disk and other young clusters. Furthermore, the atmospheres of the discovered PMOs are similar to those of extrasolar giant planets and provide excellent tests for atmospheric models.

1.5 Student Declaration

The core content of this thesis consists of three articles detailing original scientific works. Two of these articles, of which I was the first author, have already been published in peer-reviewed journals. The third article, which I also wrote, is in the final draft stage and will hopefully be submitted to a peer-reviewed journal prior to my thesis defence. The first article (chapter two) details my work where I assembled the prototype Fabry-Perot etalon and control electronics while spending approximately four months in Ottawa, Ontario at COM DEV Canada, over a period of 1.5 years. During this time I also performed the optical and optomechanical design of the test bed at the Université de Montréal. After purchasing and procuring the necessary components, I assembled and aligned the system. I also performed the measurements of the surface quality of the optics, as well as the numerical model used to simulate the expected results.

The second article, described in chapter three, discusses a detailed optical model of *JWST* and TFI. I obtained the wavefront error (WFE) map of the optical telescope element from Ball Aerospace and the WFE maps of the TFI optical components from COM DEV, Canada. I then extracted and re-created new high-resolution WFE maps based upon the measured properties of the originals. Using these WFE maps, I then created an on-axis optical prescription of the telescope and instrument that was used in the optical model. I developed the model with the aid of existing publicly available

Fresnel Propagation Software and determined the optimal observing configurations as well as the exoplanet detection and characterization capabilities in collaboration with R. Doyon and D. Lafrenière.

Chapter 4 presents the results of my data reduction of multi-object spectroscopy observations obtained at the Canada France Hawaii Telescope in 2003. For this project, I wrote the entire data reduction pipeline and analysis software. I also performed the analysis and gathered the previous literature associated with all observed objects. Upon completion of the analysis, I also wrote the article. The paper is in the final draft stage and we anticipate to submit this work to a refereed journal shortly after the thesis defence.

R. Doyon advised the research and writing of all three articles as well as providing funding throughout my PhD. His precise attention to detail and multiple revisions provided a significant improvement to the quality of this research.

Bibliography

Baraffe, I., Chabrier, G., Barman, T. S., Allard, F., & Hauschildt, P. H. 2003, Astronomy and Astrophysics, 402, 701

Barge, P., Baglin, A., Auvergne, M., & CoRoT Team. 2008, in IAU Symposium, Vol. 249, IAU Symposium, ed. Y.-S. Sun, S. Ferraz-Mello, & J.-L. Zhou, 3–16

Barman, T. S., Hauschildt, P. H., & Allard, F. 2005, The Astrophysical Journal, 632, 1132

Basri, G., Borucki, W. J., & Koch, D. 2005, New Astronomy Reviews, 49, 478

Beaulieu, J.-P., Bennett, D. P., Fouqué, P., Williams, A., Dominik, M., Jørgensen, U. G., Kubas, D., Cassan, A., Coutures, C., Greenhill, J., Hill, K., Menzies, J., Sackett, P. D., Albrow, M., Brillant, S., Caldwell, J. A. R., Calitz, J. J., Cook, K. H., Corrales, E., Desort, M., Dieters, S., Dominis, D., Donatowicz, J., Hoffman, M., Kane, S., Marquette, J.-B., Martin, R., Meintjes, P., Pollard, K., Sahu, K., Vinter, C., Wambsganss, J., Woller, K., Horne, K., Steele, I., Bramich, D. M., Burgdorf, M., Snodgrass, C., Bode, M., Udalski, A., Szymański, M. K., Kubiak, M., Więckowski, T., Pietrzyński, G., Soszyński, I., Szewczyk, O., Wyrzykowski, Ł., Paczyński, B., Abe, F., Bond, I. A., Britton, T. R., Gilmore, A. C., Hearnshaw, J. B., Itow, Y., Kamiya, K., Kilmartin, P. M., Korpela, A. V., Masuda, K., Matsubara, Y., Motomura, M., Muraki, Y., Nakamura, S., Okada, C., Ohnishi, K., Rattenbury, N. J., Sako, T., Sato, S., Sasaki, M., Sekiguchi, T., Sullivan, D. J., Tristram, P. J., Yock, P. C. M., & Yoshioka, T. 2006, Nature, 439, 437

Beichman, C. A., Woolf, N. J., & Lindensmith, C. A. 1999, The Terrestrial Planet Finder (TPF) : a NASA Origins Program to search for habitable planets

Benedict, G. F., McArthur, B. E., Forveille, T., Delfosse, X., Nelan, E., Butler, R. P., Spiesman, W., Marcy, G., Goldman, B., Perrier, C., Jefferys, W. H., & Mayor, M. 2002, The Astrophysical Journal, 581, L115

Bennett, D. P., Bond, I., Cheng, E., Friedman, S., Garnavich, P., Gaudi, B. S., Gilliland, R., Gould, A., Greenhouse, M. A., Griest, K., Kimble, R. A., Lunine, J. I., Mather, J. C., Minniti, D., Niedner, M., Paczynski, B., Peale, S., Rauscher, B. J., Rich, R. M., Sahu, K., Tenerelli, D., Udalski, A., Woolf, N., & Yock, P. 2004, in Society of Photo-Optical Instrumentation Engineers (SPIE) Conference Series, ed. J. C. Mather, Vol. 5487, 1453–1464

Beuzit, J.-L., Feldt, M., Dohlen, K., Mouillet, D., Puget, P., Wildi, F., Abe, L., Antichi, J., Baruffolo, A., Baudoz, P., Boccaletti, A., Carbillet, M., Charton, J., Claudi, R., Downing, M., Fabron, C., Feautrier, P., Fedrigo, E., Fusco, T., Gach, J.-L., Gratton, R., Henning, T., Hubin, N., Joos, F., Kasper, M., Langlois, M., Lenzen, R., Moutou, C., Pavlov, A., Petit, C., Pragt, J., Rabou, P., Rigal, F., Roelfsema, R., Rousset, G., Saisse, M., Schmid, H.-M., Stadler, E., Thalmann, C., Turatto, M., Udry, S., Vakili, F., & Waters, R. 2008, in Society of Photo-Optical Instrumentation Engineers (SPIE) Conference Series, Vol. 7014, 701418

Biller, B. A., Close, L., Lenzen, R., Brandner, W., McCarthy, D. W., Nielsen, E., & Hartung, M. 2004, in Society of Photo-Optical Instrumentation Engineers (SPIE) Conference Series, Vol. 5490, 389–397

Borucki, W. J., Koch, D. G., Batalha, N., Bryson, S. T., Rowe, J., Fressin, F., Torres, G., Caldwell, D. A., Christensen-Dalsgaard, J., Cochran, W. D., DeVore, E., Gautier, T. N., Geary, J. C., Gilliland, R., Gould, A., Howell, S. B., Jenkins, J. M., Latham, D. W., Lissauer, J. J., Marcy, G. W., Sasselov, D., Boss, A., Charbonneau, D., Ciardi, D., Kaltenegger, L., Doyle, L., Dupree, A. K., Ford, E. B., Fortney, J., Holman, M. J., Steffen, J. H., Mullally, F., Still, M., Tarter, J., Ballard, S., Buchhave, L. A., Carter, J., Christiansen, J. L., Demory, B.-O., Désert, J.-M., Dressing, C., Endl, M., Fabrycky, D., Fischer, D., Haas, M. R., Henze, C., Horch, E., Howard, A. W., Isaacson, H., Kjeldsen, H., Johnson, J. A., Klaus, T., Kolodziejczak, J., Barclay, T., Li, J., Meibom, S., Prsa, A., Quinn, S. N., Quintana, E. V., Robertson, P., Sherry, W., Shporer, A., Tenenbaum, P., Thompson, S. E., Twicken, J. D., Van Cleve, J., Welsh, W. F., Basu, S., Chaplin, W., Miglio, A., Kawaler, S. D., Arentoft, T., Stello, D., Metcalfe, T. S.,

Verner, G. A., Karoff, C., Lundkvist, M., Lund, M. N., Handberg, R., Elsworth, Y., Hekker, S., Huber, D., Bedding, T. R., & Rapin, W. 2012, The Astrophysical Journal, 745, 120

Brown, T. M., Charbonneau, D., Gilliland, R. L., Noyes, R. W., & Burrows, A. 2001, The Astrophysical Journal, 552, 699

Burrows, A., Hubbard, W. B., Lunine, J. I., & Liebert, J. 2001, Reviews of Modern Physics, 73, 719

Burrows, A., Sudarsky, D., & Hubeny, I. 2004, The Astrophysical Journal, 609, 407

Cahoy, K. L., Marley, M. S., & Fortney, J. J. 2010, The Astrophysical Journal, 724, 189

Casertano, S., Lattanzi, M. G., Sozzetti, A., Spagna, A., Jancart, S., Morbidelli, R., Pannunzio, R., Pourbaix, D., & Queloz, D. 2008, Astronomy and Astrophysics, 482, 699

Charbonneau, D., Brown, T. M., Latham, D. W., & Mayor, M. 2000, The Astrophysical Journal, 529, L45

Charbonneau, D., Brown, T. M., Noyes, R. W., & Gilliland, R. L. 2002, The Astrophysical Journal, 568, 377

Charpinet, S., Fontaine, G., Brassard, P., Green, E. M., Van Grootel, V., Randall, S. K., Silvotti, R., Baran, A. S., Østensen, R. H., Kawaler, S. D., & Telting, J. H. 2011, Nature, 480, 496

Christou, J. C., Neichel, B., Rigaut, F., Sheehan, M., McDermid, R. M., Trancho, G., Trujillo, C., & Walls, B. 2010, in Society of Photo-Optical Instrumentation Engineers (SPIE) Conference Series, Vol. 7736, 77361R

Chun, M., Toomey, D., Wahhaj, Z., Biller, B., Artigau, E., Hayward, T., Liu, M., Close, L., Hartung, M., Rigaut, F., & Ftaclas, C. 2008, in Society of Photo-Optical Instrumentation Engineers (SPIE) Conference Series, Vol. 7015, 70151V

Close, L. M., Lenzen, R., Guirado, J. C., Nielsen, E. L., Mamajek, E. E., Brandner, W., Hartung, M., Lidman, C., & Biller, B. 2005, Nature, 433, 286

Committee for a Decadal Survey of Astronomy and Astrophysics and National Research Council. 2010, New Worlds, New Horizons in Astronomy and Astrophysics (The National Academies), 1–225

Deming, D., Seager, S., Winn, J., Miller-Ricci, E., Clampin, M., Lindler, D., Greene, T., Charbonneau, D., Laughlin, G., Ricker, G., Latham, D., & Ennico, K. 2009, Publications of the Astronomical Society of the Pacific, 121, 952

Donati, J.-F. 2010, SPIRou, a nIR echelle spectropolarimeter for CFHT, `http://www.ast.obs-mip.fr/article.php3?id_article=637`

Doyon, R., Hutchings, J., Rowlands, N., Evans, C. E., Greenberg, E., Haley, C., Scott, A. D., Touahri, D., Beaulieu, M., Lafrenière, D., Abraham, R., Barton, E., Chayer, P., Ferrarese, L., Fullerton, A. W., Jayawardhana, R., Johnstone, D., Martel, A., Meyer, A. W. M. R., Pipher, J., Saad, K., Sawicki, M., Sivaramakrishnan, A., & Volk, K. 2010, in Society of Photo-Optical Instrumentation Engineers (SPIE) Conference Series, Vol. 7731, 77310F

Fortney, J. J., Marley, M. S., & Barnes, J. W. 2007, The Astrophysical Journal, 659, 1661

Fried, D. L. 1965, Journal of the Optical Society of America, 55, 1427

Gould, A., & Loeb, A. 1992, Astrophysical Journal, 396, 104

Guyon, O., Pluzhnik, E., Martinache, F., Totems, J., Tanaka, S., Matsuo, T., Blain, C., & Belikov, R. 2010a, The Publications of the Astronomical Society of the Pacific, 122, 71

Guyon, O., Pluzhnik, E. A., Galicher, R., Martinache, F., Ridgway, S. T., & Woodruff, R. A. 2005, The Astrophysical Journal, 622, 744

Guyon, O., Shaklan, S., Levine, M., Cahoy, K., Tenerelli, D., Belikov, R., & Kern, B. 2010b, in Society of Photo-Optical Instrumentation Engineers (SPIE) Conference Series, Vol. 7731, 773129

Hardy, J. W. 1998, Adaptive Optics for Astronomical Telescopes (Oxford University Press)

Hodapp, K. W., Suzuki, R., Tamura, M., Abe, L., Suto, H., Kandori, R., Morino, J., Nishimura, T., Takami, H., Guyon, O., Jacobson, S., Stahlberger, V., Yamada, H., Shelton, R., Hashimoto, J., Tavrov, A., Nishikawa, J., Ukita, N., Izumiura, H., Hayashi, M., Nakajima, T., Yamada, T., & Usuda, T. 2008, in Society of Photo-Optical Instrumentation Engineers (SPIE) Conference Series, Vol. 7014, 286

Janson, M., Carson, J. C., Lafrenière, D., Spiegel, D. S., Bent, J. R., & Wong, P. 2012, The Astrophysical Journal, 747, 116

Joshi, M. M., Haberle, R. M., & Reynolds, R. T. 1997, Icarus, 129, 450

Kalas, P., Graham, J. R., Chiang, E., Fitzgerald, M. P., Clampin, M., Kite, E. S., Stapelfeldt, K., Marois, C., & Krist, J. 2008, Science, 322, 1345

Kasper, M. E., Beuzit, J.-L., Verinaud, C., Yaitskova, N., Baudoz, P., Boccaletti, A., Gratton, R. G., Hubin, N., Kerber, F., Roelfsema, R., Schmid, H. M., Thatte, N. A., Dohlen, K., Feldt, M., Venema, L., & Wolf, S. 2008, in Society of Photo-Optical Instrumentation Engineers (SPIE) Conference Series, Vol. 7015, 70151S

Kasting, J. F., & Catling, D. 2003, Annual Review of Astronomy &Astrophysics, 41, 429

Kolmogorov, A. 1941, Dokl. Akad. Nauk SSSR, 30, 301

Lafrenière, D., Doyon, R., Nadeau, D., Artigau, É., Marois, C., & Beaulieu, M. 2007a, The Astrophysical Journal, 661, 1208

Lafrenière, D., Jayawardhana, R., & van Kerkwijk, M. H. 2008, The Astrophysical Journal, 689, L153

Lafrenière, D., Marois, C., Doyon, R., Nadeau, D., & Artigau, É. 2007b, The Astrophysical Journal, 660, 770

Lagrange, A.-M., Bonnefoy, M., Chauvin, G., Apai, D., Ehrenreich, D., Boccaletti, A., Gratadour, D., Rouan, D., Mouillet, D., Lacour, S., & Kasper, M. 2010, Science, 329, 57

Lyot, B. 1939, Monthly Notices RAS, 99, 580

Macintosh, B., Troy, M., Doyon, R., Graham, J., Baker, K., Bauman, B., Marois, C., Palmer, D., Phillion, D., Poyneer, L., Crossfield, I., Dumont, P., Levine, B. M., Shao, M., Serabyn, G., Shelton, C., Vasisht, G., Wallace, J. K., Lavigne, J.-F., Valee, P., Rowlands, N., Tam, K., & Hackett, D. 2006, in Society of Photo-Optical Instrumentation Engineers (SPIE) Conference Series, Vol. 6272, 62720N

Macintosh, B. A., Graham, J. R., Palmer, D. W., Doyon, R., Dunn, J., Gavel, D. T., Larkin, J., Oppenheimer, B., Saddlemyer, L., Sivaramakrishnan, A., Wallace, J. K., Bauman, B., Erickson, D. A., Marois, C., Poyneer, L. A., & Soummer, R. 2008, in Society of Photo-Optical Instrumentation Engineers (SPIE) Conference Series, Vol. 7015, 701518

Marengo, M., Stapelfeldt, K., Werner, M. W., Hora, J. L., Fazio, G. G., Schuster, M. T., Carson, J. C., & Megeath, S. T. 2009, The Astrophysical Journal, 700, 1647

Marois, C., Doyon, R., Nadeau, D., Racine, R., Riopel, M., Vallée, P., & Lafrenière, D. 2005, The Publications of the Astronomical Society of the Pacific, 117, 745

Marois, C., Doyon, R., Racine, R., & Nadeau, D. 2000, The Publications of the Astronomical Society of the Pacific, 112, 91

Marois, C., Lafrenière, D., Doyon, R., Macintosh, B., & Nadeau, D. 2006, The Astrophysical Journal, 641, 556

Marois, C., Macintosh, B., Barman, T., Zuckerman, B., Song, I., Patience, J., Lafrenière, D., & Doyon, R. 2008, Science, 322, 1348

Martinache, F., & Guyon, O. 2009, in Society of Photo-Optical Instrumentation Engineers (SPIE) Conference Series, Vol. 7440, 74400O

Mayor, M., Pepe, F., Queloz, D., Bouchy, F., Rupprecht, G., Lo Curto, G., Avila, G., Benz, W., Bertaux, J.-L., Bonfils, X., Dall, T., Dekker, H., Delabre, B., Eckert, W., Fleury, M., Gilliotte, A., Gojak, D., Guzman, J. C., Kohler, D., Lizon, J.-L., Longinotti, A., Lovis, C., Megevand, D., Pasquini, L., Reyes, J., Sivan, J.-P., Sosnowska, D., Soto, R., Udry, S., van Kesteren, A., Weber, L., & Weilenmann, U. 2003, The Messenger, 114, 20

Mayor, M., & Queloz, D. 1995, Nature, 378, 355

Mayor, M., Udry, S., Lovis, C., Pepe, F., Queloz, D., Benz, W., Bertaux, J.-L., Bouchy, F., Mordasini, C., & Segransan, D. 2009, Astronomy and Astrophysics, 493, 639

McLean, I. S. 2008, Electronic Imaging in Astronomy: Detectors and Instrumentation (Second Edition) (Praxis Publishing)

Murakawa, K., Suto, H., Tamura, M., Kaifu, N., Takami, H., Takato, N., Oya, S., Hayano, Y., Gaessler, W., & Kamata, Y. 2004, Publications of the Astronomical Society of Japan, 56, 509

Pasquini, L., Cristiani, S., Garcia-Lopez, R., Haehnelt, M., & Mayor, M. 2010, The Messenger, 140, 20

Queloz, D. 2006, Nature, 439, 400

Racine, R., Walker, G. A. H., Nadeau, D., Doyon, R., & Marois, C. 1999, The Publications of the Astronomical Society of the Pacific, 111, 587

Rouan, D., Riaud, P., Boccaletti, A., Clénet, Y., & Labeyrie, A. 2000, The Publications of the Astronomical Society of the Pacific, 112, 1479

Schneider, J. 2010, The Extrasolar Planets Encyclopaedia, `http://exoplanet.eu/catalog.php`

Sivaramakrishnan, A., Koresko, C. D., Makidon, R. B., Berkefeld, T., & Kuchner, M. J. 2001, The Astrophysical Journal, 552, 397

Soummer, R., Aime, C., & Falloon, P. E. 2003, Astronomy and Astrophysics, 397, 1161

Soummer, R., Valenti, J., Brown, R. A., Seager, S., Tumlinson, J., Cash, W., Jordan, I., Postman, M., Mountain, M., Glassman, T., Pueyo, L., & Roberge, A. 2010, in Society of Photo-Optical Instrumentation Engineers (SPIE) Conference Series, Vol. 7731, 77312I

Sparks, W. B., & Ford, H. C. 2002, The Astrophysical Journal, 578, 543

Spiegel, D. S., Burrows, A., & Milsom, J. A. 2011, The Astrophysical Journal, 727, 57

Sudarsky, D., Burrows, A., & Hubeny, I. 2003, The Astrophysical Journal, 588, 1121

Unwin, S. C., Shao, M., Tanner, A. M., Allen, R. J., Beichman, C. A., Boboltz, D., Catanzarite, J. H., Chaboyer, B. C., Ciardi, D. R., Edberg, S. J., Fey, A. L., Fischer, D. A., Gelino, C. R., Gould, A. P., Grillmair, C., Henry, T. J., Johnston, K. V., Johnston, K. J., Jones, D. L., Kulkarni, S. R., Law, N. M., Majewski, S. R., Makarov, V. V., Marcy, G. W., Meier, D. L., Olling, R. P., Pan, X., Patterson, R. J., Pitesky, J. E., Quirrenbach, A., Shaklan, S. B., Shaya, E. J., Strigari, L. E., Tomsick, J. A., Wehrle, A. E., & Worthey, G. 2008, Publications of the Astronomical Society of the Pacific, 120, 38

Vogt, S. S. 2009, Astro2010: The Astronomy and Astrophysics Decadal Survey, 2010, 306

Wambsganss, J. 1997, Monthly Notices RAS, 284, 172

Wolszczan, A., & Frail, D. A. 1992, Nature, 355, 145

CHAPTER 2

HIGH-CONTRAST IMAGING PERFORMANCE OF A TUNABLE FILTER FOR SPACE-BASED APPLICATIONS I: LABORATORY PERFORMANCE

P. INGRAHAM[1], R. DOYON[1], M. BEAULIEU[1], N. ROWLANDS[2], A. SCOTT[2]

Published in: *Publications of the Astronomical Society of the Pacific*, vol. 123 p. 1412 (2011)

Abstract

The scanning capability of a tunable filter represents an attractive option for performing high-contrast imaging through spectral differential imaging (SDI), a speckle-suppression technique widely used by current ground-based high-contrast imaging instruments. The performance of such a tunable filter is illustrated through the Tunable Filter Imager (TFI) which used to be part of the science instrument complement of the James Webb Space Telescope (*JWST*). The TFI features a low-order Fabry-Perot etalon which enables imaging spectroscopy at an average resolving power of 100. Also included is a high-contrast imaging mode featuring a Lyot coronagraph aided by spectral differential imaging (SDI). Using a TFI prototype etalon, we demonstrate the calibration technique to be used in the parallelization of the etalons reflective plates and then evaluate the etalon's ability to perform speckle-suppression through SDI. The improvement in contrast ranges from a factor of $\sim$10 at working angles greater than 11 λ/D increasing up to a factor of $\sim$60 at 5 λ/D. These results are consistent with a Fresnel optical propagation model which we use to show that the contrast improvement is limited by the test bed, and not the etalon. Our results demonstrate that a tunable filter such as the *JWST* TFI is an attractive solution for performing speckle-suppression in space through

1. Département de Physique, Université de Montréal, Montréal PQ, H3T 1J4, Canada
2. COM DEV Canada, Ottawa ON, K2K 3J1, Canada

multi-wavelength imaging.

Keywords: Astronomical Instrumentation, Data Analysis and Techniques, Astronomical Techniques

2.1 Introduction

The development of faint companion detection via differential imaging techniques has already produced direct images of planetary mass companions orbiting nearby stars (Kalas et al. 2008; Lafrenière et al. 2009; Lagrange et al. 2010; Marois et al. 2008). The search and identification of substellar and planetary companions of nearby stars is crucial for understanding the formation of planetary systems, including our own. Even null results have produced important constraints on the gas giant planet frequency at large separations for main-sequence stars (Biller et al. 2007; Lafrenière et al. 2007a; Nielsen et al. 2008). The primary challenges of high-contrast imaging are scattered light induced by atmospheric turbulence and quasi-static speckles resulting from optical path differences (OPDs) due to aberrations introduced by the optical elements of the telescope and instrument (Marois et al. 2000).

Currently, ground-based high-contrast imaging observations are limited by aberrations caused by atmospheric correction residuals and the instrument's imperfect optical surfaces. Building an instrument optimized for high-contrast imaging involves combining an optical system with very few instrumental aberrations with state-of-the-art extreme adaptive optics to perform the best possible atmospheric correction. Future dedicated planet finder instruments such as the Gemini Planet Imager (GPI; Macintosh et al. 2008), SPHERE (Spectro-Polarimetric High-contrast Exoplanet REsearch; Beuzit et al. 2008), HiCIAO (High-Contrast Coronagraphic Imager for Adaptive Optics; Hodapp et al. 2008) and the PALM-3000 AO system used with the Project 1640 instrument (Hinkley et al. 2008; Hinkley et al. 2011) are designed specifically to optimize companion detection and will provide a major step forward for detecting very faint companions at small angular separation around relatively bright stars. GPI, SPHERE, and Project 1640 are specifically designed to perform simultaneous spectral differential

imaging (SSDI), a technique used to reduce the impact of these speckles by simultaneously obtaining several narrowband images at specific regions of the spectrum, such as the methane absorption feature near 1.6 μm. In this region, the stellar spectrum is smooth whereas the relatively cool companion exhibits a large flux difference. By subtracting spectrally adjacent images, the signal of the host star and the quasi-static speckles are attenuated, leaving the difference in flux of the methane feature (Marois et al. 2000; Sparks & Ford 2002). Because the quasi-static speckle pattern scales radially with wavelength, the images must be scaled accordingly prior to subtraction (Racine et al. 1999).

The SSDI technique was first tested on sky at the Canada-France-Hawaii Telescope (CFHT) using the multichannel imager TRIDENT (Marois et al. 2005) and at the Very Large Telescope using NACO-SDI (Close et al. 2005; Lenzen et al. 2004) but yielded only marginal speckle-suppression performance. Further laboratory experiments showed that the OPDs occurring after the beam splitter severely hampered the SSDI speckle-suppression performance. A variety of methods exist to partially overcome this problem, for instance, inserting a holographic diffuser (Lafrenière et al. 2007b) or equivalently, a lenslet array (Macintosh et al. 2008) at the focal plane to destroy the coherence of the wavefront. However, in order to obtain the greatest speckle attenuation, the wavefront error of the telescope and instrument should be kept to a minimum and the images must be obtained using the same optical path (Cavarroc et al. 2006). Performing SDI from the ground requires both atmospheric correction and that each image for a given wavelength be observed simultaneously. When observing in space, the high stability of the point-spread function (PSF) allows images of differing wavelengths to be obtained non-simultaneously, however, significant speckle attenuation may only occur as long as the optical path is conserved.

JWST is a future space-based infrared observatory with a 6.5m diameter segmented mirror operating between 0.6 and 28 μm and is scheduled to be launched to the second Lagrange point this decade. All *JWST* instruments will be used for exoplanet applications. More specifically, the Near-Infrared Camera (NIRCam; Rieke et al. 2005) and the Mid-Infrared Imager (MIRI; Wright et al. 2008) will include coronagraphic modes and the Near-Infrared Spectrograph (NIRSpec; Bagnasco et al. 2007) will be used for transit

work. The fourth science instrument on board *JWST* is the Fine Guidance Sensor (FGS; Doyon et al. 2010), provided as part of the Canadian contribution to *JWST*. FGS includes two functionalities: a 1-5 μm camera dedicated to guiding the observatory and a 1-5 μm science camera module. Up until recently, the FGS science module was implemented as the Tunable Filter Imager (TFI) featuring a low-order Fabry-Perot etalon enabling imaging spectroscopy between 1.6 μm and 5 μm with an average resolving power of 100. Originally designed to detect the primeval galaxies (high-redshift Lyman alpha emitters) near the epoch of reionization, a Lyot coronagraph was later added for high-contrast imaging applications such as exoplanet imaging. The coronagraph possesses four occulting masks with diameters of 0.58", 0.75", 1.5" and 2" with three corresponding Lyot masks. TFI also features a non-redundant mask enabling contrasts of $\sim 10^{-4}$ between 70 and 500 *mas* (Sivaramakrishnan et al. 2010).

The TFI etalon acts as a tunable narrowband filter by adjusting the gap between two highly reflective plates. Each plate is driven by three low-voltage piezoelectric actuators controlled in a closed-loop mode by continuously measuring the distance via three capacitive sensors attached to the plates. Because no filters are moved in and out of the beam, the optical path is conserved therefore providing an ideal setup to perform speckle-suppression through SDI. Unfortunately, due to technical risks associated with the TFI etalon that could not be resolved within the tight schedule, it was decided to remove the etalon from the instrument. TFI was rescoped into a simplified instrument (without an etalon) featuring several grisms operated in a slitless mode to preserve the main science goals of the TFI to detect primeval galaxies and detect/characterize exoplanets. The original NRM mode was preserved with discrete filters and a new slitless spectroscopic mode specialized for transit work, complementary to NIRSpec, was introduced. The new instrument, called NIRISS (Near-InfraRed Imager and Slitless Spectrograph, will be described elsewhere (Doyon et al, in preparation). Even though the TFI etalon will not fly on *JWST*, it is very representative of a space-based tunable filter that could be used in the future for high-contrast imaging applications. It should be noted that none of the reasons contributing to the removal of the etalon from TFI were a result of its capability to perform high-contrast imaging, which is the focus of this article. Etalons remain

a viable and attractive option to perform high-contrast imagery using SDI in space.

Although speckle-suppression using an etalon has never been performed experimentally, previous theoretical estimates of the TFI etalon's ability to perform SDI produces excellent results. However, they do not account for two possibly contributing effects, etalon calibration error resulting in an induced wedge, and induced phase errors by the etalon's reflective surfaces (Doyon et al. 2008). Modeling the phase errors caused by the multiple reflections is difficult as it is dependent upon the surface quality of the individual layers composing each reflective surface. The best way to measure both effects is experimentally using an etalon prototype analogous to that of TFI. Moreover, prototyping provides an opportunity to simultaneously test and optimize the etalon calibration routine used to ensure plate parallelism. Our goal is to have a more accurate theoretical characterization of the speckle-suppression performance of a TFI-like etalon. Having characterized the speckle-suppression performance of such a prototype etalon, a follow-up article dedicated to modeling the on-sky performance of a space-based etalon instrument will be presented in a forthcoming article. This will be accomplished using an end-to-end Fresnel propagation model with TFI on *JWST* as an example of an implementation.

The first article is organized as follows. The laboratory test bed is described in section 2.2 with the prototype etalon design in section 2.3. The prototype etalon calibration procedure, which is directly comparable with that of TFI, is discussed and demonstrated in section 2.4. This is followed by a description of the acquired data (section 2.5) and the resulting speckle-suppression performance of the etalon. These results are then compared in section 2.6 with theoretical predictions calculated from a detailed Fresnel propagation model of the optical test bed.

2.2 Test Bed Description

A test bed was constructed at the Université de Montréal to quantify the speckle-suppression performance of TFI and validate the parallelization method to be applied to the TFI etalon. For these reasons, the optical bench has two configurations: one for

etalon calibration, the other for SDI measurements. The two modes are easily interchangeable by inserting a fold mirror in the optical path as shown in Figure 2.1.

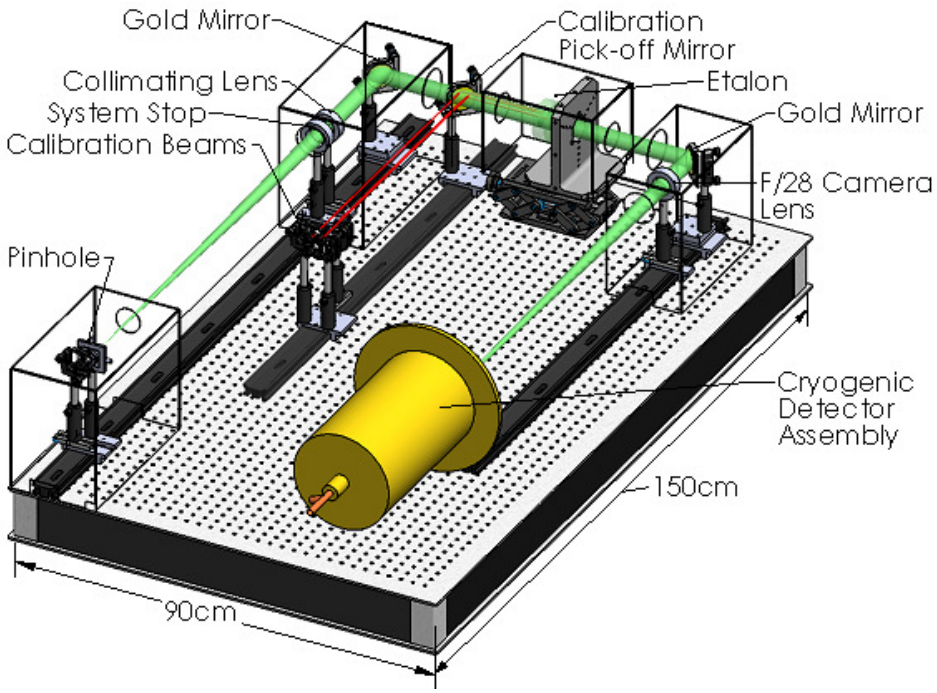

Figure 2.1: Two system setups of the test bed. The three collimated beams of the calibration setup, shown in red, are passed through the etalon with the insertion of a pickoff mirror. Upon removal of the mirror, the f/28 science beam is passed through the etalon (shown in green).

The SDI setup begins by a halogen light source illuminating a pinhole whose light is collimated after passing through a mask acting as the system stop (see Figure 2.2). The stop is one of the early TFI Lyot masks that is used here to create a highly structured PSF. The beam is then collimated using a 38.1 mm diameter f/28 calcium fluoride plano-convex lens with 1 λ peak-to-valley (PTV) surface error at 632 nm.[1] The beam is redirected by a 45° $\lambda/10$ PTV gold-coated fold mirror and then passed through the etalon. The beam is then redirected by another identical fold mirror, and passed through a camera lens. This camera lens is identical to the collimating lens, hence the optical magnification of unity. The beam then enters a cryostat via a $\lambda/10$ PTV window,

1. Measured transmitted wavefront error shows that the lens exceeds this specification.

then propagates through a cold $\lambda/4$ PTV H band filter through to a HAWAII-I HgCdTe 1024x1024 array. The 18.5 μm pixel size allows a sampling of 2.5 pixels per λ/D at 1.65 μm. This optical design is optimized for the H band and has Strehl ratios greater than 95% between 1.59 μm and 1.70 μm. The degradation in Strehl outside this spectral band is a result of chromatic aberration induced by the lenses. All science data are taken with the system fully enclosed in black baffles to minimize scattered light.

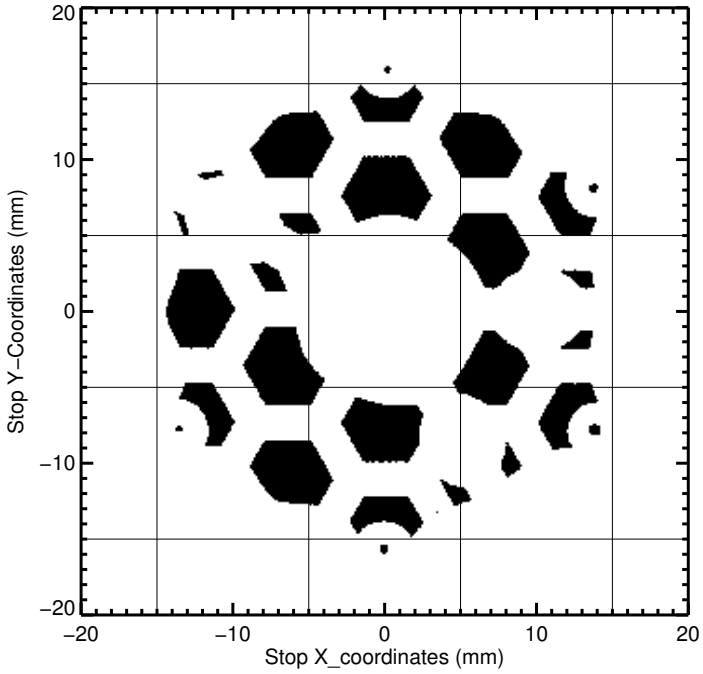

Figure 2.2: Lyot mask used as the system stop in the test bed. The dark regions correspond to the transmissive regions of the mask.

The second configuration of the test bed is used to calibrate the etalon for both transmitted wavelength as a function of gap size and plate parallelization. By inserting a fold mirror before the etalon (shown as the calibration pickoff mirror in Figure 2.1), three collimated beams generated from a 1.550 μm fiber-coupled laser are passed through the etalon. The beams are nearly parallel to the optical axis [2] and intersect the etalon close

2. The beam angles are slightly offset to ensure they focus at different physical locations on the detector.

to each capacitive displacement sensor. The light then follows the same path as the SDI configuration creating three individual spots on the detector. The intensities of the spots are modulated by the gap size at their relative positions on the etalon. When the etalon plates are not parallel and exhibit a wedge, each spot experiences a different gap size and hence transmission resulting in the spots exhibiting different intensities. When the plates are parallel, all spots have the same intensity. This behavior is the basis of the calibration routines described in section 2.4.

2.3 Etalon Prototype

Originally designed and constructed as a proof of concept, a short-wave etalon prototype (hereafter P0) was used to measure the speckle-suppression performance of TFI. While P0 is designed to operate at shorter wavelengths, it is conceptually identical to the TFI etalon. The wavelength range of P0 is between 0.9 and 2.0 μm, and the operational gap range is from 3.1 to 10.0 μm. Designed and built at COM DEV Canada, P0 is constructed of two 20 mm thick plates of fused silica with PTV transmitted wavefront errors of $\lambda/20$. Each plate is independently mounted on a common base plate that is mounted to an aluminum support structure, as shown in Figure 2.3. The bottom plate rests directly on three piezoelectric transducers (PZTs) which are held in position with respect to the baseplate using insulating spindles. The top plate sits on spacers that pass through the bottom plate, and rests on another three PZTs. Each plate is held against the PZTs using simple springs that are compressed using a long threaded rod that passes through the entire system and is bolted to the rear of the baseplate. This provides an isolated system where each plate can be actuated with respect to the other.

The mirrored side of each plate is coated with several alternating layers of silicon dioxide and amorphous silicate of varying thicknesses, providing a 40 mm diameter semi-reflective surface. Gold pads deposited on each plate near each pair of PZTs create three capacitive displacement sensors (CDS) which are used by auxiliary control electronics to measure the capacitance between etalon plates. The gap size is then determined via a derived relationship between the capacitance and gap. Each CDS with its

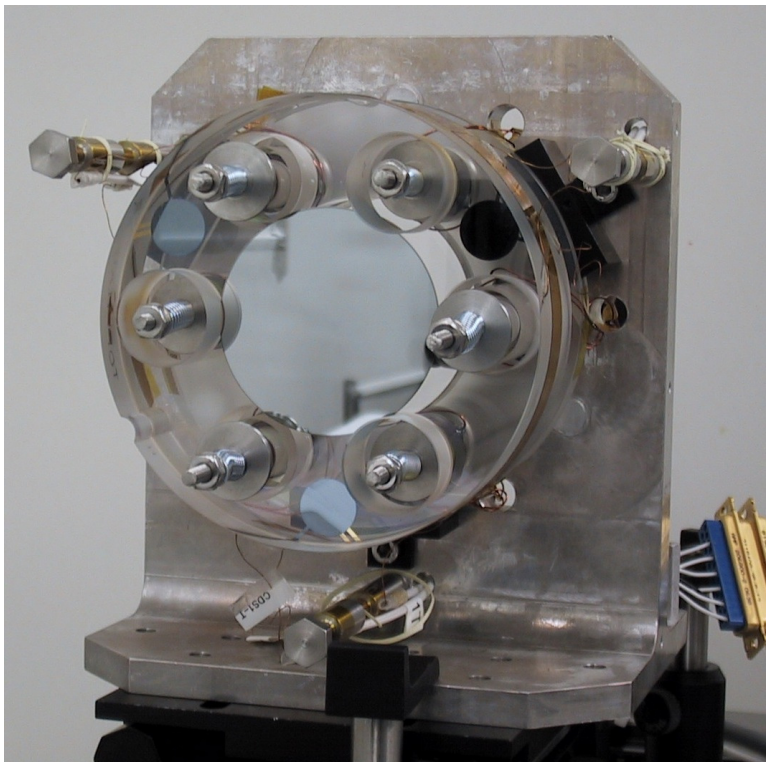

Figure 2.3: The short-wave etalon prototype, conceptually identical to the TFI etalon but built to work at ambient temperatures with a bandpass of 0.9-2.0 μm. The three capacitive displacement sensors are shown with the threaded rod and springs holding the plates against their associated PZTs.

corresponding upper- and lower-plate PZTs are referred to as a *channel*. Both the TFI and P0 etalons have three channels: 0, 1, and 2.

P0 is controlled using the Multi-Application Low-Voltage PZT Instrument Control Electronics (MALICE Scott et al. 2004). This system is also used to control the Flamingos-2 Tandem Tunable (F2T2) filter, an instrument built by COM DEV Canada and the University of Toronto using two etalons in series to scan between 0.95 and 1.35 μm at a resolution of R$\sim$800 (Mentuch et al. 2008). The MALICE system is very analogous to the etalon control electronics (ECE) to be used with the flight TFI etalon, except that MALICE is not designed for operation in a space environment. The MALICE box is controlled via a serial port from a Macintosh laptop running windows. The MALICE graphical user interface (GUI) was developed by COM DEV Canada and utilizes

an Analog Devices DSP 2191M EZKIT evaluation board using Analog Devices VisualDSP++ environment. The user is able to specify a gap size and to also step through a series of predefined gaps. The gap size is related to a capacitance that is constantly measured and corrected in closed-loop mode to correct for the hysteresis and creep associated with each PZT. The control electronics accuracy is limited by how well one can calibrate the etalon gap and the measured capacitance.

In normal operation, a user requires a central transmission wavelength. The necessary gap for this wavelength is determined using a theoretical transmission model of the etalon. This gap size is assigned a capacitance using a numerical relationship between the gap size and capacitance. The etalon is then moved to this capacitance value and held for the duration of the observation.

2.4 Etalon Calibration

The calibration procedure is twofold: 1) obtaining an accurate relationship between the gap size and capacitance and 2) keeping the plates parallel at every gap size.

The precision of the etalon's central gap size is proportional to the precision of the transmission wavelength. This is important since the size of the PSF is wavelength-dependent, which results in an incorrect radial scaling of the adjacent wavelengths' PSFs. This leads to a poor subtraction of speckles and therefore a degraded contrast. Moreover, the wavelengths used when performing SDI are preferably (yet not necessarily) chosen near sharp spectral features expected from a cool companion. Should the etalon be incorrectly tuned to the wrong wavelength/gap size, a significant (differential) signal loss may result.

A poor parallelization of the two etalon plates results in the gap size changing across the etalon aperture. This results in a degradation of the etalon's spectral resolution since the transmission profile is enlarged. Moreover, this decreases the transmission of the desired wavelength. Simulations have shown that in order to have less than 5% loss in transmission at a desired wavelength, the plates must be held parallel to 10 nm or better over the entire 40 mm clear aperture of the TFI etalon. Therefore, the calibration

procedure is required to be capable of keeping the etalon plates parallel to better than 10 nm.

2.4.1 Calibration of Gap Size Versus Capacitance

Ensuring an accurate gap size requires an accurate relationship between the gap size and capacitance. This is because the etalon control electronics only measure the capacitance of each CDS sensor then adjust the PZTs until the desired capacitance is measured. The first step in obtaining the relationship is performed by measuring the capacitance for several parallel plate positions using an optical feedback. This is accomplished by passing a collimated YAG laser (λ_{YAG}=1.06 μm) beam through the full etalon aperture and focusing it on a detector.[3] If the etalon plates are highly nonparallel, interference fringes are observed. If the plates are parallel to better than $\lambda_{YAG}/2$, a uniform illumination pattern is observed. At this point the gap size corresponds to $\frac{m\lambda_{YAG}}{2}$, where m is the transmission order. This position is found by manually driving the PZTs with external power supplies. Once determined, the capacitance of each CDS and the voltage applied to the associated PZTs are measured and the voltages of the PZTs are then increased until the subsequent order (Δm=1) is observed.[4] This process is repeated for several orders to determine an approximate relationship between capacitance and applied voltage. Given the PZT response ($\sim$10 Volts/μm), the relationship is converted to capacitance versus *relative* gap. This procedure does not measure the absolute gap because there is no way to determine which order m was first observed. Obtaining a relationship between the capacitance as a function of absolute gap requires the determination of a gap size for at least one order.

The absolute gap size for a given order is determined with the aid of a theoretical model of the etalon transmission vs wavelength. This model was constructed using the deposited layer thicknesses as determined by the coating supplier (INO, Quebec City) using ellipsometry measurements. This model allowed us to derive a theoretical

3. This setup is not shown in Figure 2.1

4. Slightly different capacitances are expected between channels due to the slight variation in circuitry components.

throughput spectrum for any given etalon gap and source function. Using a grating spectrometer, a measured spectrum of the etalon transmission at a given voltage was obtained and compared with a theoretical spectrum, allowing a determination of the absolute gap size (shown in Figure 2.4). Note that the measured spectrum was obtained while the etalon was adjusted using the collimated YAG laser beam and is therefore not perfectly parallel. This probably accounts for the variation between the theoretical and observed spectra. This absolute measurement of a given transmission order m, is used to calibrate the previously determined capacitance versus relative gap measurement. This relationship allows the etalon to be controlled electronically using either the TFI-ECE, or as in our case, MALICE.

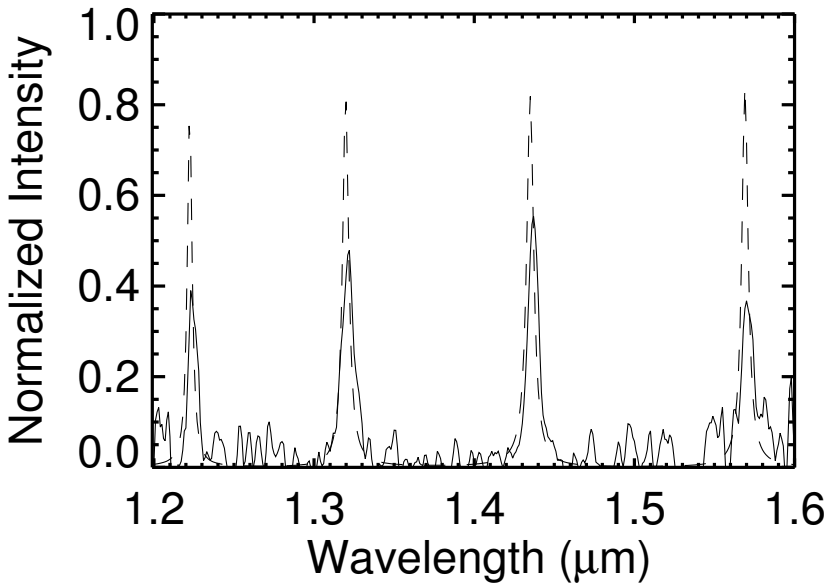

Figure 2.4: Measured spectrum (solid line) obtained at the largest possible operating gap. Overplotting a theoretical spectrum (dashed line) reveals a gap size of 7.88 μm. The theoretical spectrum includes an 8% loss due to Fresnel reflection. The difference in line width and intensity is expected of a poorly parallelized etalon.

2.4.2 Etalon Plate Parallelization

Due to the unpredictability of hysteresis and creep in PZTs, to obtain a well-calibrated etalon, the capacitance at each gap must be measured while in closed-loop mode. In this second stage of calibration, both the parallelization and gap size calibrations are greatly improved by using three collimated beams positioned near each CDS. As discussed in section 2.2, ensuring parallelization requires the beams' intensities to be simultaneously at their maxima. To determine the capacitance/gap sizes corresponding to the maxima, an iterative sequence measuring the intensities for small changes in capacitance was run using MALICE. This process was repeated for five different etalon orders of the 1.550 μm laser. This method allows gap positioning to better than 3 nm at each order. Fitting a second-order polynomial to the capacitance as a function of gap size provides an analytical relationship for each channel and ensures a gap/wedge precision within 10 nm. This relationship is then input into the MALICE GUI which interpolates the necessary capacitance for any desired gap size between 3.8 and 7.0 μm. This calibration scheme was used to calibrate the etalon prior to measuring its speckle-suppression performance.

2.4.3 Verification of the On Orbit Calibration Procedure

The operation of TFI requires that the etalon be calibrated from space with only its onboard instruments and a prelaunch ground calibration. Also required is that the on-orbit calibration performs no onboard data processing. This makes the iterative single image/single correction calibration method used with P0 unfeasible, due to the large time delay between data transmissions. Moreover, the FGS-TFI instrument does not house a spectrometer. For these reasons, a slightly different calibration scheme from the preceding one was conceived. Although the optical setups between the test bed and TFI are different, the fundamental calibration design uses the same method, both using three nearly parallel beams feeding the etalon near the capacitive sensors in order to measure and correct the plate parallelism.

The optomechanical design of TFI features a tungsten filament whose light is used to

create three collimated beams that pass through a comb filter [5] and project into the pupil wheel. The projection optics are contained off-axis to not interfere with any science operations. At the pupil wheel, the beams pass through three specially clocked prisms that redirect the light to create three nearly parallel beams propagating down the optical path. The beams propagate through the etalon near each CDS. They then continue into the camera create three spots on the detector.

Prior to launch, the etalon will be fully calibrated, having both a capacitance to gap relationship and a proper parallelization calibration. This calibration will be used as a starting point for the recalibration which will be performed after launch and cooldown and prior to science observations. Using this relationship, the etalon is stepped in specified increments over a gap range corresponding to a transmission peak of the comb filter. The intensities of the three collimated beams are measured at each position. If the etalon plates are parallel, all three spots will exhibit a maximum intensity at the same gap position. If the transmitted wavelength-to-gap calibration is correct, this gap size will correspond to the required gap size to transmit the observed wavelength of the comb filter. Should the etalon plates not be parallel, the maximum intensity of each channel will occur at different gap sizes, as specified to the software. The difference between the gap position as specified to the software and known gap size, as determined from the filter and etalon transmission model, provides the necessary information to determine a correction to the original gap to capacitance calibration. The scanning process is repeated until a central gap accuracy of 10 nm is achieved and the wedge across the entire reflective surface is less than 10 nm, at every transmission peak of the comb filter. We demonstrate this method using the P0 prototype etalon and the three collimated beams described in section 2.2. A schematic showing the critical components along with an example of the three spots on the detector is shown in Figure 2.5.

To simulate the change of calibration state of the TFI etalon due to launch and cooldown, a month-old calibration file was loaded into MALICE and an estimated 1 μm wedge was induced on channel 0 corresponding to a wedge of $\sim$500 nm across the

5. This filter has very sharp transmission peaks at 1.59, 1.76, 1.89, 2.05, and 2.34 μm, while being opaque in between.

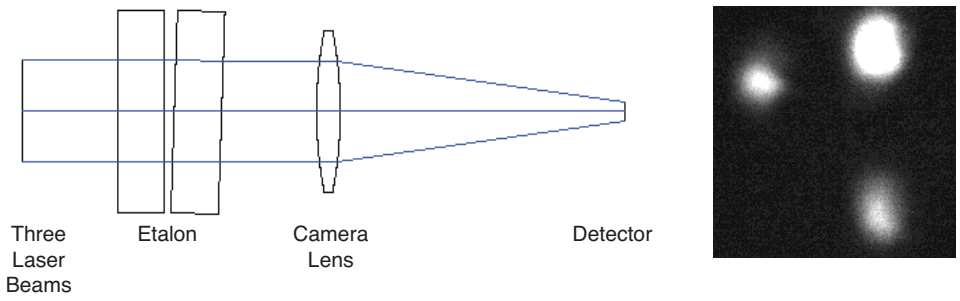

Figure 2.5: **Left:** A basic schematic of the calibration components. Three pencil beams, each positioned near a capacitive displacement sensor, are propagated though the etalon and are focused onto a detector using an f/28 lens. **Right:** The three spots on the detector. The difference in intensity between the spot indicates the gap size is different at each pencil beam position on the etalon.

entire aperture. We then scanned the etalon over six transmission orders of the 1.550 μm laser. Figure 2.6 (left) shows the original scan of the highly wedged etalon where the x-axis is the gap size inserted into the software, and channels 0, 1 and 2 are shown as black diamonds, red triangles, and blue squares, respectively. The collimated pencil beams undergo their maximum transmission when the gap size of the etalon at the location of pencil beam is 3.889 μm. The effect of all three transmission peaks being below this value is expected since the decrease in gap of channel 0 causes the etalon to pivot about the axis connecting the channels 1 and 2 PZTs. This in turn decreases the gap where the three collimated beams are present. The gap difference between the peaks in Figure 2.6 represents the gap difference in the position of each channel's collimated beams, not the gap difference over the entire etalon aperture.

The capacitance at each maximum transmission and the known gap size from the theoretical etalon transmission model are then used in the new determination of a new transmitted wavelength-to-gap relationship. After 12 iterations, this method performed gap positioning to better than 10 nm for each channel. This corresponds to a central wavelength accuracy of 4 nm. The wedge over the entire aperture is less than 10 nm for all five gap sizes ranging from 3.8 to 7.0 μm. Figure 2.6 (right) shows the 12th scan

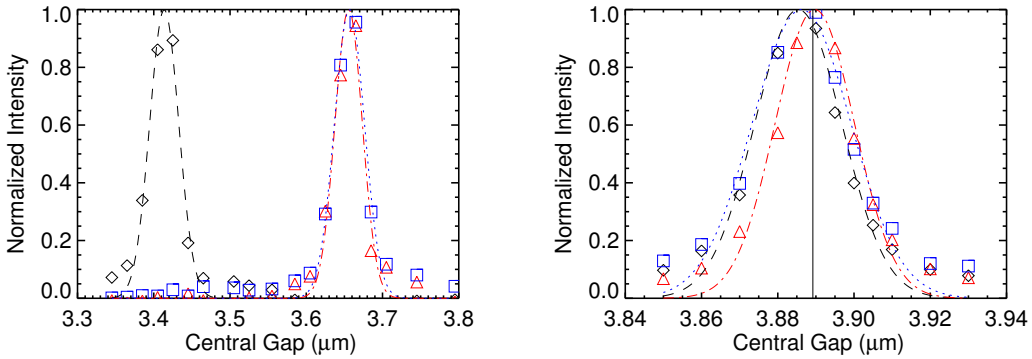

Figure 2.6: Stepping over order 5 of the 1.550 μm laser which corresponds to a gap of 3.889 μm. Channels 0, 1 and 2 are shown as black triangles, red diamonds, and blue squares respectively. Each channel's profile is fit using a Gaussian. **Left:** The original gap vs wavelength relationship containing a 480 nm wedge across the 40mm clear aperture. **Right:** The 12th iteration of the parallelization process yielding an mean offset of -2 nm from the desired gap with a 8 nm wedge across the aperture. The vertical line indicates the target peak for each channel.

stepping over the transmission of order 5 of the 1.550 μm laser, which corresponds to a gap of 3.889 μm. The measured wedge is 8 nm over the entire 40 mm aperture. We should stress that the preceding example represents an extreme case of a starting etalon wedge of 500 nm. In practice this calibration technique would be used after the etalon has been characterized using other techniques, so that the starting wedge is significantly smaller, hence the values obtained previously should be regarded as a worst case of what would be achieved in practice.

The large number of iterations required to parallelize the etalon is a direct result of not compensating for the positional offset between the collimated beams and PZTs. This caused a significant under-correction for each calibration step, resulting in an asymptotic approach to the desired calibration. The true TFI parallelization routine will include a geometrical model to compensate for these effects. Moreover, when fitting the second-order polynomials, each coefficient was left to float for every iteration. This is most likely unnecessary, especially in the presence of a large wedge as the slope and curvature is not expected to change significantly. Such improvements to the calibration routine are currently being used to optimize the calibration procedure for TFI.

2.5 Speckle-Suppression Performance

Once the etalon is well calibrated for both gap size and parallelism, the speckle-suppression performance can be determined. To do this, PSFs were acquired at five different wavelengths, however, for simplicity we consider only two wavelengths: 1.647 μm and 1.660 μm; the corresponding gap sizes are 4.177 μm and 4.220 μm, respectively. The 3 nm uncertainty on the central gap size corresponds to a $\sim$1 nm uncertainty in the wavelength of peak transmission. However, due to the low resolution ($R \sim 140$) and slightly asymmetric nature of the transmission function this value is likely underestimated. The central wavelengths were chosen to represent a difference of one resolution element. This represents the ideal case of a companion exhibiting an infinite contrast difference between these two wavelengths. This scenario was chosen in order to determine if any wavefront-error (WFE) is introduced by adjusting the gap size of the etalon and is not necessarily representative of an observation aimed at detecting a companion. The problem of detecting a companion with an arbitrary spectral energy distribution will be treated in our forthcoming article.

Each image to be used for contrast measurements consists of two separate images: one short-exposure image to sample the inner PSF regions and a longer one saturating the inner region but providing an adequate signal-to-noise ratio to the outer regions. The core of the image is always saturated: therefore, a theoretical PSF core with a radius of 1.22 λ/D (3 pixels) is used based on the model described in section 2.5.1. All data were flat-fielded and dark-subtracted prior to any image manipulation. The intensity of the long-exposure was scaled to match the intensity of the short exposure. The short-exposure image was then cropped at a radius of $\sim$8 λ/D and replaced by the longer-exposure image. The final images were then registered and the 1.660 μm image was scaled down radially by the ratio of the wavelengths.[6] Because the wavelengths are so well calibrated, no measurable error is introduced due to an uncertain scaling factor. The 1.660 μm image is shown on the left of Figure 2.7. After normalization, the two images are then subtracted to create the final difference image shown in Figure 2.8.

6. The 1.660 μm image is scaled radially inward to avoid extrapolation errors that would result if the

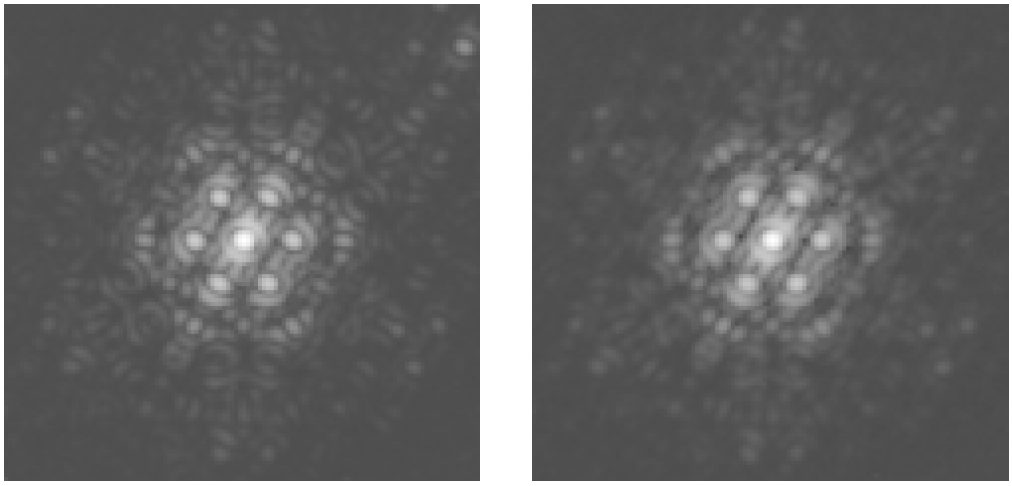

Figure 2.7: **Left:** The 1.647 μm PSF obtained using the test bed. The upper right-hand corner shows a ghost. **Right:** The corresponding theoretical PSF obtained from the Fresnel propagation of the test bed. Each image has a field of view of 29' by 29'.

The measurement of the speckle attenuation between the original image and difference image is best portrayed in a contrast curve. Each 5σ contrast curve is created by performing the standard deviation (σ) of individual radial bins of 1 pixel. This is performed on both the 1.647 μm image and on the difference images shown on the left side of Figures 2.7 and 2.8, respectively. The black solid curve of Figure 2.9 shows the contrast of the 1.647 μm image, and the contrast of the difference image is shown as the blue dot-dashed curve. Analyzing Figure 2.9 in the regions of high signal (5 λ/D), the contrast is improved by a factor of $\sim$60, whereas in the regions greater than 12 λ/D , the improvement is more modest with factors of $\sim$10. The region less than 1.5 λ/D is masked out due to saturation. Because the Lyot stop used generates a highly structured PSF, representative of on-orbit observations with *JWST*, the improvement in contrast is expected to vary with separation. In order to accurately determine the effect of the etalon on the speckle-suppression performance, the result must be compared with a theoretical model.

1.647 μm image is scaled outward.

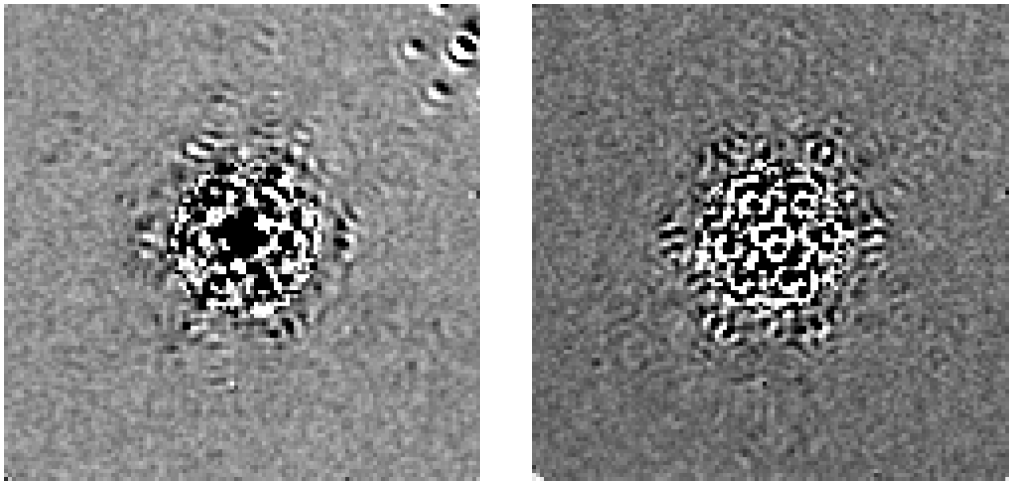

Figure 2.8: **Left:** The observed difference image between the 1.647 and 1.660 μm PSFs. **Right:** The corresponding theoretical difference image obtained using the Fresnel propagation of the test bed. Each image has a field of view of 29' by 29'.

2.5.1 Simulated Performance

A theoretical model was created using the IDL (Interactive Data Language) code PROPER (Krist 2007) to perform a Fresnel propagation of the test bed. Each end-to-end propagation accounts for the diffraction and WFE induced by each surface along the optical path. This allows accurate measurement of the effects of out-of-pupil wavefront error and determines the lower limit of the test bed to perform speckle-suppression. By comparing the theoretical contrast obtainable with the test bed with the experimentally measured contrast using the etalon, it is possible to quantify aberrations induced from the multiple reflections occurring inside the etalon.

The generated transmitted WFE maps were constructed following the example in the PROPER manual [7]. For the fold mirrors, surface maps were measured using a Zygo interferometer and were then used to create transmitted WFE maps. Due to the resolution of the measured surface map being lower than the sampling of the simulation, a higher-resolution map was created by combining the measured map with a simulated surface error map generated using a power law with a slope of -2.0. The low-frequency errors of the measured maps were fit using Zernike polynomials. The same number of Zernike

7. See http://downloads.openchannelsoftware.org/.DIRECT/PROPER_manual_ v1.0.pdf

polynomials were then subtracted from the generated map. The rms of the generated map was then normalized to the rms value of the measured map with the low-frequency aberrations removed. The low-frequency errors of the measured map were then added to the simulated map to create a high-resolution surface map. The transmitted WFE of the fold mirrors is simply twice the surface error. The transmitted WFE of the window and lenses were calculated using the same technique, however in this case the Zygo interferometer measures twice the transmitted WFE rather than the surface error.

The etalon plates and H-band filter did not have WFE maps available therefore they were generated using a power law with a slope of -2.0. The maps were normalized to have a transmitted rms WFE over their clear apertures calculated using $\sqrt{2}(n-1)\frac{PTV}{3.5}$, where PTV is the peak-to-valley surface irregularity and n is the index of refraction. Due to the minute beam size when propagating through the H-band filter, a map of the entire clear aperture could not be generated. Therefore, the WFE map of reduced size was generated and the rms value was scaled down proportionally with surface area. The WFE budget for the test bed is shown in Table 2.I. The transmitted rms WFE is calculated by measuring the standard deviation of the WFE map over the footprint of the beam.

Optical element	Transmitted RMS WFE (nm)	Beam diameter (mm)
Stop	0.0	33.3
Collimator Lens	17.7	33.5
Fold Mirror #1	4.3	33.5
Etalon Top Plate	1.7	33.5
Etalon Bottom Plate	1.9	33.5
Fold Mirror #2	4.6	33.5
Camera Lens	27.9	33.5
Cryostat window	0.3	2.2
H-band filter	0.4	1.3
Total	33.7	

Table 2.I: The wavefront error budget of the test bed.

In order to include the effects of polychromatism in the simulation, each science image is the composition of 121 monochromatic images distributed over the bandpass of

the H filter (1.488-1.788 μm). To account for the chromatic aberration induced by the lenses, the focal lengths were adjusted for each wavelength corresponding to the value measured in Zemax. Each monochromatic PSF is multiplied by its corresponding etalon transmission as determined by the theoretical etalon transmission model. The images are then integrated to create a single polychromatic image that is scaled to the flux of the science data (in photons). Photon noise and readout noise are then added to the image. Due to a increased noise component most likely resulting from electrical interference, the readout noise could not be modeled using a standard Gaussian distribution. Therefore, the readout noise maps added to the simulation were generated using the measured dark images. The simulated 1.647 μm PSF is shown on the right side of Figure 2.7. The simulated images are then passed though the same data reduction as described in section 2.5 to create the difference image shown on the right side of Figure 2.8. The resulting 5σ contrast curves of both images are shown in Figure 2.9, where the red dashed curve represents the PSF of Figure 2.7, and the red triple-dot-dashed line represents the theoretical simple difference image. The photon plus readout noise limit of our observations is shown as the short-dashed brown line. This curve is derived from passing the combined photon and readout noise maps of the data through the data reduction procedure, no OPDs are included.

2.6 Discussion

Comparing the observed and theoretical contrast curves shown in Figure 2.9 demonstrates the etalon's ability to perform SDI. Because the theoretical contrast curve is obtained assuming no etalon surfaces, any large variation would be a result of OPDs occurring due to WFE induced by the etalon. Figure 2.9 shows that the observational contrast does not significantly differ from the theoretical contrast. Such consistency shows that the speckle behavior is largely unperturbed by the presence of the etalon.

The contrast of the theoretical model's difference image has four contributing factors: chromatic aberration of the lenses, noncommon path aberrations due to the WFE induced by each optical element, image interpolation/manipulation error and photon/readout noise.

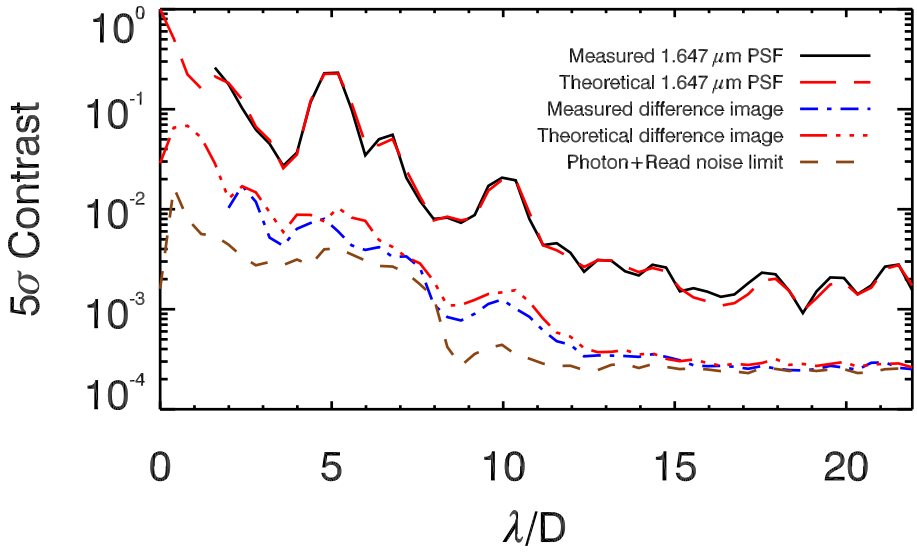

Figure 2.9: Speckle-suppression performance of the etalon is determined by comparing the measured 1.647 μm PSF 5σ contrast curve (solid line) with the 5σ contrast curve of the difference image (dash-dotted line). Comparing the theoretical 5σ contrast curve for the 1.647 μm PSF (red long-dashed line) with that of the theoretical difference image (triple-dot-dashed line) shows the maximum achievable contrast assuming no etalon is present. The combined photon and readout noise limit is shown as the brown short-dashed line. The contrast curve is truncated at 22 λ/D (13.4') to avoid any contamination from the ghost.

To quantify their effects, the obtainable contrast including only the individual sources of error was performed. Figure 2.10 shows the contrast achievable for each scenario. The fundamental limit, shown as a red dotted line, represents a scenario without WFE, chromatic aberration of the lenses, and photon and readout noise, and all image manipulation is performed in Fourier space to minimize any interpolation error. The contrast is limited by the shape and chromaticity of the PSFs. The orange dash-dotted line represents the contrast achievable when WFEs of the optical elements are included; this is seen to be negligible. The contribution of image interpolation error, shown as a cyan triple-dot-dashed line is computed by performing the data manipulation in image space. The highly dominant error is the chromatism of the lenses effect on the PSF, shown as the dashed

line. This is the primary constraint on the achievable contrast for separations smaller than $\sim$15 λ/D, where photon and readout noise become dominant [8]. It should be noted that the chromatism is inherent to our test bed and not necessarily representative of the optical configuration of the instrument. For example, this would not be a limitation for an all-reflective optical system such as that of the *JWST* TFI.

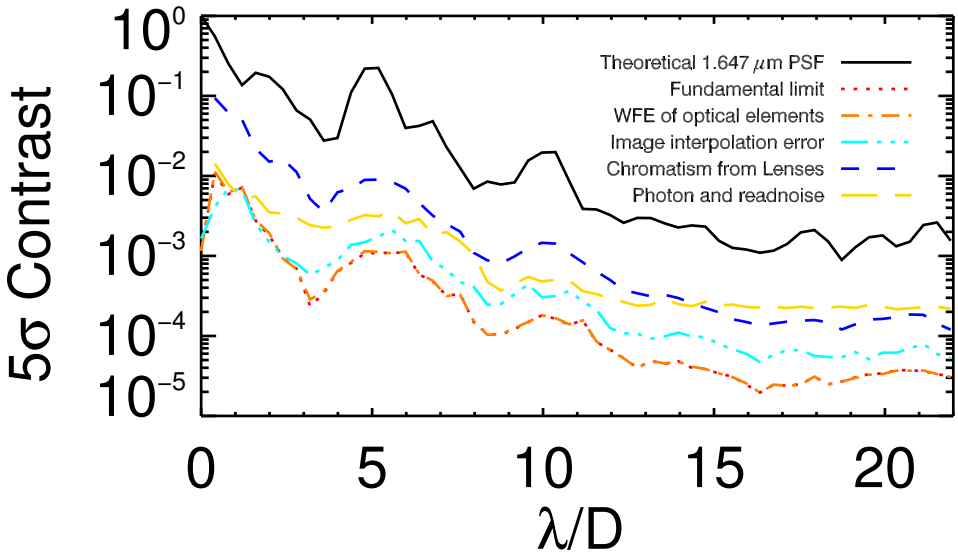

Figure 2.10: The speckle-suppression performance limits based on different noise contributions. The form of the modeled 1.647 μm PSF 5σ contrast curve (solid black line) is dominated by the diffraction from the highly structured Lyot stop used in the test bed. The fundamental limit where no noise, no WFE, and no image manipulation error are present is shown as a dotted red line. The WFE of the optical components (orange dash-dotted line, virtually superimposed on the dotted red line) does not contribute an appreciable amount of error. The dominant effect on the measured contrast is the chromatic aberration induced by the lenses (blue dashed line). At large separations, the photon and readout noise become the limiting error source.

For the first time, an etalon has been used to perform multiwavelength imaging. Performing speckle-suppression using an etalon has not previously been performed in

8. The image manipulation when including photon and readout noise was performed in image space. Significant numerical error is introduced when performing Fourier transforms of noisy images.

part because the OPD's caused by the multiple reflections inside the etalon are not easily modeled theoretically, therefore leaving its performance in question. However, because we observe consistent behavior in the speckle evolution with wavelength, this shows that the OPDs generated inside the etalon are minimal. In short, etalons can be very effective at performing high-contrast imaging.

The optimal observing scenario when using an etalon is dependent upon the telescope PSF, object, host, and separation. The host star and companion's spectrum determine which spectral features to use, which then determines the required broadband filter. A combination of the telescope PSF, the depth of the companion's spectral feature and its distance from the host will determine the required coronagraph setup to be used in order to detect and/or characterize the companion. In the observing scenario where the goal is detection, the companions spectrum and location are unknown, therefore understanding the limits of the instrument is key to determining the best possible detection efficiency. In the case of a known planet, the ability to characterize an object is also dependent upon the telescope and coronagraph. Having concluded that the etalon is efficient at performing speckle-suppression and utilizing the performance analysis of the coronagraph occulters (Beaulieu et al. 2008), realistic contrast curves for observations with *JWST* and a TFI-like instrument are now within reach. This would offer an accurate representation of the planet-detection capabilities using an etalon.

By performing an end-to-end Fresnel propagation of both the *JWST* telescope and TFI, Ingraham et al 2012 (in preparation) determine the planet-detection capabilities that would be capable with *JWST* and TFI. The ideal wavelength separation to detect a companions positive/negative signature is determined. For each coronagraphic setup, the detection contrasts between the host star and companion are measured. This is performed for two scenarios: 1) where the companion exhibits a flat spectrum and 2) where the companion exhibits an infinite contrast between two wavelengths (i.e. a sharp spectral feature). The characterization capabilities of *JWST* with TFI are demonstrated using the HR8799 and Fomalhaut systems as examples.

2.7 Conclusion

Because no filter change is required when using an etalon, the optical path is conserved, making this a potentially powerful device for exoplanet imaging. However, the ability to perform high-contrast imaging was questioned due to the potential OPDs induced by the multiple reflections between the etalons plates. To quantify these effects, a test bed was constructed at the Université de Montréal. Using an etalon prototype, the speckle-suppression performance was measured in the laboratory. To determine the limit of achievable speckle-suppression using the test bed and data reduction technique, a theoretical model was created by performing a Fresnel propagation model using PROPER. When the known test-bed and data reduction limitations are incorporated into the theoretical model, the result is consistent with the measured results. The small difference between theoretical and observed contrast curves shows that the speckle pattern's evolution with wavelength is coherent and that the OPDs introduced by the etalon are minimal. This confirms that the introduction of the etalon has no appreciable effect on the contrast attainable using the SDI technique. Having confirmed this, a more realistic scenario of detecting companions using a real telescope, such as *JWST*, can be considered. In a follow-up article, the achievable contrasts of a TFI-like instrument are determined by performing an end-to-end Fresnel propagation of the telescope and instrument.

Bibliography

Bagnasco, G., Kolm, M., Ferruit, P., Honnen, K., Koehler, J., Lemke, R., Maschmann, M., Melf, M., Noyer, G., Rumler, P., Salvignol, J.-C., Strada, P., & Te Plate, M. 2007, in Society of Photo-Optical Instrumentation Engineers (SPIE) Conference Series, Vol. 6692, 66920M

Beaulieu, M., Doyon, R., & Lafrenière, D. 2008, in Society of Photo-Optical Instrumentation Engineers (SPIE) Conference Series, Vol. 7010, 70103J

Beuzit, J.-L., Feldt, M., Dohlen, K., Mouillet, D., Puget, P., Wildi, F., Abe, L., Antichi, J., Baruffolo, A., Baudoz, P., Boccaletti, A., Carbillet, M., Charton, J., Claudi, R.,

Downing, M., Fabron, C., Feautrier, P., Fedrigo, E., Fusco, T., Gach, J.-L., Gratton, R., Henning, T., Hubin, N., Joos, F., Kasper, M., Langlois, M., Lenzen, R., Moutou, C., Pavlov, A., Petit, C., Pragt, J., Rabou, P., Rigal, F., Roelfsema, R., Rousset, G., Saisse, M., Schmid, H.-M., Stadler, E., Thalmann, C., Turatto, M., Udry, S., Vakili, F., & Waters, R. 2008, in Society of Photo-Optical Instrumentation Engineers (SPIE) Conference Series, Vol. 7014, 701418

Biller, B. A., Close, L. M., Masciadri, E., Nielsen, E., Lenzen, R., Brandner, W., McCarthy, D., Hartung, M., Kellner, S., Mamajek, E., Henning, T., Miller, D., Kenworthy, M., & Kulesa, C. 2007, The Astrophysical Journal Supplement Series, 173, 143

Cavarroc, C., Boccaletti, A., Baudoz, P., Fusco, T., & Rouan, D. 2006, Astronomy and Astrophysics, 447, 397

Close, L. M., Lenzen, R., Guirado, J. C., Nielsen, E. L., Mamajek, E. E., Brandner, W., Hartung, M., Lidman, C., & Biller, B. 2005, Nature, 433, 286

Doyon, R., Hutchings, J., Rowlands, N., Evans, C. E., Greenberg, E., Haley, C., Scott, A. D., Touahri, D., Beaulieu, M., Lafrenière, D., Abraham, R., Barton, E., Chayer, P., Ferrarese, L., Fullerton, A. W., Jayawardhana, R., Johnstone, D., Martel, A., Meyer, A. W. M. R., Pipher, J., Saad, K., Sawicki, M., Sivaramakrishnan, A., & Volk, K. 2010, in Society of Photo-Optical Instrumentation Engineers (SPIE) Conference Series, Vol. 7731, 77310F

Doyon, R., Rowlands, N., Hutchings, J., Evans, C. E., Greenberg, E., Scott, A. D., Touhari, D., Beaulieu, M., Abraham, R., Ferrarese, L., Fullerton, A. W., Jayawardhana, R., Johnston, D., Meyer, M. R., Pipher, J., & Sawicki, M. 2008, in Society of Photo-Optical Instrumentation Engineers (SPIE) Conference Series, Vol. 7010, 70100X

Hinkley, S., Oppenheimer, B. R., Brenner, D., Parry, I. R., Sivaramakrishnan, A., Soummer, R., & King, D. 2008, in Society of Photo-Optical Instrumentation Engineers (SPIE) Conference Series, Vol. 7015, 701519

Hinkley, S., Oppenheimer, B. R., Zimmerman, N., Brenner, D., Parry, I. R., Crepp, J. R., Vasisht, G., Ligon, E., King, D., Soummer, R., Sivaramakrishnan, A., Beichman, C., Shao, M., Roberts, L. C., Bouchez, A., Dekany, R., Pueyo, L., Roberts, J. E., Lockhart, T., Zhai, C., Shelton, C., & Burruss, R. 2011, Publications of the Astronomical Society of the Pacific, 123, 74

Hodapp, K. W., Suzuki, R., Tamura, M., Abe, L., Suto, H., Kandori, R., Morino, J., Nishimura, T., Takami, H., Guyon, O., Jacobson, S., Stahlberger, V., Yamada, H., Shelton, R., Hashimoto, J., Tavrov, A., Nishikawa, J., Ukita, N., Izumiura, H., Hayashi, M., Nakajima, T., Yamada, T., & Usuda, T. 2008, in Society of Photo-Optical Instrumentation Engineers (SPIE) Conference Series, Vol. 7014, 286

Kalas, P., Graham, J. R., Chiang, E., Fitzgerald, M. P., Clampin, M., Kite, E. S., Stapelfeldt, K., Marois, C., & Krist, J. 2008, Science, 322, 1345

Krist, J. E. 2007, in Society of Photo-Optical Instrumentation Engineers (SPIE) Conference Series, Vol. 6675, 66750P

Lafrenière, D., Doyon, R., Marois, C., Nadeau, D., Oppenheimer, B. R., Roche, P. F., Rigaut, F., Graham, J. R., Jayawardhana, R., Johnstone, D., Kalas, P. G., Macintosh, B., & Racine, R. 2007a, The Astrophysical Journal, 670, 1367

Lafrenière, D., Doyon, R., Nadeau, D., Artigau, É., Marois, C., & Beaulieu, M. 2007b, The Astrophysical Journal, 661, 1208

Lafrenière, D., Marois, C., Doyon, R., & Barman, T. 2009, The Astrophysical Journal Letters, 694, L148

Lagrange, A.-M., Bonnefoy, M., Chauvin, G., Apai, D., Ehrenreich, D., Boccaletti, A., Gratadour, D., Rouan, D., Mouillet, D., Lacour, S., & Kasper, M. 2010, Science, 329, 57

Lenzen, R., Close, L., Brandner, W., Biller, B., & Hartung, M. 2004, in Society of Photo-Optical Instrumentation Engineers (SPIE) Conference Series, Vol. 5492, 970–977

Macintosh, B. A., Graham, J. R., Palmer, D. W., Doyon, R., Dunn, J., Gavel, D. T., Larkin, J., Oppenheimer, B., Saddlemyer, L., Sivaramakrishnan, A., Wallace, J. K., Bauman, B., Erickson, D. A., Marois, C., Poyneer, L. A., & Soummer, R. 2008, in Society of Photo-Optical Instrumentation Engineers (SPIE) Conference Series, Vol. 7015, 701518

Marois, C., Doyon, R., Nadeau, D., Racine, R., Riopel, M., Vallée, P., & Lafrenière, D. 2005, The Publications of the Astronomical Society of the Pacific, 117, 745

Marois, C., Doyon, R., Racine, R., & Nadeau, D. 2000, The Publications of the Astronomical Society of the Pacific, 112, 91

Marois, C., Macintosh, B., Barman, T., Zuckerman, B., Song, I., Patience, J., Lafrenière, D., & Doyon, R. 2008, Science, 322, 1348

Mentuch, E., Scott, A., Abraham, R., Barton, E., Bershady, M., Bland-Hawthorn, J., Crampton, D., Doyon, R., Eikenberry, S., Gladders, M., Glazebrook, K., Jenson, J., Julian, J., Julian, R., Kneib, J.-P., Loop, D., Raines, N., Rowlands, N., & Smith, J. D. 2008, in Society of Photo-Optical Instrumentation Engineers (SPIE) Conference Series, Vol. 7014, 701476

Nielsen, E. L., Close, L. M., Biller, B. A., Masciadri, E., & Lenzen, R. 2008, The Astrophysical Journal, 674, 466

Racine, R., Walker, G. A. H., Nadeau, D., Doyon, R., & Marois, C. 1999, The Publications of the Astronomical Society of the Pacific, 111, 587

Rieke, M. J., Kelly, D., & Horner, S. 2005, in Society of Photo-Optical Instrumentation Engineers (SPIE) Conference Series, Vol. 5904, 1–8

Scott, A. D., Norman, R., & Zhou, L. 2004, in Society of Photo-Optical Instrumentation Engineers (SPIE) Conference Series, Vol. 5492, 1755–1762

Sivaramakrishnan, A., Lafrenière, D., Tuthill, P. G., Ireland, M. J., Lloyd, J. P., Martinache, F., Makidon, R. B., Soummer, R., Doyon, R., Beaulieu, M., Parmentier, S., &

Beichman, C. A. 2010, in Society of Photo-Optical Instrumentation Engineers (SPIE) Conference Series, Vol. 7731, 77313W

Sparks, W. B., & Ford, H. C. 2002, The Astrophysical Journal, 578, 543

Wright, G. S., Reike, G., Barella, P., Boeker, T., Colina, L., van Dishoeck, E., Driggers, P., Goodson, G., Greene, T., Heske, A., Henning, T., Lagage, P.-O., Meixner, M., Norgaard-Nielsen, H., Olofsson, G., Ray, T., Ressler, M., Thatcher, J., Waelkens, C., Wright, D., & Zehnder, A. 2008, in Society of Photo-Optical Instrumentation Engineers (SPIE) Conference Series, Vol. 7010, 70100T

CHAPTER 3

HIGH-CONTRAST IMAGING PERFORMANCE OF A TUNABLE FILTER FOR SPACE-BASED APPLICATIONS II: DETECTION AND CHARACTERIZATION CAPABILITIES

P. INGRAHAM[1], R. DOYON[1], D. LAFRENIÈRE, M. BEAULIEU

Published in: *Publications of the Astronomical Society of the Pacific*, vol. 124, p. 454 (2012)

Abstract

The scanning capability of a tunable filter represents an attractive option for performing high-contrast observations through spectral differential imaging (SDI), a speckle attenuation technique widely used by current ground-based, high-contrast imaging instruments. The performance of such a tunable filter is illustrated through the Tunable Filter Imager (TFI) which used to be part of the science instrument complement of the *James Webb Space Telescope* (*JWST*). TFI features a low-order Fabry-Perot etalon enabling imaging spectroscopy at an average resolution of 100 in the 1.5 to 5 μm range. TFI also includes a high-contrast imaging mode featuring a Lyot coronagraph aided by SDI. TFI's on-sky performance is determined by performing an end-to-end Fresnel propagation of the telescope and instrument using the measured wavefront error maps of TFI's optical elements and the theoretical wavefront error maps of the optical telescope assembly. Using this simulation, we determine that SDI offers an improvement in contrast ranging from a factor of $\sim$7 to $\sim$100 depending on the instrument's configuration. We present the companion detection capability using both the coronagraphic and non-coronagraphic modes of TFI and demonstrate the characterization capability using the HR 8799 and Fomalhaut systems. The performance of roll-subtraction is also determined and com-

1. Département de Physique, Université de Montréal, Montréal PQ, H3T 1J4, Canada

pared to that of SDI. We also present the SDI capability of the Near-Infrared Imager and Slitless Spectrograph, the science instrument module to replace TFI in the *JWST* Fine Guidance Sensor.

Keywords: Astronomical Instrumentation, Data Analysis and Techniques, Astronomical Techniques, Extrasolar Planets

3.1 Introduction

The challenge of direct imaging is to detect a faint companion in near proximity to a bright star. The primary difficulty is minimizing the scattered light from the bright primary star that dominates the signal originating from the faint companion. This scattered light is caused by diffraction from the telescope, atmospheric turbulence and quasi-static speckles resulting from optical path differences due to aberrations introduced by optical surfaces of the telescope and instrument. Suppressing the light of the star is accomplished using a variety of techniques that have already led to a handful of detections. Ground-based observations with adaptive optics (AO) resulted in the detection of a planetary mass companion in Upper Scorpius (Lafrenière et al. 2008). The planetary system of HR 8799 was detected using AO in combination with a novel observing and data reduction technique (angular differential imaging, Marois et al. 2006) to help suppress the halo of the host star (Marois et al. 2008b). Lagrange et al. (2010) used AO as well as point-spread function (PSF) subtraction in the detection of β Pictoris b. Fomalhaut b was detected by performing PSF subtraction while using the coronagraph inside the Hubble Space Telescope's (HST) Advanced Camera for Surveys (Kalas et al. 2008). Future exoplanet detections will involve a combination of all the techniques mentioned above and build on previous experience from the construction of past instruments.

Ground-based high-contrast imaging is limited by both atmospheric correction and the optical surface aberrations causing quasi-static speckles. One of the first techniques developed attempting to suppress these effects entitled, "Simultaneous Spectral Differential Imaging (SSDI)," simultaneously obtains multiple narrow-band images of the star-planet system at wavelengths where the cool companion exhibits a sharp spectral feature,

such as the methane absorption feature near 1.6 μm, but the host stars spectrum remains flat (Racine et al. 1999). After radially scaling the images to correct for the PSF evolution with wavelength, the images are subtracted to create a difference image. In this image, the quasi-static speckles are attenuated and a positive-negative signature of the companion from the flux difference of the spectral feature remains. Although efficient in theory (Marois et al. 2000; Sparks & Ford 2002), the performance was limited by noncommon path aberrations resulting in a marginal gain in speckle-suppression (Close et al. 2005; Lenzen et al. 2004; Marois et al. 2005). This problem can be partially overcome by inserting a holographic diffuser (Lafrenière et al. 2007a) or a lenslet array (Macintosh et al. 2008) at an intermediate focal plane to destroy the coherence of the wavefront prior to splitting the beam into different wavelengths. Of course, in order to obtain the greatest speckle attenuation, the wavefront error of the telescope and instrument should be kept to a minimum and the images must be obtained using the same optical path (Cavarroc et al. 2006). Previous experiments simulating space-based, moderate contrast ($10^{-6} - 10^{-7}$) systems measured a factor of $\sim$6 improvement in contrast when performing non-simultaneous spectral differential imaging (SDI) using individual filters (Biller et al. 2009).

Using a space-based observatory, such as HST, speckle-suppression can be performed using PSFs obtained at several different roll positions of the telescope. These PSFs can then be subtracted producing a positive-negative signal of the companion (Schneider & Silverstone 2003). This technique, often referred to as roll subtraction or roll deconvolution, was used in detecting Fomalhaut b. An analogous technique, Angular Differential Imaging (ADI; Marois et al. 2006), was implemented on the ground using a telescope with an altitude-azimuth mount. ADI is performed by disabling the Cassegrain rotator and allowing the field to rotate about the central star while the telescope and instrument setup remain fixed. By performing a median, the companion is filtered out leaving only the host star PSF. By subtracting this median frame from each image, rotating them to compensate for the image rotation and collapsing the stack, the companion can be detected. Although optimized for detection at relatively large separation, ADI in combination with novel image reduction techniques such as the Locally

Optimized Combination of Images (Lafrenière et al. 2007b) has detected companions at close separations (Lafrenière et al. 2009; Marois et al. 2010; Soummer et al. 2011).

Future ground-based high-contrast imaging instruments, designed specifically for companion detection, will combine state-of-the-art extreme AO with high surface quality optical elements and are optimized to perform SSDI and ADI. Instruments such as the Gemini Planet Imager (GPI; Macintosh et al. 2008), the Spectro-Polarimetric High-Contrast Exoplanet Research (SPHERE; Beuzit et al. 2008), HiCIAO (High-Contrast Coronagraphic Imager for Adaptive Optics; Hodapp et al. 2008), and the PALM-3000 AO system used with the Project 1640 instrument (Hinkley et al. 2008; Hinkley et al. 2011), will perform spectrophotometry in the *J*, *H* and *K* bandpasses of faint companions at small separations around relatively bright nearby stars and provide the next major step forward in exoplanet science. Due to atmospheric absorption, observing exoplanets past 2.5 μm from the ground is extremely difficult. However, this area of the spectrum (from 3.5-5.1 μm) is particularly interesting since it contains the peak of the spectral energy distribution (SED) of young, Jupiter mass companions. Observing this area of the spectrum is important in order to constrain planetary atmosphere models. Such observations are ideally accomplished using a space-based infrared telescope.

The *James Webb Space Telescope* (*JWST*) is a future 6.5 m diameter segmented mirror infrared optimized telescope to be launched late in this decade. From its orbit at the second Lagrange point, it is designed to take observations between 0.6-28 μm for a maximum of ten years (Gardner et al. 2009). All four scientific instruments will contribute to exoplanet science, however only three offer direct imaging capabilities (Beichman et al. 2010). The Near-Infrared Camera (NIRCam) high-contrast imagery capabilities will offer medium and broadband coronagraphic observations between $\sim$2-4.5 μm (Rieke et al. 2005). The Mid-Infrared Instrument (MIRI) houses three four-quadrant phase masks and a hard mask occulter optimized to perform coronagraphic observations at 10.65, 11.4, 15.5 and 23 μm respectively (Wright et al. 2008). The third instrument with high-contrast imaging capability is the Fine Guidance Sensor (FGS; Doyon et al. 2010). This instrument includes two functionalities: a 1-5 μm camera dedicated to guiding the observatory and a 1-5 μm science camera module. Until recently, the FGS science mod-

ule was implemented as the Tunable Filter Imager (TFI). Although designed to detect the primeval galaxies (high-redshift Lyman-alpha emitters) near the epoch of reionization, the instrument also featured a Lyot coronagraph with four occulters and three Lyot stops. TFI also contained a nonredundant mask (NRM) enabling contrasts of $\sim 10^{-4}$ between 70 and 500 mas (Sivaramakrishnan et al. 2010). At the heart of the instrument was a low-order Fabry-Perot etalon, enabling high-contrast imaging spectroscopy (R$\sim$100) from 3.2-5.0 μm. TFI possessed the unique quality of minimizing noncommon path errors for multiwavelength imaging because it uses the same optical path for each wavelength and no narrowband filters moved in nor out of the beam. This enables the observer to efficiently perform speckle-suppression via non-simultaneous SDI.

The ability of an etalon to perform high-contrast imaging with SDI was unknown due to the possible noncommon path errors introduced from the multiple reflections inside the etalon. In Ingraham et al. (2011), we demonstrated experimentally that an etalon does not contribute an appreciable amount of WFE when performing SDI with a highly-structured pupil such as the segmented mirror of *JWST*. This article provides the basis to determine the planet-detection and characterization capabilities of an etalon when used with a realistic telescope and instrument combination such as *JWST* and TFI. Unfortunately, due to technical risks that were not resolvable prior to the required delivery of the FGS to NASA, the etalon subsystem was removed. Therefore, TFI was reconfigured into an instrument without the etalon and coronagraph but featuring several grisms operated in a slitless mode to preserve the primary science goals of detecting primeval galaxies and to detect and characterize exoplanets using both the NRM mode and by performing transit spectroscopy, complementary to Near-Infrared Spectrograph (NIRSpec; Bagnasco et al. 2007). The new instrument, entitled the Near-Infrared Imager and Slitless Spectrograph (NIRISS) will be described elsewhere (Doyon et al 2011, in preparation). Although TFI is no longer part of the *JWST* instrument complement, it is an excellent representation of a space-based tunable filter instrument that could be used for future high-contrast imaging missions. Therefore, in this article, we use TFI as an example to demonstrate the detection and characterization capabilities of a space-based tunable filter. We also examine the SDI capability of NIRISS using three of its

medium-band filters.

Because the SDI performance is limited by the wavefront error (WFE) of the telescope and instrument, the expected performance can be determined using an end-to-end Fresnel propagation. In using the simulated WFE maps of the optical telescope element (OTE) in combination with the measured WFE maps of TFI, the simulation provides an accurate expectation of the high-contrast imaging performance. The TFI instrument and optical design are discussed in section 3.2 with an overview of the Fresnel propagation explained in section 3.3. The speckle attenuation performance using SDI is demonstrated and the planet-detection capabilities quantified in section 3.4. TFI's ability to detect and characterize exoplanets using SDI is then demonstrated using the HR 8799 and Fomalhaut systems in section 3.5. The potential effectiveness of roll subtraction is shown and discussed in section 3.6. The SDI capability of NIRISS is discussed in section 3.7.

3.2 The TFI Instrument

The TFI was designed to allow narrow-band imaging between 1.6 and 2.6 μm and 3.2 to 4.9 μm to enable scientific programs to find "First light" objects and to perform faint-companion detection and characterization. Along with the coronagraphic mode, TFI also featured a nonredundant mask (NRM) allowing high resolution observations ($\lambda/2D$) of bright objects at small separations (Sivaramakrishnan et al. 2010). Composed of both reflective and transmissive optics, the TFI optical design, shown in Figure 3.1, consists of nine optical elements. The light originates from the OTE which is composed of the primary, secondary, tertiary and fine steering mirrors that form a focal plane on TFI's gold coated pickoff mirror. This mirror exhibits a 3° tilt and is mounted on a stage to allow a focus adjustment. Engraved on the mirror's edge are four occulters located precisely at the entrance focal plane. The $0.58''$, $0.75''$, $1.50''$ and $2.00''$ diameter occulters are engraved conic features that effectively act as a hole. Their performance has been demonstrated through prototyping (Beaulieu et al. 2008). Each occulting spot is allotted a $20'' \times 20''$ field of view (FOV) and is to be used with the corresponding Lyot stop as indicated in Table 3.I. The shape of the Lyot stops were optimized for use at 4.4

μm, at specific separations and to be robust against a pupil shear of up to 4%. From the pickoff mirror, the F/20 beam is directed into the collimator. The collimator is composed of three gold-coated, aluminum aspheric mirrors that both collimate the beam and form a conjugate pupil image.

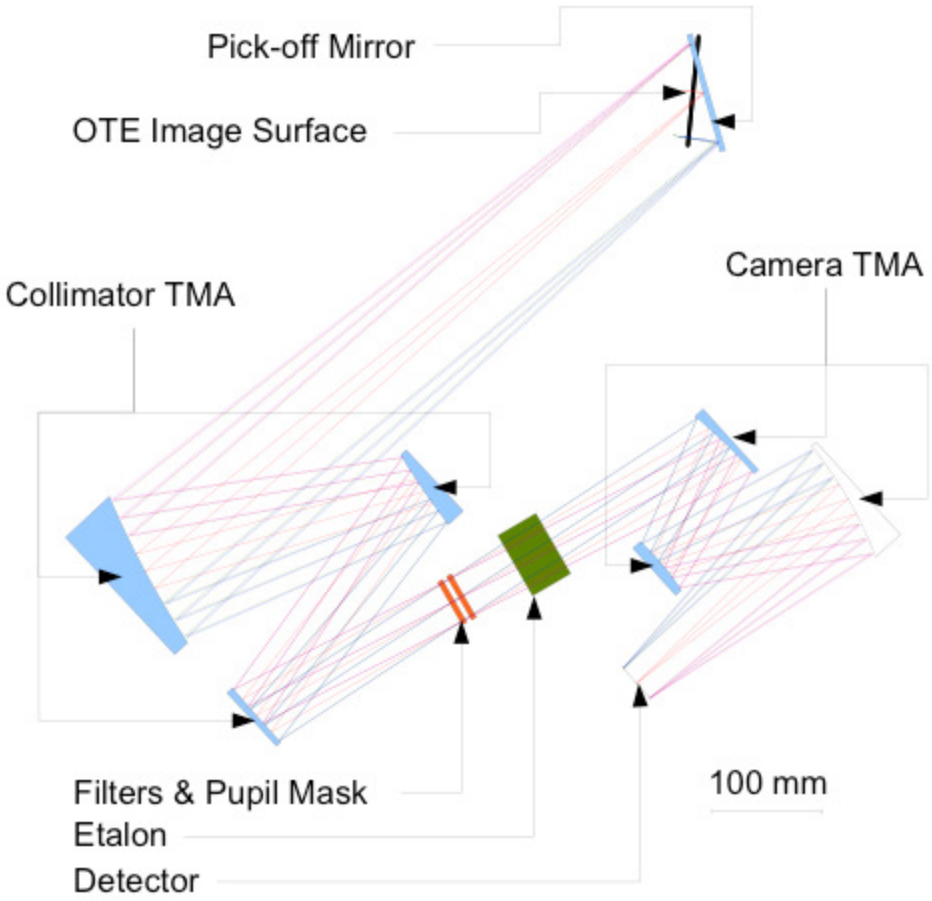

Figure 3.1: The optical design of the TFI instrument. The light from the telescope is directed into the instrument using the Pick-Off mirror that houses four occulters. The beam is then collimated and the filter and Lyot wheel reside at a conjugate pupil with the etalon located just afterwards. The three-mirror camera then focuses the beam onto the HAWAII 2-RG detector.

The dual wheel assembly contains a pupil wheel, located precisely at the conjugate pupil position and a filter wheel, located 14.7 mm behind the pupil wheel. Each wheel contains nine positions. The pupil wheel contains: the nominal Lyot stop, three

Lyot stops used for coronagraphy, the NRM mask, a neutral density filter, an opaque position and two calibration units (for wavelength calibration/etalon parallelization and flat-field illumination). The neutral density filter is used for positioning bright stars on the occulting spots. The filter wheel holds 8 blocking filters used to block the undesired transmission orders of the etalon plus one clear filter. Following the dual filter wheel assembly is the Fabry-Perot etalon.

The etalon consists of two highly polished ($\lambda/40$ peak-to-valley (PTV) at 632 nm) 20 mm thick plates of silicon each actuated using three piezoelectric transducers (PZTs). The gap between the plates is measured using three capacitive displacement sensors. The etalon is then controlled in a closed-loop mode to correct for any hysteresis and creep of the PZTs. The interior side of each plate is coated with alternating layers of silicon dioxide and amorphous silicate over a 40 mm aperture creating two highly reflective surfaces with a surface quality of $\lambda/20$ PTV. The wavelength of transmission is controlled by adjusting the distance between the two plates. A theoretical transmission model of the etalon provides a transmission profile for any desired gap size. Because no filters are moved in and out of the beam all PSFs result from a very similar wavefront. This is of critical importance when performing SDI. The etalon is built to operate over a gap range of 2.5 to 5.5 μm producing spectral resolutions between 80 and 140 over the 1.5 to 4.9 μm wavelength interval. After the etalon, the collimated beam is focused onto the detector using a three-mirror camera.

Separation ($''$)	Occulter	Lyot Stop
0.04-0.5	N/A	NRM
0.35-1.0	$0.58''$	C71N
0.42-1.0	$0.75''$	C71N
1.0-2.3	$1.50''$	C66N
≥ 2.3	$2.00''$	C21N

Table 3.I: TFI optimal coronagraphic configurations for a given separation. The number in the Lyot stop name is the throughput percentage. Each stop was designed to be used at specific separations and to be robust against pupil shear.

The 2.2'x2.2' field of view of TFI is imaged using a 2048X2048 HAWAII 2-RG

detector with an 18 μm pixel size. The corresponding image is Nyquist sampled at 4 μm and has pixel scale of $0.065''$. The (double correlated sampling) read noise and dark current has been measured to be 21 e^- and 0.012 e^-/s respectively. Lower read noise ($5e^-$) is possible through 88 up-the-ramp non-destructive reads. The image quality and coronagraphic performance are primarily a function of the total WFE of the system, that is largely dominated by the primary mirror of the OTE. Using the WFE budgets of the telescope and instrument, an adequate performance estimate can be calculated. To determine the performance of SDI requires an understanding of the WFE introduced by each individual optical element.

3.3 Optical Model

In traditional diffraction theory, the PSF of an optical system is calculated using the Fraunhofer (or far-field) approximation, where the PSF is the modulus squared of Fourier Transform of the *total* WFE of the system multiplied by the pupil shape. As the wavelength changes, the PSF shape is observed to expand or contract radially, however, the intrinsic pattern remains largely the same. This approach is often used successfully in the design of coronagraphs as it provides a straightforward relationship between the pupil plane, focal plane (with occulter), Lyot plane, and the image plane. By assuming that all of the WFE resides in a pupil plane and that the scaling relationship is only a function of wavelength, SDI is expected to suppress the PSF of the host star by a large factor ($\sim$1000; Marois et al. 2000). In practice, all optical surfaces contribute to the distortion of the wavefront, introducing both phase and amplitude errors. As they propagate, some phase errors are converted into amplitude error and vice versa through the Talbot effect.

The Talbot effect is most easily understood by considering the propagation of a plane wave of wavelength λ in a collimated space. If the plane wave undergoes a spatially periodic phase offset of period T, as it propagates, the pure phase error will evolve into a pure amplitude error, a purely negative phase error, a purely negative amplitude error, then oscillate back to the original phase. The propagation length, or Talbot length, cor-

responding to the full cycle is equal to $2T^2/\lambda$. For low-frequency (large period) errors, such as a defocus of the secondary mirror, the talbot length is very large compared to the propagation distance. Therefore, the aberration will not change significantly from phase to amplitude as it propagates to the image plane. For high-frequency errors, such as grooves that are often introduced when a mirror shape is figured through diamond-turning, this effect becomes non-negligible and may affect the high-contrast imaging performance. For systems using AO, phase aberrations can be partially corrected using a deformable mirror at a pupil plane whereas amplitude error correction requires a deformable mirror placed outside a pupil plane. In the case of *JWST*, there is no available correction, therefore the image quality is directly dependent upon the surface error of each optical element and its position in the beam.

Because the Talbot effect is chromatic, the wavefront becomes less coherent with increasing wavelength separation leading to the PSF having increasingly different speckle patterns. When performing SDI, these speckle patterns are re-scaled and subtracted and the differing speckle patterns leave residuals in the difference image, as demonstrated in Figure 3.2. If the WFE is introduced at a pupil plane, the speckle pattern will be well subtracted whereas if the aberration occurs outside a pupil plane, the effectiveness of SDI is greatly reduced (Marois et al. 2006). The remaining residuals become the dominant noise in the resulting difference image and limit the imager's ability to detect faint companions. This is demonstrated in section 3.4.

Performing a polychromatic Fresnel propagation accounts for the Talbot effect and any diffraction that occurs from the edges of the optical elements. Similar simulations have been performed on other high-contrast imagers such as GPI (Marois et al. 2008), SPHERE (Boccaletti et al. 2008) and NIRCam (Krist et al. 2007), to predict their performance and determine WFE tolerances. In our Fresnel propagation of *JWST* and TFI, we employ the IDL code PROPER (Krist 2007). This code propagates a wavefront between individual optical surfaces and allows the user to include custom phase or amplitude WFE maps. The imposed limitations are: the inserted optical design must be on-axis, any powered surface be represented by a simple spherical lens, and that each call to the propagation script be monochromatic.

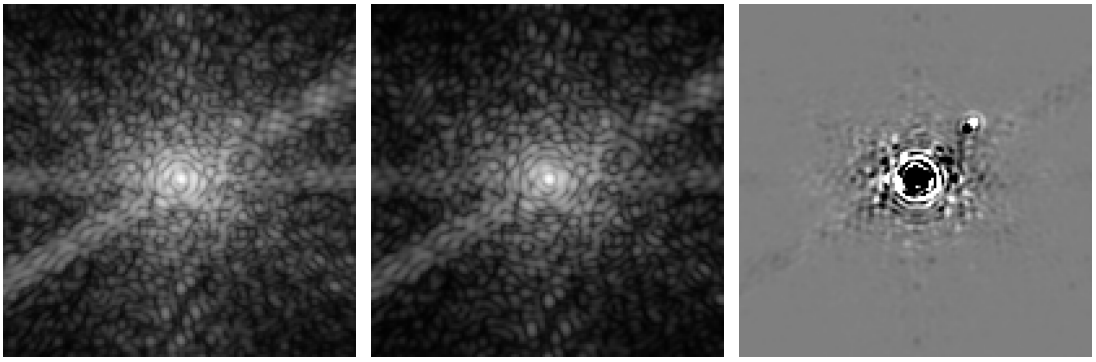

Figure 3.2: The simulated TFI coronagraphic PSFs at 4.220 μm (left) and 4.700 μm (center) shown in log scale. Their resulting difference image (right), shown in a linear scale, is created by radially scaling the 4.700 μm PSF inwards by the ratio of the wavelengths then subtracting the two images. The remaining speckle pattern is a result of the chromaticity of the Talbot effect. The positive-negative signature of a companion is seen towards the upper right. The field-of-view of each image is $8.9\times8.9''$.

Modifying the *JWST*+TFI optical design to create an on-axis version requires very few changes. The distances between each optical surface were extracted directly from the optical design. The power of the non-spherical surfaces was approximated by measuring the effective focal length of the surface, this was necessary for the TFI collimator and camera. The result of this approximation was the pupil image being moved against the direction of propagation by 11 mm. To conserve the length of the optical train, the dual filter wheel and etalon surfaces were moved ahead by this distance. Approximating the camera mirrors to be spherical elements resulted in an increase in the back focal length by 4 mm. Upon inserting the optical design, the next step is to add the associated transmitted WFE to each surface. In the case of TFI, the optical components have been built, assembled and wavefront errors measured. These direct measurements are incorporated into the propagation. For the OTE, the final mirrors have yet to be completed therefore we use a simulated WFE map provided by Ball Aerospace, based on the “Revision V" version. However, recent testing shows the mirror segments are expected to meet or exceed the specification (Gallagher et al. 2011). The on-axis optical prescription is shown in Table 3.II.

The supplied OTE WFE map has an rms WFE of 162 nm with a sampling of 6.34

Optical element	Eff. Focal length (mm)	Beam diameter (mm)	Dist. to next surface (mm)	Trans. rms WFE (nm)
Primary mirror	7940	6610	7169	162
Secondary mirror	-889.5	641.7	7965	0.0
Tertiary mirror	1507	242.8	1844	0.0
Fine-steering mirror	-	150.4	3018	0.0
Pick-off mirror	-	0.1	706.8	0.0
Collimator mirror 1	387.2	35.3	256.2	17.6
Collimator mirror 2	-268.7	24.8	245.5	16.0
Collimator mirror 3	731.9	37.4	194.1	21.2
Lyot stop	-	37.4	14.7	0.0
F425 blocking filter	-	37.4	54.3	11.5
Etalon front plate	-	37.4	40.0	9.4
Etalon rear plate	-	37.4	190.3	5.2
Camera mirror 1	271.1	37.4	117.7	31.0
Camera mirror 2	-111.9	21.2	173.6	15.3
Camera mirror 3	181.8	30.1	263.7	21.32
Detector	-	0.04	-	-
Total				170.7

Table 3.II: The on-axis prescription of *JWST* and the TFI instrument.

mm/pixel across the primary mirror. The TFI optical system has a rms WFE of 54.0 nm. The simulated map includes the WFE of the secondary, tertiary and fine steering mirror (FSM) but is dominated by tip-tilt and figuring errors of the individual primary segments. Because no information could be extracted about the secondary, tertiary and FSM mirrors, all of the WFE was assumed to originate from the primary. The WFE of the pickoff mirror was not included since it rests at a focal plane and is therefore negligible. To simulate the occulters, the complex wavefront was multiplied by a binary mask being 0 behind the occulter and 1 everywhere else. For the remaining surfaces, individual maps were derived from the measured WFE maps.

The transmitted WFE of the cryogenic collimator and camera systems were measured individually during the cryogenic testing of the FGS optical elements (Evans et al. 2010). This was accomplished using a ZYGO interferometer to pass a collimated beam through each system. At the focal point, a high-surface quality reflective sphere was used to reflect the light back through the system and into the ZYGO. Each measured WFE map is the total WFE from its three mirrors. The fabrication errors from the diamond turning of the concave surfaces is identifiable in each measured map and can be associated with the appropriate optical element. These errors were extracted using filtering in Fourier space and were used in creating the maps of the individual surfaces. The low and mid frequency errors could not be associated to individual optical components. Therefore, they were fitted using 100 Zernike polynomials then randomly distributed over the three surfaces. Tip, tilt and defocus were omitted. The high-frequency component was determined from measuring the rms error and slope of the power spectral density distribution of measured map minus the fitted low order aberrations. This slope was then used to create a random phase screen for each surface with rms equal to the measured value divided by $\sqrt{3}$.

All SDI simulations are performed using the F425 blocking filter (3.64 to 4.92) μm that was chosen due to its large bandpass to allow SDI observations without a change of filter. The F425 filter did not have WFE maps available therefore they were generated using a power law power spectral density with a slope of -2.5. The filter WFE map was normalized to have a transmitted rms WFE of 13.7 nm over the clear surface as

determined from a combination of measured substrate WFE and estimated WFE induced by the coating. For the etalon, the rms transmitted WFE was derived using the measured surface irregularities of the coated and uncoated surfaces. Each plate is represented by a single WFE map generated using a power law power spectral density slope of -2.5 with an rms of $(n-1)\sqrt{(\sigma_{RMS\_uncoated})^2+(\sigma_{RMS\_coated})^2}$, where n is the index of refraction of silicon (n=3.4). The WFE generated by the multiple reflections inside the etalon was assumed to be zero. Under moderate contrast improvement, this assumption is shown to be valid by Ingraham et al. (2011), who achieved an average contrast improvement of $\sim$10 using a TFI prototype etalon. The contrast improvement was limited by their optical test bed and not the etalon therefore larger contrast improvements with a better performing test bed are very probable.

Each monochromatic propagation was run with a 2048x2048 pixel resolution with the ratio of the initial beam diameter to the grid width being 0.4. This provides adequate sampling of the primary mirror and other optical surfaces while ensuring the sampling of the PSF remained less than $0.065''$ per pixel and offering sufficient padding to minimize numerical error. The resulting images are then resampled to match the detector pixel size (18 μm). To create polychromatic images, a cube of monochromatic images was integrated over the broadband and etalon transmission filter profiles. Each polychromatic image is composed of 256 monochromatic images ranging over the blocking filter bandpass in 6 nm increments. The weighting of each image is determined by the transmission of both the blocking filter and the etalon transmission function for the chosen wavelength. Because we wish to show the limits of the instrument independent of the observed object, detector noise is not added to any of the following simulations except when specified (section 3.5). Because the quantity of the pupil shear is only constrained to be between 1-4% of the pupil diameter in any direction, we performed all simulations assuming a pupil shear of 2%.

3.4 Planet-Detection with SDI

Speckle attenuation performance is directly dependent upon the decorrelation of the wavefront due to the chromaticity of the Talbot effect. Therefore when performing SDI, increasing the wavelength difference increases the residuals and decreases the contrast. This effect is demonstrated in Figure 3.3, where the contrast is measured as the standard deviation (σ) of pixel values for an annulus with a width of 1 pixel (0.065″). The solid black line represents the contrast of the non-coronagraphic 4 μm PSF and the 4 μm coronagraphic PSF is shown as a dashed red line. The remaining lines are the contrast obtained with SDI as a function of wavelength spacing that is increased arbitrarily by 200 nm increments. Because speckle noise follows a non-Gaussian probability density function, we have chosen to use 10σ to represent our speckle-suppression and detection limits. This value is more representative of the 5σ confidence levels generally used when working with a Gaussian probability density function (Marois et al. 2008a). The coronagraph offers a factor of $\sim$10 improvement in contrast, with SDI offering another factor of $\sim$10 depending on the wavelength separation. An observer should minimize the wavelength separation to maximize speckle-suppression, however, when aiming to detect a companion one must also consider the ability to detect the signal of the planet.

The ability to detect a companion with SDI is dependent upon the companion's separation and spectral features. We shall consider two extreme cases of spectral features. When the companion is detected at only one wavelength due to a large intrinsic signal difference, we refer to this as the *sharp spectrum* scenario. This type of detection represents relatively cold companions exhibiting sharp spectral features, such as what is predicted at $\sim$4.3 μm (Burrows et al. 2003). One can also expect to detect companions with much flatter, featureless spectra, such as what is observed for HR 8799 b (Barman et al. 2011; Bowler et al. 2010) and predicted for the other HR 8799 planets (Madhusudhan et al. 2011). To represent this case we consider the conservative case of a *flat spectrum* (in flux). Detecting this type of spectrum is more challenging because the individual components of the companion's positive-negative signature in the difference image must be adequately separated. Because the separation is given by the ratio of the observed

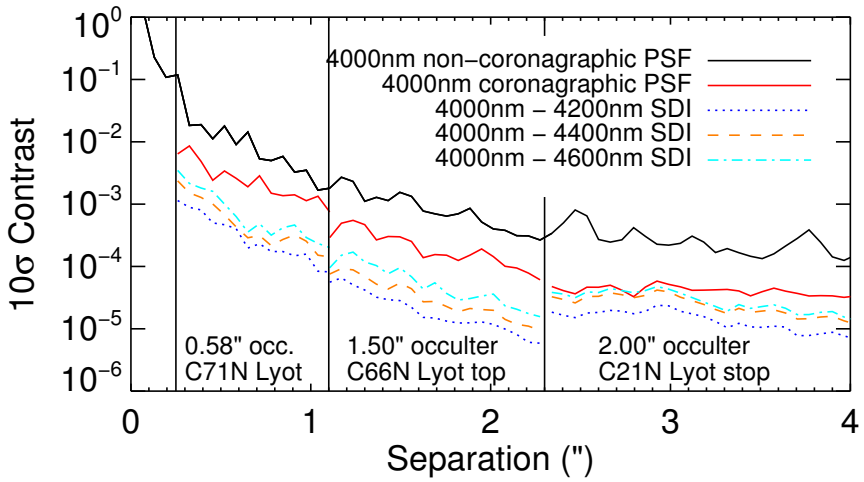

Figure 3.3: Speckle-suppression achieved using a simple difference as a function of wavelength separation. The plotted portions of each coronagraphic setup show the regions of highest achievable contrast assuming a 2% pupil shear. The 0.75″ occulter is not shown for clarity as it produces similar results to the 0.58″ occulter and only exceeds its performance in the case of a larger pupil shear. The reduction in contrast with increasing wavelength separation is a result of the PSF speckle pattern decorrelating due to the Talbot effect.

wavelengths multiplied by the separation, if the wavelengths are not sufficiently different, the separation between the components of the positive-negative signature will be too small and the planet signal will self-subtract. If the wavelength separation is too large, the positive-negative signature will be sufficiently separated but the increased speckle noise due wavelength separation might render the companion undetectable. Therefore, it is necessary to find a balance between these two effects.

To determine the optimal separation of the components in the positive-negative signature, the signal to noise of the companion as a function of wavelength separation (and hence spatial separation in the difference image) was measured for each coronagraph setup. The companion PSF's were generated using the same setup as the coronagraphic PSF, but without the occulter. These PSFs were then shifted in Fourier space to the desired position and added to the image of interest. To determine the signal-to-noise of the detection, we utilize a template with an intensity normalized to unity, that corresponds

to the expected signature for a given observation type. For example, in a purely coronagraphic observation, the template is simply a non-occulted PSF of the corresponding coronagraphic Lyot stop. In the case of roll subtraction, the template has a positive and negative components with equal intensities and a separation corresponding to the roll angle. The signal at any given position in the image is determined by integrating the intensity of the image at that position, multiplied by the template PSF. The noise is determined by placing the template PSF at several different positions of the same radius in the image, then integrating the intensity of the image multiplied by template PSF. The standard deviation of these intensity values is a measure of the noise.

In the case of SDI, the components of the positive-negative signature will have a known separation but the component's individual intensities will vary depending on the intrinsic spectrum of the companion. Therefore, the template PSF must be determined by fitting the relative fluxes of the positive-negative components in the image. Once fit, the template PSF is normalized by the total intensity of the absolute value of the template. The signal to noise is then determined using the previously described method. For a companion with a *flat spectrum*, the optimal separation of the positive-negative signature was determined to be 0.4 λ/D for each coronagraph setup. The constant value between coronagraph setups is expected since the ability to fit the positive-negative signature is dominated by the sampling. In the case of the *sharp spectrum*, where the companion is only detected in one wavelength, the wavelength separation should be at least one resolution element ($\sim$0.045 μm for a central wavelength of 4.2 μm). Since a spectral feature is often larger than this, in the following plots we consider a more realistic case of a wavelength separation of 0.1 μm.

To quantify the detection capabilities of TFI when performing SDI, we calculated the flux ratio (contrast) between the host star and companion corresponding to an average detection of 10σ. Each average was calculated for several angular separations using a minimum of 25 different position angles. This was performed for each coronagraph setup. Figures 3.4 and 3.5 show the detection capabilities with SDI using a simple difference with each coronagraph setup. The minimum simulated angular separations correspond to a 1.0 λ/D beyond the edge of the occulter. This ensures that photometry

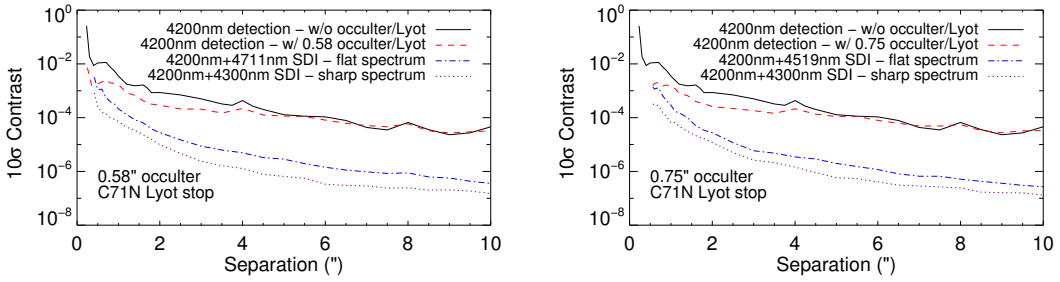

Figure 3.4: The planet-to-star contrast corresponding to a 10σ detection of a companion for the $0.58''$ and $0.75''$ occulters and C71N Lyot stop. The solid curve shows the contrast achieved when no coronagraph is used. The dashed red curves indicate the coronagraphic performance for the given setup. The SDI contrast performance is dependent upon the companion's atmosphere. Two limiting cases are shown: a flat spectrum (blue dot-dashed line) and where the companion exhibits an extremely sharp spectral feature (purple dotted line). The optical wavelengths used for performing SDI with a given occulter is shown in each legend and justified in the text.

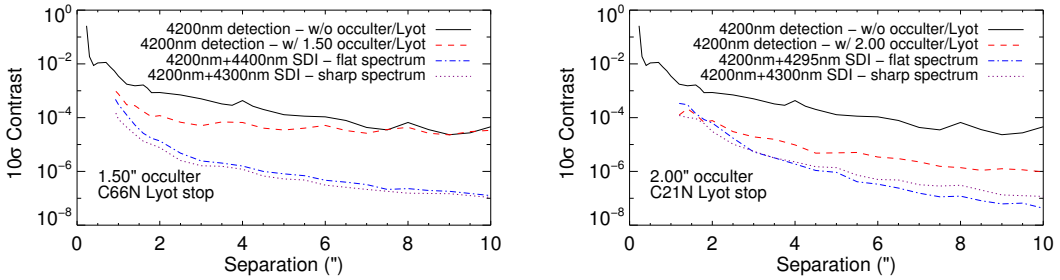

Figure 3.5: The planet-to-star contrast corresponding to a 10σ detection of a companion for the $1.50''$ and $2.00''$ occulters and C66N and C21N Lyot stops. The curves are identical to those described in Figure 3.4.

of companions inserted at this separation is recovered accurately. If the companion were significantly closer it would be partially occulted and its PSF would change significantly. The wavelength separation for the flat spectrum scenario was chosen such that the individual components of the positive-negative companion signature would be separated by $0.4\ \lambda/D$ at the smallest inner working angle of each coronagraph configuration.

The contrast curves shown in Figures 3.4 and 3.5 illustrate the important contribution of SDI to high-contrast observations. For the coronagraph configurations looking at small separations (Figure 3.4), the improvement offered by SDI is dependent upon

the type of companion. In the case of the sharp spectrum scenario, a increase in the detection contrast over the coronagraph of $\sim$10 is observed at the inner working angle, whereas a factor of $\sim$100 is achieved for separations greater than $3''$. The improvement in contrast when observing a flat-spectrum companion is reduced due to the increase in wavelength separation between the two images that is required to ensure the components of the positive-negative signature are adequately separated. For the coronagraph configurations designed for observing companions at larger separations (Figure 3.5), there is no significant difference between the type of companion being detected. This is because the wavelength separation required to separate the components of the positive-negative signature is similar to the wavelength separation used in the sharp spectrum scenario. The wavelength separation is an important component in the fundamental limit of SDI's speckle attenuation abilities.

The SDI performance is limited by two separate effects. At separations smaller than $\sim 5''$, the performance is limited by speckle residuals resulting from the chromaticity of the Talbot effect. At larger separations, the improvement in contrast is limited by the pupil geometry (and hence the PSF structure). [1] This is a result of diffraction from the secondary support structures that diffracts light in non-radial directions. Because SDI scales the PSF radially for subtraction, any non-radial diffraction effects are not well subtracted. This creates a fundamental limit for performing SDI with *JWST* and is the reason for the contrast curves descending at a constant slope (in log space) at large separations. An interesting result in these simulations is how SDI is effective at improving the achievable detection contrasts at all separations even where the coronagraph performs poorly. To detect companions covering both the sharp and flat spectrum scenarios for all available separations, switching coronagraph setups may not be necessary. The observer could simply observe three wavelengths using the smallest occulter and obtain a comparable sensitivity and spatial coverage as would be achieved using multiple coronagraph configurations. The fact that SDI offers an improvement at all separations also advocates the possible implementation of a non-coronagraphic SDI mode.

1. For the $2.00''$ occulter, the transition occurs towards $8''$ due the highly structured Lyot stop that dampens the PSF structure more efficiently. Of course, this efficiency comes at the price of a significantly reduced throughput.

3.4.1 SDI Without a Coronagraph

The advantages of performing SDI without a coronagraph is the possibility of probing very small inner working angles with the highest possible transmission since no undersized Lyot stop is required in this configuration. Of course, this comes at the price of a lower contrast but it may be interesting for some applications like detection of brown dwarfs and massive planets around late-type stars. The minimum working angle in this mode requires the innermost component of the positive-negative signature to be separated from the primary star by at least 1 λ/D and that the individual positive-negative components be separated by 0.4 λ/D. If we consider the maximum wavelength ranges of the F425 filter (3.7 & 4.9 μm), the inner working allowing a 0.4 λ/D separation is 0.262″ (2.2 λ/D). The sharp spectrum case is also considered where the inner working angle is 1.5 λ/D. Both scenarios are shown in Figure 3.6.

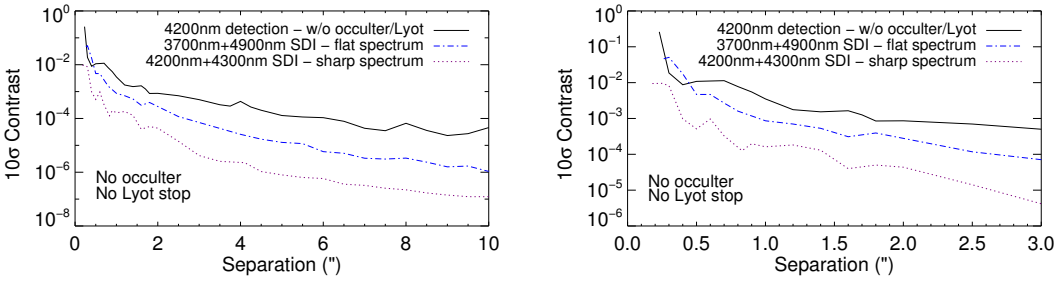

Figure 3.6: The planet-to-star contrast corresponding to a 10σ detection of a companion without using a coronagraph. The solid curve shows the contrast of the non-coronagraphic PSF. The case of a flat spectrum is shown as the blue dot-dashed line, where the case of the companion exhibiting an extremely sharp spectral feature is shown as the purple dotted line. The curves are identical to those described in Figure 3.4. The rightmost plot is a zoomed in section of the left plot to show the innermost working angles.

Using only SDI, one can achieve contrasts similar to what is achievable using the ideal wavelengths for each coronagraph setup but using only single instrument configuration. The most significant gain is achieved when considering the spectrum scenario (cold companions). This is because the required large wavelength separation to separate the positive-negative components is not necessary. This allows the observer to probe

regions inside what would normally be masked or affected by an occulter. This effect is best seen in the rightmost plot of Figure 3.6. In the case of performing SDI with a coronagraph, the contrast achieved at small separations is limited from residual speckles due to the chromaticity of the Talbot effect. When observing without a coronagraph, this is not the case and the performance is limited by the sharp PSF structure at all separations.

3.5 Simulated SDI Observations of Known Systems

One of the science goals of TFI is to perform follow-up observations of the previous planet finding campaigns using either the NRM and/or SDI observing modes. Two targets already of significant interest are those of HR 8799 and Fomalhaut b. In this section, we present realistic *JWST* simulations of these systems that include photon and read noise.

3.5.1 HR 8799

Since its discovery by Marois et al. (2008b), the HR 8799 planetary system has been the focus of several observations in efforts to constrain the age, mass, and composition of its companions. To date, models cannot accurately reproduce all the observations (Barman et al. 2011; Bowler et al. 2010; Currie et al. 2011; Madhusudhan et al. 2011). An advantage of observing with TFI is its capability of performing spectrophotometry near 4 μm, where the companions exhibit their maximum flux allowing high signal-to-noise observations.

To simulate an observation of the HR 8799 system, companions b, c and d were added to coronagraphic images of the host star. Companion e (Marois et al. 2010) was not included because it is inside the minimum inner working angle when observed using SDI and it is too close to the occulter to be accurately represented by a non-occulted PSF. The adopted M-band magnitude of HR 8799 a was $M_M = 5.21$ as measured by (Galicher et al. 2011). The spectra of companions were assigned fluxes from the model spectra of Madhusudhan et al. (2011). Recent *M* band photometry (Galicher et al. 2011) is consistent with the predicted models of Madhusudhan et al. (2011) for the HR 8799

c and d planets, but are $\sim$1 magnitude fainter for HR 8799 b. Because this article aims to demonstrate the capabilities of etalons, and is not focused on comparing atmospheric models to current data, we simply adopt the atmospheric models of Madhusudhan et al. (2011) for our analysis. The model names for b, c and d are AE60.850.cloud.g4.3, AE60.1000.cloud.g4.2 and AE60.900.cloud.g3.8, respectively. The format of the name indicates the cloud-type, particle size, effective temperature, cloud composition, and gravity. The total exposure time for each image is 10 minutes using the 0.58″ occulter with the C71N Lyot stop. Images at four different wavelengths (3.90, 4.00, 4.41 and 4.55 μm) were simulated to create two difference images (3.90 & 4.41 μm and 4.00 & 4.55 μm). All three companions are easily detected in the difference image shown in Figure 3.7. We do not explore the spectral deconvolution technique (Sparks & Ford 2002; Thatte et al. 2007) due to the object's separations and the efficiency of the simple difference method to adequately measure the SED with a minimal number of exposures.

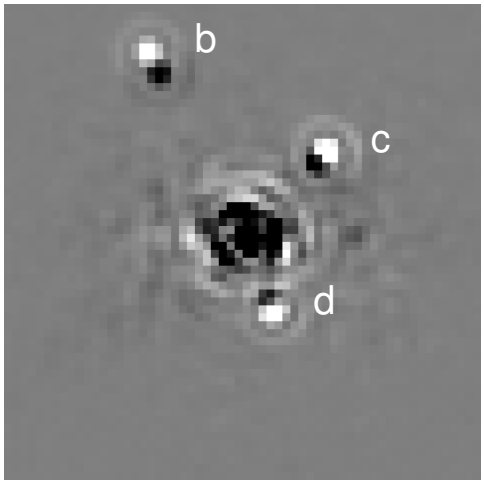

Figure 3.7: The difference image of the simulated HR 8799 system created from subtracting the 3.90 and 4.41 μm coronagraphic images using the 0.58″ occulter with the C71N Lyot stop. Planets b, c and d are easily detected but planet e falls too close to the occulter to be accurately modeled. The difference image shown has a 3.9″ by 3.9″ field-of-view where each image corresponds to 10 minutes of exposure time.

Using the difference images, the fluxes associated with each wavelength were extracted using PSF fitting to the positive-negative signature of each planet. The absolute flux measurement assumes the transmission function of the telescope and instrument is

perfectly calibrated. Figure 3.8 shows the measured flux over-plotted with the theoretical best-fit spectra of Madhusudhan et al. (2011) binned to the resolution of TFI. The adopted models are shown as solid red lines. The 1σ error bars are determined from standard deviation of the measured signal when the planet is placed at various position angles. These figures show how a TFI-like instrument would be able to constrain or differentiate the potential models of the companions. The extracted spectra of HR 8799 b is not shown because there is no distinction between the two suggested atmospheric scenarios at the spectral resolution of TFI for the simulated wavelengths.

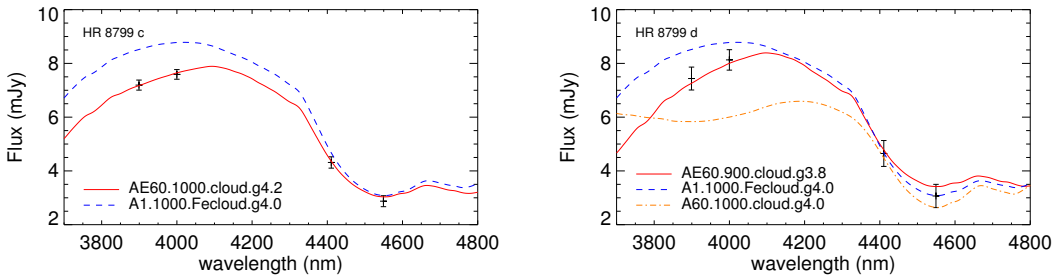

Figure 3.8: The extracted fluxes of HR 8799 c (left) and d (right). Each wavelength corresponds to 10 minutes of exposure time. In both cases, TFI will be able to differentiate between the different cloud models.

3.5.2 Fomalhaut b

Another companion of particular interest is Fomalhaut b, discovered by Kalas et al. (2008). Previous studies suggest that the detected signal originates from either a circumplanetary disk or ring system seen in reflected light, or a self-luminous object with a mass less than 3 M_J, assuming an age of 200 Myr. More recent observations contest this result (Janson et al. 2012; Marengo et al. 2009). To demonstrate the potential of *JWST* and TFI's contribution to characterizing this object, we simulated three three-hour exposures using the $2.00''$ occulter with the C21N Lyot stop. The M-band flux from Fomalhaut (m_M=1.01) was approximated using the m_v magnitude and the color transformations of Tokunaga (2000) for a A2V star. We simulated Fomalhaut b assuming a 0.5 M_J object with an conservative age estimate of 300 Myr.

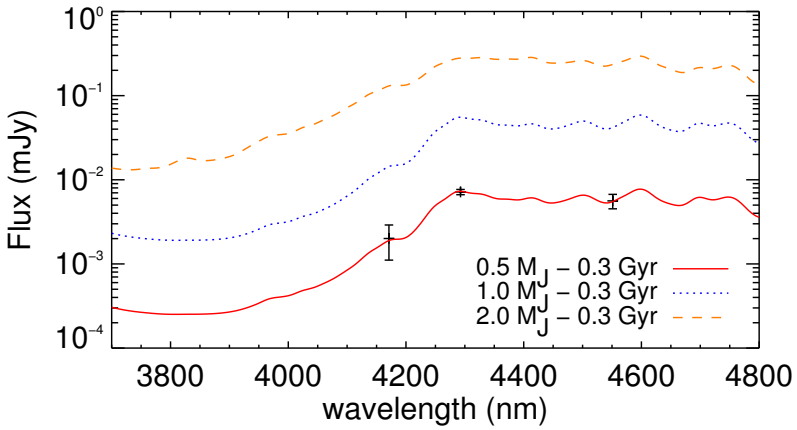

Figure 3.9: The extracted spectro-photometry of Fomalhaut b after being observed for three hours at each wavelength. TFI will be able to detect and characterize Fomalhaut b if it is a self-luminous object on the order of 0.5 M_J.

As a proxy of the spectral energy distribution of this object, we have adopted the 1 M_J, 300 Myr model of Burrows et al. (2003) but decreased the M-band flux by 2.2 magnitudes to be consistent with the total flux determined using an extension to the evolutionary models of Baraffe et al. (2003) reported in Beichman et al. (2010) (m_M = 19.77). This is $\sim$1 magnitude fainter than what is calculated when extrapolating the 300 Myr models of Burrows et al. (2003) to 0.5 M_J. Naturally, the true atmospheric flux distribution will most likely differ from the approximation we use here, however the goal of this exercise is simply to demonstrate the capability of characterizing a Fomalhaut b planet having a mass less than 1 M_J. Figure 3.9 shows the extracted signal for three data points that were used to create two individual difference images. The overlaying spectra are the atmospheric models of Burrows et al. (2003) binned to the resolution of TFI. This simulation shows how TFI accurately recovers the inputted flux and can therefore put strong constraints on the mass of the object. Detecting the hypothesized circumplanetary disk using SDI is not possible due to the residual speckle noise. One method to lower the speckle noise may be to perform roll subtraction.

3.6 Roll Subtraction

Roll subtraction offers another speckle attenuation technique that does not suffer from chromaticity like SDI. This technique will be used extensively to perform high-contrast imaging with *JWST*. The amount of roll achievable with *JWST* is limited by the size and shape of the sunshield. The maximum achievable roll is $\pm 5^{\circ}$. If we presume a required separation of $0.4\,\lambda/D$ for the components of the positive-negative signature, roll subtraction may be beneficial for any separations larger than $0.3''$ assuming maximum roll is achieved. In the case of SDI, the detection capabilities are limited by diffraction effects and the speckle patterns varying with wavelength. In the case of roll subtraction, neither the wavelength nor optical components are adjusted.

The speckle attenuation using roll subtraction is limited by two individual effects that introduce optical path differences between roll positions. The first effect is the physical change in the optical components due to the temperature of the telescope changing with time. This results in a “breathing" of the PSF causing residuals in the difference image. A preliminary study into the effects of PSF breathing on PSF subtraction assuming a telescope slew between the thermal extremes examines this effect (Makidon et al. 2008) and demonstrates that good contrasts can still be achieved. However, this observing scenario is most likely unrealistic for a roll subtraction observations where the telescope remains pointed in a similar direction. To accurately determine the effects of PSF breathing requires an accurate thermal model of the telescope and an understanding of how the WFE changes in time. This is beyond the scope of this article. However, when performing coronagraphic observations with exposures on the order of several hours, differential WFE introduced due to pointing errors is expected to dominate.

The target acquisition accuracy specification of the *JWST* Fine Guidance Sensor is 10 mas rms. In order to simulate the effects of pointing error on the speckle-suppression performance of roll subtraction, a phase offset is applied at the primary mirror to offset the star on the occulter. Each difference image is composed of one image perfectly centred on the occulter while the other is offset by 5 or 10 mas. Figure 3.10 shows the speckle-suppression performance of TFI using a difference image created using roll

subtraction with the $0.58''$ occulter with the C71N Lyot stop. Each curve represents the 10σ contrast of the difference image for an annulus for the given separation. It can be seen that the difference in pointing offset has affects the achieved contrast by a factor of $\sim$2. Figure 3.10 shows the contrast curves of roll-subtraction and SDI remain very similar until a separation of $\sim 3''$ where they exhibit a contrast of 10^{-5}. Beyond this, roll subtraction offers an improvement over SDI because the non-radial diffraction originating from the secondary support structure is better attenuated. This illustrates that roll-subtraction will be a powerful observing technique with *JWST*, particularly at long wavelengths ($\lambda > 4\mu$m), where the PSF is better sampled. Furthermore, having the companion fall in two areas on the detector may also be advantageous as it has a higher probability to avoid the noisy regions of the PSF.

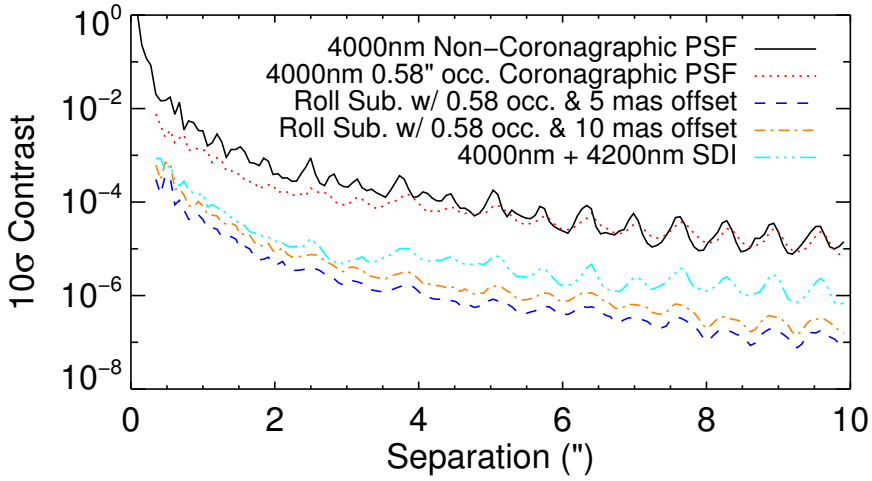

Figure 3.10: Roll subtraction is an alternative method to SDI to attenuate speckles and is limited by pointing error. This plot shows the achieved contrast of a difference image obtained at 4.0 μm using roll subtraction with a roll angle of $\pm 5^{\circ}$, for two different pointing offsets. This figure illustrates that roll subtraction performs as well as SDI at small separations and surpasses the SDI performance at large separations.

The true performance of roll-subtraction will only be known once tested on-sky. This is dependent upon the aberrations induced by each pointing encountering slightly difference areas of the optical elements as well as the PSF breathing. More importantly, the relative positions of the star on the occulter for each image will influence the speckle-

suppression abilities. A 10 mas rms of random pointing error will offer a poorer performance than a pointing error causing a systematic offset on the occulter in the same direction. Although any offset reduces the coronagraphic performance, repeatability and stability of the PSF are the important factors when performing both roll subtraction and SDI. The true maximum on-sky roll angle will also determine the achievable minimum inner working angle.

Choosing to use either SDI or roll subtraction will depend on the observers goals. A decrease in the inner working angle for roll subtraction would provide a distinct advantage to observing with an SDI mode. SDI is more advantageous for characterization of bright targets and requires less observing overhead. Roll subtraction may be more beneficial when trying to detect cold objects at specific wavelengths, where a possible detection at two wavelengths with SDI may require too much exposure time. Combining SDI with roll subtraction does not offer a gain in contrast because the residuals are caused by different effects. SDI residuals originate from out-of-pupil aberrations introducing speckles that do not scale radially with wavelength whereas roll-subtraction residuals are a result of noncommon path errors introduced between the target acquisitions. Therefore, combining the methods actually causes a decrease in the obtainable contrast.

3.7 SDI with NIRISS

NIRISS does not feature an etalon nor a Lyot coronagraph therefore SDI can only be performed by interchanging filters. Although noncommon path errors will be introduced by changing the filters, the amount of WFE introduced by the filters is small in comparison to the total WFE of the telescope and instrument. The all-reflective optics of NIRISS provides the ideal optical configuration for performing SDI since no chromatic aberration is introduced. Furthermore, the fact that the NIRISS filters have relatively good transmitted WFE suggests that SDI may offer a contrast improvement. To determine the SDI performance of NIRISS, we have removed the etalon from the optical model and created PSFs using three medium-band NIRISS filters. The central wave-

lengths of each filter are 3.8, 4.3, and 4.8 μm with bandwidths of 0.2, 0.2 and 0.4 μm, respectively. The WFE map for each filter is generated using a power law power spectral density with a slope of -2.5 and normalized to have a transmitted rms WFE of 40 nm, the value specified to the vendor. The detection performance using SDI is calculated using the method described in section 3.4. However, because of the large passbands, the radial scaling factor that minimizes the speckles in the difference image is no longer the ratio of the wavelengths. The new factor is determined empirically by measuring the speckle-suppression as a function of scale factor. The resulting change in scale factors is less than 2%.

The SDI performance of the three filter combinations are shown in Figures 3.11 and 3.12. The Figure 3.11 illustrates that performing SDI offers a gain in contrast of a factor of $\sim$15 for the 3.8 and 4.3 μm and a factor of $\sim$10 for the 4.3 and 4.8 μm filter combinations. Although the difference in central wavelengths between both filter combinations are equal, the bandpasses differ significantly. This results in differences between the spot sizes in the diffraction patterns of the 4.3 and 4.8 μm images that cause residuals in the difference image and limit the speckle-suppression performance beyond $\sim 1''$. At separations smaller than this, the performance is limited by speckle residuals resulting from the chromaticity of the Talbot effect. This effect is amplified for the 3.8 and 4.8 μm filter combination, shown in Figure 3.12, resulting in an increase in speckle noise and a decrease in performance at small inner working angles. The performance at larger working angles is again limited by the difference in filter bandpasses.

For all filter combinations, the sharp and flat spectrum scenarios offer very similar performances. This is different from the result obtained when observing using an etalon as shown in section 3.4.1, where the sharp spectrum scenario offered a significant detection gain. With TFI, the wavelength separation used in the flat spectrum scenario was significantly larger than the sharp spectrum scenario. This decreased wavelength separation provided an increased speckle attenuation. With NIRISS, the filter bandpasses are fixed, therefore the speckle noise is constant for both scenarios. Although the achieved contrasts are lower than those of TFI, NIRISS will be a powerful instrument to perform SDI and can help in detecting and characterizing faint companions. The filter bandpasses

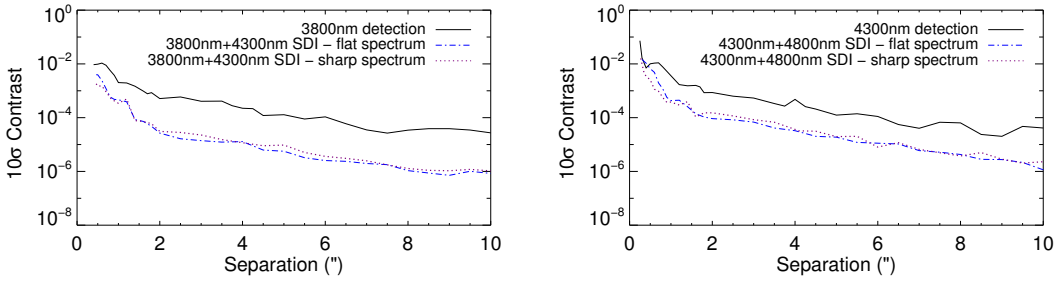

Figure 3.11: The SDI performance using the NIRISS 3.8 and 4.3 μm filters (left) as well as the 3.8 and 4.3 μm filters (right). SDI offers a factor of $\sim$10-15 improvement in contrast depending on the separation. Contrary to non-coronagraphic measurements with TFI, there is no overwhelming advantage between detecting planets of varying spectral scenarios.

are also chosen specifically to be powerful indicators of the atmospheric properties.

3.7.1 Atmosphere Characterization with NIRISS

The central wavelengths and bandpasses (stated above) of the three NIRISS medium-band filters were chosen to provide a first-order characterization of companions at small separations. This is of particular importance for objects only detected using the NRM mode where follow-up spectroscopy is not possible with *JWST*. Of course, these filters offer the same characterization capability for the SDI mode. The filter's wavelengths and bandpasses were chosen by examining the flux ratios between the filters as a function of atmospheric properties for various models [2]. The Ames-Cond models were chosen to represent companions with effective temperatures ranging from 600 K to 1600 K whose atmospheres contain no dust. The Ames-Dusty models were used to represent warmer companions having effective temperatures between 1500 K and 2700 K (Allard et al. 2001). The considered surface gravity (log g) for each model set ranged from 3.5 to 5.5. This large parameter space accounts for objects of various ages and masses.

In Figure 3.13, the companion characterization capability is demonstrated by exam-

2. The F430M and F480M filters are existing NIRCam filters. Only the wavelength of the third filter (3.8 μm) had to be optimized. The main constraint for this optimization was ensuring that good contrast was achievable with the NRM at this wavelength.

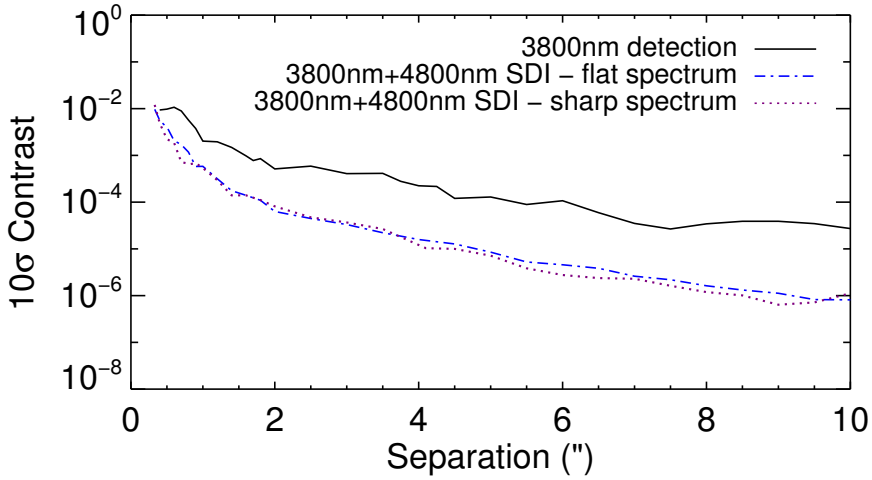

Figure 3.12: The SDI performance using the NIRISS 3.8 and 4.8 μm filters. SDI offers a factor of $\sim$5-10 improvement in contrast depending on the separation. No advantage is measured between the two companion spectral type scenarios.

ining how the flux ratios of the three filters change as a function of the atmospheric properties as predicted by the Ames-Cond models. Each solid-colored line represents a different temperature whereas the dotted lines represent various surface gravities. The ovals represent a 2.5% error of the flux ratios. This figure illustrates how using only three filters, a reasonable atmospheric characterization is achievable. A similar result is obtained with the higher temperature models, shown in Figure 3.14. The warmer companions exhibit smoother spectra with less features resulting in a smaller distribution of flux ratios. In this case, higher signal-to-noise is needed to discriminate various models.

3.8 Conclusion

Space-based observations using a Fabry-Perot etalon as a tunable filter is a powerful instrument to perform high-contrast imaging through SDI. In article I (Ingraham et al. 2011), we demonstrated the ability of an etalon to perform SDI. In this article, we have demonstrated the capabilities of an etalon to detect and characterize exoplanets in the context of a real telescope and instrument, exemplified by *JWST* and TFI. Previous

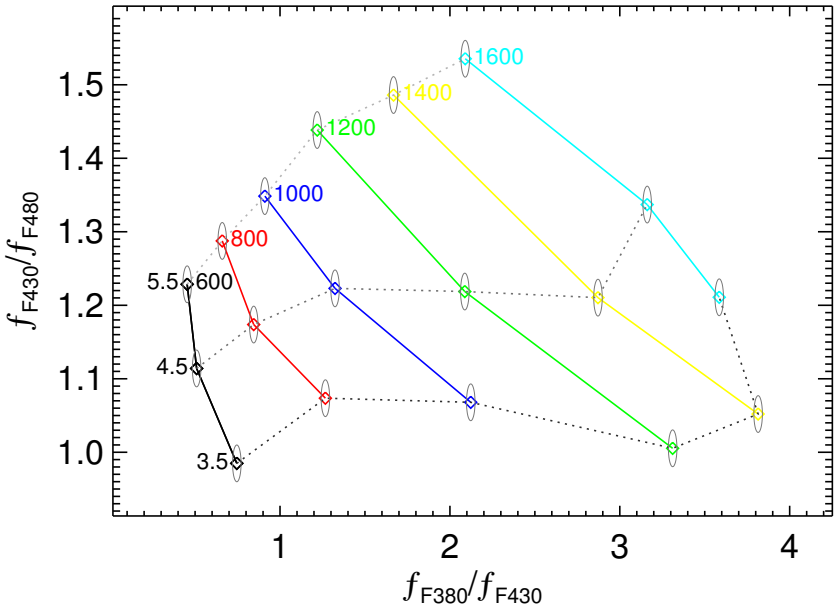

Figure 3.13: The flux ratios of various Ames-Cond model atmospheres using three NIRISS filters. Each solid-colored line represents a different temperature and the dotted lines represent different surface gravities. The ovals indicate a 2.5% uncertainty.

ground-based SDI instruments suffered from noncommon path aberrations introduced by the individual wavelength channels. An instrument like TFI does not experience the same problems since no filters are moved in and out of the beam and the same optical path is used. Therefore, the performance is limited by the pupil structure and WFE introduced at each of the individual surfaces. By performing an end-to-end Fresnel propagation we have quantified both of these effects allowing an accurate characterization of both the coronagraphic and speckle attenuation performance of SDI. Our simulation illustrates that SDI offers an improvement in contrast ranging from a factor of 7 to 100 over the coronagraphic performance depending on the instrument's configuration. The detection performance is also dependent upon the spectral features of the companion. Using only the coronagraph, a companion having a planet-to-star contrast of $10^{-2.7}$ at $1''$ separation is detectable at 10σ. Using SDI, the 10σ contrast limit is $10^{-3.7}$ for companions with flat spectra and $10^{-4.1}$ for companions exhibiting sharp spectral features.

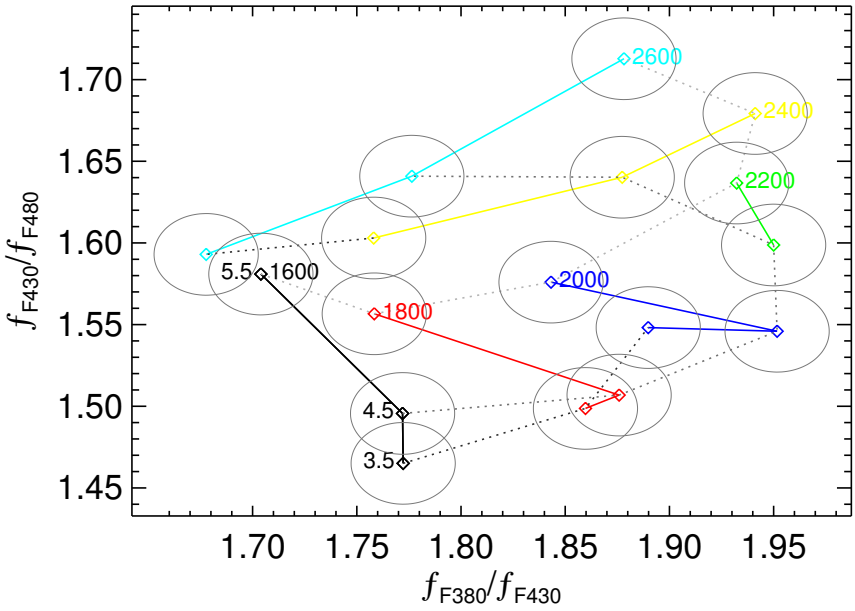

Figure 3.14: The flux ratios of various Ames-Dusty model atmospheres using three NIRISS filters. Each solid-colored line represents a different temperature and the dotted lines represent different surface gravities. The ovals indicate a 2.5% uncertainty.

We also simulated observations of the HR 8799 and Fomalhaut systems to demonstrate the ability to characterize exoplanets. Because TFI has been reconfigured into the instrument NIRISS, we also explored the possibility of performing non-coronagraphic SDI using the available medium-band filters. We determined that SDI offers a significant contrast improvement despite the noncommon path aberrations induced by the change of filters. The improvement in contrast ranges from a factor of 7-12 at all separations with the 10σ detection contrast limit at $1''$ being $10^{-3.4}$. Based on these results, we suggest that an SDI observing mode be implemented for NIRISS. The SDI performance at separations greater than $\sim 2''$ is limited by the non-radial diffraction effects of the secondary mirror support structures.

Also of critical importance, particularly when considering the SDI performance of future telescopes, is the sampling of the PSF. Because the image manipulation is performed in image space, better than Nyquist sampling is required to ensure an adequate

interpolation during the scaling and rotation of images. If the images are well sampled, our simulations demonstrate that roll subtraction is a powerful technique to subtract highly structured PSFs since no radial scaling is required. This will be the most powerful speckle-suppression technique with *JWST*, particularly at wavelengths greater than 4 μm where the PSF is better sampled.

When SSDI was first conceived, the goal was to overcome the speckle noise being introduced by the atmosphere when observing with only low-order adaptive optics systems. Performing ground-based non-simultaneous SDI was not considered due to the large decorrelation in wavefront between exposures. With the more powerful adaptive optics systems, such as the First Light AO system for the Large Binocular Telescope that exhibits Strehl ratios of $\geq$80% in H-band, ground-based non-simultaneous SDI may now be within reach (Esposito et al. 2010). At longer wavelengths such as the L and M bands, where the image quality is limited by quasi-static speckles, performing SDI using an etalon may offer a technique to obtain low-resolution spectra of exoplanets. Furthermore, performing SDI using a low-structured pupil (eg. a monolithic mirror) would limit the non-radial diffraction effects and possibly exceed the contrast improvement determined in this article for *JWST* and NIRISS.

Bibliography

Allard, F., Hauschildt, P. H., Alexander, D. R., Tamanai, A., & Schweitzer, A. 2001, The Astrophysical Journal, 556, 357

Bagnasco, G., Kolm, M., Ferruit, P., Honnen, K., Koehler, J., Lemke, R., Maschmann, M., Melf, M., Noyer, G., Rumler, P., Salvignol, J.-C., Strada, P., & Te Plate, M. 2007, in Society of Photo-Optical Instrumentation Engineers (SPIE) Conference Series, Vol. 6692, 66920M

Baraffe, I., Chabrier, G., Barman, T. S., Allard, F., & Hauschildt, P. H. 2003, Astronomy and Astrophysics, 402, 701

Barman, T. S., Macintosh, B., Konopacky, Q. M., & Marois, C. 2011, The Astrophysical Journal, 733, 65

Beaulieu, M., Doyon, R., & Lafrenière, D. 2008, in Society of Photo-Optical Instrumentation Engineers (SPIE) Conference Series, Vol. 7010, 70103J

Beichman, C. A., Krist, J., Trauger, J. T., Greene, T., Oppenheimer, B., Sivaramakrishnan, A., Doyon, R., Boccaletti, A., Barman, T. S., & Rieke, M. 2010, The Publications of the Astronomical Society of the Pacific, 122, 162

Beuzit, J.-L., Feldt, M., Dohlen, K., Mouillet, D., Puget, P., Wildi, F., Abe, L., Antichi, J., Baruffolo, A., Baudoz, P., Boccaletti, A., Carbillet, M., Charton, J., Claudi, R., Downing, M., Fabron, C., Feautrier, P., Fedrigo, E., Fusco, T., Gach, J.-L., Gratton, R., Henning, T., Hubin, N., Joos, F., Kasper, M., Langlois, M., Lenzen, R., Moutou, C., Pavlov, A., Petit, C., Pragt, J., Rabou, P., Rigal, F., Roelfsema, R., Rousset, G., Saisse, M., Schmid, H.-M., Stadler, E., Thalmann, C., Turatto, M., Udry, S., Vakili, F., & Waters, R. 2008, in Society of Photo-Optical Instrumentation Engineers (SPIE) Conference Series, Vol. 7014, 701418

Biller, B., Trauger, J., Moody, D., Close, L., Kuhnert, A., Stapelfeldt, K., Traub, W. A., & Kern, B. 2009, The Publications of the Astronomical Society of the Pacific, 121, 716

Boccaletti, A., Carbillet, M., Fusco, T., Mouillet, D., Langlois, M., Moutou, C., & Dohlen, K. 2008, in Society of Photo-Optical Instrumentation Engineers (SPIE) Conference Series, Vol. 7015, 70156E

Bowler, B. P., Liu, M. C., Dupuy, T. J., & Cushing, M. C. 2010, The Astrophysical Journal, 723, 850

Burrows, A., Sudarsky, D., & Lunine, J. I. 2003, The Astrophysical Journal, 596, 587

Cavarroc, C., Boccaletti, A., Baudoz, P., Fusco, T., & Rouan, D. 2006, Astronomy and Astrophysics, 447, 397

Close, L. M., Lenzen, R., Guirado, J. C., Nielsen, E. L., Mamajek, E. E., Brandner, W., Hartung, M., Lidman, C., & Biller, B. 2005, Nature, 433, 286

Currie, T., Burrows, A., Itoh, Y., Matsumura, S., Fukagawa, M., Apai, D., Madhusudhan, N., Hinz, P. M., Rodigas, T. J., Kasper, M., Pyo, T.-S., & Ogino, S. 2011, The Astrophysical Journal, 729, 128

Doyon, R., Hutchings, J., Rowlands, N., Evans, C. E., Greenberg, E., Haley, C., Scott, A. D., Touahri, D., Beaulieu, M., Lafrenière, D., Abraham, R., Barton, E., Chayer, P., Ferrarese, L., Fullerton, A. W., Jayawardhana, R., Johnstone, D., Martel, A., Meyer, A. W. M. R., Pipher, J., Saad, K., Sawicki, M., Sivaramakrishnan, A., & Volk, K. 2010, in Society of Photo-Optical Instrumentation Engineers (SPIE) Conference Series, Vol. 7731, 77310F

Esposito, S., Riccardi, A., Fini, L., Puglisi, A. T., Pinna, E., Xompero, M., Briguglio, R., Quirós-Pacheco, F., Stefanini, P., Guerra, J. C., Busoni, L., Tozzi, A., Pieralli, F., Agapito, G., Brusa-Zappellini, G., Demers, R., Brynnel, J., Arcidiacono, C., & Salinari, P. 2010, in Society of Photo-Optical Instrumentation Engineers (SPIE) Conference Series, Vol. 7736, 70156E

Evans, C. E., Greenberg, E. S., Aldridge, D. A., & Santman, J. J. 2010, in Society of Photo-Optical Instrumentation Engineers (SPIE) Conference Series, Vol. 7790, 779004

Galicher, R., Marois, C., Macintosh, B., Barman, T., & Konopacky, Q. 2011, The Astrophysical Journal Letters, 739, L41

Gallagher, B., Bergeland, M., Brown, B., Chaney, D., Copp, T., Lewis, J., Shogrin, B., Smith, K., Sokol, J., Hadaway, J., Glatzel, H., Johnson, P., Lee, A., Patriarca, D., Stevenson, I., Cluney, J., Parsonage, T., Calvert, J., Rodgers, B., McKay, A., Texter, S., Cohen, L., & Feinberg, L. 2011, in Society of Photo-Optical Instrumentation Engineers (SPIE) Conference Series, Vol. 8146, 814607

Gardner, J. P., Mather, J. C., Clampin, M., Doyon, R., Flanagan, K. A., Franx, M., Greenhouse, M. A., Hammel, H. B., Hutchings, J. B., Jakobsen, P., Lilly, S. J., Lunine, J. I., McCaughrean, M. J., Mountain, M., Rieke, G. H., Rieke, M. J., Sonneborn, G., Stiavelli, M., Windhorst, R., & Wright, G. S. 2009, The James Webb Space Telescope, ed. H. A. Thronson, M. Stiavelli, & A. Tielens, 1–4020

Hinkley, S., Oppenheimer, B. R., Brenner, D., Parry, I. R., Sivaramakrishnan, A., Soummer, R., & King, D. 2008, in Society of Photo-Optical Instrumentation Engineers (SPIE) Conference Series, Vol. 7015, 701519

Hinkley, S., Oppenheimer, B. R., Zimmerman, N., Brenner, D., Parry, I. R., Crepp, J. R., Vasisht, G., Ligon, E., King, D., Soummer, R., Sivaramakrishnan, A., Beichman, C., Shao, M., Roberts, L. C., Bouchez, A., Dekany, R., Pueyo, L., Roberts, J. E., Lockhart, T., Zhai, C., Shelton, C., & Burruss, R. 2011, Publications of the Astronomical Society of the Pacific, 123, 74

Hodapp, K. W., Suzuki, R., Tamura, M., Abe, L., Suto, H., Kandori, R., Morino, J., Nishimura, T., Takami, H., Guyon, O., Jacobson, S., Stahlberger, V., Yamada, H., Shelton, R., Hashimoto, J., Tavrov, A., Nishikawa, J., Ukita, N., Izumiura, H., Hayashi, M., Nakajima, T., Yamada, T., & Usuda, T. 2008, in Society of Photo-Optical Instrumentation Engineers (SPIE) Conference Series, Vol. 7014, 286

Ingraham, P., Doyon, R., Beaulieu, M., Rowlands, N., & Scott, A. 2011, Publications of the Astronomical Society of the Pacific, 123, 1412

Janson, M., Carson, J. C., Lafrenière, D., Spiegel, D. S., Bent, J. R., & Wong, P. 2012, The Astrophysical Journal, 747, 116

Kalas, P., Graham, J. R., Chiang, E., Fitzgerald, M. P., Clampin, M., Kite, E. S., Stapelfeldt, K., Marois, C., & Krist, J. 2008, Science, 322, 1345

Krist, J. E. 2007, in Society of Photo-Optical Instrumentation Engineers (SPIE) Conference Series, Vol. 6675, 66750P

Krist, J. E., Beichman, C. A., Trauger, J. T., Rieke, M. J., Somerstein, S., Green, J. J., Horner, S. D., Stansberry, J. A., Shi, F., Meyer, M. R., Stapelfeldt, K. R., & Roellig, T. L. 2007, in Society of Photo-Optical Instrumentation Engineers (SPIE) Conference Series, Vol. 6693, 66930H

Lafrenière, D., Doyon, R., Nadeau, D., Artigau, É., Marois, C., & Beaulieu, M. 2007a, The Astrophysical Journal, 661, 1208

Lafrenière, D., Jayawardhana, R., & van Kerkwijk, M. H. 2008, The Astrophysical Journal, 689, L153

Lafrenière, D., Marois, C., Doyon, R., & Barman, T. 2009, The Astrophysical Journal Letters, 694, L148

Lafrenière, D., Marois, C., Doyon, R., Nadeau, D., & Artigau, É. 2007b, The Astrophysical Journal, 660, 770

Lagrange, A.-M., Bonnefoy, M., Chauvin, G., Apai, D., Ehrenreich, D., Boccaletti, A., Gratadour, D., Rouan, D., Mouillet, D., Lacour, S., & Kasper, M. 2010, Science, 329, 57

Lenzen, R., Close, L., Brandner, W., Biller, B., & Hartung, M. 2004, in Society of Photo-Optical Instrumentation Engineers (SPIE) Conference Series, Vol. 5492, 970–977

Macintosh, B. A., Graham, J. R., Palmer, D. W., Doyon, R., Dunn, J., Gavel, D. T., Larkin, J., Oppenheimer, B., Saddlemyer, L., Sivaramakrishnan, A., Wallace, J. K., Bauman, B., Erickson, D. A., Marois, C., Poyneer, L. A., & Soummer, R. 2008, in Society of Photo-Optical Instrumentation Engineers (SPIE) Conference Series, Vol. 7015, 701518

Madhusudhan, N., Burrows, A., & Currie, T. 2011, The Astrophysical Journal, 737, 34

Makidon, R. B., Sivaramakrishnan, A., Soummer, R., Anderson, J., & van der Marel, R. P. 2008, in Society of Photo-Optical Instrumentation Engineers (SPIE) Conference Series, Vol. 7010, 70100O

Marengo, M., Stapelfeldt, K., Werner, M. W., Hora, J. L., Fazio, G. G., Schuster, M. T., Carson, J. C., & Megeath, S. T. 2009, The Astrophysical Journal, 700, 1647

Marois, C., Doyon, R., Nadeau, D., Racine, R., Riopel, M., Vallée, P., & Lafrenière, D. 2005, The Publications of the Astronomical Society of the Pacific, 117, 745

Marois, C., Doyon, R., Racine, R., & Nadeau, D. 2000, The Publications of the Astronomical Society of the Pacific, 112, 91

Marois, C., Lafrenière, D., Doyon, R., Macintosh, B., & Nadeau, D. 2006, The Astrophysical Journal, 641, 556

Marois, C., Lafrenière, D., Macintosh, B., & Doyon, R. 2008a, The Astrophysical Journal, 673, 647

Marois, C., Macintosh, B., Barman, T., Zuckerman, B., Song, I., Patience, J., Lafrenière, D., & Doyon, R. 2008b, Science, 322, 1348

Marois, C., Macintosh, B., Soummer, R., Poyneer, L., & Bauman, B. 2008, in Society of Photo-Optical Instrumentation Engineers (SPIE) Conference Series, Vol. 7015, 70151T

Marois, C., Phillion, D. W., & Macintosh, B. 2006, in Society of Photo-Optical Instrumentation Engineers (SPIE) Conference Series, Vol. 6269, 62693M

Marois, C., Zuckerman, B., Konopacky, Q. M., Macintosh, B., & Barman, T. 2010, Nature, 468, 1080

Racine, R., Walker, G. A. H., Nadeau, D., Doyon, R., & Marois, C. 1999, The Publications of the Astronomical Society of the Pacific, 111, 587

Rieke, M. J., Kelly, D., & Horner, S. 2005, in Society of Photo-Optical Instrumentation Engineers (SPIE) Conference Series, Vol. 5904, 1–8

Schneider, G., & Silverstone, M. D. 2003, in Society of Photo-Optical Instrumentation Engineers (SPIE) Conference Series, Vol. 4860, 1–9

Sivaramakrishnan, A., Lafrenière, D., Tuthill, P. G., Ireland, M. J., Lloyd, J. P., Martinache, F., Makidon, R. B., Soummer, R., Doyon, R., Beaulieu, M., Parmentier, S., & Beichman, C. A. 2010, in Society of Photo-Optical Instrumentation Engineers (SPIE) Conference Series, Vol. 7731, 77313W

Soummer, R., Hagan, J. B., Pueyo, L., Thormann, A., Rajan, A., & Marois, C. 2011, The Astrophysical Journal, 741, 55

Sparks, W. B., & Ford, H. C. 2002, The Astrophysical Journal, 578, 543

Thatte, N., Abuter, R., Tecza, M., Nielsen, E. L., Clarke, F. J., & Close, L. M. 2007, Monthly Notices RAS, 378, 1229

Tokunaga, A. T. 2000, Infrared Astronomy, ed. A. N. Cox (The Athlone Press), 143

Wright, G. S., Reike, G., Barella, P., Boeker, T., Colina, L., van Dishoeck, E., Driggers, P., Goodson, G., Greene, T., Heske, A., Henning, T., Lagage, P.-O., Meixner, M., Norgaard-Nielsen, H., Olofsson, G., Ray, T., Ressler, M., Thatcher, J., Waelkens, C., Wright, D., & Zehnder, A. 2008, in Society of Photo-Optical Instrumentation Engineers (SPIE) Conference Series, Vol. 7010, 70100T

CHAPTER 4

NEAR-INFRARED (*JHK*) SPECTROSCOPY OF YOUNG STELLAR AND SUBSTELLAR OBJECTS IN ORION

P. INGRAHAM[1], R. DOYON[1], L. ALBERT[1], E. ARTIGAU[1]

In preparation: For submission to *The Astrophysical Journal*

Abstract

We performed low-resolution (R$\sim$40) near-infrared (0.9-2.4 μm) multi-object spectroscopy of nearly every isolated point source having apparent H band magnitudes between 9.1 and 16.5 in the central $5' \times 6'$of the Orion Trapezium cluster. The observations were performed over four nights at the Canada-France-Hawaii Telescope using the visiting instrument SIMON, an infrared imager and multi-object spectrograph. We present the spectra of 104 objects with accurately derived spectral types including 7 new objects having masses below the hydrogen burning limit, and 4 objects with masses below the deuterium burning limit. The spectral classification is performed by fitting previously classified spectral templates of dwarf stars (K4-M3) and optically classified young stellar and substellar objects (M4-L0) to the entire 0.9-2.4 μm spectral energy distribution in order to assign a spectral type and visual extinction for each object. Of the 104 objects studied, 44 have been previously classified spectroscopically using various techniques. We perform a rigorous comparison between the previous classifications an our own and find them to be in good agreement. Using the dereddened H band magnitudes, the classified objects are used to create an Hertzsprung-Russell diagram for the cluster. We find that the previous age estimates of $\sim$1 Myr to be consistent with our results. Consistent with previous studies, numerous objects are observed to have luminosities several magnitudes above the 1 Myr isochrone. Numerous objects exhibiting emission features in

1. Département de Physique, Université de Montréal, Montréal PQ, H3T 1J4, Canada

the *J* band are also reported. Using the results of our spectroscopic survey we determine the log-normal functional form of the IMF to have the coefficients of $\log m_c$ and σ of -0.89±0.04 and 0.57±0.03 respectively. This result is consistent with the galactic disc IMF and the IMF of numerous other young systems.

Keywords: Brown Dwarfs, Free floating planets, planetary mass objects, Data Analysis and Techniques, Astronomical Techniques

4.1 Introduction

The initial mass function (IMF) is a fundamental characteristic of star formation history and therefore an important element in our understanding of galaxy evolution. For stars in the higher-mass regime, the IMF is known to follow the Salpeter mass function, a power-law defined as, $dN/dm = m^{\alpha}$ having a slope of $\alpha = -2.35$ (Salpeter 1955). However, at lower masses ($m \lesssim M_{\odot}$), the IMF is believed to change slope, and continue to change through the substellar ($0.072M_{\odot} \geqslant m \geqslant 0.012M_{\odot}$) and deuterium-burning limit mass regimes ($m \leqslant 0.012M_{\odot}$, Chabrier 2003; Kroupa 2001). How this slope changes, and whether its form is constant across multiple environments, is the fundamental question driving today's studies of the substellar IMF. Constraining the substellar IMF requires a large number of objects over a large range in mass. Observing low-mass objects is particularly challenging as they are relatively faint.

Performing substellar IMF studies in young clusters is advantageous because the objects are significantly more luminous than older objects of similar mass and therefore require less observation time to characterize (Burrows et al. 1997). Another fundamental advantage is that the derived mass function is a close approximation to the IMF. In observing older populations, the more massive stars are no longer present and knowledge of the star formation history of the cluster is required to determine the IMF. In young clusters, the stellar population is coeval and mass segregation complications resulting from dynamical relaxation are negligible. Lastly, the age of the cluster must be accurately determined in order to obtain the masses of objects below the hydrogen burning limit. The Orion Nebular Cluster (ONC) is one of the best studied young clusters

for multiple reasons. The high stellar density (n=1-5$\times 10^4$ pc^3, Luhman et al. 2000) of the cluster makes target characterization suitable for multi-object spectroscopy. The cluster's relative proximity (414 pc, Menten et al. 2007) and its high galactic latitude (b=-18) minimize the stellar populations' contamination from foreground stars. Another distinct advantage is the cluster's location in front of the OMC-1 molecular cloud. This ensures that any background stars will be highly absorbed and relatively easy to flag as contaminants. The age of the cluster ($\leqslant$1 Myr) is also well constrained through multiple studies (Hillenbrand 1997; Luhman et al. 2000; Prosser et al. 1994; Riddick et al. 2007a). Therefore, using a theoretical isochrone corresponding to the age of the cluster, combined with an accurate spectral type/temperature determination, a mass can be obtained for each object.

Assigning a spectral type and obtaining accurate temperatures is challenging due to the young ages of the objects. For evolved field dwarfs, spectral typing using synthetic spectra is a popular method and offers a powerful tool to derive accurate temperatures. However, theoretical atmosphere models for ages less than a few Myr become uncertain and therefore should not be relied upon as the only calibrator in determining spectral types (Lucas et al. 2001). This is especially true when deriving temperatures based purely on infrared colours. Although photometry is able to estimate both the temperature and luminosity of an object, accurate spectral typing and temperature determination requires spectroscopy (Lucas & Roche 2000). Furthermore, a spectrum offers insight into the surface gravity of the object which is useful in providing evidence of cluster membership and age.

Previous works classifying substellar and planetary mass objects (PMOs, $m \lesssim 13 M_J$) have derived extinctions, spectral types, temperatures and masses using various methods. Early works determined extinctions using photometry or by dereddening the object to a 1 Myr isochrone, then determined the spectral type using spectral indices derived from spectral templates of field dwarfs or atmosphere models (Lucas et al. 2001; Luhman et al. 2000; Slesnick et al. 2004). More recent works perform the spectral typing using indices measured from templates of young substellar objects identified in other fields (Weights et al. 2009). A recent HST study utilizes medium band photometry that ex-

ploits a single spectral feature to perform classifications down to 0.02 $M_{\odot}$ (Rio et al. 2012). Our work aims to classify objects by utilizing the shape of the spectral energy distribution (SED) from 0.9-2.5 μm, obtained simultaneously using the visiting instrument SIMON at the Canada-France-Hawaii Telescope (CFHT). We aim to increase the number of known low-mass objects in the Orion Nebular Cluster, to aid in the study of the substellar initial mass function. These observations offer a direct measurement of the reddening, as well as a better determination of the spectral type compared to methods based on photometry alone. They also provide numerous new targets that can be used to test future atmospheric models for young objects.

In this paper, we report the reddening, spectral type, temperature, and mass of 104 objects derived using the shape of the SED from 0.9-2.5 μm. Our observations and target selection are described in section 4.2 with the spectroscopic data reduction procedure outlined in section 4.3. The spectral typing procedure is explained in section 4.4, including a discussion of other methods and comparison to previously assigned spectral types. In section 4.5, we present the derived spectral types for our objects. Each object is then assigned a temperature and placed on the Hertzsprung-Russell (HR) diagram, discussed in section 4.6. The masses of each object are then derived assuming evolutionary models and a cluster age of 1 Myr. A luminosity function is the created and used to derive the incompleteness correction for the IMF determination which is presented in section 4.7.

4.2 Observations

In December 2003, we obtained 6 nights of multi-object spectroscopy (MOS) observations on CFHT of faint objects in the the central region of the Orion Trapezium cluster. The observations were performed using the infrared imager and multi-object spectrograph SIMON (Spectrometre Infrarouge de Montréal, Albert 2006). The optical design is fully achromatic between 0.8 and 2.5 μm and features a HAWAII-I 1024$\times$1024 HgCdTe detector with an image scale of 0.2$''$ on CFHT. SIMON utilizes a low-dispersion Amici prism enabling multi-object low-resolution (R$\sim$30) spectroscopy over the wavelength range of 0.9-2.4 μm.

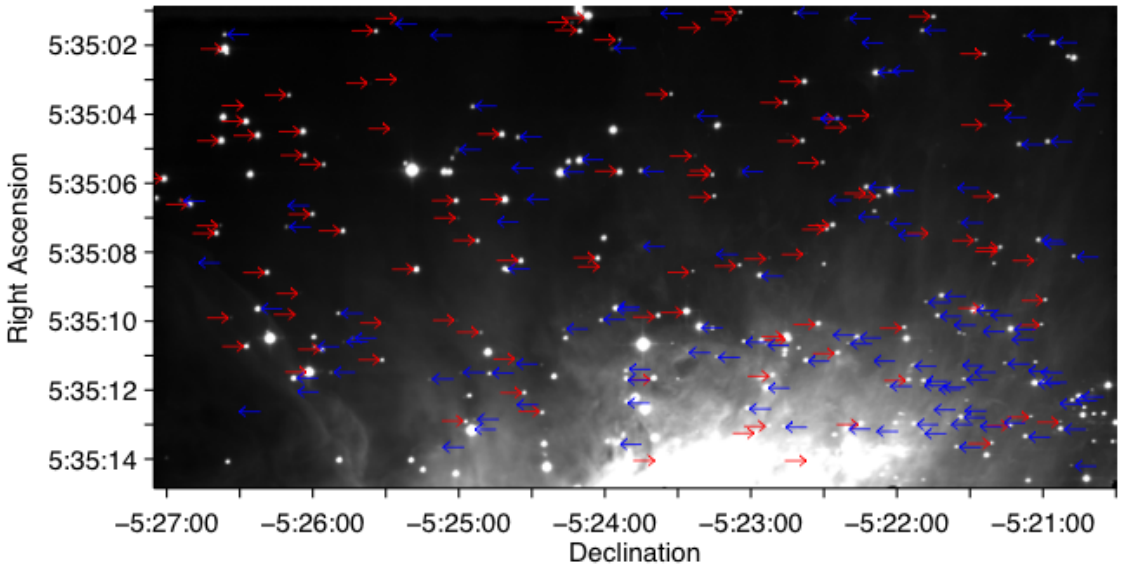

Figure 4.1: A mosaic of the north-west (right) and south-west (left) Orion *H* band pre-imaging observations. The blue arrows indicate the location of the objects where an accurate spectral type was determined. The red arrows indicate objects whose spectra indicated either a highly absorbed object (A_V>8) or an object showing only emission lines.

The original plan was to perform spectroscopic observations of all isolated targets in the central $6' \times 6'$region of the cluster but due to poor weather, only two fields totalling a $6' \times 3'$field of view was observed spectroscopically, half of the original goal.

Pre-imaging of two fields, shown as a mosaic in Figure 4.1, was performed using an *H* band filter to select the objects for spectroscopic observations. The locations of the two fields were chosen with the goals of remaining close to the center of the cluster while trying to minimize the amount of nebulosity. Also, the fields were to partially overlap with the observations of Lucas & Roche (2000) and Lucas et al. (2001) in order to obtain *J* band spectra of their discovered objects and provide a consistency check for our data reduction. The south-west (SW) field, shown as the left side of Figure 4.1, is centred at an RA and DEC of 05:35:07 and -05:25:29, respectively. The telescope was nodded 15 times between the target field and field for sky subtraction. For each nod position, $\sim$8 minutes were spent on target, and $\sim$2 minutes were spent on sky, totalling 122 minutes on target, and 25 minutes on sky. For the north-west field, shown as the right side of

Figure 4.1, is centred at an RA and DEC of 05:35:08 and -05:22:16, respectively. The telescope was nodded 13 times, for a total of 20 minutes on sky and 100 minutes on target. Dome-flats were performed at the end of each night. A standard image reduction was performed. The data was flat-fielded, sky-subtracted, and median combined. Photometry of all potential targets was obtained by performing simple aperture photometry using 2MASS stars (Skrutskie et al. 2006) to infer the zero point calibration. Due primarily to the nebulosity, the accuracy of the photometry is modest, $\sim$0.1 magnitudes in H band.

The difference in stellar density and nebulosity contamination is apparent between the two fields. However, the highly structured nature of the nebulosity remains. This structure and the content of the nebulosity had implications on the spectroscopic observation procedure, as discussed below.

4.2.1 Spectroscopic Observations

In contrast to previous observations that aimed to detect only substellar and planetary mass objects, our observations were designed assign a spectral type nearly every object in the field having a spectral type between K5-L0. This approach was chosen in order to provide the best possible census of the low-mass and substellar populations. To maximize the efficiency of our spectroscopic observations, the objects were divided into multiple groups according to their H band magnitude: bright, moderate and faint. Masks were cut to observe the maximum number of targets with similar luminosity without overcrowding the field and causing contamination due to overlapping spectra. This resulted in four masks for the NW field, and three masks for lower stellar density SW field. The MOS masks were laser cut during daytime at CFHT summit and inserted into the mask cryostat later the same day. The cryostat was then cooled in time for night-time observations. The exposure times and observing conditions for each field are summarized in Table 4.I. The slit width, in the spectral direction, was chosen to be $0.6''$ (3 pixels) to obtain a spectral resolution of R$\sim$30. In the spatial direction, the slit sizes were $5''$ and the nod sizes were chosen to be $2''$ using the pattern ABAB to optimize sky subtraction. The small nod sizes were chosen to minimize the subtraction problems due

to the non-uniform nebular emission. A spectroscopic standard star was observed before and/or after each observation using the $0.6''$ longslit mode. Using the longslit permitted a more precise residual sky subtraction and minimized any differential slit loss.

Table 4.I: Summary of Spectroscopic Observations

Field	Date	Mask	Exp. Time (m)	Obs. Conditions[a]
1	2003 Dec. 13	NW-bright-1	19.0	poor seeing, no attenuation
2	2003 Dec. 13	NW-bright-2	13.0	poor seeing, no attenuation
3	2003 Dec. 13	NW-moderate	39.0	poor seeing, no attenuation
4	2003 Dec. 14	NW-faint	188.0	variable seeing, 1-3 mags of attenuation
5	2003 Dec. 13	SW-bright-1	23.0	poor seeing, photometric
6	2003 Dec. 11	SW-moderate	27.5	good seeing, clouds
7	2003 Dec. 12	SW-faint	132.5	poor seeing, no attenuation

[a] Information obtained using the CFHT's SkyProbe data archive

In total, spectra for 279 objects were obtained. We present only the 104 objects with low extinction (A_V<8) spectra having well constrained spectral types. These spectra exhibit adequate signal to perform spectral classification using the entire wavelength region and are not compromised by high nebulosity contamination. Throughout this paper, we have adopted the naming convention of O'dell & Wong (1996), where the object name XXX-YYY signifies the coordinate having a right ascension (RA) of 05h35mXX.Xs and declination (DEC) of -05d2YmYYs (J2000).

4.3 Spectroscopic Data Reduction

The spectroscopic data reduction was a challenging endeavour, primarily due to the telescopes inaccuracies in position between nods (0.2-0.6 pixels) and instrument/telescope flexure (up to 1.5 pixels). Having the target in different positions in the slit for each nod position introduces several systematic errors that require compensation. Position error in the spatial direction (direction of the nod) results in the positions of the positive/negative components of the spectrum in the difference image to change position which also causes variable slit loss. Position error in the dispersion direction, measured to be $\sim$2 pixels, results in the entire spectrum being shifted. Without correction, this error manifests itself as an offset in the wavelength solution for each difference image as well as variable slit loss. Correction for these errors is particularly important because the signal-to-noise

(S/N) of the sharp spectral features found in the spectra of low-mass objects would be significantly degraded. Further difficulty in data reduction was introduced due to the variable seeing conditions resulting from both poor observing conditions and the targets airmass changing throughout the longer observations. These effects also caused errors due to variable slit loss as well as affecting the flux calibration when the airmass (seeing) of the target differs from the seeing of the telluric standard. Of course, the amount of slit loss is different for each individual object, therefore the solutions to each of these challenges are not universal. To perform the image reduction, a custom spectral reduction pipeline was written in IDL to incorporate the required compensations.

The first step in the pipeline is to flat-field each individual image to compensate for pixel-to-pixel variations in the detector and to flag the bad pixels. Sky subtracted difference images were then created by subtracting adjacent nod positions. Any residual OH^- contamination was removed by subtracting a constant from each line that was determined by fitting a line to the regions outside the positive-negative signature of the object's 2-D spectrum. Using the highest S/N object in the field, from now on referred to as the *reference object*, an extraction aperture was fitted to a median trace of the difference image (in the spectral direction). The extraction aperture, described in equation 4.1, consists of two Gaussians of equal width σ and amplitude A but opposite sign. The positive peak is located at positions x_+ and second peak is separated from the positive peak by the size of the nod dx. The Gaussians are both offset vertically by a constant D.

$$F(x) = Ae^{-\left(\frac{x-x_+}{\sigma}\right)^2} - Ae^{-\left(\frac{x-(x_++dx)}{\sigma}\right)^2} + D \tag{4.1}$$

Once fitted to the reference object, this aperture is normalized to have a total unit area. The width (σ) and relative position between the peaks (dx) are then frozen. This template aperture is then fitted to each difference image of each object and used to extract a spectrum. This technique differs from the more typical method of combining a large stack of difference images and performing a single spectral extraction [1]. However, this allows for compensation of the telescope pointing errors described above.

1. This method was attempted but found to produce very low-quality spectra

The spectrum from each difference image is extracted by multiplying each line of pixels in the spatial direction by the fitted aperture function. This creates a weighted sum of the flux, where the flux in the peak of the Gaussian is given more weight and the noisy, low flux regions are given less weight. This aperture is also used to compensate for the flux lost due to variable slit loss between each nod positions and dead pixels. This is performed by multiplying the measured flux by the percentage of flux truncated by the slit. If more than 5% of the total aperture is truncated, the individual spectrum is marked as bad and not used in deriving the final spectrum.

Positional errors in the spectral direction are corrected by shifting each spectra relative to a reference spectrum, formed by performing a median of the subset of the object's spectra that correspond to the airmass of the telluric standard. In theory, any subset of images or single image can be chosen. The reason for choosing this subset is for an accurate flux calibration. This is further explained in the following paragraph. The shift between the extracted spectra and its reference is determined by performing a cross-correlation. Upon completion of this step, all spectra are spectrally correlated to the reference spectrum and have the same wavelength solution (once determined). The next step in the reduction is to compensate the change in flux resulting from variable seeing/airmass and sky transparency. This is accomplished by multiplying each spectrum by a constant which brings its flux to the same level as the reference spectrum. This removes any flux variation observed over the entire spectrum and ensures the flux calibration will be correct since the reference spectrum corresponds to the airmass of the telluric standard. Of course, should the transparency between the reference spectrum and telluric standard be different, this will introduce an offset in the flux calibration. The array of spectra are then median combined to create the final observed spectrum. The uncertainty for each data point is determined by calculating the standard deviation of each data point (using the robust_sigma algorithm in IDL).

The wavelength calibration for each spectrum was accomplished using the broad atmospheric water absorption bands. Through comparison with previously observed objects, it was determined that this method is accurate for the Orion objects to ± 0.5

pixels [2]. This uncertainty corresponds to $\pm$0.005 um at 1.0 um, and 0.01 um at 2.2 um and must be accounted for when performing the spectral typing of these objects. This is discussed in further detail in section 4.4. After wavelength calibration, the spectrum is corrected for telluric absorption.

Occasionally, spectral absorption and emission features occur in the difference image and consequently the final spectrum due to an asymmetric nebulosity spectrum on either side of the nod position. In most cases, the residual does not align nor exhibit the same Gaussian-like PSF of a point source and is therefore not intrinsic to the object. To help alleviate the effects of this problem, a spectrum of the average nebulosity surrounding the region was extracted to be used in the spectral fitting procedure for hand-selected objects. This was accomplished by using the sky spectrum from an object in a region of very low nebulosity and subtracting it from the object of interest. Because its form cannot be fitted by the aperture function (as it is not a point source), no proper flux calibration can be performed. Similar to the procedure above, a spectrum is extracted for each difference image and the shifts and scaling calculated for the object spectrum are equally applied to the nebulosity spectrum.

Depending on the observation, the S/N of brighter objects are either limited by the S/N of the telluric standard or in the case of the longer observations, the variation in atmospheric dispersion throughout the observation. For faint sources, the S/N is limited by the fitting of the aperture to the positive-negative signal in each difference image. An offset from the true position introduces a random scatter that does not significantly reduce with an increased amount of difference images. The low S/N also affects the ability to correct for positional errors in the spectral direction.

4.4 Spectral Classification

To accurately determine the form of the IMF, a mass must be determined for each object. Prior to calculating a mass, accurate spectral types and uncertainties must be carefully assigned to each object. Applying spectral types to young M-stars and substel-

2. In the case of the telluric standards, whose only spectral features at R$\sim$30 are the water bands, the method is accurate to approximately $\pm$0.1 pixels.

lar objects is a challenging problem, particularly in areas of high extinction and nebular gas. Many studies of these objects in Orion classified them using spectral indices, calculated by measuring the flux ratios between two narrowband wavelength regions. Early studies calibrated the indices using high surface gravity field dwarfs (Lucas et al. 2001; Luhman et al. 2000; Slesnick et al. 2004). However, comparing a young brown dwarf to an old field dwarf of similar spectral type in the optical, yields noticeable differences in the near infrared (Allers et al. 2007). This is particularly evident in the *H* band, where the steam bands in the younger objects create sharper peaked spectra then an older counterpart. Naturally, the variation in spectral shape introduces a bias in the index calibration and thus affects any spectral types derived using these indices. Another approach has been to use indices inferred from synthetic spectra (e.g. the Ames-DUSTY models of Allard et al. 2001). These models offer improvements over the use of field dwarfs but are unable to fit both sides of the sharply peaked *H* band of young objects (Lucas et al. 2001). A similar phenomenon occurs in *K* band. Furthermore, current theoretical models become uncertain at ages below 1 Myr.

Analogous to the technique used in Weights et al. (2009) to classify substellar objects in Orion, we adopt the spectral sequence for young M stars and brown dwarfs whose near-infrared spectra have been kindly provided by Kevin Luhman. Using this catalogue, which includes spectral types ranging from M3-M9.5 from various young ($\sim$1-2 Myr) clusters, we are able to avoid the complications introduced by using field dwarfs or synthetic spectra. The objects in the Luhman catalogue have been classified using high-quality optical spectra. Their spectral sequence was derived using a combination of standard dwarfs and giants (Luhman 1999). Performing the classification using optical wavelengths is often preferred due to the temperature-sensitive molecular bands that provide accurate spectral type calibration. Once classified, near-infrared spectra of these objects were then obtained using the Spex instrument on the NASA Infrared Telescope Facility (IRTF). In order to be compared to our objects, we have dereddened the supplied spectra using previously determined values and the associated reddening law. We then Gaussian smoothed the spectra to match the resolution of our observations. In the case where multiple objects of the same spectral type were available but with greatly differ-

ing extinction, the high extinction objects were discarded as their reddening values were the most uncertain. In total, 33 template spectra from Kevin Luhman have been chosen to characterize our objects. Their spectra and corresponding extinction values can be found in Guieu et al. (2006), Grosso et al. (2007), Luhman et al. (2003), Briceño et al. (2002), Morrow et al. (2008), Luhman (2004), Luhman (1999). The uncertainty associated with the determined reddening value is $\sim$1 mag in A_V. Because we aim to classify objects outside of the range of the Luhman catalogue, we have extended our library to later spectral type by including the young L0 dwarf (2MASS J01415823-4633574) of Kirkpatrick et al. (2006). As of the date of publication, no spectra covering our spectral range has been published for young (1-2 Myr) L dwarfs. Therefore, anything classified as L0 may in fact be of later spectral type. We have also included K0V, K2V, K4V, K5V, K7V, M1V, and M2V spectral templates from the Spex catalogue. Below the M3 spectral type, standard dwarfs are adequate to determine the spectral types of our young objects (Kevin Luhman, personal communication).

Using spectral indices to characterize an object is a powerful method when correctly calibrated. This method is particularly well suited when multiple wavelength bands cannot be observed simultaneously. This is often the case of medium resolution spectroscopic observations such as those performed by Lucas et al. (2001) and Weights et al. (2009). Because the bands were not observed and calibrated simultaneously, the relative flux between the two bands could not be accurately quantified. Therefore, a spectral type was assigned based on spectral indices derived for each individual band. Depending on the index, it may not be sensitive to both surface gravity and temperature effects, or it may produce a double valued solution. Therefore, multiple indices are often required to ensure an accurate characterization. A more detailed discussion of the use of spectral indices can be found in Riddick et al. (2007b) and Weights et al. (2009).

Whereas previous studies have predominantly relied upon spectral indices, our simultaneous wavelength coverage allows spectral template fitting to the entire 0.9-2.4 μm spectrum. Fitting the shape of the SED over a large wavelength range enables the relative flux between the bands to contribute to the characterization. Furthermore, in contrast to previous studies that estimate the reddening using colours (Hillenbrand &

Carpenter 2000; Lucas & Roche 2000; Slesnick et al. 2004; Weights et al. 2009), we are able to directly derive a reddening while fitting the templates over our objects' broad spectral range.

4.4.1 Spectral Fitting Procedure

In order to assign both a spectral type and extinction with associated uncertainties, we adopt the SED fitting technique described in section 4 of Cushing et al. (2008). The goodness-of-fit statistic (G) is mathematically similar to a χ^2 statistic but introduces an additional weighting term to dampen the effect of differential wavelength sampling over the observed spectral region. If each data point in our spectrum were assigned an equal weight, the *J* band would receive a significantly higher weight than both *H* and *K* bands. Because we do not wish to favour any specific wavelength region, we have opted to weight each pixel by its width in microns. In regions having strong telluric absorption (1.3-1.5 μm and 1.8-2.05 μm), the weights have been set to zero. The only difference between the goodness-of-fit statistic used by Cushing et al. (2008) and this article, is the significance of the normalization factor. The original version fits synthetic SED's to the observed spectra and therefore requires a normalization factor (C_k) equal to $(R/d)^2$ where R is the stellar radius, and d is the distance to the object. In our case, because we are using non flux-calibrated template spectra from various clusters, C_k is purely a normalization factor and has little underlying significance.

A consequence of using this fitting technique is that the goodness-of-fit statistic does not follow a χ^2 distribution. Furthermore, the set of templates represents a set of discrete values and not a smoothly varying distribution, therefore it is incorrect to assign an uncertainty based purely on the distribution of our goodness-of-fit statistic. For example, should two discrete solutions with differing parameters be of equal quality (eg M4 with A_V=0, or M7 with A_V=3), assigning an average spectral type and extinction would not properly represent the best-fitting parameter space. For these reasons, we have opted to use a Monte-Carlo technique to better portray the nature of the uncertainties.

During the Monte-Carlo simulation, each object is classified 100 times [3]. The most-

3. Performing 1000 trials did not affect the results

common, earliest and latest spectral classification with corresponding extinctions were used to classify the object. For each of the trial, a new spectrum is created from the original by adding a random offset to the original value of the data point. The offset is derived using a normal distribution whose width is equal to the size of the error bar. Using a multi-parameter fitting routine, each spectral template is fitted to the new spectrum. The reddening value is left to float and applied to the spectral template using the reddening law of Cardelli et al. (1989), using the reddening parameter of R_V=3.1, the value corresponding to the diffuse interstellar medium and the value chosen by previous works. Although the OMC is not a typical region of the interstellar medium, the effects of varying the R_V parameter are most apparent at optical wavelengths ($\lambda < 0.9\mu$m). Therefore, our low-extinction ($A_V < 8$), infrared spectra are therefore less prone to errors resulting from the choice of reddening laws.

In fitting the spectral templates, the zero point of the wavelength solution was also left as a free parameter and allowed to vary by $\pm$0.5 pixels. Lastly, in object-specific cases where nebular contamination was obvious in the difference images, a nebulosity spectrum was also fitted to the object [4]. The best-fitting template and associated fitting parameters for each trial are used in determining the spectral type and extinction. The final classification is assigned using the most commonly occurring values. The earliest and latest spectral types and associated extinctions define the parameter space of best-fitting scenarios. The characterization solution and the histograms describing the distribution of classifications and extinctions are available online [5].

4. These cases are specifically indicated in Table 4.II
5. www.astro.umontreal.ca/~ingraham/Orion_data/SIMON_2003/ApJ_2012/index.html

Table 4.II: Properties of Observed Sources

ID[a]	Field	H	H_{dr}	SpT$^{\text{Latest}}_{\text{Earliest}}$	A$_v$ $^{\text{Latest}}_{\text{Earliest}}$	Temp (K) $^{\text{Latest}}_{\text{Earliest}}$	Mass (M$_\odot$) $^{\text{Latest}}_{\text{Earliest}}$	Notes
011-304	1	13.0	12.3	M3.75$^{\text{M5.50}}_{\text{M3.75}}$	3.9 $^{4.1}_{3.9}$	3306$^{3057}_{3306}$	0.334$^{0.124}_{0.334}$	truncated <1.05um mediocre fit
012-524	5	16.8	16.5	M9.00$^{\text{L0.00}}_{\text{M8.25}}$	1.3 $^{0.4}_{2.8}$	2400$^{2000}_{2632}$	0.014$^{0.006}_{0.026}$	
012-407	5	10.6[b]	10.5	M2.00$^{\text{M2.00}}_{\text{K0.00}}$	0.4 $^{0.4}_{2.1}$	3530$^{3530}_{5240}$	0.626$^{0.626}_{2.454}$	J-band emis
012-145	1	12.4	11.4	M6.00$^{\text{M7.25}}_{\text{M6.00}}$	5.2 $^{2.9}_{5.2}$	2990$^{2837}_{2990}$	0.097$^{0.048}_{0.097}$	J-band emis
013-306	1	15.6	14.2	M5.75$^{\text{M5.75}}_{\text{M4.75}}$	7.7 $^{7.7}_{9.9}$	3023$^{3023}_{3161}$	0.110$^{0.110}_{0.174}$	mediocre fit
013-413	5	14.6	14.1	M6.00$^{\text{M7.25}}_{\text{M6.00}}$	2.9 $^{0.8}_{2.9}$	2990$^{2837}_{2990}$	0.097$^{0.048}_{0.097}$	J-band emis
015-319	1	17.3	17.0	L0.00$^{\text{L0.00}}_{\text{M6.00}}$	1.9 $^{1.9}_{5.5}$	2000$^{2000}_{2990}$	0.006$^{0.006}_{0.097}$	trimmed <1um
016-534	5	12.9	12.6	M4.75$^{\text{M4.75}}_{\text{M4.75}}$	1.4 $^{1.3}_{1.4}$	3161$^{3161}_{3161}$	0.174$^{0.174}_{0.174}$	
016-410	5	12.4	12.0	M4.75$^{\text{M5.00}}_{\text{M4.75}}$	2.2 $^{0.6}_{2.2}$	3161$^{3125}_{3161}$	0.174$^{0.153}_{0.174}$	J-band emis
019-354	1	14.2	13.9	M6.25$^{\text{M6.25}}_{\text{M5.00}}$	1.6 $^{1.6}_{2.0}$	2963$^{2963}_{3125}$	0.088$^{0.088}_{0.153}$	J-band emis
021-636	5	10.3	9.8	M3.00$^{\text{M3.00}}_{\text{M3.00}}$	3.0 $^{3.0}_{3.0}$	3415$^{3415}_{3415}$	0.485$^{0.485}_{0.485}$	J-band emis
023-123	1	13.4	12.3	M6.25$^{\text{M7.50}}_{\text{M5.50}}$	6.2 $^{6.4}_{7.5}$	2963$^{2795}_{3057}$	0.088$^{0.041}_{0.124}$	
030-524	5	17.2	17.2	M6.25$^{\text{M8.50}}_{\text{M5.50}}$	0.2 $^{0.6}_{1.4}$	2963$^{2555}_{3057}$	0.088$^{0.021}_{0.124}$	J-band emis
031-536	5	16.2	15.9	M8.50$^{\text{M8.50}}_{\text{M7.75}}$	1.8 $^{1.8}_{0.1}$	2555$^{2555}_{2752}$	0.021$^{0.021}_{0.036}$	
031-238	1	11.2	10.7	M4.75$^{\text{M4.75}}_{\text{M4.75}}$	3.2 $^{3.2}_{3.2}$	3161$^{3161}_{3161}$	0.174$^{0.174}_{0.174}$	
034-610	5	13.2	12.9	M4.75$^{\text{M4.75}}_{\text{M4.75}}$	2.1 $^{2.1}_{2.1}$	3161$^{3161}_{3161}$	0.174$^{0.174}_{0.174}$	
034-333	1	13.3	13.3	M7.25$^{\text{M7.25}}_{\text{M6.00}}$	0.0 $^{0.0}_{2.1}$	2837$^{2837}_{2990}$	0.048$^{0.048}_{0.097}$	J-band emis
037-246	1	12.3	11.3	M5.00$^{\text{M5.25}}_{\text{M4.75}}$	5.6 $^{6.5}_{5.9}$	3125$^{3091}_{3161}$	0.153$^{0.138}_{0.174}$	
037-627	5	17.3	17.0	M9.00$^{\text{L0.00}}_{\text{M7.25}}$	1.8 $^{0.7}_{1.8}$	2400$^{2000}_{2837}$	0.014$^{0.006}_{0.048}$	
038-112	1	16.4	15.1	M8.50$^{\text{L0.00}}_{\text{M6.25}}$	7.5 $^{4.5}_{7.2}$	2555$^{2000}_{2963}$	0.021$^{0.006}_{0.088}$	trimmed <1um
041-210	1	16.3	15.3	M3.75$^{\text{M6.00}}_{\text{M3.75}}$	5.6 $^{5.2}_{5.7}$	3306$^{2990}_{3306}$	0.334$^{0.097}_{0.334}$	
042-627	5	11.1[b]	10.2	M3.75$^{\text{M3.75}}_{\text{M3.75}}$	4.7 $^{4.7}_{4.7}$	3306$^{3306}_{3306}$	0.334$^{0.334}_{0.334}$	mediocre fit
042-224	1	12.9	12.6	M4.75$^{\text{M5.00}}_{\text{M3.75}}$	1.7 $^{0.1}_{1.4}$	3161$^{3125}_{3306}$	0.174$^{0.153}_{0.334}$	
044-123	1	15.3	14.0	K5.00$^{\text{M1.00}}_{\text{K4.00}}$	7.5 $^{6.8}_{8.2}$	4340$^{3680}_{4560}$	1.544$^{0.814}_{1.767}$	mediocre fit

Continued on Next Page...

Table 4.II – Continued

ID[a]	Field	H	H_{dr}	SpT$^{\text{Latest}}_{\text{Earliest}}$	A_v $^{\text{Latest}}_{\text{Earliest}}$	Temp (K) $^{\text{Latest}}_{\text{Earliest}}$	Mass ($M_\odot$) $^{\text{Latest}}_{\text{Earliest}}$	Notes
044-527	5	16.7	16.5	M8.25$^{\text{M8.25}}_{\text{M6.00}}$	0.9 $^{0.9}_{2.1}$	2632$^{2632}_{2990}$	0.026$^{0.026}_{0.097}$	J-band emis
044-219	1	15.7	15.3	M8.00$^{\text{M8.50}}_{\text{M7.00}}$	2.2 $^{1.5}_{3.9}$	2710$^{2555}_{2880}$	0.031$^{0.021}_{0.057}$	
045-604	5	11.2[b]	10.6	M1.00$^{\text{M3.00}}_{\text{M1.00}}$	3.7 $^{3.8}_{3.7}$	3680$^{3415}_{3680}$	0.814$^{0.485}_{0.814}$	
046-442	5	11.6[b]	10.7	K7.00$^{\text{M1.00}}_{\text{K5.00}}$	5.1 $^{4.9}_{5.5}$	4040$^{3680}_{4340}$	1.252$^{0.814}_{1.544}$	
046-623	5	11.2[b]	10.3	M1.00$^{\text{M1.00}}_{\text{M1.00}}$	4.8 $^{4.6}_{4.8}$	3680$^{3680}_{3680}$	0.814$^{0.814}_{0.814}$	
047-638	5	11.0[b]	10.4	M3.75$^{\text{M3.75}}_{\text{M1.00}}$	3.7 $^{3.7}_{3.8}$	3306$^{3306}_{3680}$	0.334$^{0.334}_{0.814}$	
048-239	1	12.0	11.7	M3.75$^{\text{M3.75}}_{\text{M3.75}}$	2.0 $^{2.0}_{2.0}$	3306$^{3306}_{3306}$	0.334$^{0.334}_{0.334}$	
052-603	6	12.9	12.8	M5.00$^{\text{M5.00}}_{\text{M4.75}}$	0.6 $^{0.6}_{2.1}$	3125$^{3125}_{3161}$	0.153$^{0.153}_{0.174}$	
052-323	1	15.4	15.4	M7.50$^{\text{M8.50}}_{\text{M5.50}}$	0.3 $^{0.8}_{1.2}$	2795$^{2555}_{3057}$	0.041$^{0.021}_{0.124}$	
054-555	6	13.2	13.0	M4.75$^{\text{M5.25}}_{\text{M3.75}}$	1.3 $^{2.0}_{2.2}$	3161$^{3091}_{3306}$	0.174$^{0.138}_{0.334}$	
055-231	1	13.0	12.4	M6.00$^{\text{M7.50}}_{\text{M6.00}}$	3.3 $^{2.5}_{3.3}$	2990$^{2795}_{2990}$	0.097$^{0.041}_{0.097}$	
057-354	6	11.5[b]	11.1	M3.75$^{\text{M4.75}}_{\text{M3.75}}$	2.0 $^{2.3}_{2.0}$	3306$^{3161}_{3306}$	0.334$^{0.174}_{0.334}$	J-band emis
057-315	1	17.1	16.6	M5.50$^{\text{M6.25}}_{\text{M4.75}}$	2.3 $^{1.2}_{2.7}$	3057$^{2963}_{3161}$	0.124$^{0.088}_{0.174}$	
058-316	1	13.0	12.4	M5.50$^{\text{M6.00}}_{\text{M5.50}}$	3.0 $^{2.7}_{3.0}$	3057$^{2990}_{3057}$	0.124$^{0.097}_{0.124}$	missing half of H-band
058-701	6	11.1[b]	10.4	M3.00$^{\text{M3.00}}_{\text{M1.00}}$	3.9 $^{3.9}_{3.9}$	3415$^{3415}_{3680}$	0.485$^{0.485}_{0.814}$	Mediocre fit
064-212	2	16.2	15.3	M8.25$^{\text{L0.00}}_{\text{M3.75}}$	5.4 $^{2.8}_{7.7}$	2632$^{2000}_{3306}$	0.026$^{0.006}_{0.334}$	K-band contamination? Trimmed <1um >2.35um
064-315	2	12.6	12.6	M9.00$^{\text{M9.00}}_{\text{M9.00}}$	0.1 $^{0.1}_{0.1}$	2400$^{2400}_{2400}$	0.014$^{0.014}_{0.014}$	
064-208	2	12.8	12.5	M4.75$^{\text{M5.50}}_{\text{M4.75}}$	1.9 $^{1.4}_{1.9}$	3161$^{3057}_{3161}$	0.174$^{0.124}_{0.174}$	
065-119	2	12.8	12.4	M4.75$^{\text{M5.00}}_{\text{M3.75}}$	2.1 $^{0.4}_{1.7}$	3161$^{3125}_{3306}$	0.174$^{0.153}_{0.334}$	
065-441	6	10.7[b]	10.2	K7.00$^{\text{M1.00}}_{\text{K7.00}}$	2.6 $^{2.4}_{2.6}$	4040$^{3680}_{4040}$	1.252$^{0.814}_{1.252}$	
065-501	6	12.3	11.7	M3.75$^{\text{M4.75}}_{\text{M3.50}}$	3.3 $^{2.6}_{3.1}$	3306$^{3161}_{3342}$	0.334$^{0.174}_{0.381}$	
066-650	6	11.6[b]	11.1	M3.75$^{\text{M3.75}}_{\text{M3.75}}$	2.8 $^{2.8}_{2.8}$	3306$^{3306}_{3306}$	0.334$^{0.334}_{0.334}$	
069-600	6	12.8	12.4	M3.75$^{\text{M4.75}}_{\text{M3.75}}$	2.5 $^{2.8}_{2.5}$	3306$^{3161}_{3306}$	0.334$^{0.174}_{0.334}$	
070-500	6	15.3	14.4	M7.00$^{\text{M7.75}}_{\text{M7.00}}$	4.9 $^{2.8}_{4.9}$	2880$^{2752}_{2880}$	0.057$^{0.036}_{0.057}$	

Continued on Next Page...

Table 4.II – Continued

ID[a]	Field	H	H_{dr}	SpT$^{\text{Latest}}_{\text{Earliest}}$	A_v $^{\text{Latest}}_{\text{Earliest}}$	Temp (K) $^{\text{Latest}}_{\text{Earliest}}$	Mass ($M_\odot$) $^{\text{Latest}}_{\text{Earliest}}$	Notes
072-638	6	14.7	14.7	M6.25$^{\text{M6.25}}_{\text{M6.25}}$	0.1 $^{0.1}_{0.1}$	2963$^{2963}_{2963}$	0.088$^{0.088}_{0.088}$	
073-227	2	11.6	11.3	M4.75$^{\text{M4.75}}_{\text{M3.75}}$	1.5 $^{1.5}_{2.5}$	3161$^{3161}_{3306}$	0.174$^{0.174}_{0.334}$	
074-548	6	12.3	12.0	M6.00$^{\text{M6.00}}_{\text{M6.00}}$	1.8 $^{1.8}_{1.8}$	2990$^{2990}_{2990}$	0.097$^{0.097}_{0.097}$	
074-229	2	12.6	12.4	M4.75$^{\text{M5.25}}_{\text{M4.75}}$	1.1 $^{0.4}_{1.1}$	3161$^{3091}_{3161}$	0.174$^{0.138}_{0.174}$	
074-640	6	12.3	12.0	M4.75$^{\text{M4.75}}_{\text{M4.50}}$	1.6 $^{1.6}_{2.8}$	3161$^{3161}_{3197}$	0.174$^{0.174}_{0.204}$	
075-146	2	17.9	17.7	M9.50$^{\text{L0.00}}_{\text{M6.00}}$	1.3 $^{0.0}_{3.0}$	2200$^{2000}_{2990}$	0.009$^{0.006}_{0.097}$	low S/N
077-452	6	13.2	13.2	M5.50$^{\text{M5.50}}_{\text{M5.50}}$	0.0 $^{0.0}_{0.0}$	3057$^{3057}_{3057}$	0.124$^{0.124}_{0.124}$	
077-127	2	14.1	14.0	M9.25$^{\text{M9.50}}_{\text{M9.25}}$	0.9 $^{1.2}_{0.9}$	2350$^{2200}_{2350}$	0.012$^{0.009}_{0.012}$	
080-117	2	12.5	12.2	M3.75$^{\text{M3.75}}_{\text{M3.75}}$	2.0 $^{1.9}_{2.0}$	3306$^{3306}_{3306}$	0.334$^{0.334}_{0.334}$	mediocre fit
081-118	2	15.6	15.4	M3.75$^{\text{M5.50}}_{\text{M2.00}}$	0.6 $^{0.4}_{1.5}$	3306$^{3057}_{3530}$	0.334$^{0.124}_{0.626}$	
081-237	2	16.6	15.6	M8.50$^{\text{L0.00}}_{\text{M6.00}}$	5.3 $^{1.6}_{5.5}$	2555$^{2000}_{2990}$	0.021$^{0.006}_{0.097}$	trimmed <1um
082-403	6	12.4	11.7	M4.75$^{\text{M4.75}}_{\text{M3.75}}$	4.1 $^{4.2}_{4.7}$	3161$^{3161}_{3306}$	0.174$^{0.174}_{0.334}$	
082-253	2	15.7	15.1	M7.00$^{\text{M8.50}}_{\text{M6.00}}$	3.3 $^{0.8}_{3.2}$	2880$^{2555}_{2990}$	0.057$^{0.021}_{0.097}$	small J band contam
082-435	6	12.1	11.8	M4.75$^{\text{M5.25}}_{\text{M4.75}}$	1.5 $^{2.1}_{1.5}$	3161$^{3091}_{3161}$	0.174$^{0.138}_{0.174}$	
083-102	3	16.5	16.3	M7.25$^{\text{M9.00}}_{\text{M7.25}}$	1.4 $^{1.2}_{1.3}$	2837$^{2400}_{2837}$	0.048$^{0.014}_{0.048}$	
084-305	3	13.1	12.4	M8.25$^{\text{M9.25}}_{\text{M6.00}}$	4.0 $^{3.3}_{5.1}$	2632$^{2350}_{2990}$	0.026$^{0.012}_{0.097}$	
084-401	6	19.2	18.4	M7.75$^{\text{L0.00}}_{\text{M5.75}}$	4.5 $^{2.6}_{3.7}$	2752$^{2000}_{3023}$	0.036$^{0.006}_{0.110}$	low S/N faint gas ball
085-518	6	11.2[b]	10.4	M1.00$^{\text{M1.00}}_{\text{M1.00}}$	4.3 $^{4.2}_{4.3}$	3680$^{3680}_{3680}$	0.814$^{0.814}_{0.814}$	
086-619	6	12.3	11.7	M5.00$^{\text{M5.50}}_{\text{M3.75}}$	3.5 $^{4.6}_{4.5}$	3125$^{3057}_{3306}$	0.153$^{0.124}_{0.334}$	
086-324	3	14.2	13.4	M6.25$^{\text{M7.50}}_{\text{M5.50}}$	4.8 $^{4.9}_{6.2}$	2963$^{2795}_{3057}$	0.088$^{0.041}_{0.124}$	trimmed <1um
092-605	6	16.3	16.3	M8.50$^{\text{M9.50}}_{\text{M8.50}}$	0.1 $^{0.2}_{0.1}$	2555$^{2200}_{2555}$	0.021$^{0.009}_{0.021}$	missing sections of H and K
095-059	3	13.0	12.6	M6.00$^{\text{M7.25}}_{\text{M6.00}}$	2.0 $^{0.0}_{2.0}$	2990$^{2837}_{2990}$	0.097$^{0.048}_{0.097}$	mediocre fit
097-125	3	11.9	11.6	M3.75$^{\text{M3.75}}_{\text{M3.00}}$	1.9 $^{1.9}_{2.0}$	3306$^{3306}_{3415}$	0.334$^{0.334}_{0.485}$	mediocre fit
098-327	3	11.0	10.6	M1.00$^{\text{M1.00}}_{\text{M1.00}}$	1.8 $^{1.8}_{1.8}$	3680$^{3680}_{3680}$	0.814$^{0.814}_{0.814}$	mediocre fit

Continued on Next Page...

Table 4.II – Continued

ID[a]	Field	H	H_{dr}	SpT$^{\text{Latest}}_{\text{Earliest}}$	A_v $^{\text{Latest}}_{\text{Earliest}}$	Temp (K) $^{\text{Latest}}_{\text{Earliest}}$	Mass ($M_\odot$) $^{\text{Latest}}_{\text{Earliest}}$	Notes
098-606	7	18.7	18.2	M8.5$^{\text{L0.00}}_{\text{M7.00}}$	2.9 $^{0.9}_{4.1}$	2555$^{2000}_{2880}$	0.021$^{0.006}_{0.057}$	low S/N faint gas ball
099-634	7	15.3	14.0	M5.75$^{\text{M7.50}}_{\text{M5.00}}$	7.6 $^{9.3}_{9.5}$	3023$^{2795}_{3125}$	0.110$^{0.041}_{0.153}$	
099-339	3	12.6	12.4	M7.25$^{\text{M7.25}}_{\text{M7.25}}$	1.2 $^{1.2}_{1.2}$	2837$^{2837}_{2837}$	0.048$^{0.048}_{0.048}$	neb. contamination at 1.1um mediocre fit
100-501	7	16.1	16.0	M9.00$^{\text{M9.50}}_{\text{M9.00}}$	0.5 $^{1.5}_{0.5}$	2400$^{2200}_{2400}$	0.014$^{0.009}_{0.014}$	
100-531	7	16.8	15.7	L0.00$^{\text{L0.00}}_{\text{M5.75}}$	6.0 $^{6.0}_{7.0}$	2000$^{2000}_{3023}$	0.006$^{0.006}_{0.110}$	missing part of K-band
101-233	3	11.5	10.9	M1.00$^{\text{M3.00}}_{\text{M1.00}}$	3.4 $^{3.4}_{3.4}$	3680$^{3415}_{3680}$	0.814$^{0.485}_{0.814}$	small K-excess?
102-100	3	13.6	13.4	M6.00$^{\text{M6.00}}_{\text{M5.50}}$	1.5 $^{1.5}_{1.9}$	2990$^{2990}_{3057}$	0.097$^{0.097}_{0.124}$	
103-157	3	12.6	12.2	M5.50$^{\text{M6.00}}_{\text{M5.50}}$	2.3 $^{1.9}_{2.3}$	3057$^{2990}_{3057}$	0.124$^{0.097}_{0.124}$	
103-451	7	14.1	13.0	M8.50$^{\text{L0.00}}_{\text{M6.00}}$	5.9 $^{3.5}_{7.3}$	2555$^{2000}_{2990}$	0.021$^{0.006}_{0.097}$	low s/n - trimmed>2.35um
105-246	3	10.9	10.4	M1.00$^{\text{M1.00}}_{\text{M1.00}}$	2.6 $^{2.7}_{2.6}$	3680$^{3680}_{3680}$	0.814$^{0.814}_{0.814}$	mediocre fit - missing part of K
106-245	3	11.3	10.8	M3.75$^{\text{M3.75}}_{\text{M3.75}}$	3.0 $^{3.0}_{3.0}$	3306$^{3306}_{3306}$	0.334$^{0.334}_{0.334}$	
107-628	7	12.2	11.5	M3.00$^{\text{M3.50}}_{\text{K0.00}}$	3.7 $^{3.4}_{6.1}$	3415$^{3342}_{5240}$	0.485$^{0.381}_{2.454}$	truncated <1.2um
108-556	7	12.4	11.2	M3.75$^{\text{M6.00}}_{\text{M3.75}}$	6.3 $^{6.3}_{6.3}$	3306$^{2990}_{3306}$	0.334$^{0.097}_{0.334}$	
110-225	3	12.0	10.8	M3.50$^{\text{M4.75}}_{\text{M3.50}}$	6.7 $^{5.9}_{6.7}$	3342$^{3161}_{3342}$	0.381$^{0.174}_{0.381}$	
111-436	7	16.4	16.2	M7.25$^{\text{L0.00}}_{\text{M5.50}}$	1.3 $^{0.3}_{4.6}$	2837$^{2000}_{3057}$	0.048$^{0.006}_{0.124}$	trimmed <1.15um
111-532	7	13.1	12.7	M4.00$^{\text{M4.50}}_{\text{M4.00}}$	1.9 $^{2.7}_{1.9}$	3270$^{3197}_{3270}$	0.286$^{0.204}_{0.286}$	
115-602	7	9.1[b]	8.4	M1.00$^{\text{M1.00}}_{\text{M1.00}}$	3.5 $^{3.5}_{3.5}$	3680$^{3680}_{3680}$	0.814$^{0.814}_{0.814}$	Mild neb. contam
116-252	3	12.2	11.9	M5.00$^{\text{M5.50}}_{\text{M3.75}}$	1.6 $^{2.7}_{2.6}$	3125$^{3057}_{3306}$	0.153$^{0.124}_{0.334}$	trimmed below 1um
117-341	3	11.9[b]	11.7	M5.00$^{\text{M5.00}}_{\text{M5.00}}$	1.2 $^{1.2}_{1.2}$	3125$^{3125}_{3125}$	0.153$^{0.153}_{0.153}$	Neb. Contam. trimmed <1.15um
118-155	3	12.0	11.6	M4.75$^{\text{M5.00}}_{\text{M4.75}}$	2.2 $^{0.5}_{2.2}$	3161$^{3125}_{3161}$	0.174$^{0.153}_{0.174}$	K-excess?
121-433	7	13.1	12.3	M8.25$^{\text{M8.25}}_{\text{M6.25}}$	4.1 $^{4.2}_{4.5}$	2632$^{2632}_{2963}$	0.026$^{0.026}_{0.088}$	trimmed <1.15um
126-426	7	13.2	12.1	M6.25$^{\text{M7.50}}_{\text{M6.25}}$	6.3 $^{6.6}_{6.3}$	2963$^{2795}_{2963}$	0.088$^{0.041}_{0.088}$	
129-105	4	13.9	13.2	L0.00$^{\text{L0.00}}_{\text{M5.25}}$	3.9 $^{3.9}_{8.1}$	2000$^{2000}_{3091}$	0.006$^{0.006}_{0.138}$	mediocre fit K-band contamination
129-458	7	13.2	12.9	M4.50$^{\text{M4.75}}_{\text{M2.00}}$	2.0 $^{1.8}_{2.6}$	3197$^{3161}_{3530}$	0.204$^{0.174}_{0.626}$	trimmed <1.15um

Continued on Next Page...

Table 4.II – Continued

ID[a]	Field	H	H_{dr}	SpT $^{\text{Latest}}_{\text{Earliest}}$	A_v $^{\text{Latest}}_{\text{Earliest}}$	Temp (K) $^{\text{Latest}}_{\text{Earliest}}$	Mass ($M_\odot$) $^{\text{Latest}}_{\text{Earliest}}$	Notes
130-053	4	14.9	14.5	M7.25 $^{\text{M9.25}}_{\text{M7.25}}$	2.2 $^{3.4}_{2.3}$	2837 $^{2350}_{2837}$	0.048 $^{0.012}_{0.048}$	low S/N
131-215	4	11.5	10.8	M3.75 $^{\text{M3.75}}_{\text{M3.75}}$	3.7 $^{3.8}_{3.7}$	3306 $^{3306}_{3306}$	0.334 $^{0.334}_{0.334}$	mediocre fit
131-253	4	13.5	13.4	M5.00 $^{\text{M6.00}}_{\text{M3.75}}$	0.6 $^{1.4}_{1.6}$	3125 $^{2990}_{3306}$	0.153 $^{0.097}_{0.334}$	
131-113	4	12.6	12.1	M3.75 $^{\text{M4.75}}_{\text{M3.75}}$	2.8 $^{3.1}_{2.8}$	3306 $^{3161}_{3306}$	0.334 $^{0.174}_{0.334}$	J-band emis
133-258	4	12.8	12.5	M6.00 $^{\text{M7.00}}_{\text{M5.00}}$	1.2 $^{1.0}_{0.6}$	2990 $^{2880}_{3125}$	0.097 $^{0.057}_{0.153}$	
136-121	4	13.3	13.0	M3.75 $^{\text{M3.75}}_{\text{M3.75}}$	1.6 $^{1.6}_{1.6}$	3306 $^{3306}_{3306}$	0.334 $^{0.334}_{0.334}$	mediocre fit - neb. Contam
141-339	4	9.9[b]	9.5	M1.00 $^{\text{M3.00}}_{\text{K4.00}}$	2.0 $^{1.8}_{3.4}$	3680 $^{3415}_{4560}$	0.814 $^{0.485}_{1.767}$	J band emis
141-237	4	11.0	10.5	M3.00 $^{\text{M3.00}}_{\text{M3.00}}$	2.9 $^{2.9}_{2.9}$	3415 $^{3415}_{3415}$	0.485 $^{0.485}_{0.485}$	small Neb. Contamination in J

a. ID format follows from ODell & Wong 1996. XXX-YYY implies an RA of 05:35:XX.X and DEC of -05:2Y:YY
b. Magnitude value from 2Mass

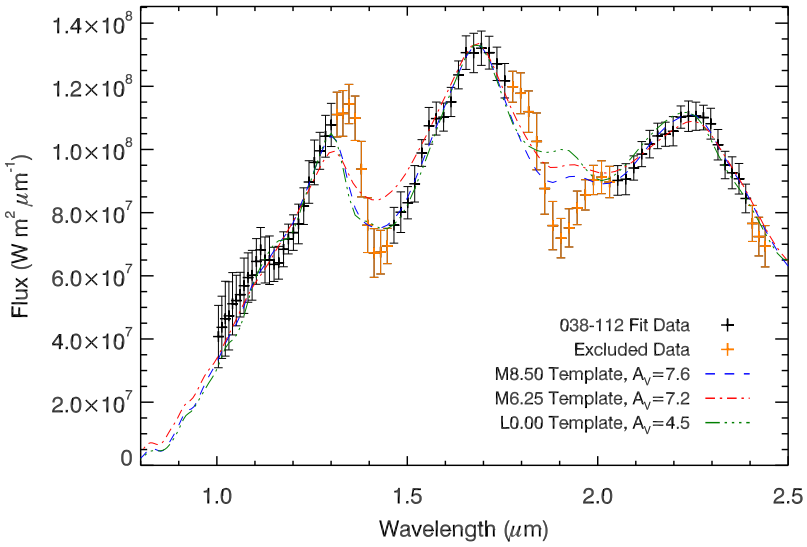

Figure 4.2: A range of fits are possible for object 038-112 whose spectrum has a relatively low S/N. The most-common fit is the M8.50 template, shown as the blue dashed line. The earliest and latest fits are shown as the red dash-dot and green dash-triple-dot lines.

The assignment of uncertainties and the confidence of the spectral fitting is affected by multiple factors, the most common being the S/N of the spectrum. As shown in Figure 4.2, the S/N of the spectrum as well as a truncation of the spectrum below 1.0 μm does not permit a precise determination of the spectral type. In this case, an ambiguity exists between having a later spectral type with a lower extinction and a earlier spectral type with higher extinction.

A similar effect can also occur due to the uncertainty in the wavelength calibration, as seen in Figure 4.3. Again, a bi-modal distribution in spectral classification is observed. In some cases, the uncertainty does not well represent the quality of the fit. This is primarily due to the spectrum of an object not matching one of the available spectral templates, as seen in Figure 4.4. In the case of 080-117 (upper plot of Figure 4.4) despite the relatively high S/N, the fit to the region below 1.1 μm is poor and the K band flux is slightly greater than the model. It is possible that this object is a background star. In the case of 095-059 (lower plot of Figure 4.4), significant variations from the best-

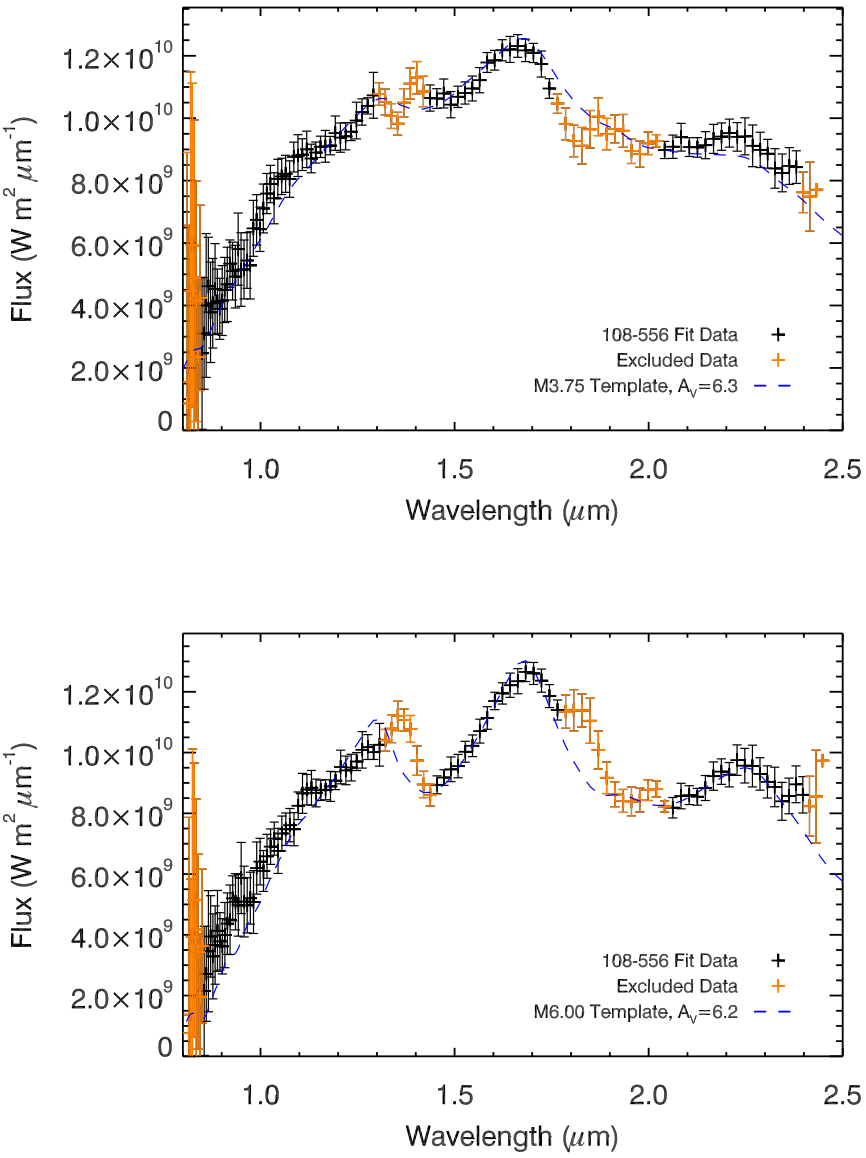

Figure 4.3: Two fits to the same object (108-556) where the uncertainty in the wavelength solution dominates the spectral typing uncertainty.

fitting spectral template are apparent in the *H* band, where the sharply peaked nature of cool young objects is not observed. In the case of object 111-532, the sharply peaked *H* band seen in the overplotted M6 template and typical in cool young objects, is not

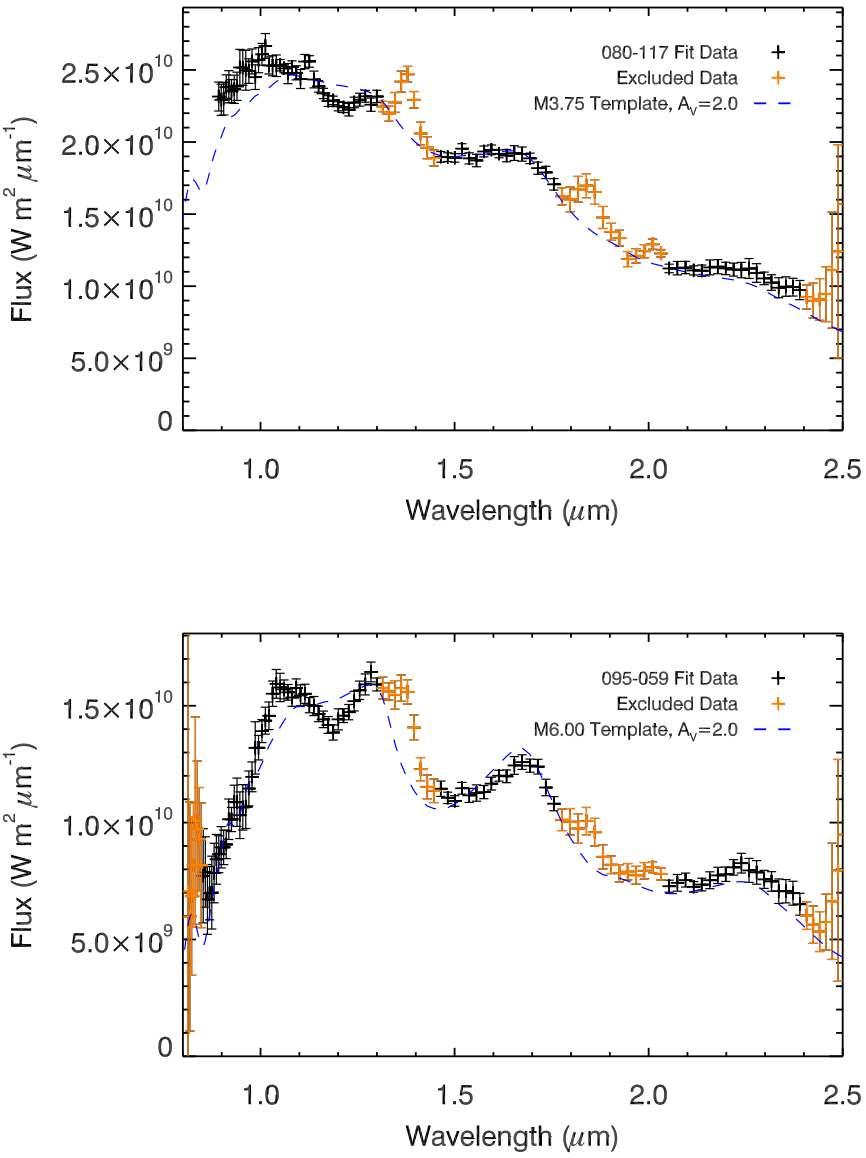

Figure 4.4: Objects 080-117 (upper plot) and 095-059 (lower plot) are examples of objects flagged as having a "Mediocre fit" in Table 4.II. These objects spectra exhibit variations from the spectra in our spectral library resulting in an uncertainty in the spectral type. Their assigned spectral type and uncertainty should be regarded as subject to unaccounted uncertainty.

observed to the same degree. Furthermore, the observed *K* band flux is greater than than the model, this could be due to hot dust surrounding the object. This excess flux would affect the assigned spectral type. In cases such as these, although the objects are assigned spectral types, they are flagged in Table 4.II as having a "Mediocre fit" and therefore their classifications should be regarded as suspect to unaccounted uncertainty. Analogous to the objects flagged as having mediocre fits are the objects indicated as possessing *J* band emission features. These spectral features, which are discussed at length in section 4.5.4, have uncertainty in their spectral classifications.

4.4.2 Comparison to Previous Observations

In total, 44 of our 104 objects have received previous spectral classification using a variety of techniques. The most comparable observations to our own are those of Lucas et al. (2001), whose spectra were reclassified by Weights et al. (2009). This group derived spectral types based on spectral indices calibrated using the same spectral templates used in this article, while their extinction values were determined based on their photometric colours (*J*-*H* and *I*-*J*). As a test to our reduction routine, Phillip Lucas kindly supplied us with reduced and dereddened spectra for his objects. Because his *H* and *K* band spectra were not observed simultaneously, the relative flux error between the bands was estimated to be $\sim$10%. For this reason the spectral bands have been fitted independently to our spectra for comparison. Figure 4.5 demonstrates the accuracy of our spectral reduction. The black line indicates the dereddened spectra of Lucas et al. (2001), whereas the blue line indicates the spectrum when Gaussian smoothed to the resolution of our observations. Our spectrum is represented by the red error bars. In all cases, our spectrum accurately reproduces the observations [6]. The relative flux error for objects 019-354 and 013-413 were measured to be 1% and 14% respectively. This is broadly consistent with the approximated relative flux error of Lucas et al. (2001). Object 055-230 exhibits a difference of 22%. However, as noted in Lucas et al. (2001), the *K*-signal was reduced by a cloud and hence most-likely explains the large discrepancy.

6. For this comparison, our spectra were dereddened using the method of Lucas et al. (2001), who employed the method of Cardelli et al. (1989) with R_V=5.5

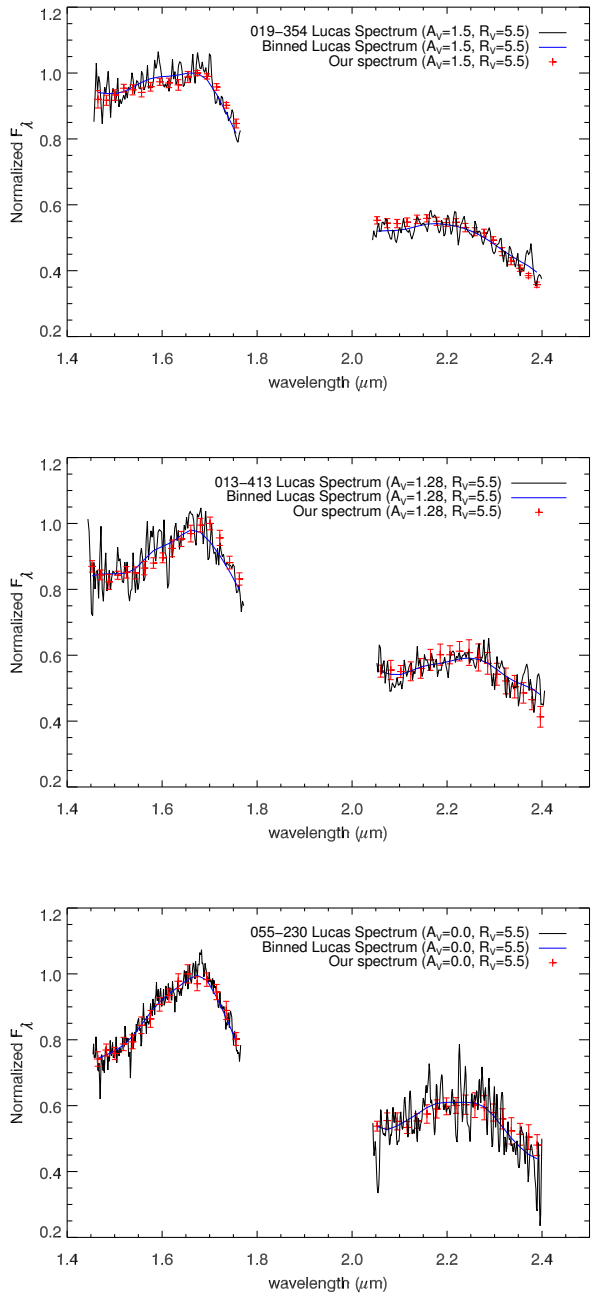

Figure 4.5: Comparison of our extracted spectra to the previously observed objects of Lucas et al. (2001) demonstrates the accuracy of our spectral reduction. In all cases, the reddening and reddening-law used by Lucas et al. (2001) was adopted for comparison.

In total, we observed 17 objects characterized by Weights et al. (2009). Of these, 11 are within the respective uncertainties, 2 objects differ by 0.5 and 2 sub types due to a difference in reddening values, 2 objects have a discrepant near-IR spectral type but consistent optical spectral type, two objects are inconsistent by 2-3 sub types. Every object exhibiting a conflicting classification is discussed in detail in Appendix A. All conflicting classifications have justification for their differences.

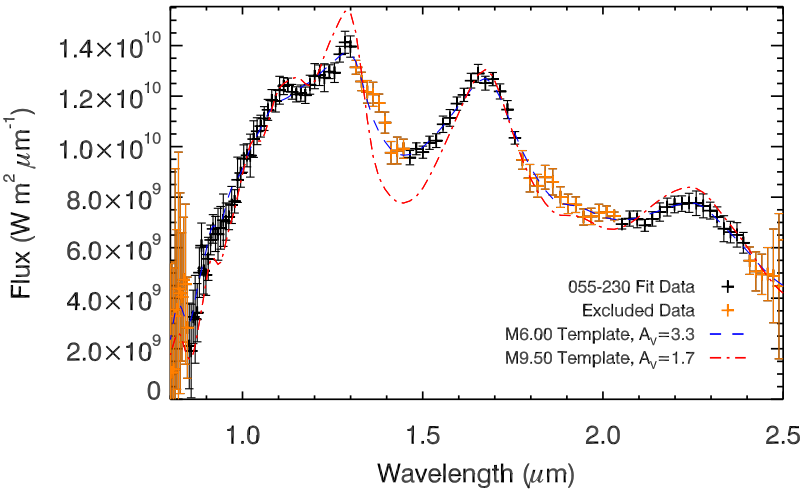

Figure 4.6: Comparison of the spectral classification of object 055-230 as performed by Weights et al. (2009) (M9.5, red dash-dot line) and this work (M6.0, blue dashed line). The observed spectrum of this object was also the subject of Figure 4.5 and shown to exhibit the same spectral shape in *H* and *K* bands as previous observations. This demonstrates the usefulness of SED fitting over large bandpasses.

One of the objects in slight disagreement is 055-230. This object is the lower plot in Figure 4.5 and is seen to match the previous observations of Lucas et al. (2001) very well. Based on this data, Weights et al. (2009) classified this object as >M9.5, with an associated extinction of A_V=1.72. Riddick et al. (2007a) classify the object using an optical spectrum as M6.5±1.5 with A_V=1.72. We classify the object as M6.0 with A_V=3.3. Figure 4.6 demonstrates the difference between the models and the observations for this object. The observed spectrum is an excellent match to the M6.00 spectral

template over the entire wavelength range. It has been suggested by Weights et al. (2009) that variability may explain the discrepancy. Object 077-452 exhibits a similar situation where our spectral classification is in agreement to the IR spectral classification but is discrepant from the optical value by 0.5 sub types. This may be due to the difference in the determined extinction.

Two objects, 052-323 and 066-650, are inconsistent with the classifications of Weights et al. (2009). Object 052-323 was loosely classified as "Early M," with A_V=0.25. Weights et al. (2009) assigned this classification for objects believed to be foreground or background stars. In this case, the object was classified as M3-M4.5 and was found to lie below the 50 Myr isochrone. Therefore, the object was deemed not to be a cluster member, in which case fitting young stellar templates may not be correct and henceforth the derived A_V is inaccurate. However, if classified as an M7.25 with A_V=0.3, the object lies directly on the 1 Myr isochrone and is consistent with being a cluster member [7].

The upper plot in Figure 4.7 demonstrates the difference in spectral shape between an early M (in this case M3.75) and a M7.25 object. Because the derived reddening value is known to be in question for objects assigned an early M classification, we allowed the reddening to float in order to obtain the best fit. Clearly, the M7.25 template provides the better fit to the observed spectrum. The other object with an inconsistent classification is 066-650. Using a single spectral index in the *H* band, Weights et al. (2009) classified this object as M6$\pm$0.75, with A_V=2.78, whereas we classified it as M3.75 with A_V=2.80. The lower plot in Figure 4.7 shows the differences between the two models and our spectrum. Because of the uncertainty of the extinction value associated with the M6.0 model, the extinction was left to float to obtain the best possible fit. The M3.75 model is clearly the better fit, especially to the 0.85-1.0 μm region of the spectrum. However, in the *J* band, there are small deviations from the model which may be attributed to hot gas either associated or in the vicinity of the object. This may have a slight effect on our derived spectral type.

Comparison to other previous classifications are discussed in detail in Appendix A. Of 56 previous spectral classifications, including the ones discussed above, 48 are in

7. Discussed further in section 4.6.2

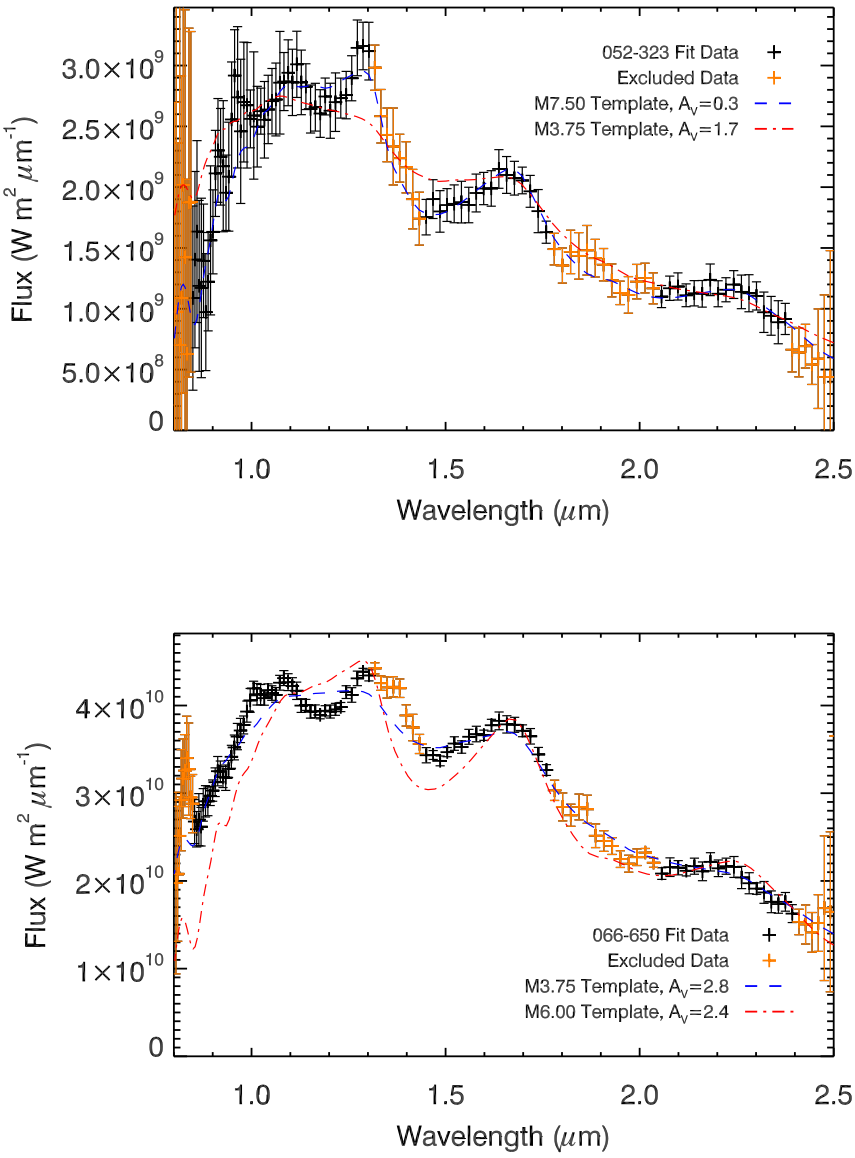

Figure 4.7: Comparison of the inconsistent spectral type classifications between our work and Weights et al. (2009). In both cases, the blue dashed line indicates the spectral template for our classification, whereas the red dash-dot-dash line indicates the spectral template associated with the previous classification.

agreement, 7 have a slight disagreement, and 2 are inconsistent. The comparisons are summarized in Table 4.IV.

4.5 Results

The results of our spectral classification method to our 104 objects is presented in Table 4.II. The table, ordered by increasing right ascension (RA), provides the reference to the observation summary, the observed and dereddened *H* band magnitudes, the most-common spectral classification with the latest and earliest types in sub- and super-script, as well as the associate reddening and other parameters derived for the object. The reader should be aware that the sub- and super-script values associated with the reddening, temperature and mass are not uncertainties. These values are the extinction, temperature and mass associated with the latest and earliest spectral type determinations. The "Notes" section provides information such as: if and where the spectrum is truncated, if mild nebulosity contamination is observed, if the object exhibits *J* band emission, a mediocre fit is observed, etc.

Due to the large number of observed spectra, only a subset of objects are plotted here, the remainder are available online. For ease of presentation, we group the subset of spectra into three spectral type (SpT) bins. As explained in section 4.6, assuming a cluster age of 1 Myr, our temperature scale as a function of spectral type, and the evolutionary models of Baraffe et al. (1998) and Chabrier (2003), the bins correspond to early M dwarfs (M1$\leqslant$SpT$<$M6), brown dwarfs (M6$\leqslant$SpT$\leqslant$M8.5), and free-floating planetary mass objects (PMOs, SpT$>$M8.5). A fourth bin is dedicated to objects showing *J* band emission features. The objects characterized as K dwarfs are not presented but can be viewed online. We emphasize that because the object is placed in one of these bins by its assigned spectral type does not confirm the object is indeed a Brown Dwarf or PMO.

4.5.1 Early M Dwarfs

In total, 59 of our 104 objects are classified as early M dwarfs, which we define as having a spectral type later than M1 and earlier than M6.00. A subsample of objects demonstrating the transition in the objects spectra is shown in Figure 4.8. The reddened template corresponding to most probable classification of the object is overlaid as a red solid line. Objects having later spectral types exhibit stronger absorption in the steam

bands which results in the H band spectrum becoming more peaked or triangular in shape. Although less obvious, the effect is similarly observed in the K band. Objects 064-208 and 045-604 exhibit features near 1.1 and 1.2 μm respectively, that deviate from the model. Analysis of the difference images showed no apparent nebulosity contamination, however one cannot be certain it is associated with the object. Numerous objects such as this one exhibit small deviations from the spectral templates but are not of sufficient significance to affect the spectral classification. Object 107-628 has been manually truncated due to possible contamination from another spectrum. A truncation or missing piece of the spectrum is particularly influential on the classification of early M dwarfs and late K dwarfs as the objects' spectra are relatively featureless. Furthermore, the difference in the slope of the SED can be partially compensated by changing the extinction value. For this reason, the spectral classification of K dwarfs and early M dwarfs are often less constrained or more ambiguous than later spectral type objects.

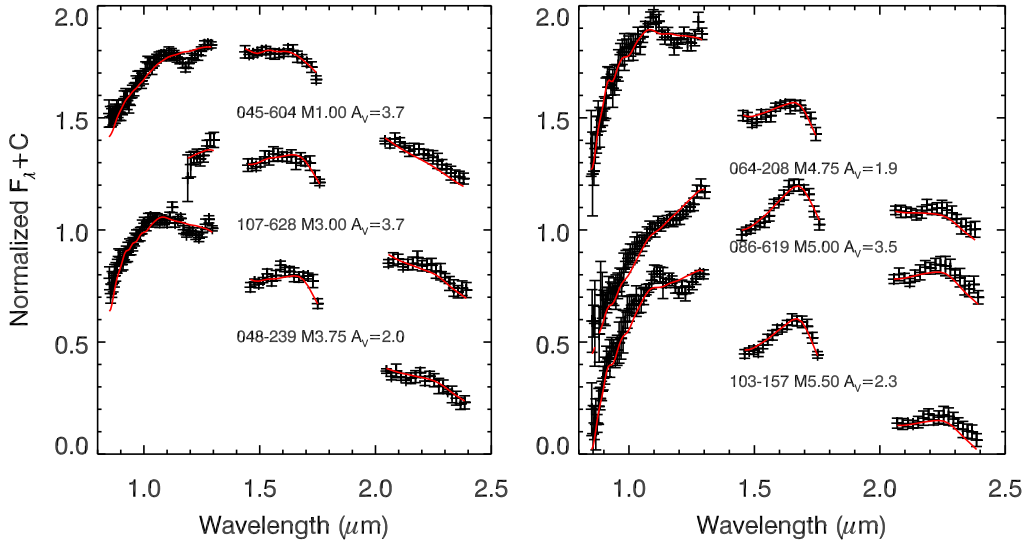

Figure 4.8: This shows a subset of the objects having spectral types between M1 and M5.75. This spectral range corresponds to the temperature range of M stars having a mass greater than the hydrogen burning limit assuming a cluster age of 1 Myr.

4.5.2 Brown Dwarf Candidates

The late-type M dwarf candidates offer stronger spectral characteristics and therefore do not suffer from the ambiguity between general slope of the SED and reddening. However, because the objects are often fainter, their S/N can be a limiting factor in their classification. Figure 4.9 shows the spectrum of numerous brown dwarf candidates. In total, we report the spectra of 33 objects ranging in spectral type from M6 to M8.5. Of these objects, 25 have been previously classified with spectral types equal to or later than M6. The 7 newly reported brown dwarfs have the ID numbers: 038-112, 052-323, 074-548, 084-401, 098-606, 099-339,126-426, 133-258. Objects 055-231 and 083-102 were previously classified as PMO's by Weights et al. (2009). These objects are discussed in detail in sections 4.4.2 and 4.A respectively. Object 052-323 was previously classified as an early M by Weights et al. (2009), as discussed in section 4.4.2.

The spectra of later-type (M6-M8.5) objects have an increased sharpness in the steam bands as well as a flattening of the spectra near 1.05 to 1.2 μm and a peak towards 1.3 μm. Another important characteristic and important constraint in spectral classification is the slope between 0.85 and 1.0 μm. Having high S/N in this region offers a strong constraint on the objects reddening. Furthermore, due to the high number of pixels in this region and the void of telluric features, it is relatively insensitive to uncertainty introduced by having an imperfect wavelength solution. Objects 126-426 and 081-536 show small variations from the template spectrum, most likely due to nebulosity contamination, however this does not affect the classification. Object 092-605 has large parts of the H and K band spectrum removed due to bad pixels, however the sharp features in the J band spectrum still provide adequate spectral coverage to yield a good spectral classification. Object 099-339 is an example of an object that upon examination of the differences images, appears to exhibit contamination from nebulosity that is not associated with the object. Fitting the nebulosity spectrum that was extracted with the spectrum was not successful and only degraded the quality of the spectrum. Therefore, the nebulosity contamination was left in the spectrum but noted in Table 4.II as a mediocre fit due to the mis-match of the sloping section below 1.0 μm.

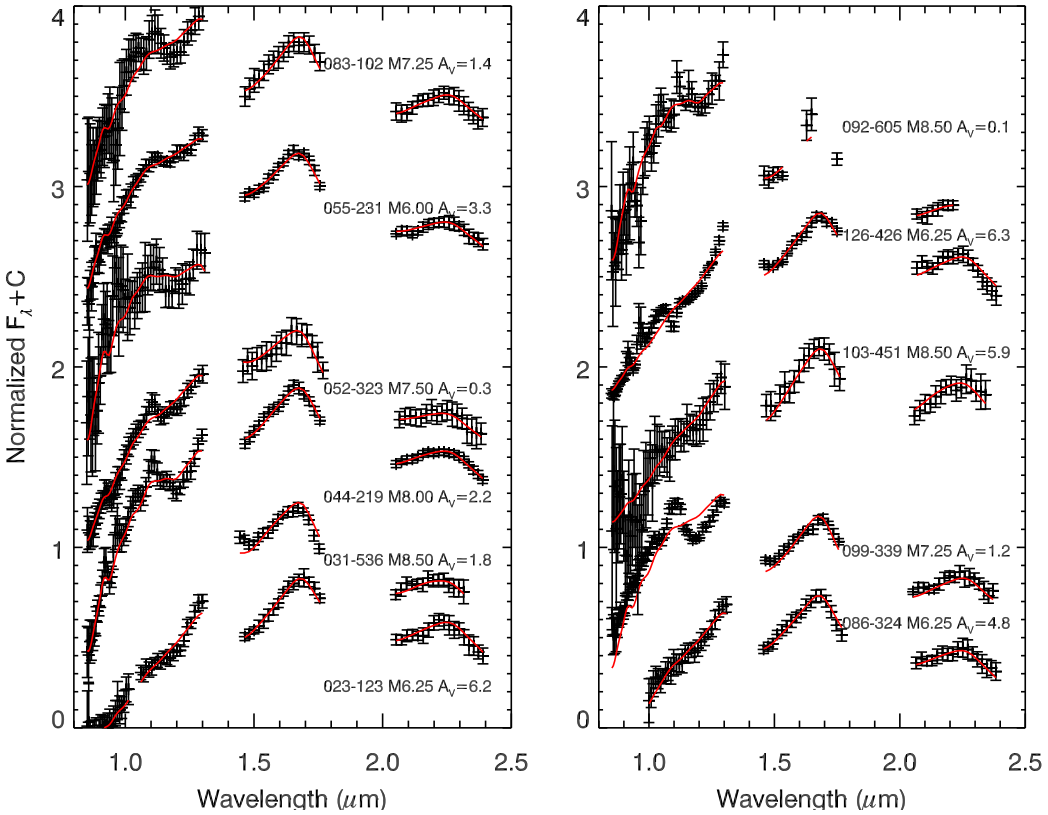

Figure 4.9: This is a subsample of the objects having a spectral classification between M6 and M8.5. This corresponds to the temperature range for brown dwarfs when an age of 1 Myr is assumed. The red line indicates the best fitting spectral template (shown in the label) to the observed spectra.

4.5.3 PMO Candidates

In total, 9 objects were characterized as having a spectral type greater than M8.5, 4 of which (012-524, 064-315, 100-531, 129-105) are newly discovered. Four others (015-319, 037-627, 077-127, 100-501) have been previously characterized (spectroscopically) as having a spectral type consistent with M8.75 or later. One other object (075-146) was proposed as a PMO candidate with a *K* band excess by Lucas et al. (2001) using photometry alone but not spectroscopically confirmed. Although still slightly uncertain due to a low S/N spectrum, our classification of M9.5 with A_V=1.0 is very consistent with their hypothesis. The extracted spectrum is plotted in Figure 4.10 along with the

other eight candidates.

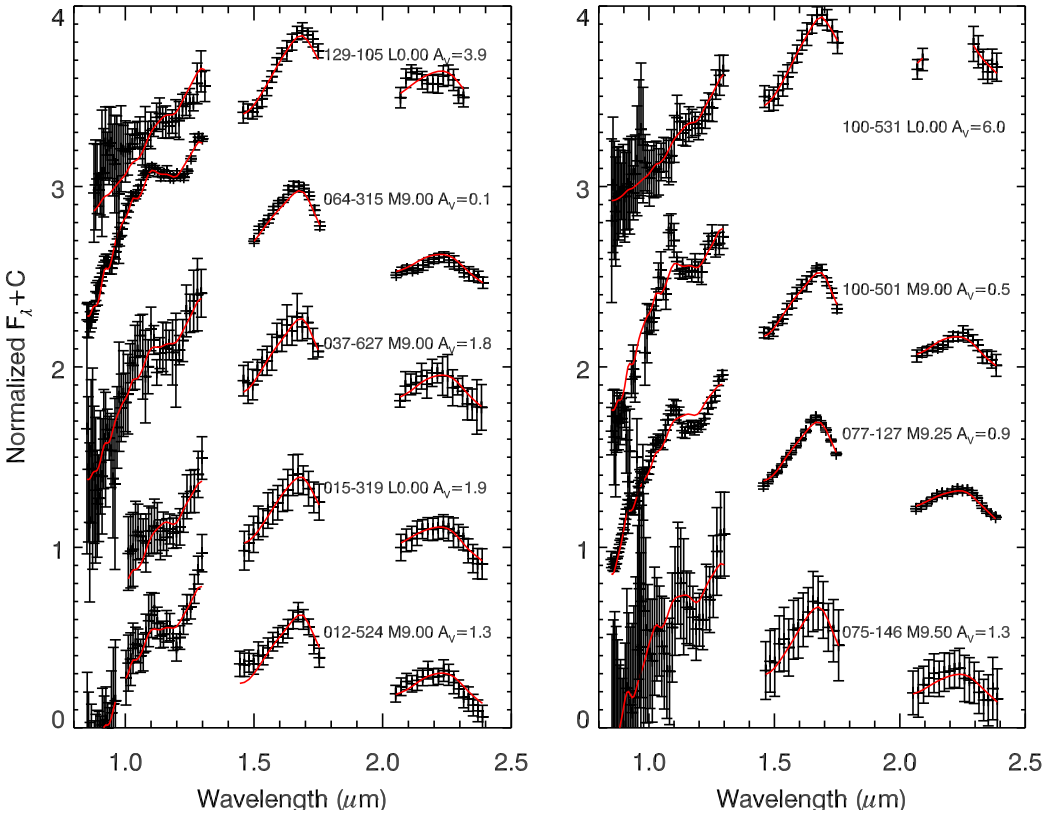

Figure 4.10: Spectra of all objects with spectral classifications greater than M8.75. This corresponds to the temperature range for objects in the planetary mass regime (M<13M_J) assuming an age of 1 Myr. The red solid line indicates the best fitting spectral template (shown in the label) to the observed spectra.

The low S/N of numerous targets is partially due to the poor weather when performing the observations of the faint targets. This often reduces the accuracy of their spectral classification. Notable exceptions include the objects of 077-127, and 064-315. Although both exhibit excellent fits, they are anomalously bright for being PMO's with an age of 1 Myr. This is also the case for objects 129-105 and 100-501. This characteristic is discussed further in section 4.6. The characterization of 129-105 is also slightly uncertain as it does suffer from nebulosity contamination and has been fitted using its associated nebulosity spectrum. There is also evidence of uncorrected *K* band contamination. This object does exhibit an excellent fit in the *H* band and for this reason is

included in this article.

4.5.4 Objects Exhibiting *J* Band Emission Features

When fitting our spectral templates, 12 objects exhibited spectral features resembling emission lines that affect the spectral characterization. In all of these cases, the feature appears to originate from the object, showing the same profile (PSF) as the spectrum (in the spatial direction). The features do not resemble nebulosity contamination, which generally exhibits a different structure, however, we cannot rule out this possibility completely. Figure 4.11 shows the spectra of 11 objects that exhibit *J* band emission features. In general, the templates still provide reasonable fits to the data. However, the determined spectral classification and associated uncertainty may not be an accurate representation of the objects true spectral type. Object 019-354, previously observed by Lucas et al. (2001) and used as a spectral comparison in Figure 4.5 (top), shows significant deviation from the spectral type template determined in this paper and by Weights et al. (2009). The derived reddening values are also subject to significant uncertainty. This is also true of the value derived in previous works that rely on *J* band colour to estimate the reddening. The fact that so many of our objects ($\sim$10%) exhibit these types of features enforces the argument that multi-wavelength spectroscopy is necessary to characterize young objects and values derived using photometry are subject to large uncertainties.

The origin of the spectral features is most likely hot gas surrounding the objects. Our low spectral resolution makes identifying the spectral lines very difficult. However, they may be associated to the Paschen series of hydrogen lines (e.g. Paβ at 1.28 μm). The feature at 1.3 μm is particularly problematic as a similar feature is seen in objects having spectral types later than $\sim$M6. The relative strength of the features is object dependent. Objects like 013-413 show two narrow features, whereas numerous other objects (e.g. 057-354, 021-636, 019-354) appear to show multiple overlapping features. Object 012-145 is unique in the fact that only the 1.3 μm feature is observed. There also appears to be no trend towards earlier or later spectral types exhibiting the features as spectral types varying from $\sim$M1 to M8.25 are observed. The objects exhibiting *J* band

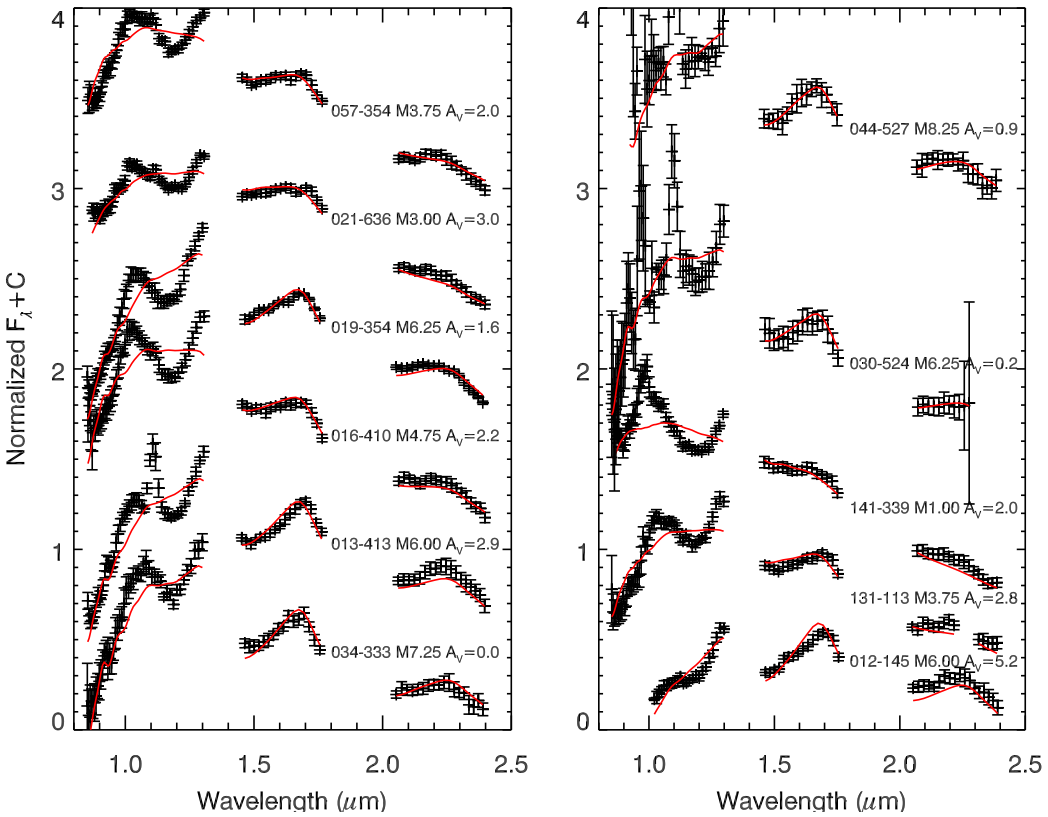

Figure 4.11: Objects showing *J* band emission features that influence the spectral classification. In all cases, the emission appears to originate from the actual object and not from adjacent nebular contamination. The red line indicates the best fitting spectral template (shown in the label) to the observed spectra.

emission are primarily in the darker regions of the observed fields, where there is more extinction. This is consistent with the measured extinction values of the objects (A_V>2). Objects 131-113 and 141-339 are found in the brighter regions of the nebula and appear to be associated with gas filaments. These objects clearly warrant further observations to determine their nature.

4.6 Discussion

In order to determine ages and masses for the objects, a temperature scale must be established to match each spectral type with a given temperature. Because we have opted to use young spectral templates rather than synthetic spectra (which have asso-

ciated temperatures), temperatures must be established using spectral characteristics of the template spectra. For this, we adopt the temperature scale defined in Luhman et al. (2003), which designates temperatures for the spectral templates ranging from M3-M9. Because our spectral library extends outside this range, we have adopted temperatures of standard dwarfs for spectral types earlier than M3 (Cox 2000) following the the advice of Kevin Luhman (personal communication). In the case of our L0 dwarf template, we adopt the temperature of 2000K determined by Kirkpatrick et al. (2006). The temperature scale is given in Table 4.III. The temperatures for the intermediate spectral types were determined using linear interpolation. Combining the temperature scale with evolutionary models allows the creation of an Hertzsprung-Russell (HR) diagram.

Table 4.III: Adopted Temperature Scale

Spectral Type	Temperature (K)
K0.00	5240
K2.00	5010
K4.00	4560
K5.00	4340
K7.00	4040
M1.00	3680
M2.00	3530
M3.00	3415
M4.00	3270
M5.00	3125
M6.00	2990
M7.00	2880
M8.00	2710
M9.00	2400
L0.00	2000

4.6.1 HR Diagram

Figure 4.12 presents the dereddened H band HR diagram of all of our classified objects. We use the H band magnitude rather than the bolometric luminosity to avoid any uncertainty associated with the correction. Although bolometric corrections exist for evolved field dwarfs (Leggett et al. 1996, 2002), there currently exists no bolometric correction for younger objects. Furthermore, the corrections are given with respect to the K band magnitudes. The four overplotted isochrones are composed of multiple evolutionary models. Although atmospheric models struggle to provide accurate fits to young

objects, the evolutionary models provide a relatively good agreement to observed data (Luhman et al. 2003). Temperatures greater than 3000K are represented by the models of Baraffe et al. (1998). At temperatures between 2300 to 3000K, the evolutionary models of Chabrier et al. (2000) are used in order to include the effects of dust opacity. Below 2300K, the evolutionary of Baraffe et al. (2003) models are utilized to include the effects of condensation. The *H* band magnitudes of all models were converted from CIT colours into 2MASS colours using transformations derived using the 2MASS final data release [8]. A cluster distance of 414 pc (Menten et al. 2007) was assumed for calculating apparent *H* band magnitudes for the models. The mass for each object is derived using the determined temperature and assuming an age of 1 Myr for every object; all values are reported in Table 4.II.

Over our entire spectral range, the 1 Myr isochrone provides a good fit to the data. This result further strengthens previous studies conclusions of the clusters age. Due to the uncertainty associated with the spectral type and temperature scale, some scatter in the HR diagram is to be expected. Binary stars having equal spectral types would create a significant increase in flux, making the object appear brighter (-0.75 mags) whereas binaries with different spectral types may produce a mediocre fit due to the convolution of the two spectra. However, the binary fraction has been measured to be relatively low ($\sim$15%, Padgett et al. 1997) and approximately half of these binaries are expected to be separated by more than $0.5''$ and would therefore be distinguishable by an elongated PSF. Another effect that could introduce an error in the spectral classification is veiling of the steam bands due to flux from warm circumstellar dust. This would bias the classification and result in an earlier spectral type being assigned, resulting in an overestimate of the temperature and hence an older age. Due to the low resolution and modest S/N of our spectra, the presence of veiling cannot be accurately detected.

Contrary to the result of Slesnick et al. (2004), who observed two populations of varying age ($\lesssim$1 Myr and $\sim$10 Myr), we observe no significant bifurcation in the HR diagram. Eleven objects lie on or below the 5 Myr isochrone, four of which are within uncertainty of the 1 Myr isochrone. Two objects, 044-527 and 030-524, exhibit *J* band

8. http://www.astro.caltech.edu/$\sim$jmc/2mass/v3/transformations/

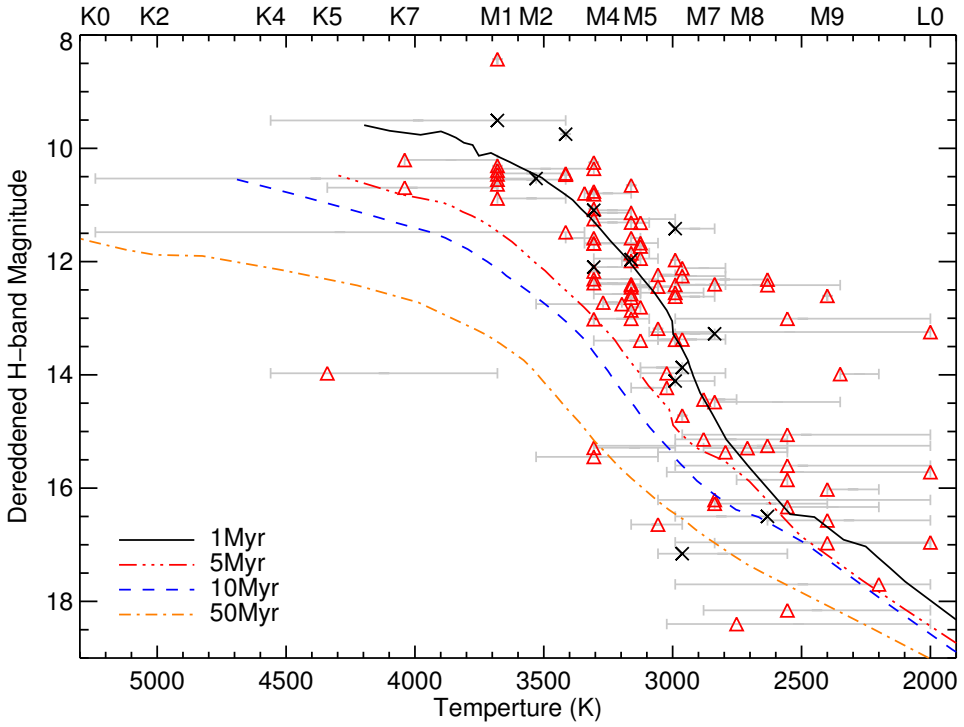

Figure 4.12: HR diagram of all of classified objects. Objects exhibiting *J* band emission features (that potentially jeopardize the spectral characterization) are indicated by a black '×'. The solid, triple-dot-dash, dashed, and long-short-dashed lines represent evolutionary models for cluster ages of 1, 5, 10 and 50 Myr respectively.

emission features and are therefore subject to uncertainty in their classification. Object 044-123, located at an x-y coordinate of (T_{eff}=4340, $m_{H_{dr}}$=14.0) in Figure 4.12, is most certainly a highly absorbed background star whereas objects 057-315 (located at 3057, 16.6) and 081-118 (located at 3306, 15.4) are believed to be foreground field dwarfs (discussed in section 4.6.2). Object 136-121, located at the x-y coordinate of (3306, 13.0) in Figure 4.12, is flagged as a mediocre fit due to nebulosity contamination. It is possible that the object possesses *J* band emission features, however, evidence for this is not sufficiently clear to be flagged as such. Object 041-210 is anomalous. Located at an x-y coordinate of (3306, 15.2) in Figure 4.12, this object exhibits large reddening ($A_V = 5.7$) and is a good fit to the low gravity templates, however its placement on the HR diagram indicates that it is possibly a background star. More data is required to

precisely determine the nature of this object.

Numerous objects in the HR diagram are observed to be significantly (>1 mag) brighter than what is expected of 1 Myr objects. This behaviour has been observed by multiple studies (Peterson et al. 2008; Riddick et al. 2007a; Rio et al. 2012; Slesnick et al. 2004; Weights et al. 2009) and has been used to suggest that numerous objects exist with ages significantly less than 1 Myr. These low-surface gravity objects could have deeper water bands for a given temperature than the 1-2 Myr objects included in our spectral template library. This would result in the object being biased towards later spectral types, and hence appearing to the right of the 1 Myr isochrone. Another possibility is that they are foreground stars. Due to the uncertainty in our spectral classification, many of the objects significantly brighter than the 1 Myr isochrone may be explained due to its uncertainty in its spectral type. However, two objects in the PMO regime lie well above (>2 mags) the 1 Myr isochrone and are very well constrained. Object 077-127, located at an x-y position of (2350, 14.1) on the HR diagram (Figure 4.12), is plotted in Figure 4.10 and shows an excellent fit to the M9.25 template. Furthermore, its reddening value of $A_V = 0.9$ suggests that it is associated with the cluster. Object 064-315, located at an x-y position of (2400, 12.75) in Figure 4.12, has a smaller reddening $A_V = 0.1$ and therefore has a higher probability of being a foreground field dwarf. To better determine if the objects are indeed foreground objects, M3.5-L5 field dwarfs have been fitted using the same Monte-Carlo technique described above, but with the reddening value fixed to zero. Figure 4.13 shows the extracted spectra overplotted with the best fitting low gravity template (blue dashed line) and field dwarf (red dash-dot line). Clearly, the low-gravity templates are the superior fit and these objects are not high-gravity foreground dwarfs. However, due to their luminosity, being classified as a PMO is most likely incorrect. We suspect that the objects are most likely very young ($\ll$1 Myr) brown dwarfs, therefore the derived masses reported in Table 4.II are most likely underestimated.

4.6.2 Cluster Membership

One of the most challenging aspects of performing IMF studies in clusters is assessing if an object is indeed a cluster member. Indicators of membership for objects in the

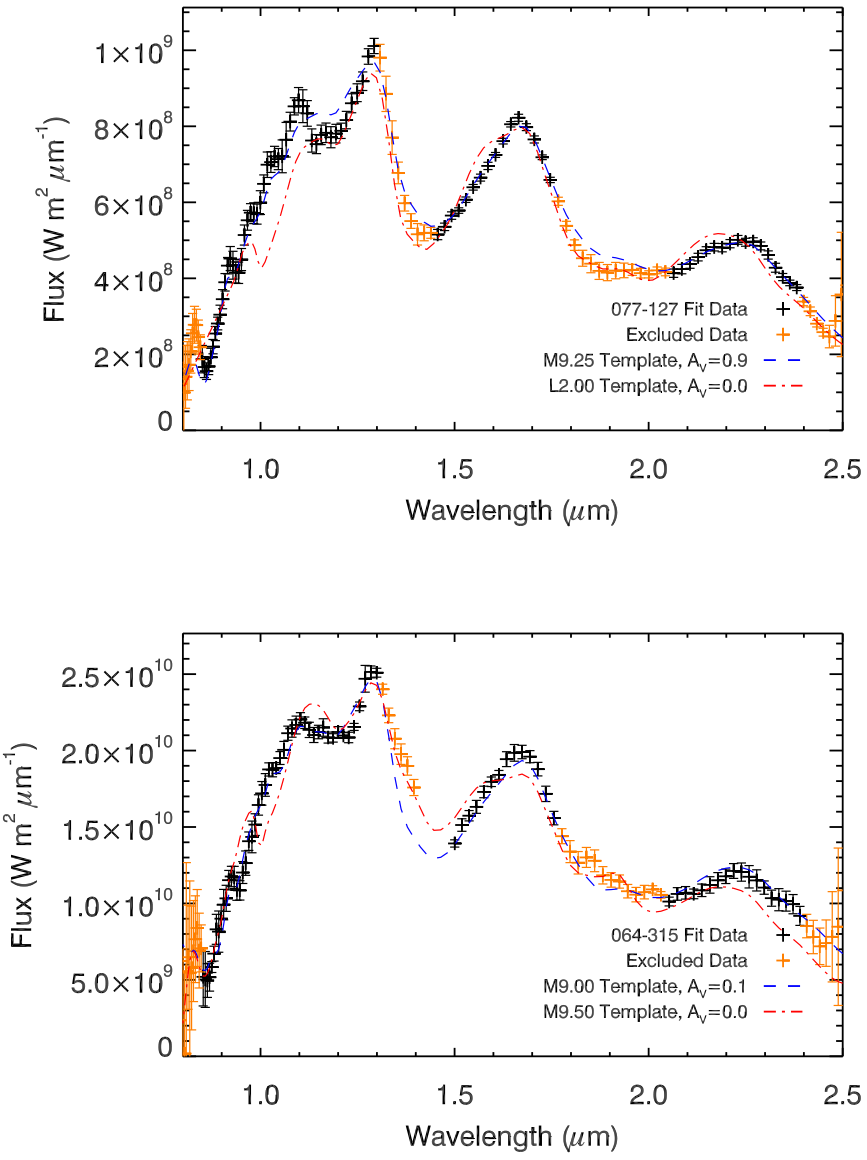

Figure 4.13: Comparison of objects 077-127 and 064-315 to the best fitting low gravity spectral template (dashed blue line) and a high gravity synthetic spectrum (red dash-dot line) indicative of a foreground field dwarf.

OMC include signatures of youth such as the presence of low-gravity spectral features. Another indicator of membership is the presence of extinction. Due to the low resolution

of our spectra, detecting individual absorption lines or narrow bands is not possible. Furthermore, objects with spectral types earlier than M3 are classified using spectra of field dwarfs, therefore the only information that provides evidence of possible membership is the presence of reddening. Nearly all objects exhibit significant reddening ($A_V \geqslant 1$) and we observe no objects earlier than M3 without reddening. For objects later than M3, we examine the possibility of each object being a field dwarf by fitting the spectra of M3.5-L5 field dwarfs to our objects with the reddening value fixed at $A_V = 0$.

No objects can be classified as foreground field dwarfs with absolute certainty. However, based on our analysis, two objects (081-118 and 057-315), are likely to be foreground field dwarfs. Due to their low S/N spectra, both high-gravity field dwarfs and our low-gravity templates yielded statistically comparable fits. However, due to their location on the HR diagram being under-luminous of the 1 Myr isochrone (discussed in section 4.6.1), they are believed to be field dwarfs. The small number of observed field dwarfs is expected. Lucas et al. (2006) calculates a possible field dwarf contamination of $\sim$1-3 objects, including unresolved binaries, between M6 and L5 over his 26 arcmin^2 field of view. As our survey covers 18 arcmin^2, we expect to observe $\sim$1-2 contaminants. With the exception of the objects discussed below which are inconclusive, all of our objects spectra are consistent with being cluster members.

Objects 077-452 and 016-534, shown in Figure 4.14, are inconclusive despite having high S/N spectra. In both cases, the low-gravity template spectrum provides slightly better fit using our fitting statistic. However, the fits are comparable for both templates. Object 016-534 exhibits *J* band features that are not well fitted by young template nor evolved field dwarfs. This is probably indicative of a young object since an older evolved field dwarf would not be expected to show large variations from the template. Moreover, the object is only $\sim$0.5 magnitudes under-luminous of the 1 Myr isochrone which indicates its youth. In the case of object 077-452, the only difference between the templates is a small region between 0.9-1.1 μm. Because this region of the spectrum often presents *J* band emission features that may arise due to nebulosity contamination and this object appears in a filamentary region of the nebulosity, we cannot be certain that this is in fact a young object from our spectral comparison. However, the placement on the HR diagram

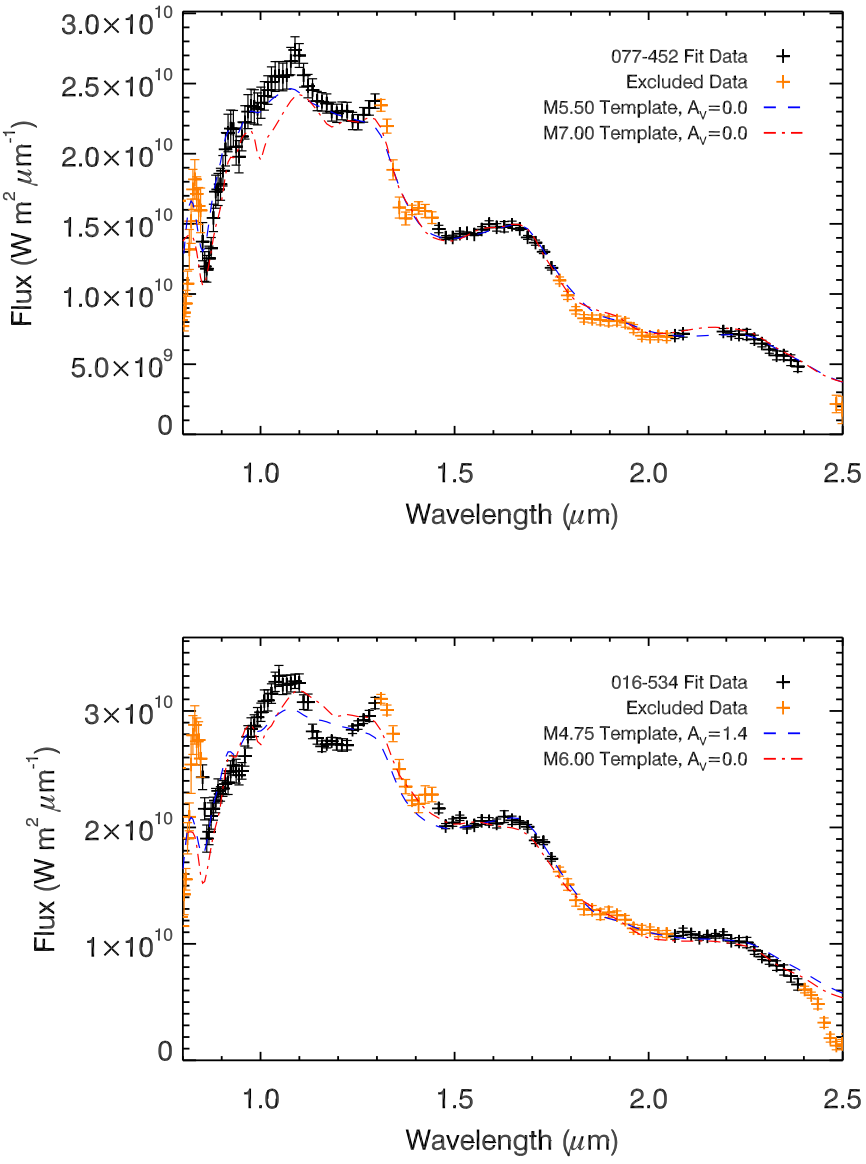

Figure 4.14: Comparison of object 077-452 and 016-534 to the best fitting low gravity spectral template (dashed blue line) and a high gravity synthetic spectrum (red dash-dot line) indicative of a foreground field dwarf. Because both objects are generally well fitted by both low-gravity objects and field dwarfs, their membership to the cluster is uncertain.

is under-luminous of the 1 Myr isochrone by only 0.5 magnitudes when classified as M5.5 using the low-gravity templates which indicates youth. However, the *I*-*J* colours measured by Lucas et al. (2001) are consistent with an M6V field dwarf located at a distance of $\sim$50 pc. For both 077-452 and 016-534, a confident differentiation between a foreground field dwarf and a low-gravity cluster member requires a higher resolution spectrum. For seven other objects, the possibility of being a foreground field dwarf using the spectral comparison alone cannot be excluded due to the spectra having insufficient S/N. However, their positions on the HR diagram are consistent with being 1 Myr objects. These objects are: 015-319, 037-627, 052-323, 075-146, 084-401, 098-606, 130-053.

4.7 Determination of the IMF

An accurate determination of the IMF requires a classification for all sources in the field. Using SExtractor, we have derived aperture photometry of the 346 point sources contained in both fields. The zero point calibration was performed using all available 2MASS sources indicated to have high photometric quality. The derived photometry was used to determine the *H*-band luminosity function shown in Figure 4.15, where the black line indicates the photometry for all sources with the exception of the objects determined to be foreground field dwarfs (057-315 and 081-118). The double-peaked luminosity function is consistent with the findings of previous studies of the central regions of the Trapezium Cluster (Lucas et al. 2005, and references therein); the stellar peaks occurring at H$\sim$13 and H$\sim$17 are thought to consist of young brown dwarfs and background contamination.

However, as discussed in section 4.6.1, Slesnick et al. (2004) report a bifurcation in the HR diagram indicating that two different epochs of star formation may have occurred (at 1 and 10 Myrs) which may also explain the bimodality of the luminosity function. Weights et al. (2009) explored this possibility by attempting to reproduce the observed luminosity function using simulations, where various age distributions and IMF slopes were considered. The authors concluded that the luminosity function is best reproduced

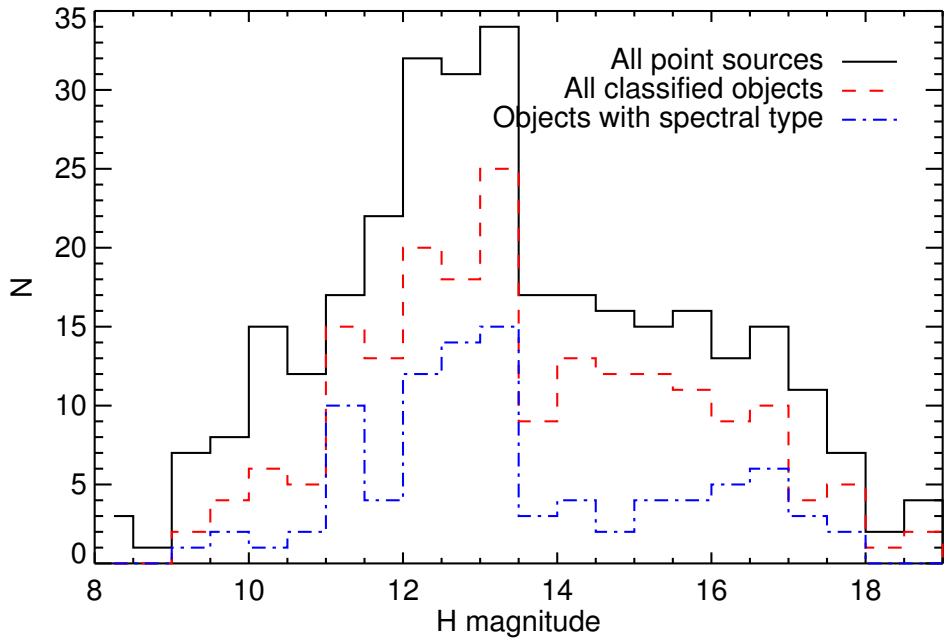

Figure 4.15: The H-band luminosity function of our survey. The solid black line indicates all point sources in the field. The blue dot-dashed line indicates all objects for which we have assigned a spectral type. The red dashed line indicates all objects for which we have a spectral type or have been spectroscopically determined to either have high extinction (A_V>8) or to be non-stellar.

with a mean cluster age of 1 Myr and a IMF of the form M^{α}, where α is either 0.31 or 0.60. Both the results of Weights et al. (2009) and our 1 Myr age estimate derived using our HR diagram in Figure 4.12, suggest that deriving masses assuming a cluster age of 1 Myr is reasonable.

Where previous studies suffered from an inability to accurately discern contaminating sources from actual cluster members (Lucas & Roche 2000; Lucas et al. 2005; Luhman et al. 2000; Slesnick et al. 2004), our spectroscopic observations of 259 point sources in the field allows us to better quantify this contamination in order to achieve a more accurate IMF determination. Of the 259 total spectra, 104 were assigned spectral types. These objects, excluding the identified foreground dwarfs and object 044-123 which was determined to be a background star, are indicated by the blue dashed line in Figure 4.15. Of the 155 remaining spectra, 41 had either inadequate S/N or had their

spectrum corrupted by field crowding or nebulosity. Therefore, no conclusion can be made regarding their origin and they have received no classification and are treated as unobserved objects throughout the analysis. For 107 objects, no spectral type can be assigned due to the objects exhibiting very large absorption (A_V>8). The high absorption leaves an obvious spectral signature where a rapid increase in flux towards longer wavelengths is observed. Some of these objects may be dust-enshrouded protostars, however, the majority are most-likely background stars. The remaining 7 spectra show only emission lines and no continuum, indicating that they are non-stellar or are still deeply enshrouded in an envelope of gas. The red dot-dashed line in Figure 4.15 includes the 7 non-stellar sources, the 107 highly absorbed sources and the 101 spectral-typed objects (already shown in blue). The relative differences between the black and red curves indicates the number objects for which we have no information and provides a measurement of the completeness of our spectroscopic study as a function of magnitude. The relative difference between the blue and red curves indicates the amount of contamination in each magnitude bin. As suggested by previous studies, the ratio of contaminants is significantly increased for fainter objects. However, our luminosity function suggests that $\sim$30% of sources in the stellar peak (H$\sim$13) are also contaminants that should not be included in the IMF calculation.

To derive the IMF, we perform a Monte-Carlo simulation using 1000 trials. For each individual trial, a spectral type for each object is randomly assigned using its distribution of solutions determined using the procedure described in section 4.4.1. Temperatures are then assigned based on the relationship shown in Table 4.III and masses are derived following the method described in section 4.6.1. The 101 objects are then assembled into equally spaced mass bins. This procedure is performed 1000 times and the median value and standard deviation of each mass bin are then calculated to obtain an IMF and its associated uncertainties. A completeness correction is performed in a similar manner.

To determine the number objects required to compensate for our completeness, we subtract the number of characterized objects (the dashed-red curve in Figure 4.15) from the total number of objects in each magnitude bin of the luminosity function (shown in black). Because our objects were selected based on their H-band magnitude alone, we

do not expect any observational bias favouring specific object types (e.g. background or cluster members) to be present. Therefore, the ratio between the number of targets determined to be cluster members and assigned a spectral type (shown as the blue curve in Figure 4.15), to the number of objects who have been classified as background or non-stellar objects (shown in red), should be constant throughout the individual magnitude bin. Based on this ratio, we calculate the number of objects from each bin that must be added to the IMF. Selecting the spectral type for these objects is completed using a 1000 trial Monte-Carlo simulation similar to the one described in the previous paragraph but where the spectral type is randomly selected based on all of the distributions of solutions for all targets grouped in a single magnitude bin. This correction and its associated uncertainties for each mass bin are then added to the non-corrected IMF to produce a completeness-corrected IMF[9]. The resulting IMF is shown as the black dotted line in Figure 4.16.

Whereas the form of the mass function for stars of medium to high masses (M $> 1\ M_{\odot}$) is primarily represented as a power-law, the functional form is observed to deviate at lower masses. For this study, we utilize the log-normal distribution presented by Chabrier (2003), where the number of objects per mass bin (ξ) is given by $\xi \propto e^{-(\log m - \log m_c)^2/2\sigma^2}$. The coefficient m_c represents the characteristic mass where the dominant term in the distribution shifts from a power-law to a normal distribution. Using this analytical form, Chabrier (2003) determine the IMF of the galactic disk, shown as the orange dashed line in Figure 4.16, to have an $\log m_c$ and σ of -1.102 and 0.69 respectively. However, this assumes no unresolved binary systems were present in the measurements. After accounting for unresolved binary systems, where $\sim$30% of M dwarfs were assumed to have an M-dwarf companion and $\sim$20% have a BD companion, the Chabrier (2003) fit to the galactic disk's "System IMF" results in the $\log m_c$ and σ coefficients to be -0.658 and 0.57, respectively. The majority of IMF determinations in young clusters have IMF forms that are well represented by the log-normal distribution with a $\sigma \sim 0.5$ and a $\log m_c \lesssim -0.69$ (Luhman 2012, and references therein). As our study does not account for binary systems or multiplicity and no correction for stellar

9. As we are working with discrete values, the uncertainties are rounded up to the nearest whole value.

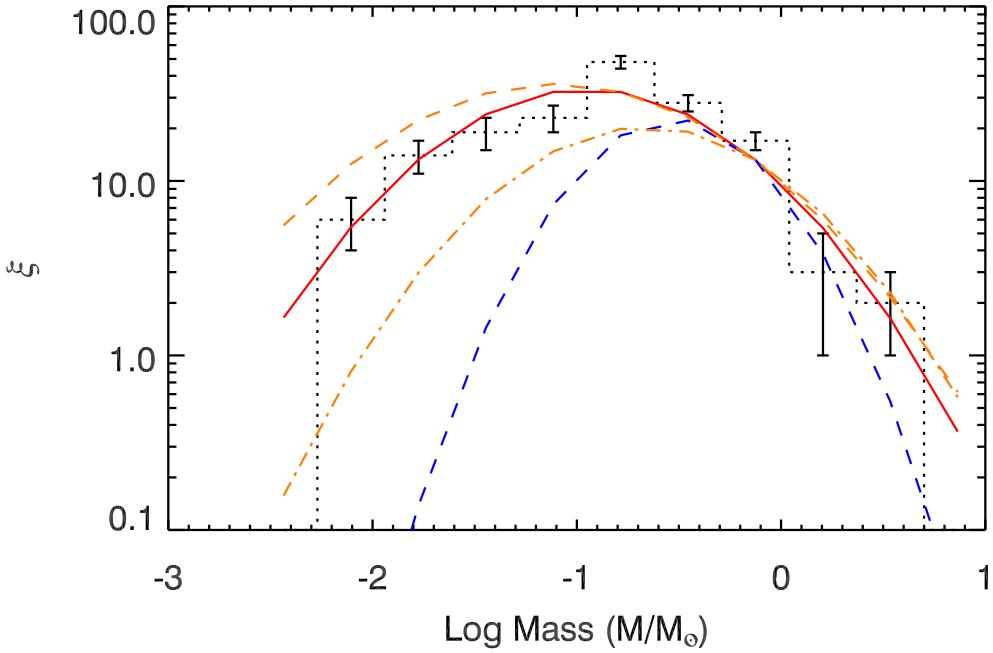

Figure 4.16: The IMF derived from our survey. The red solid line indicates our best fit of a log-normal distribution to the corrected data. The dashed and dot-dashed orange lines represent the Chabrier (2003) IMF and system IMF respectively. The dashed blue line represents the IMF fit derived by Rio et al. (2012).

evolution has been applied, our data represents a "system" mass function rather than a pure, "Initial mass function." Clearly, due to the young age of the cluster, little evolution has occurred. Furthermore, the multiplicity fraction in Orion ($\sim$15%, Padgett et al. 1997) is significantly lower than what is observed in the galactic disk and hence one would expect the characteristic mass and the width of the log-normal functional form of the IMF in Orion to lie between the disk IMF and disk system IMF values (Luhman 2012, and references therein).

To determine the coefficients and their associated uncertainties of the log-normal functional form using our data, we performed a 1000 trial Monte-Carlo simulation where each datapoint was randomly assigned a value using a normal distribution whose width was equal to the data points' uncertainty. The best fitting log-normal function to our

derived IMF (shown as the red solid line in Figure 4.16) was determined to have $\log m_c$ and σ of -0.89$\pm$0.04 and 0.57$\pm$0.03. These values lay within the coefficients determined for the galactic disk IMF and the coefficient values obtained in other young clusters (Luhman 2012, and references therein).

We do not observe the sharp falloff, shown as the blue dashed-line in Figure 4.16, determined by Rio et al. (2012), who measure the $\log m_c$ and σ coefficients to be -0.53$\pm$0.02 and 0.39 $\pm$0.03, respectively, when including all of their observed targets. The authors attribute the difference to the measurements of Slesnick et al. (2004), who observe a flattening similar to our observations but do not fit a functional form, to an inaccurate measurement of the background contamination. As mentioned above, our luminosity function demonstrates that contamination from background stars is apparent in all magnitude bins and therefore agree with Rio et al. (2012) that previous works have not adequately compensated for such effects. One distinct difference between our work and that of Rio et al. (2012) is the mass range. Their mass range extends from approximately 0.035 to 1.4 $M_{\odot}$ whereas ours covers their mass range and extends down to $\sim$0.006 $M_{\odot}$. If we truncate our IMF at the limit of their survey, the fitted $\log m_c$ and σ values are -0.79$\pm$0.04 and 0.50$\pm$0.04 respectively. This significant decrease in the width value approaches their derived value suggesting the steep decline is an observational bias. The difference in characteristic mass can be partially attributed to our respective differences in the adopted temperature-mass relationships.

4.8 Conclusion

Using low resolution, multi-band (0.85-2.4 μm) multi-object spectroscopy, 104 objects towards the central region of the Orion Nebular Cluster have been characterized including 7 new brown dwarfs, and 4 new planetary mass candidates. These objects have been characterized using well studied and previously discovered young standards from other nearby associations. Our analysis demonstrates the requirement for an accurate determination of reddening, and that numerous objects exhibit J band emission features. This shows the shortcomings of using reddening values derived using photom-

etry. We have also demonstrated the ability of using low (R$\sim$30) resolution spectroscopy to accurately characterize large quantities of objects in a relatively small amount of observation time. Utilizing the steam bands in H and K combined with the sharp flux drop-off below 1 μm offers accurate characterization over a large range of spectral types while simultaneously permitting a reddening measurement.

Using a temperature scale for the young spectral templates derived by Luhman et al. (2003), our objects were plotted on an HR diagram. Overplotting the evolutionary isochrones of Baraffe et al. (1998) and Chabrier et al. (2000) demonstrates that previously determined cluster ages of 1 Myr are consistent with our observations. Although some scatter in age is present, we observe no obvious bifurcation in the HR diagram as was observed by Slesnick et al. (2004). Assuming an age of 1 Myr, masses are determined for each object. Consistent with previous works, we observe objects several magnitudes above (or several hundred Kelvin beside) the 1 Myr isochrone that are not foreground objects. These objects are believed to be very young ($\ll$1 Myr) objects, and despite having a spectral type consistent with a planetary mass object at 1 Myr, they are most likely brown dwarfs. Such objects will be useful for testing new models of young substellar objects.

The derived masses for our objects were then used to create a cluster IMF where our completeness correction was defined based on an H-band luminosity function that was created by performing PSF photometry to every point-source in our survey. Using the ratio of the 104 objects that were assigned spectral types to the 114 objects that were spectroscopically classified as being highly absorbed or non-stellar, a completeness correction for each magnitude bin was determined. This correction was applied to our IMF determination to create a spectroscopically determined IMF ranging in mass from 0.006 to 3.16 $M_{\odot}$ based on an assumed cluster age of 1 Myr. Fitting a log-normal distribution yields a $\log m_c$ and σ of -0.89$\pm$0.04 and 0.57$\pm$0.03 respectively. These values lay between the IMF's measured for the galactic disk and are consistent with measurements in other young clusters.

4.9 Acknowledgements

We are thankful to both Kevin Luhman for providing his template spectra used in this analysis as well as Phillip Lucas for providing his spectra for comparison with ours. This work also made use of the IRTF Spectral Library, the SIMBAD database, and the 2Mass All-sky point source catalogue.

Bibliography

Albert, L. 2006, PhD thesis, Université de Montréal, Canada

Allard, F., Hauschildt, P. H., Alexander, D. R., Tamanai, A., & Schweitzer, A. 2001, Astrophysical Journal, 556, 357

Allers, K. N., Jaffe, D. T., Luhman, K. L., Liu, M. C., Wilson, J. C., Skrutskie, M. F., Nelson, M., Peterson, D. E., Smith, J. D., & Cushing, M. C. 2007, Astrophysical Journal, 657, 511

Baraffe, I., Chabrier, G., Allard, F., & Hauschildt, P. H. 1998, Astronomy and Astrophysics, 337, 403

Baraffe, I., Chabrier, G., Barman, T. S., Allard, F., & Hauschildt, P. H. 2003, Astronomy and Astrophysics, 402, 701

Briceño, C., Luhman, K. L., Hartmann, L., Stauffer, J. R., & Kirkpatrick, J. D. 2002, Astrophysical Journal, 580, 317

Burrows, A., Marley, M., Hubbard, W. B., Lunine, J. I., Guillot, T., Saumon, D., Freedman, R., Sudarsky, D., & Sharp, C. 1997, Astrophysical Journal, 491, 856

Cardelli, J. A., Clayton, G. C., & Mathis, J. S. 1989, Astrophysical Journal, 345, 245

Chabrier, G. 2003, The Publications of the Astronomical Society of the Pacific, 115, 763

Chabrier, G., Baraffe, I., Allard, F., & Hauschildt, P. 2000, Astrophysical Journal, 542, 464

Cox, A. N. 2000, Allen's astrophysical quantities, ed. A. N. Cox (The Athlone Press)

Cushing, M. C., Marley, M. S., Saumon, D., Kelly, B. C., Vacca, W. D., Rayner, J. T., Freedman, R. S., Lodders, K., & Roellig, T. L. 2008, Astrophysical Journal, 678, 1372

Grosso, N., Briggs, K. R., Güdel, M., Guieu, S., Franciosini, E., Palla, F., Dougados, C., Monin, J.-L., Ménard, F., Bouvier, J., Audard, M., & Telleschi, A. 2007, Astronomy and Astrophysics, 468, 391

Guieu, S., Dougados, C., Monin, J.-L., Magnier, E., & Martín, E. L. 2006, Astronomy and Astrophysics, 446, 485

Hillenbrand, L. A. 1997, Astronomical Journal, 113, 1733

Hillenbrand, L. A., & Carpenter, J. M. 2000, Astrophysical Journal, 540, 236

Kirkpatrick, J., Barman, T., Burgasser, A., Mcgovern, M., Mclean, I., Tinney, C., & Lowrance, P. 2006, Astrophysical Journal, 639, 1120

Kroupa, P. 2001, Monthly Notices of the Royal Astronomical Society, 322, 231

Leggett, S. K., Allard, F., Berriman, G., Dahn, C. C., & Hauschildt, P. H. 1996, Astrophysical Journal Supplement, 104, 117

Leggett, S. K., Golimowski, D. A., Fan, X., Geballe, T. R., Knapp, G. R., Brinkmann, J., Csabai, I., Gunn, J. E., Hawley, S. L., Henry, T. J., Hindsley, R., Ivezić, Ž., Lupton, R. H., Pier, J. R., Schneider, D. P., Smith, J. A., Strauss, M. A., Uomoto, A., & York, D. G. 2002, Astrophysical Journal, 564, 452

Lodieu, N., Hambly, N. C., Jameson, R. F., & Hodgkin, S. T. 2008, Monthly Notices of the Royal Astronomical Society, 383, 1385

Lucas, P. W., & Roche, P. F. 2000, Monthly Notices of the Royal Astronomical Society, 314, 858

Lucas, P. W., Roche, P. F., Allard, F., & Hauschildt, P. H. 2001, Monthly Notices of the Royal Astronomical Society, 326, 695

Lucas, P. W., Roche, P. F., & Tamura, M. 2005, Monthly Notices of the Royal Astronomical Society, 361, 211

Lucas, P. W., Weights, D. J., Roche, P. F., & Riddick, F. C. 2006, Monthly Notices of the Royal Astronomical Society, 373, L60

Luhman, K. L. 1999, Astrophysical Journal, 525, 466

—. 2004, Astrophysical Journal, 617, 1216

—. 2012, Annual Review of Astronomy and Astrophysics, 50, 65

Luhman, K. L., Rieke, G. H., Young, E. T., Cotera, A. S., Chen, H., Rieke, M. J., Schneider, G., & Thompson, R. I. 2000, Astrophysical Journal, 540, 1016

Luhman, K. L., Stauffer, J. R., Muench, A. A., Rieke, G. H., Lada, E. A., Bouvier, J., & Lada, C. J. 2003, Astrophysical Journal, 593, 1093

Menten, K. M., Reid, M. J., Forbrich, J., & Brunthaler, A. 2007, Astronomy and Astrophysics, 474, 515

Morrow, A. L., Luhman, K. L., Espaillat, C., D'Alessio, P., Adame, L., Calvet, N., Forrest, W. J., Sargent, B., Hartmann, L., Watson, D. M., & Bohac, C. J. 2008, Astrophysical Journal, 676, L143

O'dell, C. R., & Wong, K. 1996, Astronomical Journal, 111, 846

Padgett, D. L., Strom, S. E., & Ghez, A. 1997, Astrophysical Journal, 477, 705

Peterson, D. E., Megeath, S. T., Luhman, K. L., Pipher, J. L., Stauffer, J. R., y Navascués, D. B., Wilson, J. C., Skrutskie, M. F., Nelson, M. J., & Smith, J. D. 2008, Astrophysical Journal, 685, 313

Prosser, C. F., Stauffer, J. R., Hartmann, L., Soderblom, D. R., Jones, B. F., Werner, M. W., & McCaughrean, M. J. 1994, Astrophysical Journal, 421, 517

Riddick, F. C., Roche, P. F., & Lucas, P. W. 2007a, Monthly Notices of the Royal Astronomical Society, 381, 1077

—. 2007b, Monthly Notices of the Royal Astronomical Society, 381, 1067

Rio, N. D., Robberto, M., Hillenbrand, L. A., Henning, T., & Stassun, K. G. 2012, Astrophysical Journal, 748, 14

Salpeter, E. E. 1955, Astrophysical Journal, 121, 161

Skrutskie, M. F., Cutri, R. M., Stiening, R., Weinberg, M. D., Schneider, S., Carpenter, J. M., Beichman, C., Capps, R., Chester, T., Elias, J., Huchra, J., Liebert, J., Lonsdale, C., Monet, D. G., Price, S., Seitzer, P., Jarrett, T., Kirkpatrick, J. D., Gizis, J. E., Howard, E., Evans, T., Fowler, J., Fullmer, L., Hurt, R., Light, R., Kopan, E. L., Marsh, K. A., McCallon, H. L., Tam, R., Dyk, S. V., & Wheelock, S. 2006, Astronomical Journal, 131, 1163

Slesnick, C. L., Hillenbrand, L. A., & Carpenter, J. M. 2004, Astrophysical Journal, 610, 1045

Weights, D. J., Lucas, P. W., Roche, P. F., Pinfield, D. J., & Riddick, F. 2009, Monthly Notices of the Royal Astronomical Society, 392, 817

4.A Comparison to Previous Observations

Previous classifications of our objects were carried out by Weights et al. (2009) and Slesnick et al. (2004). A comparison of the classifications derived in these studies is shown in Table 4.IV. Horizontal lines divide the objects that are in agreement, slight disagreement, and inconsistent. Previous groups of authors use spectral indices to characterize their objects. Slesnick et al. (2004) calibrate their indices using main-sequence dwarf standards. In theory, this would cause their classifications to be systematically later. This is broadly seen to be true, however, no distinct trend is observed due to the uncertainties associated with each object. All of our spectral classifications are consistent

with those of Slesnick et al. (2004). However, the determined uncertainties can differ greatly, particularly for the later type objects (e.g. 081-237, 082-253, 100-501, 111-436) and may explain why the systematic offset in spectral classification is not clearly observed. Their reddenings and spectral classifications are derived using a multi-step approach where a reddening is estimated using the 1 Myr isochrone, a spectral-type is then determined, and the final reddening value is determined using the H-K colours of main-sequence dwarfs. For an M6 object, they estimate an uncertainty in their derived A_V of 1.6 magnitudes. For later spectral types and objects that are observed to lie well above the 1 Myr isochrone as observed by Weights et al. (2009) and in this paper, the uncertainty is most certainly larger. Of course, uncertainty in our extinction values also exist. However this is primarily due to the uncertainty in the extinctions of the objects in the spectral library, no assumption of age, evolutionary model, nor atmospheric model is used.

Table 4.IV: Previously Classified Objects

Our ID[a]	Reference[b]	Ref. ID	Ref. SpT	Our SpT Latest / Earliest	Ref A_V	A_V Latest / Earliest	Comparison Summary
012-145	2	205	M7±1.5	M6.00 M7.25 / M6.00	N/A	5.2 2.9 / 5.2	In agreement
013-413	1	014-413	M7.5±0.75	M6.00 M7.25 / M6.00	1.3	2.9 0.8 / 2.9	In agreement
"	3	014-413	M6.5±1.0	"	1.6[d]	"	In agreement
015-319	1	015-319	>M9.5	L0.00 L0.00 / M6.00	4.26	1.9 1.9 / 5.5	In agreement (A_V differs, but A_V is not for M9.5)
016-534	3	016-534	M5.25±0.5	M4.75 M4.75 / M4.75	0.0[d]	1.4 1.3 / 1.4	In agreement
016-410	1	016-410	M5±1.0	M4.75 M5.00 / M4.75	1.2[d]	2.2 0.6 / 2.2	In agreement
019-354	1	019-354	M6.5±1.0	M6.25 M6.25 / M5.00	1.5[d]	1.6 1.6 / 2.0	In agreement
"	3	019-354	M5.75±0.5	"	1.5[d]	"	In agreement
030-524	1	030-524	M8.0±0.75	M6.25 M8.50 / M5.50	0.0	0.2 0.6 / 1.4	In agreement (improves when A_V forced to 0.0)
"	3	030-524	M7.5±1.5	"	0.8[d]	"	In agreement
031-536	1	031-536	M9.5±1.5	M8.50 M8.50 / M7.75	0.0	1.8 1.8 / 0.1	In agreement
"	3	031-536	M8.75±1.0	"	0.0	"	In agreement
034-610	3	034-610	M5.25±0.5	M4.75 M4.75 / M4.75	0.0[d]	2.1 2.1 / 2.1	In agreement
034-333	3	035-333	M6.75±0.5	M7.25 M7.25 / M6.00	0.0[d]	0.0 0.0 / 2.1	In agreement
037-246	2	5100	M2-M5±1.5	M5.00 M5.25 / M4.75	N/A	5.6 6.5 / 5.9	In agreement
"	3	037-246	M5.5±1.0	"	3.4[d]	"	In agreement
037-627	1	037-628	>M9.5	M9.00 L0.00 / M7.25	2.2[d]	1.8 0.7 / 1.8	In agreement
041-210	3	041-210	M	M3.75 M6.00 / M3.75	4.0[d]	5.6 5.2 / 5.7	In agreement
044-527	1	044-527	M8.5±0.5	M8.25 M8.25 / M6.00	0.0	0.9 0.9 / 2.1	In agreement
044-219	3	044-219	Late-M	M8.00 M8.50 / M7.00	2.9[d]	2.2 1.5 / 3.9	In agreement
064-212	2	509	M2-M7±1.5	M8.25 L0.00 / M3.75	4.86[c]	5.4 2.8 / 7.7	In agreement
070-500	2	64	M7-M9±1.5	M7.00 M7.75 / M7.00	4.46[c]	4.9 2.8 / 4.9	In agreement
072-638	3	072-638	M6.5±0.5	M6.25 M6.25 / M6.25	0.2[d]	0.1 0.1 / 0.1	In agreement
073-227	2	467	M6±1.5	M4.75 M4.75 / M3.75	2.55[c]	1.5 1.5 / 2.5	In agreement

Continued on Next Page...

Table 4.IV – Continued

Our ID[a]	Reference[b]	Ref. ID	Ref. SpT	Our SpT$^{\text{Latest}}_{\text{Earliest}}$	Ref A_V	$A_V{}^{\text{Latest}}_{\text{Earliest}}$	Comparison Summary
074-229	2	459	M6±1.5	M4.75$^{\text{M5.25}}_{\text{M4.75}}$	1.59[c]	1.1 $^{0.4}_{1.1}$	In agreement
077-127	3	077-127	M8.5±1.0	M9.25$^{\text{M9.50}}_{\text{M9.25}}$	0.9[d]	0.9 $^{1.2}_{0.9}$	In agreement
081-237	2	433	M8±1.5	M8.50$^{\text{L0.00}}_{\text{M6.00}}$	10.44[c]	5.3 $^{1.6}_{5.5}$	In agreement
082-403	3	082-403	M4.75±0.5	M4.75$^{\text{M4.75}}_{\text{M3.75}}$	4.1[d]	4.1 $^{4.2}_{4.7}$	In agreement
082-253	2	429	M9±1.5	M7.00$^{\text{M8.50}}_{\text{M6.00}}$	5.53[c]	3.3 $^{0.8}_{3.2}$	In agreement
"	3	082-253	M8.5±1.5	"	3.2[d]	"	In agreement
084-305	3	084-305	M7.0±0.5	M8.25$^{\text{M9.25}}_{\text{M6.00}}$	4.0[d]	4.0 $^{3.3}_{5.1}$	In agreement
086-324	2	290	M5.5±1.5	M6.25$^{\text{M7.50}}_{\text{M5.50}}$	6.64[c]	4.8 $^{4.9}_{6.2}$	In agreement
"	3	086-324	M	"	4.8[d]	"	In agreement
092-605	3	092-606	M8.0±2.0	M8.50$^{\text{M9.50}}_{\text{M8.50}}$	1.4[d]	0.1 $^{0.2}_{0.1}$	In agreement
100-501	2	62	M9±1.5	M9.00$^{\text{M9.50}}_{\text{M9.00}}$	5.85[c]	0.5 $^{1.5}_{0.5}$	In agreement
102-100	3	102-102	M6.25±0.5	M6.00$^{\text{M6.00}}_{\text{M5.50}}$	0.0[d]	1.5 $^{1.5}_{1.9}$	In agreement
103-157	2	553	M5±1.5	M5.50$^{\text{M6.00}}_{\text{M5.50}}$	5.77[c]	2.3 $^{1.9}_{2.3}$	In agreement
"	3	103-157	M5.75±0.5	"	1.0[d]	"	In agreement
103-451	2	90	M7.5±1.5	M8.50$^{\text{L0.00}}_{\text{M6.00}}$	6.77[c]	5.9 $^{3.5}_{7.3}$	In agreement
111-436	2	111	M9±1.5	M7.25$^{\text{L0.00}}_{\text{M5.50}}$	8.61[c]	1.3 $^{0.3}_{4.6}$	In agreement
111-532	1	112-532	M4.75±0.5	M4.00$^{\text{M4.50}}_{\text{M4.00}}$	3.6[d]	1.9 $^{2.7}_{1.9}$	In agreement
118-155	2	555	M6±1.5	M4.75$^{\text{M5.00}}_{\text{M4.75}}$	1.56[c]	2.2 $^{0.5}_{2.2}$	In agreement
121-433	1	121-434	M7.0±0.25	M8.25$^{\text{M8.25}}_{\text{M6.25}}$	4.44	4.1 $^{4.2}_{4.5}$	In agreement
"	3	121-434	M5.5±1.0	"	4.4[d]	"	In agreement
129-458	3	130-458	M5.25±0.5	M4.50$^{\text{M4.75}}_{\text{M2.00}}$	4.0[d]	2.0 $^{1.8}_{2.6}$	In agreement
130-053	3	130-053	M8.5±2.0	M7.25$^{\text{M9.25}}_{\text{M7.25}}$	0.4[d]	2.2 $^{3.4}_{2.3}$	In agreement
023-123	1	024-124	>M9.5	M6.25$^{\text{M7.50}}_{\text{M5.50}}$	3.6	6.2 $^{6.4}_{7.5}$	Disagrees. Within error if A_V=3.6 is forced
055-231	1	055-230	M9.5±0.75	M6.00$^{\text{M7.50}}_{\text{M6.00}}$	0.0	3.3 $^{2.5}_{3.3}$	Disagrees. Agrees if J-band removed and A_V=0

Continued on Next Page...

Table 4.IV – Continued

Our ID[a]	Reference[b]	Ref. ID	Ref. SpT	Our SpT$^{\text{Latest}}_{\text{Earliest}}$	Ref A_V	$A_V{}^{\text{Latest}}_{\text{Earliest}}$	Comparison Summary
"	3	055-230	M6.75±1.5	"	0.9[d]	"	In agreement
077-452	1	077-453	M6±0.75	M5.50$^{\text{M5.50}}_{\text{M5.50}}$	1.9	0.0 $^{0.0}_{0.0}$	In agreement
"	3	077-453	M6.5±0.5	"	1.9[d]	"	Slight disagreement
083-102	1	084-104	>M9.5	M7.25$^{\text{M9.00}}_{\text{M7.25}}$	0.05	1.4 $^{1.2}_{1.3}$	Slight disagreement. L0 if A_V=0.05 is forced
095-059	1	095-058	M7.5±0.75	M6.00$^{\text{M7.25}}_{\text{M6.00}}$	0.0	2.0 $^{0.0}_{2.0}$	In agreement but mediocre fit
"	3	095-058	M6.25±0.5	"	0.0[d]	"	In agreement
052-323	1	053-323	Early M	M7.50$^{\text{M8.50}}_{\text{M5.50}}$	0.25	0.3 $^{0.8}_{1.2}$	Inconsistent
066-650	1	067-651	M6.0±0.5	M3.75$^{\text{M3.75}}_{\text{M3.75}}$	2.78	2.8 $^{2.8}_{2.8}$	Inconsistent. Mediocre fit in J

a. ID format follows from ODell & Wong 1996. XXX-YYY implies an RA of 05:35:XX.X and DEC of -05:2Y:YY
b. 1. Weights et al 2008, 2. Slesnick et al 2004 and reference therein, 3. Riddick et al 2007
c. Reddening derived assuming an age of 1Myr. Uses reddening law of Cohen et al 1981
d. Derived by dereddening photometric J and H colors to the 1 Myr isocrone

The extinctions of the objects derived by Riddick et al. (2007a), Lucas et al. (2001) and Weights et al. (2009) also rely on photometric colours. This most likely results in an uncertainty in their derived reddening but because their spectral indices used to derive a spectral type are largely insensitive to reddening, their spectral classification should not be greatly affected. In general, we find our spectral classifications to be in excellent agreement with the results of Riddick et al. (2007a) and Weights et al. (2009), with only a few discrepancies; some of which were previously observed by the previous authors. As objects 055-230, 052-323, 066-650, 077-452 were addressed in section 4.4.2, we address the remaining objects here.

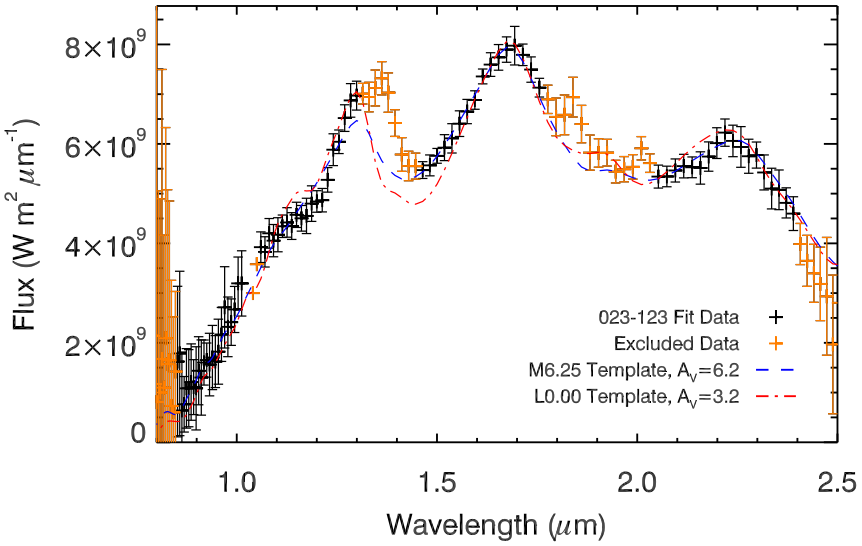

Figure 4.17: Comparison of the spectral classification of object 023-123 as performed by Weights et al. (2009) (>M9.5, represented as L0, red dash-dot line) and this work (M6.25, blue dashed line).

Object 023-123 was determined by Weights et al. (2009) to have a spectral type of >M9.5 with an extinction of A_V=3.6. This classification was derived using a single spectral index in *H* band and reinforced by comparing the spectrum ($1.56-1.63\mu$m) with that of an $\sim$5 Myr, L0 dwarf of Lodieu et al. (2008). Our derived spectral type is M6.25 with an extinction of A_V=6.2. The difference in these classifications is largely

due to the derived reddening value. If we force an A_V to be equal to 3.6, a spectral type of L0 is one of the plausible solutions. Figure 4.17 shows our derived template and the best fit of the L0 template. The M6.25 template does provide the better fit, particularly to region between 1.45-1.55 μm where the spectrum of Weights et al. (2009) was truncated. The fit in K band of the M6.25 template is also superior. One curious characteristic is the flattening of the J band near 1.15μm. This flattening is often observed in late-type objects and is not readily apparent in the spectrum of the M6.25 template. Higher S/N data is required to discern the significance of this feature. If true, this may signify a later spectral type, possibly later than anything in our spectral library. Incidentally, on the HR diagram, our spectral classification and extinction value puts the object $\sim$1 magnitude above the 1 Myr isochrone whereas the classification of Weights et al. (2009) puts the object $\sim$1.7 magnitudes above the 1 Myr isochrone. However, because numerous objects have been observed above the 1 Myr isochrone, the difference of placement on the HR diagram does not rule out the late-type spectral classification.

The optically determined spectral type of object 095-059 by Riddick et al. (2007a) was found by Weights et al. (2009) to be discrepant from the near-IR spectral type. This object is discussed in their appendix. The near-IR spectral type was derived using H band indices because the K band indices may be bias due to the possibility of circumstellar dust introducing a near-IR excess. Our spectral classification is consistent with the optically derived value and inconsistent with the near-IR spectral type. However, we report a mediocre fit as the template shows multiple discrepancies in J, H and K bands. If an infrared excess is indeed present, this could explain how none of our template spectra produce an accurate representation of the object.

Object 083-102 was classified by Weights et al. (2009) as having a spectral type of >M9.5 with an associated extinction of A_V=0.05. As shown in Table 4.IV, this is slightly discrepant from our derived value. We believe this is due to the differences in the reddening values. Because this object was not detected in the I band observations of Lucas et al. (2001), it was dereddened to the 1 Myr isochrone and therefore may be uncertain. To determine the effect of using their determined reddening value, we re-classified the object while forcing an A_V=0.05. When doing so, the L0 and M9 spectral

templates are highly favoured as the best fitting spectral type (64 of 100) trials, whereas the M7.25 spectral template is the best fit in 36 trials.

CHAPTER 5

CONCLUSION

The amount of wavefront error in an optical system is one of the fundamental limitations to performing direct imaging of exoplanets. Wavefront errors scatter the light out of the core of the PSF which manifests itself as quasi-static speckles in the image plane. These speckles dominate over the signal of the exoplanet, rendering it undetectable. Multiple techniques have been developed to attenuate these speckles. This thesis explores speckle suppression technique of SDI using a Fabry-Perot etalon as a tunable narrowband filter.

Previous experiments performing ground-based SDI used beam splitters to simultaneously image an object at multiple wavelengths. Their performance was limited by the differential wavefront error introduced in each wavelength channel. Performing space-based, non-simultaneous SDI eliminates the need for atmospheric correction and hence the multiple channels. Space-based imagers using multiple interference filters also introduce differential wavefront error that could limit the speckle suppression performance. The principle advantage of using an etalon as a tunable filter is that the wavefront error for each wavelength is equal and therefore no differential WFE is introduced. Prior to this thesis, this concept had never been tested and the amount of differential WFE resulting from the multiple reflections inside the etalon had never been measured.

Using a low-order Fabry-Perot prototype etalon and a custom designed optical test bed, it was determined that performing speckle suppression using an etalon resulted in a contrast improvement ranging from a factor of 10 at working angles greater than 11 λ/D increasing up to a factor of $\sim$60 at a separation of 5 λ/D. Comparison to a theoretical optical model determined that the increase in contrast was limited by the imaging capabilities of the test bed and not the etalon. This work demonstrated the ability of an etalon to perform space-based high contrast imaging through SDI. It was also demonstrated that when dealing with moderate contrast gains, the WFE originating from the multiple reflections between the plates is negligible. This conclusion enabled accurate

modelling of high-contrast imaging observations using a real telescope and instrument configuration.

This thesis also investigated the companion detection and characterization capability of a Fabry-Perot etalon in the context of the TFI, an infrared imager featuring a Fabry-Perot etalon designed to be part of the scientific instrument complement on board JWST. By combining the theoretical WFE map for the optical telescope elements with the measured WFE maps of the TFI instrument components, a detailed optical model was developed to simulate realistic SDI observations of faint companions. This simulation demonstrated that SDI offers a contrast improvement ranging from a factor of $\sim$7 to $\sim$100 depending on the instrument's configuration. TFI's four coronagraphic modes and a non-coronagraphic mode were simulated and the observational challenges encountered when performing SDI were addressed. This included optimizing the wavelength separation required to obtain a maximum detection probability while minimizing the effects of out-of-pupil WFE and how to properly utilize the features of the positive-negative signature to maximize the characterization potential and to determine the S/N of the measurement. Purely coronagraphic observations yield 10σ detections at a separation of $1''$ when the companion-to-star ratio is $10^{-2.7}$ at 4.0 μm. Using SDI, the detection contrast is dependent upon the atmospheric features of the companion. The 10σ contrast limit is increased to $10^{-3.7}$ for companions with flat spectra and $10^{-4.1}$ for companions exhibiting sharp spectral features.

The effectiveness of SDI observations and the developed signal extraction methods to perform faint companion characterization were demonstrated using JWST simulations of the HR 8799 and Fomalhaut systems. Using the optical model, the effect of pointing error on speckle attenuation using roll-subtraction was also demonstrated. Should the pointing requirements for JWST be achieved, roll-subtraction will offer speckle attenuation equivalent to that of SDI at separations less than $\sim 2''$ and will exceed SDI attenuations at larger separations. Because NIRISS, the reconfigured version of TFI, utilizes many of the same optical components, the non-coronagraphic SDI capability was determined using a modified version of the TFI optical model. The improvement in contrast ranges from a factor of 7-12 at all separations with the 10σ detection contrast limit

at $1''$ being $10^{-3.4}$. Based on these results and the characterization capabilities of the NIRISS filters, it is suggested that an SDI observing mode be implemented for NIRISS.

Finally, the results of a survey for young stellar and substellar objects in the Orion Trapezium Cluster was presented. This survey characterized 104 objects towards the central region of the Orion Nebular Cluster through low resolution, multi-band (0.85-2.4 μm) multi-object spectroscopy,. This includes 7 newly discovered brown dwarfs and 4 new planetary mass candidates. Whereas previous studies utilize spectral indices from narrow wavelength regions to perform spectral classification, we demonstrate the effectiveness of using a large spectral range at a lower resolution. This type of measurement enables the determination of both the spectral type and reddening. Furthermore, signatures of youth, such as low gravity, are detectable from distinct features in the spectra. When the classified objects are plotted on an HR diagram, the results indicate a cluster age of 1 Myr, consistent with previous studies. Combining these data with the 114 other objects that were spectroscopically characterized to be either highly absorbed objects (A_V>8) or non-stellar objects, we spectroscopically classified 218 of the 346 point sources in our survey area. After applying a completeness correction, we determined that the IMF is accurately described by a log-normal distribution having a characteristic mass (m_c) and width (σ) of 0.12$\pm$0.01 $M_\odot$ and 0.57$\pm$0.03, respectively. These coefficients are consistent with the values determined for the galactic disk and other young clusters. The objects in this survey are also excellent test cases for future atmospheric models of young objects. Furthermore, they may aid in understanding the relationship between exoplanets, free-floating planets, and brown dwarfs; particularly in the mass regimes where both objects are known to simultaneously exist. Numerous objects were found to be several magnitudes brighter than what is expected of a 1 Myr object. These are expected to be very young objects and therefore their mass is not well constrained, however they may prove to be an excellent test to future theoretical models of young substellar objects. Further spectroscopic observations are required to better constrain the nature of these objects.

With the new wave of high-contrast imaging instruments such as SPHERE and GPI coming online within a year, exoplanetary science will be provided with a plethora of

new information that will further our understanding of planetary formation and evolution. The new parameter space that these instruments will explore is fully complementary to RV and transit studies already underway. These instruments will also produce near-infrared low-resolution spectra of exoplanets, providing new data which will be used to constrain atmospheric models of young planetary mass objects. The launch of JWST late in this decade will provide mid- and far infrared followup observations to many of these objects. Lessons learned from these studies will provide insight into the design of future ground- and space-based telescopes and exoplanet imaging instruments, such as the TMT, E-ELT, and TPF projects. With the discovery of exoplanets, the field of planetary science has experienced significant growth and much work remains to be done before we will understand planet formation and evolution. The field is merely in its infancy.